Quantitative Thermal Performance Assessment of Building Envelopes – Emergent Practices and Infrared Thermography

by

Milad Mahmoodzadeh
MASc, University of Victoria, Canada, 2018
BSc, Persian Gulf University, Iran, 2010

A Dissertation Submitted in Partial Fulfillment of the Requirements for the Degree of
DOCTOR OF PHILOSOPHY
in the Department of Civil Engineering

University of Victoria

Quantitative Thermal Performance Assessment of Building Envelopes – Emergent Practices and Infrared Thermography

by

Milad Mahmoodzadeh
MASc, University of Victoria, Canada, 2018
BSc, Persian Gulf University, Iran, 2010

Supervisory Committee

Dr. Phalguni Mukhopadhyaya, Supervisor
Department of Civil Engineering

Dr. Lina Zhou, Academic Unit Member
Department of Civil Engineering

Dr. Caterina Valeo, Non-Unit Member
Department of Mechanical Engineering

Abstract

Since many buildings in Canada were built prior to the advent of national and provincial energy codes and standards, quantifying building envelope thermal performance in existing buildings is an important step in identifying retrofit opportunities. Due to the lack of building codes or standards for existing buildings in Canada, development of a rapid and robust quantitative approach to evaluate and rank buildings for vertical envelope retrofits is required. Hence, this dissertation sought to develop quantitative approaches to evaluate existing building envelope thermal performance in Canada and beyond.

Following current professional practices, in Chapter 1, a comprehensive study was conducted on 49 campus buildings at the University of Victoria (UVic) to evaluate potential energy savings from vertical envelope retrofits, and to further validate those savings through more detailed energy models and parametric analyses for a subset of buildings. To this end, the thermal performance of a building envelope was quantified based on its heat loss coefficient (UA), obtained from multiplying its surface area (A) by its thermal transmittance (U-value). Heat loss calculations were used as a metric to inform envelope rehabilitation prioritization, while considering other data such as age and physical condition in parallel. Archetype energy models for selected buildings were used to evaluate the impacts of envelope retrofits on energy and GHG savings. The outcomes of this study allowed the University to weigh the benefits of improved energy performance from envelope retrofits against associated capital cost expenditures. Also, the implemented methodology and studied parameters unveiled a new horizon in evaluating the thermal performance of existing building envelopes in Canada, where a building code for existing buildings has not yet been established. Considering the economic findings of the envelope retrofits studied, it was concluded that in the absence of an existing building energy code, the University would likely require additional incentives, such as higher utility costs, higher carbon taxes, or qualifying for utility incentive programs to justify improving existing building envelope performance on the basis of energy only.

The strength of the proposed methodology in Chapter 1 was in its balance of effort and ultimate decision-making utility, where reasonable thermal bridging approximations based on simulation models for existing buildings can yield data accurate enough to inform a ranking exercise on a large breadth of subject buildings. However, since numerical models do not consider degradation of building materials, real moisture content, and errors associated with manufacturing and installation, actual building envelope thermal performance differs from 3D simulation models. To study this limitation, in-situ thermal assessments of building envelopes were performed to quantify their actual thermal performances. To this end, Chapters 2 to 4 of this dissertation attempted to determine the viability of an external infrared thermography (IRT) survey technique for quantification of heat losses through the opaque building envelope, and also explores its potential application in identifying and comparing sources of air leakage. The experiments were performed on wood-framed wall assemblies commonly used in Canada due to growing interest among designers, builders, and governments to encourage the use of wood as a building material.

In these studies, (Chapter 2 to Chapter 4), thermal transmittances (U-values) of wall assemblies were estimated with external IRT and compared with 3D computer simulations. Furthermore, the impact of the accuracy of U-values estimated with IRT on the deviation of energy simulation outputs with metered data was examined. Finally, a novel relative quantitative infrared index (IRI) was proposed as a means to facilitate rapid evaluation and subsequent ranking of building envelope thermal performance. From the experiments in Chapters 2 & 3, it was found that the U-values obtained with IRT were comparable with simulated values suggesting IRT can be a reliable tool for estimating the thermal performance of wood-framed wall assemblies. Results also demonstrated that thermal imaging artefacts including nonlinear characteristics of infrared (IR) camera focal array, a.k.a. non-uniformity corrections (NUC) and vignetting could have a substantial influence on the accuracy of results, in particular energy model outputs. This limitation was resolved by introducing a practical approach where thermal images were taken from different incident angle. Overall, IRI was found to be a reliable metric for relative quantitative comparison of building envelope thermal performance regardless of boundary conditions. Moreover, outcomes of the IRT air leakage study in Chapter 4 indicated that combined qualitative and quantitative IRT approaches could potentially be implemented by practitioners to identify sources of air leakage and thermal bridges in buildings and compare their relative severity. Since blower door testing is gradually being introduced as a building code requirement to measure building envelope airtightness in an increasing number of Canadian jurisdictions, performing IRT simultaneously is potentially valuable exercise in this context. Ultimately, the methodologies outlined in Chapters 2 to 4 can help decision-makers to characterize building envelope retrofits from a performance perspective, and potentially serve as a basis for governments to develop policies to improve existing building energy performance.

The methodologies in Chapters 2 to 4 prompted opportunities to utilize the emergent technology of small unmanned aerial vehicles (UAVs) equipped with an infrared camera for quick thermal assessments of building envelopes. The last chapter of this dissertation, Chapter 5, outlines advantages and limitations of aerial IRT (UAV-IRT) surveys compared to conventional stationary IRT. Furthermore, a set of best practices for UAV-IRT were presented to minimize dynamic measurement uncertainty. It was concluded that with the current IR camera technology, aerial surveys for quantitative thermal assessment of building envelope are not as accurate as with conventional infrared thermography; further investigations by manufacturers and researchers are recommended.

Table of Contents

List of Figures

List of Tables

List of Publications

This dissertation is based on the following published manuscripts:

i. M. Mahmoodzadeh, V. Gretka, S. Wong, T. Froese, P. Mukhopadhyaya, Evaluating Patterns of Building Envelope Air Leakage with Infrared Thermography, ***Energies***. (2020) 13 (14), 3545.
https://www.mdpi.com/1996-1073/13/14/3545

ii. M. Mahmoodzadeh, V. Gretka, A. Blue, D. Adams, B. Dallimore, P. Mukhopadhyaya, Evaluating thermal performance of vertical building envelopes: Case studies in a Canadian university campus***, Journal of Building Engineering***. 40 (2021) 102712.
https://doi.org/10.1016/j.jobe.2021.102712

iii. M. Mahmoodzadeh, V. Gretka, K. Hay, C. Steele, P. Mukhopadhyaya, Determining overall heat transfer coefficient (U-Value) of wood-framed wall assemblies in Canada using external infrared thermography, ***Journal of Building and Environment***. 199 (2021): 107897.
https://doi.org/10.1016/j.buildenv.2021.107897

iv. M. Mahmoodzadeh, V. Gretka, I. Lee, P. Mukhopadhyaya, Utilizing External Infrared Thermography to Assess Thermal Performance of Wood-Framed Building Envelopes in Canada, ***Journal of Energy and Buildings***. (2021) 111807.
https://doi.org/10.1016/j.enbuild.2021.111807

Acknowledgment

I have been fortunate to have had the support, guidance, enthusiasm, wisdom, and friendship of many individuals throughout three years of my PhD studies at the University of Victoria. This dissertation is dedicated to all who have made this journey such an enjoyable learning process.

First and foremost, I would like to express my special appreciation and thanks to my supervisor Dr. Phalguni Mukhopadhyaya, who has been a tremendous mentor for me. I appreciate all his contributions (time, ideas, support and patience) to make my PhD experience productive and stimulating. I would like to thank him for encouraging my research and allowing me to grow both personally and professionally.

My sincere thanks also go out to my committee members: Drs. Lina Zhou and Caterina Valeo for their time, interest, and constructive comments. I also want to thank them for the brilliant comments and suggestions. Among many other things, I am thankful to both technical and administrative staffs in Civil engineering department for their supports to my research activities.

I am thankful to Morrison Hershfield Ltd., BC Housing, NSERC, CFI and MITACS to fund this research project directly or indirectly. My special appreciation extends to Mr. Voytek Gretka at Morrsion Hershfield Ltd for his unique blend of leadership and friendship, which made our research collaboration productive and enjoyable. He generously agreed to support this project, and was always available to answer technical questions as they arose. I could not have asked for a better mentor from the industry and I am very grateful for the opportunity, training, and encouragement he provided me with.

I would like to thank my friends for their support and encouragement over the past three years. To my siblings, who have always been reliable supporters during tough times, standing by me with compassion and selflessness without whom the completion of this dissertation would have never been possible. Last, but definitely not the least, to my parents for instilling in me the drive to persevere, and the freedom to make my own choices, and for always providing a listening ear, I would like to say thank you.

Introduction

Background and motivation

Energy consumption in the built environment has increased considerably over the past decades mainly as a result of population growth, occupants spending more time indoors, higher expectations of indoor comfort (thermal and air quality), and a changing climate. According to the International Energy Agency (IEA), building operation and construction collectively consume 36% of total global energy, and are responsible for almost 40% of direct and indirect greenhouse gas (GHG) emissions. Most regulations and building energy codes focus on the energy efficiency of new buildings. However, energy consumption of existing buildings is an area which deserves more attentions from long-term energy policy makers and regulators since: (1) existing buildings often have higher energy use intensities (EUIs) than new constructions, and (2) the vast majority of building stock at any given period are existing and in need of some form of rehabilitation or retro-commissioning due to deteriorating building envelopes and/or mechanical and electrical systems, presenting an economic opportunity to increase their energy efficiency.

In Canada, building codes are evolving to meet multiple objectives, including reducing energy consumption and greenhouse gas emissions, increasing resiliency and passive survivability. For example, the City of Toronto, City of Vancouver and the Province of British Columbia have included the Thermal Energy Demand Intensity (TEDI) metric in addition to Energy Use Intensity (EUI) into policy document in an effort to address the performance of the building envelope and ventilation air heating requirements in new construction. TEDI elevates the importance of the building envelope, which is viewed as one of the more robust energy saving measures in a building. However, no Canadian jurisdictions have adopted energy performance requirements for existing buildings. The federal government of Canada has plan to introduce a building code for evaluation of existing buildings in 2022. Provincial codes will be created and developed to meet the requirements of federal standards and line up with a range of other priorities, including energy efficiency, earthquake safety, and occupant health and safety. The province will perform research and consult with stakeholders to implement the building code within two years of the national publication (i.e. by 2024).

Among retrofit strategies, upgrading the building envelope plays a key role in improving existing building energy performance. Previous studies have introduced different methodologies for prioritizing buildings in a portfolio for energy retrofits, however; using particular criteria as a methodology to evaluate and rank buildings for envelope retrofits is missing in literature. In practice, building envelopes undergo retrofits when its physical condition dictates. However, physical condition of a building envelope should not be used as the only metric for determining a retrofit priority in a portfolio since it does not necessarily correlate with its thermal performance. Another criterion sometimes used by portfolio managers for ranking buildings is energy use intensity (EUI). However, this metric can be a misleading indicator for opportunities to improve building envelope performance, since EUI apart from building envelope, depends on other variables such as internal loads, building typology, schedules, and efficiency and controls of mechanical systems. Furthermore, EUI data is not always available for existing buildings due to lack of metering, which would prevent even the most basic energy consumption benchmarking. Consequently, building envelope thermal performance should be evaluated independently for more accurate prioritization.

Current quantitative methods for thermal assessments of building envelopes are based on simplified assumptions from historical codes and references. This approach does not reflect actual performance due to temporal degradation of components, and ignores the increased heat losses from thermal bridges. For instance, disregarding thermal bridges can result in a 20% to 70% underestimation of the total heat flow through walls. In recent years, modern computer simulation tools have enabled a better estimation of thermal bridging effects, in turn facilitating more accurate (effective) U-value estimates; common assemblies and transitions catalogued as in the Building Envelope Thermal Bridging Guide (BETBG) or its online analog ThermalEnvelope.ca are facilitating more widespread adoption of the technique by practitioners. Nonetheless, these approaches do not reflect the actual performance of existing building envelopes due to the temporal degradation of components, material density and moisture content, and limitations in construction effectiveness. Therefore, thermal assessments of building envelopes require a comprehensive approach which considers the impact of thermal bridges and architectural design parameters of buildings, and should be rapid and based on the real conditions of building envelopes.

In recent years, utilizing in-situ measurements such as heat flux meter (HFM) or infrared thermography (IRT) have drawn more attention as a potential U-value estimation tools. In-situ U-

values are evaluated by standardized methods described in ISO 9869 and ASTM C1155. HFMs and thermocouples are used to measure interior and exterior surface temperatures temporally, from which the U-value can be derived through progressive averaging. However, point source HFMs and thermocouples cannot reasonably show imperfections and non-homogenous areas in the building envelope. Furthermore, a HFM is invasive and the duration of the test is lengthy (72+ hours), altogether cumbersome and prohibitive.

Hoping to create a less invasive and more accurate means of U-Value measurement, researchers have developed methodologies which utilize infrared cameras as a means of data collection. Over the last 25 years, IRT has been widely utilized in the inspection of building envelope physical deterioration. Most building envelope defects are ultimately a result of moisture accumulation, which can occur either by poor envelope detailing allowing precipitation ingress from the exterior, or by via condensation at locations with thermal bridging from air leakage. However, thermal patterns associated with either scenario are different, which are important to identify. For instance, moisture or pooling water within the building envelope presents as a non-homogenous thermal pattern on the surfaces, often reducing the measured temperature due to evaporative cooling. Areas of potential air leakage can also be identified with IRT, as air leakage induces temperature differences at and around the point of air leakage. The magnitude of temperature differences can depend on the size of the leakage point, pressure differences between the inside and outside, and the indoor–outdoor temperature difference. These areas can be identifiable with IRT from the inside when the building is depressurized, or from the outside when the building is pressurized. Areas with thermal bridging have a higher pixel intensity compared to undisturbed areas when analyzed with external IRT, in general. Likewise, hot spots in building envelope due to the degradation/missing of thermal insulation or air leakage effects are detectable by IRT. These anomalies in thermal behavior of building components are mainly determined with qualitative IRT, while quantification of thermal irregularities and assessment of insulation thermal performance require quantitative methods. Generally, in both quantitative and qualitative approaches, anomalies on the surface are evaluated visually or numerically based on their temperature patterns in thermal images.

Over the last decade, researchers have developed methodologies that utilize infrared cameras as a means of data collection to quantify thermal anomalies, measure in-situ U-value, determine dynamic characterization of building elements, estimate linear thermal transmittance (psi-value),

evaluate insulation effectiveness, and identify moisture ingress. These methodologies study the subject under in-situ conditions (passive thermography), in contrast to active thermography which utilizes an external thermal stimulus. However, a few investigations have devoted attention to the development of IRT methodologies to quantify the contribution of thermal bridges on measured U-values. In these studies, the variations in U-value due to thermal bridging were mainly determined based on the calculation of heat flux, linear thermal transmittance (psi-values) and incidence factor of thermal bridging.

IRT surveys are performed both from the interior and exterior; typically indoor IRT results are more acceptable than external IRT due to reduced climatic fluctuations and unknown thermal reflections from the surroundings, and relatively mitigated air movement implying a only minor variations in convective heat transfer coefficient. Although the stability of indoor conditions in indoor IRT can help practitioners obtain more precise results, current methodologies in literature suggest it is possible to estimate the U-value of a building element, and in turn estimate heat loss through it utilizing an external thermographic survey and accompanying internal temperature measurement of the walls' surface or internal air temperature. This leads to the potential of creating a strictly external thermographic survey methodology auditing the entire building envelope in a short period of time. Consequently, development of this kind of external IRT technique facilitates future utilization of unmanned aerial vehicles (UAVs) equipped with infrared cameras for conducting large-scale quantitative surveys in a fraction of the time without the need for current intrusive methods.

Published literatures clearly indicated that: (1) Traditional thermal assessment of vertical building envelope neglected the effect of thermal bridges and architectural design parameters on the actual or effective U-value, (2) Effective and clear wall U-value measurement of vertical building envelope using external infrared thermography (IRT) has not been investigated in previous studies, (3) Identification and prioritization of areas of air leakage using combined qualitative and quantitative IRT has not been focused in previous studies , and (4) Quantification of thermal assessment of vertical building envelope using the emergent technology of small unmanned aerial vehicles, UAVs, or drones, equipped with an infrared camera is missed in the literature. Finally, development of a rapid in-situ ranking metric is required for rapid evaluation and subsequent ranking of building envelope thermal performance.

Research objectives

This dissertation has four major objectives:

1. Develop a robust and rapid quantitative approach for large-scale evaluating and ranking building envelope thermal performance using conventional approach.
2. Develop in-situ quantitative approaches for U-value estimation and air leakage characterization of wall assemblies using external and internal IRT.
3. Develop a whole building envelope in-situ thermal assessment ranking metric based on external IRT.
4. Evaluate the potential of IRT with Unmanned Aerial Vehicles (UAV) for quantitative thermal assessment of building envelopes.

Dissertation outline

As the starting point of this study, **Chapter 1** focuses on building envelope thermal assessment of 49 non-residential buildings across the university campus portfolio, and to further validate those savings through more detailed energy models for a subset of buildings. To this end, the thermal performance of a building envelope is quantified based on its heat loss coefficient (UA), obtained from multiplying its surface area (A) by its thermal transmittance (U-value). Heat loss (UA) calculations are used as an energy loss metric to inform envelope rehabilitation prioritization, in addition to data gathered from building envelope condition assessments (BECAs). UA data are also analyzed against other building data such as floor area, vertical envelope area, vertical area to floor area ratio (VFAR), window-wall ratio (WWR), age, and type of construction for potential correlations. Finally, archetype energy models are used to evaluate the impacts of envelope retrofits on energy and GHG savings on three selected buildings. At the end of this chapter, the outcomes inform the University to weigh the benefits of improved energy performance from envelope retrofits against associated capital cost expenditures.

To address the limitations of theoretical method, **Chapters 2 to 5** focus on development of in-situ quantitative thermal assessment of building envelope using external IRT. To this end, in **Chapters 2 and 3**, experimental studies are carried out on a wood-framed test structure adjacent to an existing conditioned campus building at the University of Victoria, Victoria, BC. The structure consists of four different rain-screen wall assemblies, which are representative of low-rise Canadian west-coast construction. In **Chapter 2**, the attempt is made to develop an external IRT

method to determine clear wall U-values, where the impacts of repeating members (studs) are considered. The proposed method is compared with two established practices in Canada, namely the parallel path method and 3D thermal simulations. Also, the importance of region of interest (ROI) size and location on the accuracy results are evaluated. Besides the importance of environmental conditions on the thermal images, two thermal imaging artefacts are assessed and discussed in the chapter, including nonlinear characteristics of infrared (IR) camera focal array, a.k.a. non-uniformity corrections (NUC) and vignetting. IRT technique is extended in **Chapter 3** to estimate the effective U-value of wood-framed wall assemblies to estimate opaque building envelope effective U-value (considering the impact of thermal bridging). Furthermore, the effect of vignetting artefacts on effective U-value calculations is assessed, followed by a practical approach to correcting for it to improve accuracy. The impact of measured U-values on overall energy consumption is also investigated, utilizing building energy models calibrated to metered energy data. Additionally, a comprehensive uncertainty analysis is performed to evaluate the impact of input variables on the accuracy and uncertainty of results. Finally, apart from qualitative and quantitative thermal assessment of the building envelope, a relative quantitative infrared index (IRI) methodology is proposed as a means to facilitate rapid evaluation and subsequent ranking of building envelope thermal performance.

Since air leakage can have a significant impact on building energy consumption in cold climates, like in Canada, **Chapter 4** aims to demonstrate a method involving qualitative and quantitative components that can be used to characterize locations of air leakage with infrared thermography. The experiments are performed in a room of a laboratory building constructed in 1948 and is located in Victoria, BC. Fan-pressurized tests are performed to quantify the air leakage characteristics of the room. Furthermore, to detect the areas of air leakage with IRT, thermal images are taken simultaneously while the room is depressurized with the fan. The qualitative and quantitative approaches in this study will provide opportunities for practitioners to identify and prioritize the sources of air leakage in buildings.

Finally, in **Chapter 5**, the potential of IRT with Unmanned Aerial Vehicles (UAV) for quantitative thermal assessment of building envelopes is evaluated. This study outlines the advantages and limitations of aerial surveys compared to conventional stationary infrared thermography (IRT). Furthermore, a set of best practices for UAV-IRT are presented to minimize dynamic measurement

uncertainty. This work will initiate a step towards a highly automated and reliable method for inspecting and quantifying a building envelope thermal performance.

Chapter 1: Thermal Performance of Vertical Building Envelopes: Case Studies in a Canadian University Campus

The content in this chapter was published in the following publication:

M. Mahmoodzadeh, V. Gretka, A. Blue, D. Adams, B. Dallimore, P. Mukhopadhyaya, Evaluating thermal performance of vertical building envelopes: Case studies in a Canadian university campus, ***Journal of Building Engineering***. 40 (2021) 102712. https://doi.org/10.1016/j.jobe.2021.102712

1.1 Abstract

Campus buildings at the University of Victoria (UVic) were largely constructed before the advent of building energy codes. The University is in the process of commissioning vertical building envelope upgrades/retrofits with added intention of addressing potential energy and greenhouse gas (GHG) savings in their building stock. The aim of this chapter is to present the methodology adopted to evaluate potential energy savings from vertical envelope retrofits of 49 non-residential buildings across the campus portfolio, and to further validate those savings through more detailed energy models for a subset of buildings. To this end, the thermal performance of a building envelope was quantified based on its heat loss coefficient (UA), obtained from multiplying its surface area (A) by its thermal transmittance (U-value). Heat loss (UA) calculations were used as an energy loss metric to inform envelope rehabilitation prioritization, in addition to data gathered from building envelope condition assessments (BECAs). UA data were also analyzed against other building data such as floor area, vertical envelope area, vertical area to floor area ratio (VFAR), window-wall ratio (WWR), age, and type of construction for potential correlations. Finally, archetype energy models were used to evaluate the impacts of envelope retrofits on energy and GHG savings on three selected buildings. The outcomes of this study allow the University to weigh the benefits of improved energy performance from envelope retrofits against associated capital cost expenditures.

Keywords: Heat loss coefficient (UA); Building envelope retrofits; Greenhouse gas (GHG) emission; Energy model; Thermal energy demand intensity (TEDI); Energy use intensity (EUI)

1.2 Introduction

Energy consumption in the built environment has increased considerably over the past decades mainly as a result of population growth, occupants spending more time indoors, higher expectations of indoor comfort (thermal and air quality), and a changing climate. According to the International Energy Agency (IEA), building operation and construction collectively consume over one-third of total global energy, and are responsible for almost 40% of direct and indirect greenhouse gas (GHG) emissions [1]. Most building energy codes and regulations focus on improving energy efficiency of new buildings. However, energy consumption of existing buildings is an area which deserves more attention by energy policymakers since existing buildings often have higher energy use intensities (EUIs) than new construction; further, the vast majority of building stock in any given period are existing and are in need of some form of rehabilitation or retro-commissioning due to deteriorating building envelopes and/or mechanical and electrical systems, presenting an economic opportunity to reduce their energy consumption [2]. To this end, various energy assessment methods have been developed to enhance the energy performance of existing buildings [3-9].

Studies analyzing existing building energy performance have typically focused on commercial and residential buildings, while studies focused on educational (university/school) buildings are limited despite their relatively high energy consumption, large size, and different occupancy schedules. Some university campuses contain a substantial number of buildings within their portfolio, collectively accounting for significant GHG emissions. For instance, in the UK, GHG emissions generated by universities increased from 1.78 to 2.05 tCO2e between 1990 and 2005. In China, 40% of the public sector's energy is consumed by universities, representing the largest sector of public building GHG emissions [10]. Similarly, universities and colleges in the US spend almost USD $6 billion annually on energy; a substantial 25% of this cost could be saved by improving the energy performance of this sector, according to the U.S. Department of Energy (DOE) [11]. In Canada, educational buildings contribute almost 16% of total greenhouse gas (GHG) emissions among 11 sectors. Higher education institutions such as universities and colleges account for almost 60% of the total energy consumed by the educational sector [12]. Given their sizeable share of building energy consumption, addressing energy efficiency of educational buildings presents a considerable opportunity to curb GHG emissions.

Among retrofit strategies, upgrading the building envelope plays a key role in improving existing building energy performance. Previous studies have introduced different methodologies for prioritizing buildings in a portfolio for energy retrofits [13-16], however; using particular criteria as a methodology to evaluate and rank buildings for envelope retofits is missing in literature. In practice, building envelopes undergo retrofits when its physical condition dictates. However, physical condition of a building envelope should not be used as the only metric for determining a retrofit priority in a portfolio since it does not necessarily correlate with its thermal performance. Another criterion sometimes used by portfolio managers for ranking buildings is energy use intensity (EUI). However, this metric can be a misleading indicator for opportunities to improve building envelope performance, since EUI apart from building envelope, depends on other variables such as internal loads, building typology, schedules, and efficiency and controls of mechanical systems. Furthermore, EUI data is not always available for existing buildings due to lack of metering, which would prevent even the most basic energy consumption benchmarking. Consequently, building envelope thermal performance should be evaluated independently for more accurate prioritization.

Current quantitative methods for thermal assessments of building envelopes are based on simplified assumptions from historical codes and references [17-20]. This approach does not reflect actual performance due to temporal degradation of components, and ignores the increased heat losses from thermal bridges. For instance, disregarding thermal bridges can result in a 20% to 70% underestimation of the total heat flow through walls [21]. In recent years, modern computer simulation tools have enabled a better estimation of thermal bridging effects. However, a large-scale simulation-based thermal assessment of building envelopes requires access to component details in architectural drawings and is time-consuming. Therefore, large-scale assessments of this nature require balancing accuracy of results with work efficiency (time & cost). It should also be noted that architectural design parameters such as building geometry, window to wall ratio (WWR), and structural framing type can affect building envelope thermal performance. Collectively, these aspects form the motivation to develop an approach for evaluating and ranking building envelope thermal performance.

Effectiveness of retrofit strategies should be evaluated in terms of energy and cost savings by considering regional climate differences. Previous campus-level investigations mainly focused on energy savings of buildings in Europe, where retrofits are more economically justifiable due to

high energy costs [22-29]. However, very few studies investigated the energy and cost savings associated with retrofits in Canadian school/university buildings, where climate, construction practices, building codes, utility costs, carbon emission factors, and carbon taxes are different [30-32]. In Canada, building codes are evolving to meet multiple objectives, including reducing energy consumption and greenhouse gas emissions, increasing resiliency and passive survivability. For example, the City of Toronto, City of Vancouver and the Province of British Columbia have included the Thermal Energy Demand Intensity (TEDI) metric in addition to Energy Use Intensity (EUI) into policy document in an effort to address the performance of the building envelope and ventilation air heating requirements in new construction. While EUI target is typically attainable by mechanical or lighting system upgrades, TEDI elevates the importance of the building envelope, which is viewed as one of the most robust energy saving measures in a building. Notably, no Canadian jurisdictions have adopted energy performance requirements for existing buildings. Hence, an absence of building codes for existing buildings along with differences in climate and energy costs from those in Europe prompted the researchers of this study to contribute some insights into literature, which could be informative for Canadian universities to reduce GHG emissions within their portfolio as the Canadian government targets an 80% GHG emissions reduction in its operations by 2050, relative to 2005 [33].

This chapter presents a study conducted at the University of Victoria (UVic) campus in British Columbia, Canada. The university has initiated a comprehensive building investigation process to prioritize and plan envelope rehabilitation work across their portfolio, intending to incorporate potential energy and GHG savings into their decision-making criteria. Recent building envelope condition assessments (BECAs) identified that vertical building envelopes on many buildings on campus were in poor condition and would likely require rehabilitation in 5-10 years, while roofs were generally in good condition.

Hence, the proposed study aimed to demonstrate a practical approach to rapidly assess vertical building envelope thermal performance of 49 non-residential buildings across the university campus. This methodology yields metrics that serve as a complementary decision-making criteria to BECAs that routinely carried out by building envelope engineers/professionals. In addition, whole-building energy simulations were conducted using EnergyPlus v8.8 to evaluate the impacts of envelope retrofits on energy efficiency, cost and GHG savings.

1.3 Methodology

1.3.1 Overview and data collection

In this study, vertical building envelope thermal performance quantified by performing heat loss (UA) calculations, obtained by multiplying the surface area (A) of building envelope by its thermal transmittance (U-value), while also taking into account heat losses through linear thermal bridges. This process of evaluation was found to be faster than individual whole-building simulations or energy audits. Critical analyses were performed to assess the impact of architectural parameters such as floor area, vertical envelope area, vertical envelope area to floor area ratio (VFAR), window wall ratio (WWR), age, and type of construction on (UA) calculations. The VFAR metric is similar to a building's surface areas to volume ratio, (compactness); however, VFAR may be considered a more informative shape metric since walls and windows have significantly higher U-values than roofs and floors. Since this study focuses on the evaluation of vertical building envelopes, this metric was considered more appropriate for comparative analysis.

Subsequent to the UA analysis, whole-building energy models of three selected buildings were developed by EnergyPlus 8.8 energy simulation software [34]. Two of the buildings were selected based on the highest envelope energy losses as indicated by UA calculations, while the third was based on a poor overall condition of its building envelope (per the BECA). The purpose of energy modeling was to investigate economics of available energy savings from implementing envelope energy conservation measures (ECMs). The energy model for the smaller building was developed based on actual space layouts, while archetype (approximate) models were developed for the other two larger and more complex buildings. The value of archetype models is realized in cases where other buildings are very similar in shape, internal loads, and operations, such that it could be possible to apply conclusions from one building to other similar buildings. Archetype modeling methodology is explained further in Section 3.2.

Input data required for UA calculations were collected from technical documents such as building drawings, literature sources such as ASHRAE Handbook of Fundamentals [35], the Building Envelope Thermal Bridging Guide (BETBG) [21], and a simple on-site audit of fenestration. For building energy simulations, input data were obtained from a variety of sources:

• Measured electricity and natural gas consumption data for each building provided by the university

• National Energy Code of Canada for Buildings (NECB 2015) [36]

• ASHRAE Standard for Ventilation for Acceptable Indoor Air Quality (ASHRAE 62.1-2010) [37]

• Original (as-built) architectural and mechanical drawings

• Thermal transmittance of building envelope (U-values) obtained from preliminary UA calculations

The analysis framework conducted on the case studies is illustrated in Figure 1.1.

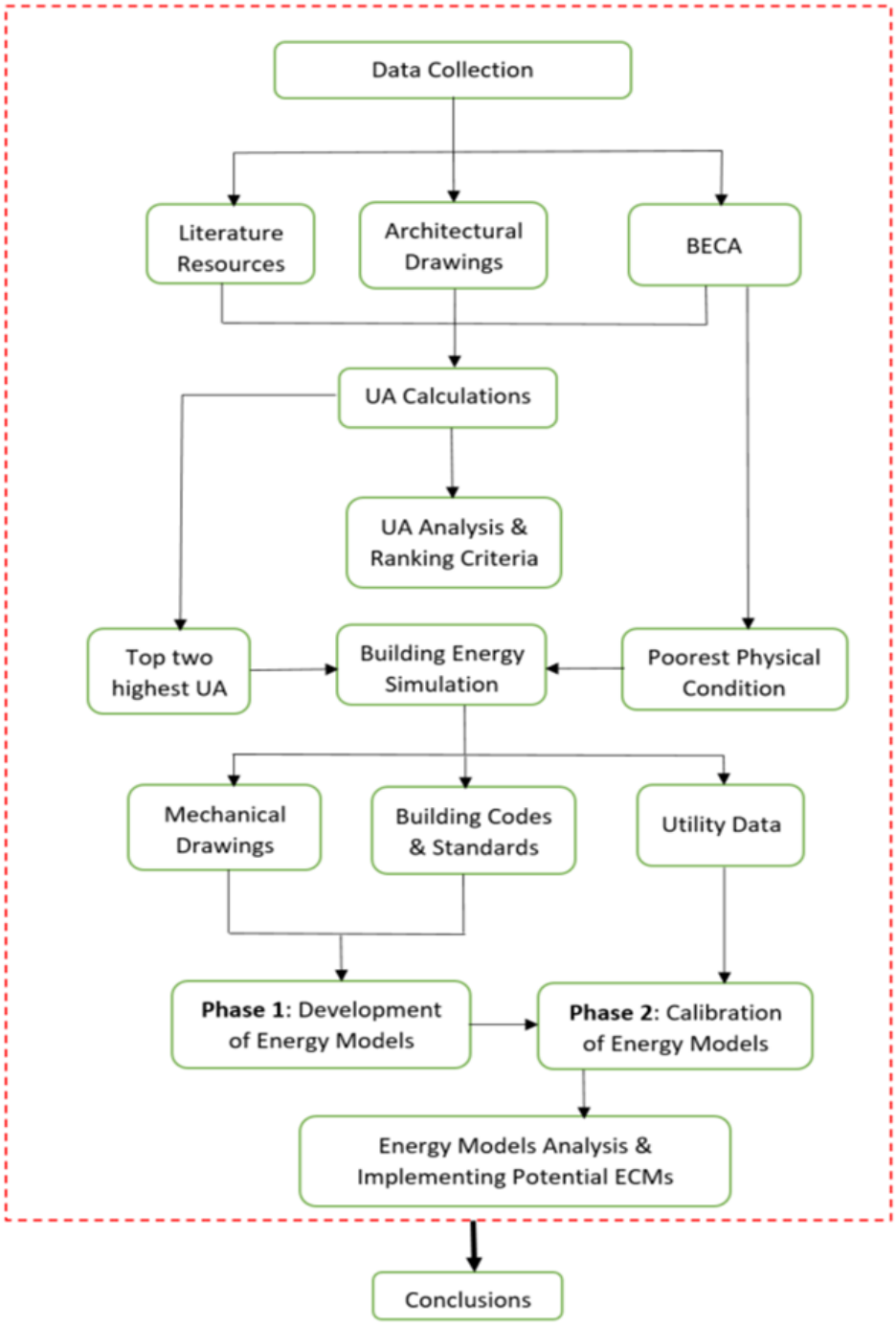

Figure 1.1 Case study analysis in flowchart

1.3.2 Case studies

Figure 1.2 shows the layout of buildings on campus. The 49 non-residential buildings studied are categorized into four groups according to high, moderate, low or minimal potential risks of building envelope failure (see Figure 1.2). The category assigned to each building is determined according to its BECA 'score'. The results of the condition assessment formed one criterion for building prioritization.

The names of buildings studied are provided in Appendix A1, and mainly consisted of classrooms, laboratory and administrative offices. Heating systems are electric, gas, or district hot-water (hydronic) based. Cooling on campus is limited to special utilities such as data centres and selected laboratories. There were some buildings which did not make sense to compare in the context of this study or were otherwise omitted from analysis. For instance, three buildings did not have enough information from available sources to warrant analysis, two were not heated and one was a greenhouse building with an intentionally high glazing ratio for growing vegetation.

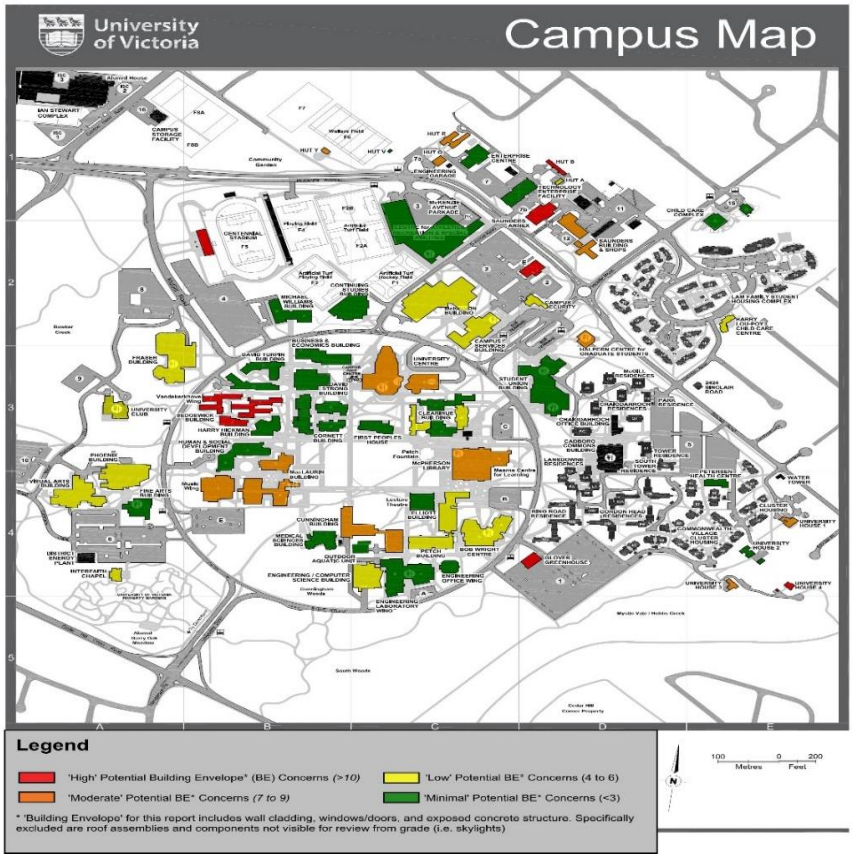

Figure 1.2 Campus map (studied buildings depicted with colours)

To analyze high-level trends in the building portfolio, a variety of characteristics including age, construction type, size, space types and heat transfer coefficients were considered. It was found that older and smaller buildings were mainly wood framed, while newer and larger buildings were concrete framed with steel stud framed walls. Furthermore, offices buildings were largely wood framed while classroom and laboratory buildings were mostly concrete construction with steel stud framed walls. Finally, since envelope heat losses (both planar and linear contributions) depend considerably on their frame type, it was decided to categorize the buildings based on wood, steel stud, steel stud/concrete, and concrete wall assemblies. Building characteristics such as floor area (m^2), vertical building envelope area (m^2), window area (m^2), as well as age and space types are summarized in Table 1.1. The standard deviations of values in Table 1.1 demonstrate the variability of data that can be expected due to variations in architectural design trends and building codes over time.

Table 1.1 Buildings in study (Mean ± Standard deviation)

Building Wall Frame type	**Number of buildings**	**Building Characteristics**				
		Floor Area (m^2)	**Vertical Envelope Area (m^2)**	**Window Area (m^2)**	**Age (yrs)**	**Space types**
Wood	19	883±675	664±538	132±64	43±23	Office, clinic, lab
Steel stud	18	8037±4867	3954±2454	989±368	28±15	Office, lab, library, classroom, lecture hall, sport facility, food facility, theater space
Steel stud-concrete	10	9309±6816	4155±2516	1121±302	39±15	Office, lab, library, classroom, lecture hall
Concrete	2	6220±3650	4082±2785	1183±389	22±11	Office, lab

1.3.3 Overall Vertical Envelope Heat Loss (UA)

Overall heat loss (UA) calculations of vertical building envelope assemblies were based on heat losses through opaque (wall) and transparent (window) components as well as linear heat losses through thermal bridges obtained from simulation values in catalogues. An example of how to account for linear transition details with length and area takeoffs is presented in Figure 1.3. It is to be noted that performing 3D simulation models for every single building based on real constructive elements requires complete architectural drawings. Given so many buildings are older, these details are often not shown on drawings but are otherwise detailed on site during construction according to the trades, as was customary during that era. Further, some drawing sets were not complete or otherwise missing for several buildings on campus. Knowing the construction industry only started to devote attention to mitigating thermal bridging in the mid-2010 era, the amount of thermal bridging expected at linear interface details is very predictable, as noted in the preface of the BC Hydro Building Envelope Thermal Bridging Guide [21], based on research formally vetted by peers in ASHRAE RP 1365 [38]. Hence, the increase in accuracy in assessing linear thermal transmittances with simulations will not affect the overall conclusions of the UA exercise or the energy model.

Furthermore, even 3D models based on the real constructive elements would certainly differ from their actual values since numerical models does not consider degradation of building materials, real moisture content, and errors associated with manufacturing. Hence, in-situ measurements tools (i.e. infrared thermography & heat flux meters) could be potential candidates to measure the actual U-values and linear thermal transmittances of building envelopes. However, in-situ measurement for large-scale evaluations of buildings is challenging and practically not feasible due to limitations in terms of time, cost and experimental set-up. Consequently, the focus of this study is to develop a rapid and robust approach that balances the effort required with obtaining practical direction or solutions.

Mathematically, the overall UA-value for any vertical building envelope section is expressed as:

$$(UA)_{overall} = U_{wall}A_{wall} + \sum(\Psi \cdot L) + \sum(\chi) + U_{window}A_{window} \quad (1.1)$$

where:

- (U_{wall}) is the clear field assembly thermal transmittance, estimated using ASHRAE 90.1-2010, Appendix A [39], Natural Resources Canada (NRCan) Tables for Calculating Effective Thermal Resistance of Opaque Assemblies [40], or the BETBG [21].
- A_{wall} and A_{window} are the areas of the opaque wall and windows, and (L) is the length of the thermal bridge, both measured with Bluebeam software from building architectural drawings.
- (Ψ) is the linear heat loss coefficient, which was obtained from simulation values in BETBG [21] and ISO 14683 [41] (Table 1.2). It is to be noted that for continuous exterior insulated assemblies, intermediate floor intersections were ignored. Also, corners were disregarded due to their small contributions to total heat loss.
- (χ) is the point source heat transmittance coefficients, which was disregarded in this study for simplification.
- (U_{window}) is the fenestration thermal transmittance, approximated from the ASHRAE Handbook of Fundamentals (2017) [35] according to their type (Table 1.3). Given the vintage of buildings, cavities in insulating glazing units (IGUs) for the majority of buildings were filled with air; additionally, glazing did not have low-e coatings, except for a select few newer buildings with triple and quadruple glazed windows.

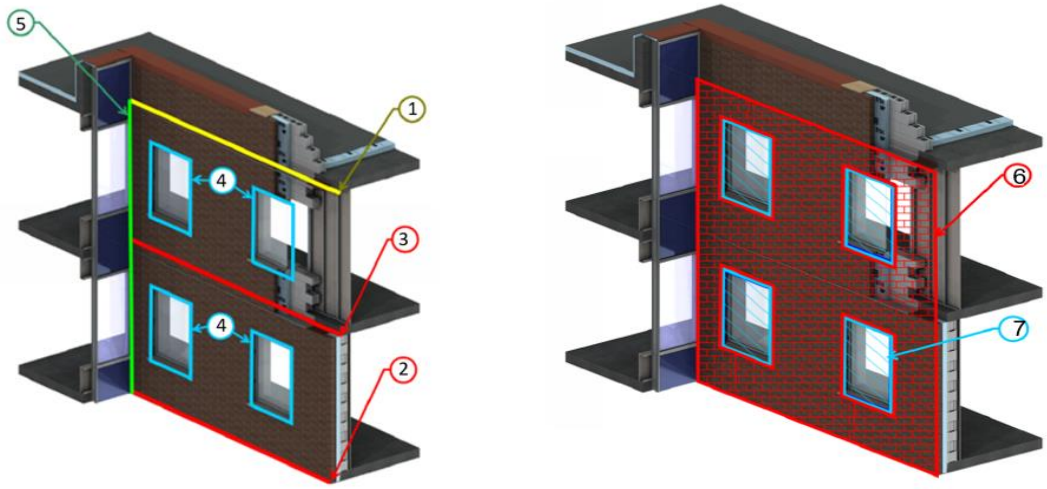

Figure 1.3 Example of building length and area takeoffs: (1) Parapet length; (2) Slab lengths; (3) Intermediate floor; (4) Wall to window transition lengths; (5) Corner length; (6) Opaque wall area, and; (7) Glazing area [21]

Table 1.2 Linear heat loss coefficients based on the BETBG

Thermal Bridge Type: Interface with Opaque Wall	**Concrete/Steel Frame Assembly**		**Wood Frame Assembly**	
	Ψ (W/mK)	**Source**	**Ψ (W/mK)**	**Source**
Ground Slab	1.0	BETBG Table 2	0.65	ISO 14683
Intermediate Floor	1.0	BETBG Table 2	0.12	BETBG 7.2.1
Fenestration	0.5	BETBG Table 3	0.24	BETBG 7.3.2
Parapet	0.8	BETBG Table 4	0.03	BETBG 7.4.2

Table 1.3 Estimated Thermal Performance of Fenestration

Fenestration Type		U_{window} **(W/m² K)**
Single Glazed	Metal	6.5
	Non-Metal	5.5
Double Glazed	Metal	3.2
	Non-Metal	2.6
Triple Glazed	Metal	2.2
Quadruple Glazed	Metal	1.7

1.4 Results and Discussion

1.4.1 Correlations between envelope heat loss and building geometry

Building geometry often plays an important role in its overall energy efficiency. The parameters which were considered in this chapter are: floor area, vertical envelope area, window to wall ratio (WWR) and vertical envelope area to floor area ratio (VFAR). Correlations between these parameters and overall thermal transmittance values were critically investigated. To this end, a statistical analysis based on Pearson's correlation was carried out using SPSS Statistics Software. A Pearson correlation (r-value) indicates the strength of linear relationship between two variables. It has a value between +1 and −1, where 1 is total positive linear correlation, 0 is no linear correlation, and −1 is total negative linear correlation. A normal distribution at 95% confidence level where the P-value is 0.05 was assumed in SPSS software. The P-value is the probability that indicates data did not occur by chance, and determines whether the correlation between variables is significant. If this probability is lower than 5% or 1% ($P<0.05$; $P<0.01$) the correlation coefficient is statistically significant, shown with * and ** symbols in Table 1.4, respectively. The results (r-values) are summarized in Table 1.4. To obtain the percentage variance, the square of the Pearson correlation coefficient (r^2) is multiplied by 100. The r-squared (r^2) value indicates to what extent the variance of a variable can be predicted by the variance of a second variable.

Table 1.4 Pearson correlations between building characteristics (r-value)

Metrics	UA	UA/Floor Area	UA/ Vertical Envelope Area	Floor Area	Vertical Envelope Area	WWR	VFAR	AGE
UA	1	-0.232	0.045	0.905**	0.929**	0.288*	-0.467**	0.105
UA / Floor Area	-0.232	1	0.705**	-0.362**	-0.337*	0.004	0.564**	-0.373**
UA /Vert. Envelope Area	0.045	0.705**	1	-0.055	-0.127	0.351*	-0.024	-0.113
Floor Area	0.905**	-0.362**	-0.055	1	0.921**	0.227	-0.543**	0.131
Vertical Envelope Area	0.929**	-0.337*	-0.127	0.921**	1	0.14	-0.456**	0.182
WWR	0.288*	0.004	0.351*	0.227	0.14	1	-0.472**	0.413**
VFAR	-0.467**	0.564**	-0.024	-0.543**	-0.456**	-0.472**	1	-0.433**
AGE	0.105	-0.373**	-0.113	0.131	0.182	0.413**	-0.433**	1

** Correlation is significant at the 0.01 level (2-tailed).

* Correlation is significant at the 0.05 level (2-tailed).

The results in Table 1.4 show that UA has a strong correlation with floor area (r= +0.905), where 81.9% (r^2) of the variance in UA can be attributed to a difference in floor area only. UA has an even better correlation with vertical envelope area (r = +0.929), where 86.3% of the variance in UA could be attributed to a difference in vertical envelope area only. It is also seen that vertical envelope area and floor area are linearly correlated (r = +0.921; r^2 = 0.848). Furthermore, results show that the normalized indices UA per unit floor area and UA per unit vertical envelope area have a modest linear correlation (r= +0.705; r^2= 0.497). VFAR and WWR showed a poor linear correlation (r= -0.472; r^2= 0.222). Finally, age appears to hold a moderate negative correlation with VFAR (r= -0.433; r^2= 0.187), and a moderate positive correlation with WWR (r= +0.413; r^2= 0.171), suggesting that older buildings have poorer (less efficient) geometry due to their smaller overall size less window area. Characteristics with significant relationships are presented in Figures 1.4-1.7.

Figure 1.4 depicts the results of the UA calculations as a function of useable floor area in the building. Wood framed buildings are generally smaller in floor area, while larger buildings are typically non-wood construction. Notably, a line of best fit through the data suggests there is a linear scaling of UA with increasing floor area regardless of building framing types, ages, and geometries. Hence, UVic may consider UA as one criterion for ranking thermal performance of building envelopes since both size and U-value are incorporated in this metric.

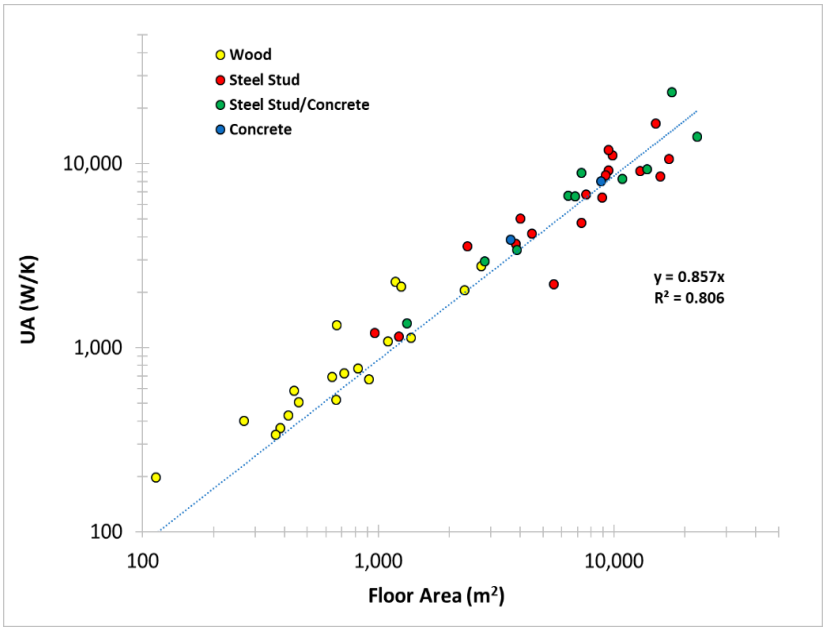

Figure 1.4 Variation of UA with Floor Area

Figure 1.5 shows the relationship of UA as a function of vertical envelope area for each of the buildings. The slope of the line of best fit represents the vertical area-weighted average U-value of the buildings studied. It is seen that wood framed buildings are mainly below the trend line, due in part to reduced impacts of thermal bridging. Wood has a lower thermal conductivity than steel or concrete, which in general results in lower thermal transmittance (U-value) assemblies, which can yield more energy efficient envelopes. Furthermore, from Figures 1.4 and 1.5 it can be seen that UA values are more dependent on vertical building envelope area (R^2= 0.86) than floor area (R^2= 0.81). Therefore, vertical building envelope area can be a more representative characteristic in describing building envelope thermal performance on campus than floor area.

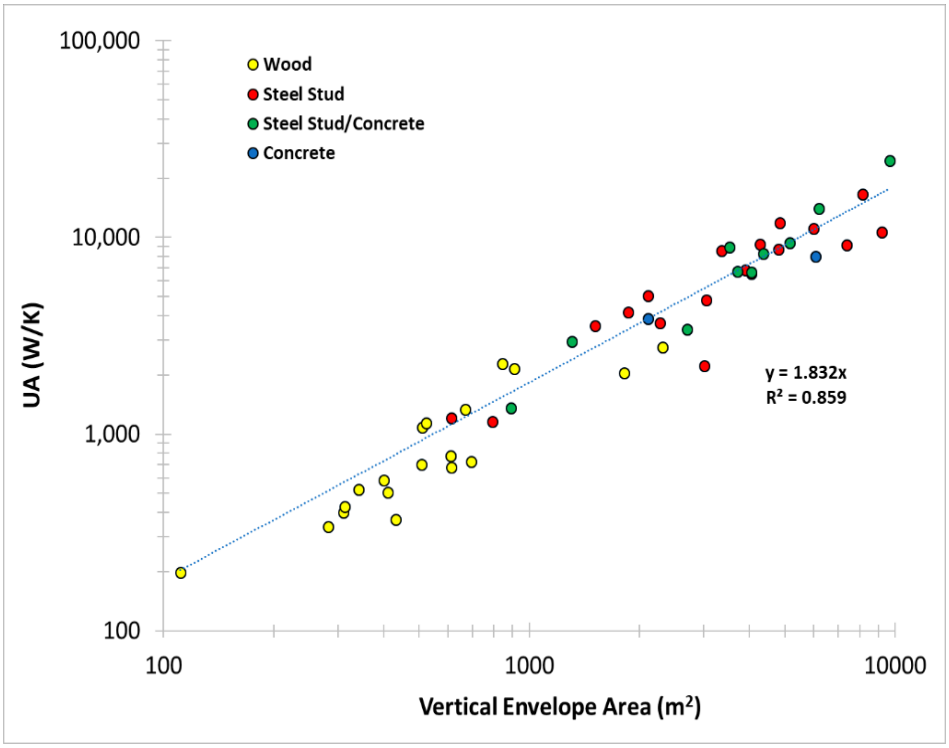

Figure 1.5 Variation of UA with Vertical Envelope Area

Figure 1.6 describes the relationship between geometry and window area, represented by VFAR and WWR, respectively, for the buildings studied. It shows that wood framed buildings generally have higher VFAR (on average 0.80), and lower WWR, consistent with the age of the buildings (maximizing glazing area was not the focus of early 20th century building design. The Pearson correlation (Table 1.4) also confirms that age correlated with both VFAR and WWR. In general, non-wood framed buildings are larger and newer, have more stories, and therefore have a lower VFAR (on average 0.52). In practice, buildings with 'compact'

geometries have a VFAR of 0.49-0.6, those with 'complex' massing including more articulations have a VFAR in the range of 0.59-0.72, and those with highly complex geometries are considered 'narrow' and have a VFAR of 0.7-0.86 [42].

From a practical standpoint, since building characteristics such as VFAR are not typically changed during its lifetime except where additions are made to the existing building, UVic should consider exploring a policy for a prescriptive maximum VFAR for new construction to help optimize building energy efficiency. Furthermore, where windows are approaching the end of their service life, buildings with high WWR should be prioritized for retrofit. These kinds of buildings have disproportionately poorer performance, even if they are newer (<15 years old) and have a good compactness (low VFAR). Prioritizing these buildings will also afford the opportunity to improve a more substantial length of window-wall transition detailing, reducing its associated thermal bridge, effectively resulting in a multi-beneficial upgrade.

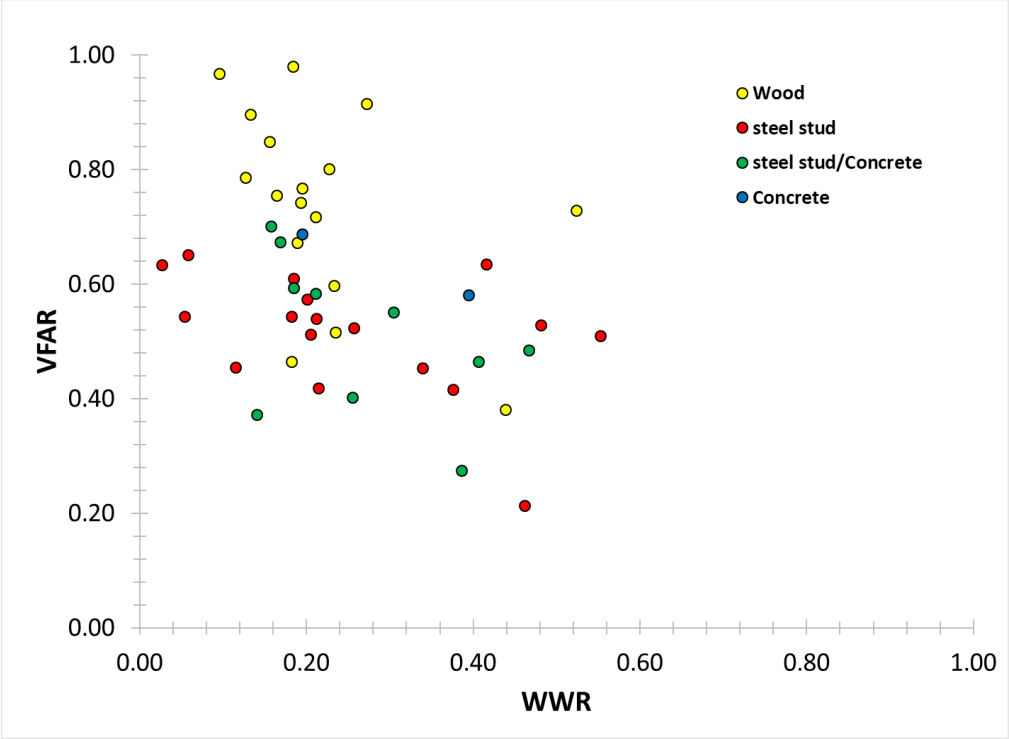

Figure 1.6 Variation of VFAR with WWR

Figure 1.7 is a plot of UA per unit floor area versus UA per unit vertical envelope area. Wood-framed buildings have higher normalized UA per floor area due to higher VFAR. Normalizing a building's UA by its vertical area is a measure of its "average vertical envelope U-value". It can be observed that wood-framed buildings have a lower average U-value compared to other

buildings on campus. This appears to be due to (1) wood-framed buildings on campus were generally older vintage with a much lower WWR (Figure 1.6) than non-wood framed buildings, and (2) wood-framed buildings on campus are limited to a single story which excludes the thermal bridging penalty of intermediate floors. Also, it can be seen that the distribution of data in Figure 1.4 and Figure 1.7 are different, which can change prioritization rankings of buildings proposed to undergo envelope retrofits. For instance, based on normalized UA (Figure 1.7), wood-framed buildings (small buildings) should be prioritized, while UA values (Figure 1.4) suggest larger buildings are a priority. Both metrics are potentially useful for ranking buildings for envelope retrofits depending on priorities set out by University policymakers.

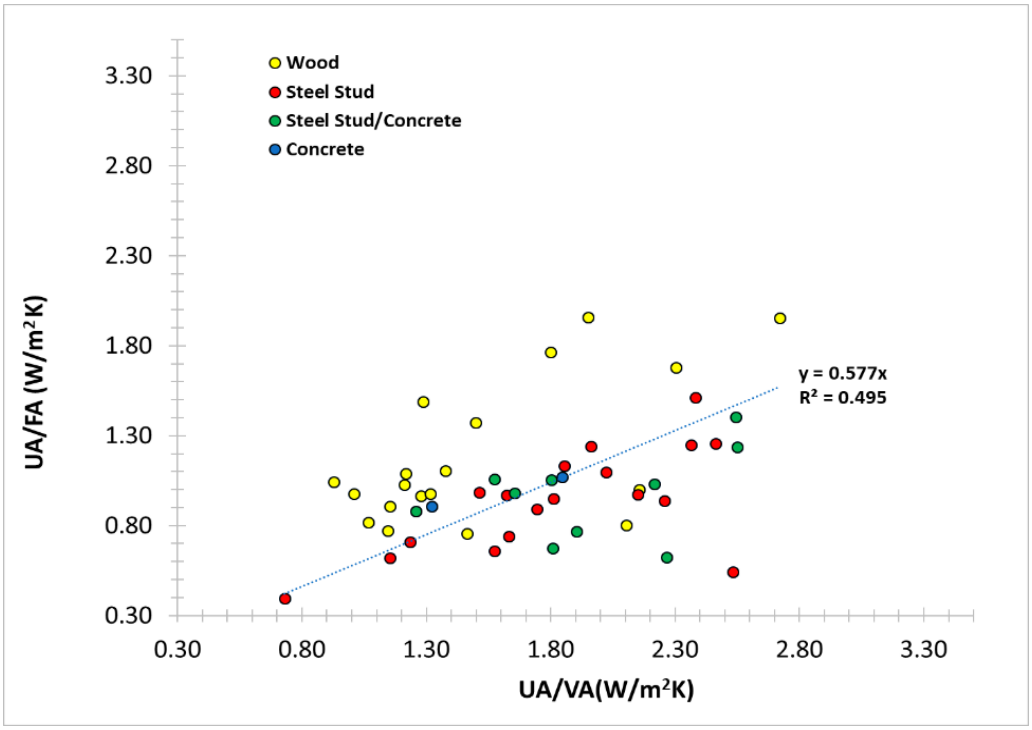

Figure 1.7 Variation of UA per floor area with UA per vertical area

Table 1.5 is a summary of the data presented in Figures 1.4-1.7. Notable observations are:

- By virtue of their age, even though wood framed buildings on campus have poorer geometry (i.e. high VFAR), they have a lower average U-value due to mitigated thermal bridging penalties.
- Based on floor area, wood framed buildings have a 50% higher normalized UA than other buildings, due mainly to a poor geometry (i.e. high VFAR).

- Absolute UA for wood framed buildings is much lower than other buildings, mostly due to their smaller overall size.
- Newer buildings, generally of non-wood construction, exhibited more efficient geometries (lower VFAR) due to additional storeys and were built in an era with an architectural predisposition to higher glazing ratios.
- NECB 2015 prescriptive U-values for walls are considerably lower than any building on campus, highlighting the relatively poor thermal performance of campus building opaque envelopes compared to current building code requirements in British Columbia. It should be noted that NECB 2015 does not require the inclusion of all thermal bridging effects in determining compliance with prescriptive U-values. Similarly, prescribed fenestration U-values in NECB 2015 are lower than almost all buildings on campus, except for those with triple and quadruple glazed units.

Table 1.5 Performance of different structure based on various indices

Wall Framing	UA (W/K)	UA/FA (W/m^2 K)	UA/VA Average (U-Value W/m^2 K)	VFAR	WWR	Floor Area (m^2)	Vertical Envelope Area (m^2)	Minimum Prescriptive NECB 2015 Average U-value[1] (W/m^2 K)
Wood (n = 19)	1000± 768	1.18 ±0.39	1.53±0.50	0.80±0.21	0.20±0.12	883±675	664±538	0.39±0.06
Steel Stud (n= 18)	6939±4115	0.94±0.28	1.83±0.49	0.52±0.10	0.25±0.15	8037±4867	3954±2454	0.42±0.08
Steel Stud/ Concrete (n=10)	8630±6703	0.97±0.24	1.96±0.42	0.51±0.14	0.27 ±0.12	9309±6816	4155±2516	0.42±0.05
Concrete (n=2)	5950±2899	0.99±0.12	1.58±0.37	0.63±0.07	0.29±0.14	6220±3650	4082±2785	0.43±0.07

[1] Calculated considering overall clear wall U-value 0.315 W/m^2K and window U-value 2.4 W/m^2K for Climate Zone 4.

The analysis illustrated how building envelope thermal metrics can be used as complementary criteria to rank buildings for retrofits, along with typology, size, age, and overall condition. Figure 1.8 is a summary of various metrics analyzed for the portfolio of buildings in the study, and are based on building envelope thermal benchmarking and professional experience. The results are highlighted using a color bar scale based on percentile, where yellow represents the 50^{th} percentile, red is the 100^{th} percentile (highest priority), and green is the 0^{th} percentile (lowest priority). In this case, buildings are ranked based on envelope heat loss (UA), but can otherwise be sorted by any other metric. Importantly, the results show that ranking of buildings by envelope heat loss (UA) yields different rankings than if the list was sorted by other metrics, similar to the findings when comparing rankings suggested by Figure 1.4 and Figure 1.7. It is seen there is no meaningful correlation between UA losses and condition score of buildings. For instance, DTB and COR are in the top five buildings with largest UA losses, while they are considered low risk by virtue of their condition score. In contrast, low envelope heat loss (UA) buildings like HTB and HTE are considered high risk in terms of their condition score. Additionally, some buildings with a high priority based on UA losses were largely categorized as low priority buildings in terms of normalized UA metrics (UA per floor area or UA per vertical area). Interestingly, newer buildings such as DTB, CARSA and ECS had high thermal losses (UA) due to a high WWR, high envelope area, and poor opaque wall performance, respectively, highlighting the importance of any one of these characteristics alone to absolute UA. Similarly, ranking buildings using other metrics such as age, wall framing type and average U-values yields different conclusions.

Given the focus on greenhouse gas (GHG) reductions per UVic policies, and that heating energy accounts for a substantial fraction of GHG emissions on campus, ranking building envelope performance with these metrics has practical merit for capital planning purposes. Ultimately, UVic's final decision will depend on a multitude of factors including capital costs associated with envelope retrofits (material & labour), programming requirements and limitations, achievable energy cost savings, and aesthetic benefits to name a few. Nonetheless, this type of analysis will facilitate the grouping and/or ranking of certain buildings versus others, streamlining the decision-making process.

Bldg	Frame	Overall UA (W/K)	Average of vertical envelope U-value (W/m^2K)	Vertical Envelope Area (m^2)	UA per Floor Area (W/m^2K)	Floor Area (m^2)	Year Built	Condition Score
CLE	steel stud/concrete	24,600	2.54	9670	1.40	17,537	1972	6
MAC	steel	16,500	2.02	8162	1.10	15,020	1978	9
LIB	steel stud/concrete	14,000	2.26	6181	0.62	22,473	1974	8
DTB	steel	11,900	2.46	4831	1.26	9,477	2008	2
COR	steel	11,100	1.85	5990	1.13	9,811	1966	2
CARSA	steel	10,600	1.15	9199	0.62	17,043	2015	2
ELL	steel stud/concrete	9,300	1.81	5143	0.67	13,803	1963	3
FRA	steel	9,200	2.15	4280	0.97	9,441	1980	5
BWC	steel	9,100	1.23	7374	0.71	12,849	2009	4
PCH	steel stud/concrete	9,000	2.55	3529	1.24	7,270	1984	5
BEC	steel	8,700	1.81	4803	0.95	9,169	1997	2
UVC	steel	8,500	2.53	3356	0.54	15,677	1978	9
ELW	steel stud/concrete	8,300	1.90	4357	0.77	10,832	1995	1
ECS	concrete	8,000	1.32	6052	0.91	8,801	2006	4
HSD	steel	6,800	1.74	3901	0.89	7,611	1992	3
CUN	steel stud/concrete	6,700	1.80	3715	1.05	6,361	1971	9
SUB	steel stud/concrete	6,700	1.65	4051	0.98	6,825	1962	3
MCK	steel	6,600	1.63	4042	0.74	8,892	1975	6
MWB	steel	5,000	2.36	2116	1.25	4,000	2008	2
CST	steel	4,800	1.57	3048	0.66	7,274	2003	2
CSR	steel	4,200	2.26	1860	0.94	4,474	1996	5
EOW	concrete	3,900	1.85	2112	1.07	3,639	1990	1
MSB	steel	3,700	1.62	2279	0.97	3,817	2003	2
FIA	steel	3,600	2.38	1512	1.51	2,378	1990	2
VIA	steel stud/concrete	3,400	1.26	2705	0.88	3,856	1992	5
TEF	steel stud/concrete	2,900	2.22	1308	1.03	2,817	2003	2
SED	wood	2,800	1.21	2312	1.03	2,725	1975	10
SAA	wood	2,300	2.72	845	1.95	1,178	1974	10
PNX	steel	2,200	0.73	3016	0.40	5,552	1981	4
FPH	wood	2,100	2.30	911	1.68	1,251	2010	2
SAU	wood	2,100	1.15	1819	0.91	2,312	1965	7
HHB	steel stud/concrete	1,400	1.57	890	1.06	1,321	1999	3
HTR	wood	1,300	1.95	667	1.96	664	1940	9
STA	steel	1,200	1.96	612	1.24	966	1974	10
EDC	steel	1,200	1.51	794	0.98	1,219	2009	1
CSF	wood	1,100	2.16	510	1.00	1,098	1989	5
UCL	wood	1,100	2.10	523	0.80	1,371	1982	5
UH1	wood	800	1.31	609	0.98	819	1969	7
GSC	wood	700	1.38	508	1.10	634	1990	7
CCC	wood	700	1.14	612	0.77	909	1993	1
HTE	wood	700	1.01	693	0.98	716	1992	10
CHA	wood	600	1.50	400	1.37	437	1984	6
HEA	wood	500	1.46	342	0.75	663	1969	1
SEC	wood	500	1.22	411	1.09	459	1996	4
HTB	wood	400	1.29	311	1.49	269	1940	10
HLP	wood	400	1.28	313	0.96	415	2001	6
HTQ	wood	400	0.93	431	1.04	383	1940	7
UH2	wood	300	1.07	281	0.82	367	2014	3
HTA	wood	200	1.80	111	1.76	113	1940	6

Figure 1.8 Rank of buildings based on different criteria; color bar percentile scale from red (100^{th}) to green (0^{th})

1.4.2 Energy Simulation

1.4.2.1 Phase 1: Initial development of energy models

Three buildings on campus were selected for energy simulation to quantify the economic impacts of envelope energy conservation measures (ECMs). Buildings were selected based on worst case scenarios where (1) all three selected buildings had a poor physical condition and required envelope upgrades, and (2) two of those buildings had the highest envelope energy losses (UA), and were among the largest and oldest buildings on campus. Since the established energy models are based on worst case scenarios and selected buildings have very different characteristics in terms of size, internal loads, space type, construction type, occupancy, and heating systems, the diversity of conclusions can inform decision-making for other campus buildings if they share relatively similar combinations of those characteristics; this is justifiable because utility costs, climate data, and carbon taxes are identical. Table 1.6 presents an overview of the studied buildings. Clearihue (CLE) and MacLaurin (MAC) have among the highest vertical envelope heat losses (See Appendices A2 & A3) and are also among the oldest buildings on campus that likely require envelope upgrades. The CLE building was one of the first large construction projects at the University of Victoria, completed in four stages ("wings") from 1965 to 1977. Since energy costs were relatively meager at the time of construction, little attention was devoted to building enclosure thermal performance or energy performance of heating and ventilation methods. Original windows have since been upgraded to double-glazed in aluminum frames throughout. Likewise, the MAC building was constructed in the late 1960s; however, only some windows have been upgraded from the original single glazed type.

Building energy simulations were performed using EnergyPlus v8.8, and for CLE and MAC, were based on archetype buildings due to their large size and number of rooms/zones. Archetype energy models are an effective representation of actual building energy models, accomplished by virtue of simplifying building geometry and grouping interior zones while assigning actual mechanical assumptions and internal loads. This simplification facilitates expediting model construction and simulation times for large buildings. In the archetype models developed for this study, each floor was divided into roughly 5 zones using the core/perimeter zoning strategy: four "perimeter" zones for each cardinal direction (i.e. north, south, east, west) and a "core" zone (see Figure 1.9). A space within ~4m of the façade on each cardinal direction was considered as a perimeter zone to capture

the effect of zone solar gain at different times of day. Zones were grouped together roughly according to the predominant space type in each area.

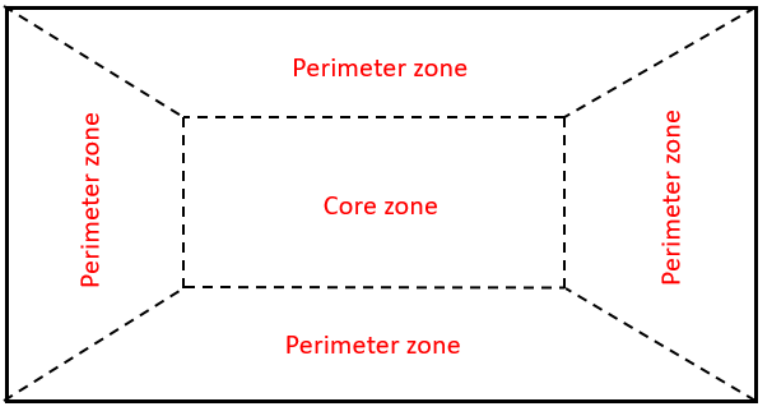

Figure 1.9 Thermal zoning in archetype models

Although Sedgewick (SED) was one of the lowest UA candidates, even among the lowest average envelope U-values, the building envelope condition assessment identified it as the most critically in need of an envelope upgrade (shown in red in Figure 1.2). The SED facility was one of the first construction projects at the University of Victoria, completed as four separate buildings from 1968 to 2010. The buildings were originally intended to be temporary structures but have remained operational in part due to their unique and/or historic architectural appeal. Due to its small overall size, the SED building was modeled using actual zoning rather than archetype simplifications as in the other larger buildings. Building geometries were developed in SketchUp, integrated with an OpenStudio plug-in that translates information to EnergyPlus syntax. Building renderings are shown in Figure 1.10.

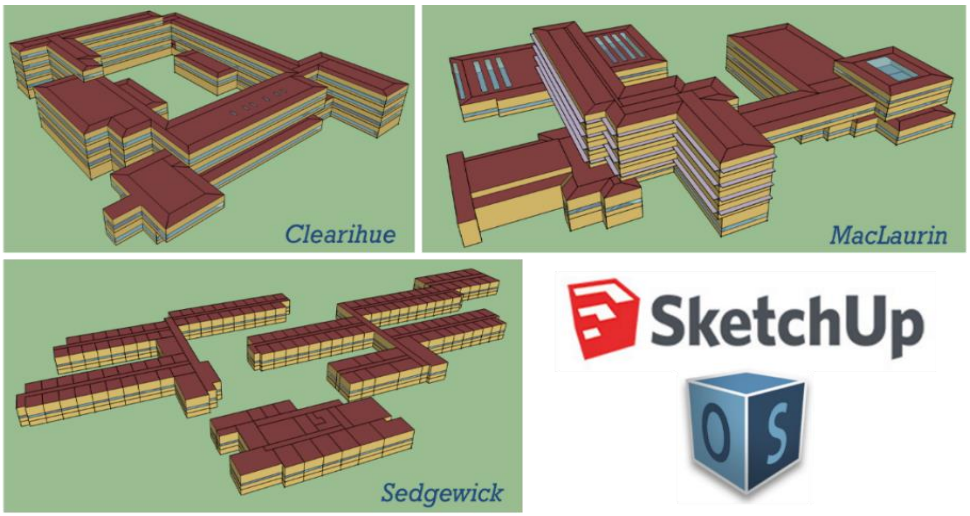

Figure 1.10 SketchUp/OpenStudio renderings of modeled buildings

The information available at the time of model construction included original architectural and mechanical drawings for each of the buildings. Access was granted to the UVic building automation system (BAS) to evaluate real operating conditions in terms of supply air and zone temperature setpoints and equipment schedules. For gas-heated buildings (CLE & MAC) the thermal energy is provided by the UVic central gas-fired boiler plant for hydronic heating coils in air handling units (AHUs) and radiant hydronic terminal units. AHUs in CLE and MAC had economizers. SED was heated with electric-based systems (electric heating coils in AHUs and electric baseboards). Mechanical systems details are provided in Table 1.7.

Each building had a mix of space types identified in architectural drawings that were assigned approximately according to the archetype zoning in the model. Spaces in CLE included classroom, circulation (corridors & stairs), laboratory, library, lounge, office, mechanical, storage, and washrooms. MAC also included spaces defined as art studio, café, lecture theatre, and a large entrance lobby. SED had mostly office space, but also had boardrooms to facilitate meetings for administrative staff. Total areas of a particular space type in the model was approximately equivalent to its total area shown in architectural drawings. Internal loads such as lighting, occupants and plug loads were assigned according to the particular space type per unit area.

Fenestration was assigned to the model with an automated window wall ratio (WWR) script in Sketchup/OpenStudio. Both WWR and wall U-values (including the effect of thermal bridges, equivalent U-value) were obtained from the UA exercise in Section 1.3. It is to be noted that the effect of dynamic 3D thermal bridges and equivalent U-value (calculated in stead conditions) on

the accuracy building energy simulations have been conducted in previous studies. The work done by Concordia University compares [43, 44] the impact of dynamic thermal bridges on whole building energy-use for an archetype Canadian multi-unit-residential building, in climate zones 4 to 7. The results indicated that the higher the thermal mass the higher the differences between dynamic thermal bridge and equivalent U-value. However, for light-weight construction, i.e. wood-frame, and even heavy wood structures utilizing cross-laminated timber, the dynamic effect is not significant. The authors also suggested that with a decrease in the amount of thermal bridges (i.e. length or number) and by mitigating the heat loss through them (lower psi or chi values), the difference between utilizing the equivalent U-value and 3D dynamic modeling for energy modeling purposes decreases. From the conducted studies, it can be deduced that using linear thermal transmittance based on the BETBG to calculate the equivalent U-value in building energy models would not have a substantial influence on the conclusions obtained for buildings with steel-stud and wood-framed wall assemblies. Even in the case of heavyweight construction, dynamic thermal bridging is not a major consideration in a mild coastal climate. While the previous studies suggested deviations can be as high as 13%, results in the mild coastal Vancouver climate case for non-spandrel assemblies were significantly smaller (<5%), within acceptable limits of error in energy modeling in general [43, 44]. Given these findings, the increased level of accuracy from dynamic simulations of thermal bridging was not warranted in this study.

Given limited information about installed lighting power and that the last major lighting retrofit was known to have complied with minimum code, lighting power densities (LPDs) were estimated based on the ASHRAE 90.1-2010 [39] space by space method. Plug loads, occupant densities, and all internal load and temperature setpoint schedules were based on NECB 2015 schedules corresponding to the space type. Air leakage, inclusive of manual "airing", was similarly assumed based on the NECB 2015 default value for building energy performance path (0.25 L/s/m^2 of exterior envelope area). Ventilation rates and mechanical system design were obtained from original mechanical drawings, and by cross referencing assumptions in the BAS where available.

1.4.2.2 Phase 2: Calibration of energy models

The energy models were calibrated based on measured energy data to represent actual performance, using ASHRAE Guideline 14-2014 [45]. The two uncertainty indices used in the calibration of natural gas and electricity were: (1) Normalized Mean Bias Error (NMBE) < 5%,

and (2) the Coefficient of Variation of the Root Mean Square Error (CVRMSE) < 15%. The NMBE is a normalized MBE (Mean Bias Error). MBE is the average of the errors in a sample of data and is a good indicator of the behavior of simulated data. The NMBE is determined by diving MBE to the mean of measured values ($\bar{m}$). Equation 1.2 shows the correlation of NMBE where mi is the measured value s_i is the simulated data, n is the number of measured data points, and p is the number of adjustable model parameters, which for calibration is suggested to be zero [46].

$$\text{NMBE} = \frac{1}{\bar{m}} . \frac{\sum_{i=1}^{n}(m_i - s_i)}{n-p} \times 100\ (\%) \tag{1.2}$$

CV (RMSE) measures the variability of the errors between measured and simulated values. It is obtained based on Equation 1.3, where the value of p is suggested to be 1 [43].

$$\text{CV (RMSE)} = \frac{1}{\bar{m}} \sqrt{\frac{\sum_{i=1}^{n}(m_i - s_{i)}{}^{2}}{n-p}} \times 100\ (\%) \tag{1.3}$$

The calibration process starts by adjusting one parameter at a time, running the EnergyPlus simulation, then comparing the simulated energy data with the actual energy data to determine whether the calibration criteria are met. If not, based on the deviation of the calibration pattern, the parameter is changed again or other parameters are adjusted. The calibration procedure continues until the calibration criteria of ASHRAE Guidelines 14-2014 have been met. Positive values in Equation 1.2 imply that the model under-predicts measured data, while a negative one implies over-prediction. Difference in calibration patterns indicate how different sets of model parameters should be adjusted during the calibration to minimize the deviation of the energy model from actual building operation [47].

Model inputs that were used for calibration included LPD, ventilation rate, and air leakage rate. Each building had a different strategy for calibration depending on how the initial model results compared to metered energy data. For example, given the mechanical systems were likely updated or re-commissioned a few times since the buildings were originally constructed, it was assumed that ventilation rates were updated according to ASHRAE 62.1 [37] as a starting point (higher than original drawings suggested). Ventilation rates were calculated from original mechanical drawings. For each AHU, the total rate of supply, return and exhausted air was calculated as a baseline ventilation rate. Systems were set up in the energy model serving the appropriate zones or building wings accordingly. Next, air leakage rates were adjusted to increase heating consumption in winter months, up to an order of magnitude higher than current code baselines.

Finally, LPD was decreased to better match electricity consumption. Higher outdoor air rates were assumed (up to 4 ACH in the case of CLE) due to a combination of a better air barrier than other buildings, and higher lab/data centre space breakdown. A summary of model inputs is shown in Table 1.7.

It is worth noting that while internal loads influence the balance point temperature of the building, and consequently its heating demand, for the purposes of this study it was acceptable to use inputs from nationally recognized codes (i.e., NECB and ASHRAE 62.1, and ASHRAE 90.1) that are intended to be used for energy modelling purposes. In other words, since the energy data was provided for the archetype buildings and showed a clear seasonal (heating) variability, and because it is known that TEDI is accounted for primarily by air leakage, conduction heat transfer, and internal loads, the balance point temperature effect on envelope ECMs is not likely to have a demonstrable influence. While measuring air flow in air handling units would better inform air leakage assumptions in the energy model, it would nonetheless be confounded by the combined effect of occupant behavior with operable windows, versus the actual effect of air leakage. Therefore, a full blower door test (air leakage test) would be required to ascertain relative breakdowns of the above. To validate these inputs further would require a full ASHRAE Level II energy audit which was beyond the scope of the project, and would not increase the level of calibration accuracy to change any conclusions in the study; therefore, this level of calibration did not warrant the extra effort required to inform guidance for the University.

Even if the air leakage rates and mechanical ventilation rates were calibrated more accurately, the envelope's conduction heat transfer contribution to thermal energy demand intensity (TEDI) is independently known from UA calculations. In the case where envelope upgrades do in fact increase air tightness, it may cause unintended consequences to adequate ventilation rates for occupants. In this scenario, occupants may feel air quality is reduced, a condition which could trigger either a higher mechanical ventilation rate, or more frequent opening of windows: both conditions effectively would negate any potential energy savings from reduced air leakage rates by requiring an equivalent amount of heating energy. Therefore, for this kind of study in existing buildings, it is not professionally justifiable to claim air leakage savings with envelope upgrades alone.

Table 1.6 Description of buildings studied

Building	Floor Area (m^2)	Year Built	VFAR	WWR	Envelope construction	Heating Energy Source	Hot water	Space types
Clearihue (CLE)	18,115	1972	0.55	0.30	Steel stud/Concrete	district hot water	gas-fired boiler plant	classrooms, offices, storage rooms, teaching labs, lounge, library, and a data centre
MacLaurin (MAC)	11,802	1978	0.54	0.18	Steel stud	district hot water	Electric	classrooms, offices, storage rooms, practice rooms, art studios, multiple main lobbies, teaching labs, a 300-seat lecture theatre, and a two-storey library
Sedgewick (SED)	3,003	1975	0.85	0.16	Wood	Electric	Electric	offices, storage rooms, mechanical room, staff lounge, boardroom, restrooms, library, and a crawlspace

Table 1.7 List of inputs for energy models

Characteristic	Model Inputs		
	CLE	MAC	SED
Climate File	Victoria-Univ.of.Victoria.717830_CWEC2016, with 2,772 HDD (Base 18.3ºC)		
Infiltration	0.25 L/s/m^2 of exterior wall area, continuously	0.5 L/s/m^2 of exterior wall area, continuously (calibrated)	2 L/s/m^2 of exterior wall area, continuously (calibrated)
Plug loads	1 W/m^2: Library, Lounge, and Storage; 10 W/m^2: Classrooms; 15 W/m^2 Office and Teaching Lab (calibrated)	0.5 W/m^2: Lecture Theatre, Library, Lobby, and Storage; 10 W/m^2: Classrooms; 2.5 W/m^2 Office and Café (calibrated)	1 W/m^2 : Library, Mechanical room, Restroom, Staff Lounge, and Storage room; 5 W/m^2: Office
Outdoor Air	4 ACH in all zones (calibrated)	Per ASHRAE 62.1-2001	Per ASHRAE 62.1-2001
Interior Lighting	Per ASHRAE 90.1-2010 (fluorescent lighting power density)	7 W/m^2 (calibrated)	8 W/m^2 (calibrated)
HVAC Systems	Constant volume systems with economizers; hydronic heating coils with terminal reheat and hydronic baseboards; hot water for heating coils supplied by natural gas district hot water plant Select classrooms with unit ventilators (dedicated outdoor air zone-level equipment with hydronic heating coil)	Constant volume systems with economizers; hydronic heating coils with terminal reheat and hydronic baseboards; hot water for heating coils supplied by natural gas district hot water plant Select classrooms and studios with unit ventilators (dedicated outdoor air zone-level equipment with hydronic heating coil) 7am-7pm weekday supply/return fan schedule	Constant volume system with electric heating coil and return air; all spaces include electric baseboard heating

1.4.2.3 Analysis of calibrated models

In order to evaluate the effects of energy conservation measures (ECMs) on the energy performance of buildings, it was necessary to obtain a case simulation model that represented the existing thermal behavior of the building as closely as possible. In this respect, the values of indices provided by ASHRAE Guideline 14 were calculated, as shown in Table 1.8. It is seen that NMBE and CVRMSE for electricity consumption were met for all buildings. Likewise, NMBE and CVRMSE for natural gas was met for CLE and MAC. Hence, it can be concluded that the models were calibrated within acceptable values determined by ASHRAE Guideline 14. Interestingly, even though more utility data was available for the SED building compared to CLE and MAC, the model for SED was more challenging to calibrate than CLE, possibly due to the fact that heating and equipment loads cannot be disaggregated in SED electrical utility data, as in the other buildings that are heated with gas only.

Table 1.8 Analyzing the magnitude of error between calibrated model and actual data

Calibration criteria	Natural gas		Electricity			ASHRAE Guideline 14
	CLE	MAC	CLE	MAC	SED	
NMBE (%)	-0.06	-4.12	-1.51	-2.32	-4.33	±5%
CVRMSE (%)	0.22	14.85	5.24	8.04	15.00	15%

Figure 1.11 is an illustration of monthly energy profiles in the buildings studied. Electricity data for CLE (Figure 1.11a) was provided for the period of 2014-2018; however, only the data from 2014 was inclusive of all meters for each building wing. It can be observed that electricity consumption is higher in January to April than the model predicts, and lower in June to December. This could be explained by atypical occupant schedules as can be expected in University buildings where courses are structured by semester. Due to classes occurring during the summer semester, electricity consumption is still high during June-August. Furthermore, cooling load provided for the data centre as well as auxiliary equipment such as pumps result in higher electricity usage compared to the other buildings.

Substantially complete district hot water data was provided for 2018. Where data was missing over 1-2 weeks in two separate occurrences in February and April 2018, a reasonable estimate was

calculated based on a simple extrapolation. Expectedly, district hot water consumption is larger during the heating seasons since the building is heated with natural gas (Figure 1.11b). Heating water consumption in the model is overestimated in some months and underestimated in others, likely due in part to occupant schedule deviations from standard building code model assumptions.

Similarly, electricity data in MAC was manipulated to account for data gaps and to disaggregate data from main meters serving multiple buildings. District hot water data was provided from 2016-2018; where data was missing over 1-2 weeks in two separate occurrences in February and April 2018, a reasonable estimate was calculated based on a simple extrapolation. Figure 1.11c shows that district hot water usage is substantially lower compared to CLE due to the smaller building size, and also because domestic hot water is served by electricity (unlike CLE). Moreover, variation in modeled results compared to actual data can be expected due to anomalous weather patterns over the last few years in Victoria. Similarly, variability in class and occupant schedules affects the monthly energy usage profile. Smaller deviations in monthly electricity consumption compared to district hot water can be explained by summer classes at UVic (see Figure 1.11d).

Finally, calibration of SED was based on electricity data from 2014 to 2018 for the entire building, which is shown in Figure 1.11e. It can be observed that the electricity usage pattern in SED is different with CLE and MAC during the summer, which can be attributed to its smaller size and that it is occupied only partially by full-time administrative staff (no students or large classes).

It is to be noted that the following mechanical assumptions in the energy model should ultimately be verified by means of an energy audit:

- total air flow rates
- fan motor specifications
- minimum outdoor air damper positions and behavior
- fan schedules
- office occupancies
- Intent of, and actual performance of, mechanical control strategies (demand control ventilation etc.)
- typical operation of operable windows by occupants

This information was not readily available in drawings or Building Automation System (BAS) data.

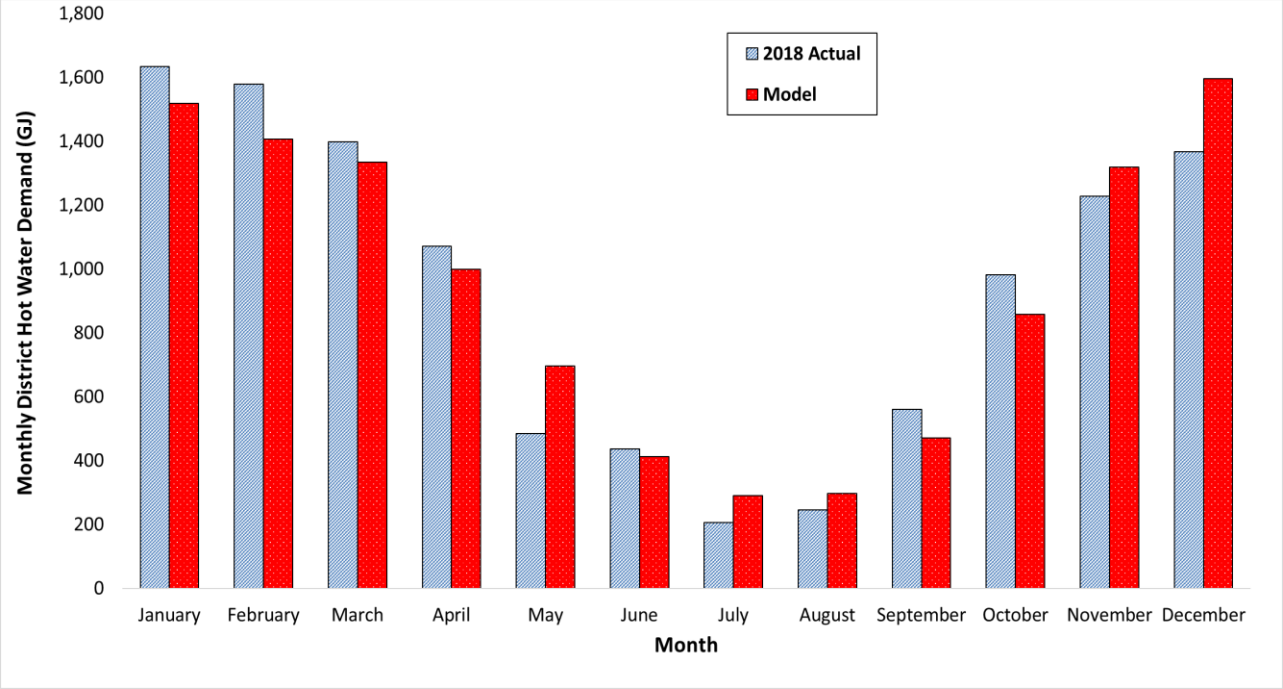
1,800
1,600
1,400
1,200
1,000
800
600
400
200
0
Monthly District Hot Water Demand (GJ)
2018 Actual
Model
January
February
March
April
May
June
July
August
September
October
November
December
Month

(a)

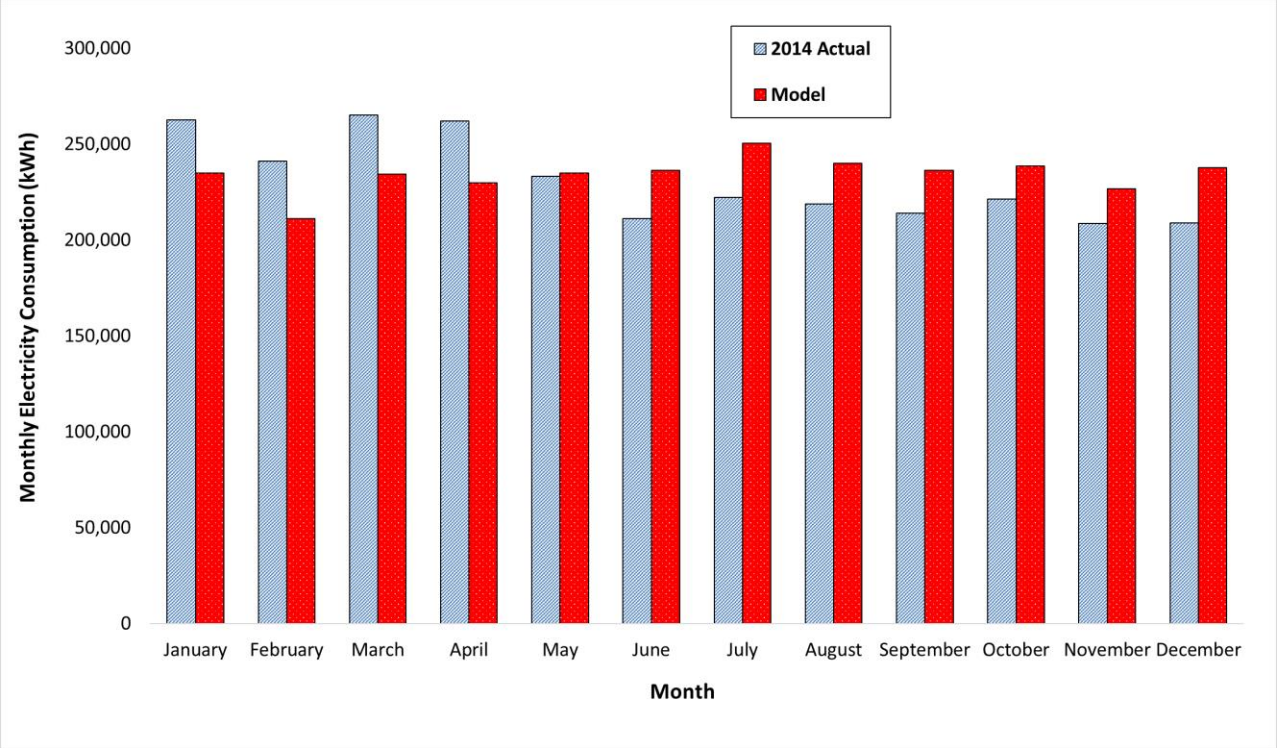
300,000
250,000
200,000
150,000
100,000
50,000
0
Monthly Electricity Consumption (kWh)
2014 Actual
Model
January
February
March
April
May
June
July
August
September
October
November
December
Month

(b)

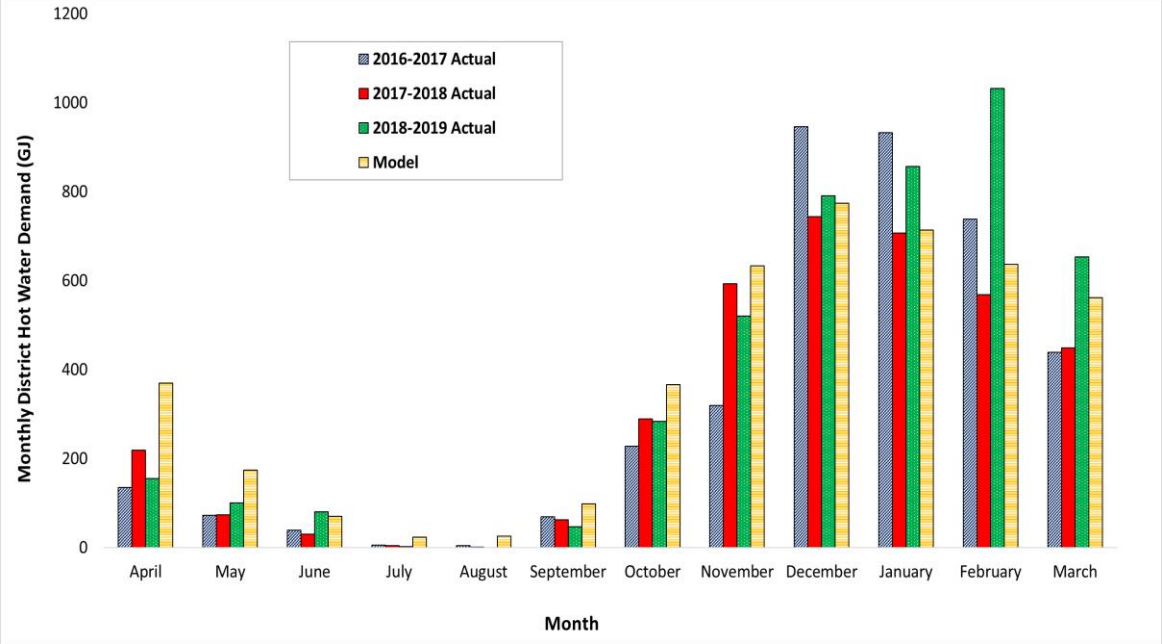
1200
1000
800
600
400
200
0
Monthly District Hot Water Demand (GJ)
2016-2017 Actual
2017-2018 Actual
2018-2019 Actual
Model
April
May
June
July
August
September
October
November
December
January
February
March
Month

(c)

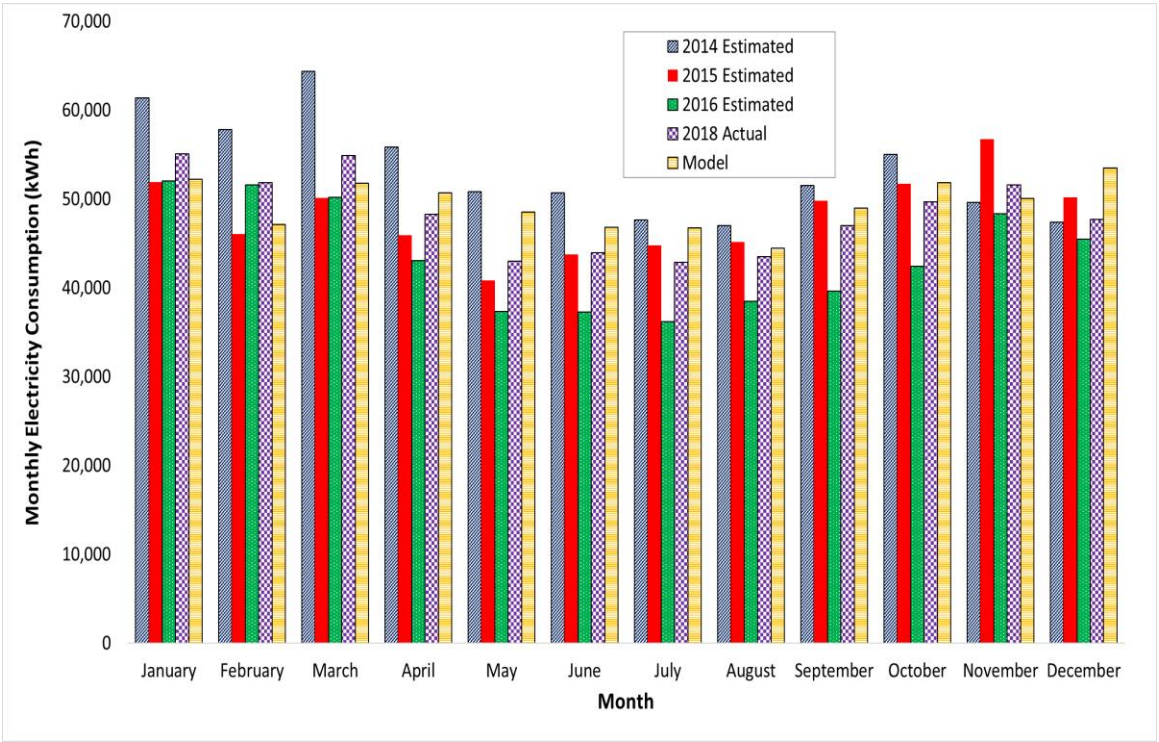
70,000
60,000
50,000
40,000
30,000
20,000
10,000
0
Monthly Electricity Consumption (kWh)
2014 Estimated
2015 Estimated
2016 Estimated
2018 Actual
Model
January
February
March
April
May
June
July
August
September
October
November
December
Month

(d)

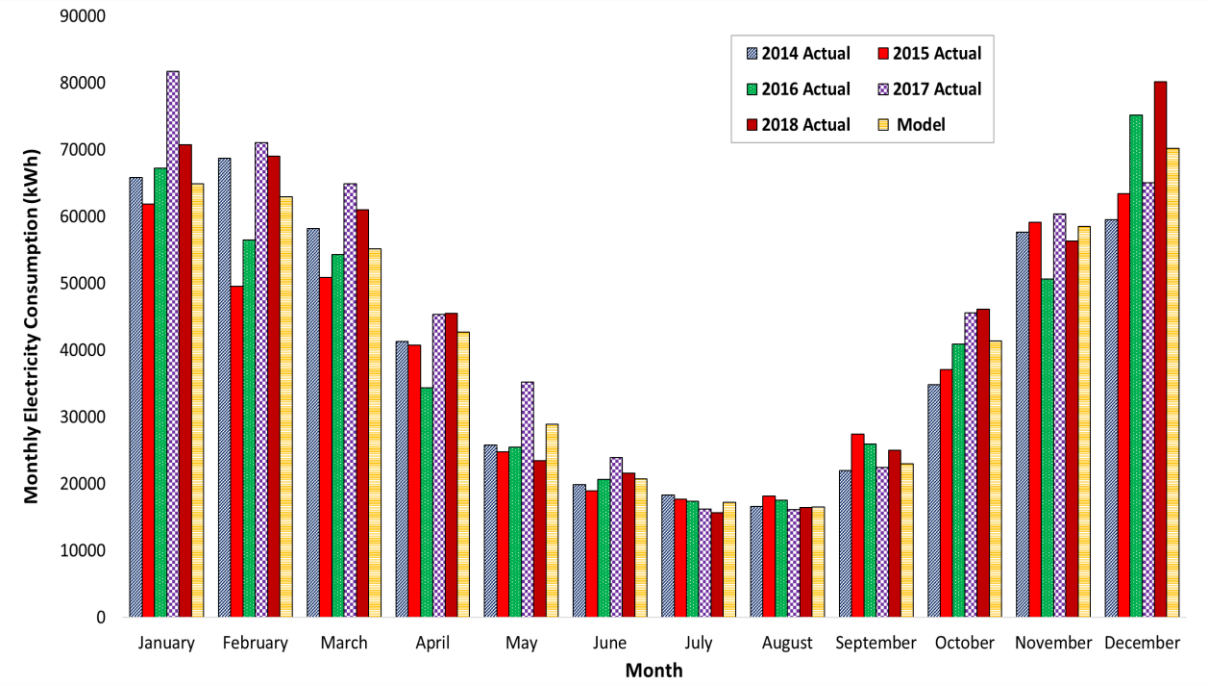

(e)

Figure 1.11 Monthly Electricity Consumption and District Hot Water Demand of Modeled Buildings vs. Utility Data; (a) & (b) CLE; (c) & (d) MAC; (e) SED

1.4.2.4 Impact of energy conservation measures on energy and cost savings

The calibrated energy models were used to evaluate the magnitude of energy and energy cost savings from potential building envelope and ventilation system retrofits. The strategies considered were: (1) improving window performance with a complete window replacement; (2) improving roof performance with added insulation; (3) improving wall thermal performance; (4) reducing the rate of air leakage; (5) Adding heat recovery of ventilation air with 70% efficiency. Strategies were analyzed based on two emerging building energy metrics in Canada:

- TEDI (Thermal Energy Demand Intensity): annual heating energy requirement from all types of space & ventilation heating equipment, per unit of modelled floor area.
- EUI (Energy Use Intensity): the sum of all energy used on site, minus all renewable energy generated on site, per unit of modelled floor area.

Costing assumptions are summarized in Table 1.9.

Table 1.9 Cost savings assumptions

Costs	Rates
Electricity	$0.064/kWh and $12.56/kW monthly peak demand
Natural gas	$7.88/GJ 75% campus district hot water plant efficiency, accounting for combustion and distribution losses
Carbon Taxes	$30/t$CO_2$e included in utility rates; Additional $25/t$CO_2$e external tax; Currently no internal tax

The results of the energy model analysis in Table 1.10 and Table 1.11 show that window/wall upgrades to modern standards have a relatively minor effect on TEDI and EUI, and an even smaller effect on utility cost savings (Figures 1.12 & 1.13) due to: (1) a substantially larger fraction of energy consumed for heating of ventilation air; (2) relatively low carbon taxes; (3) relatively modest campus electricity rates, and; (4) a mild heating climate in Victoria, BC. Although retrofit measures in CLE and MAC did not have a major effect on energy efficiency, potentially improving the indoor environment quality (IEQ) for students is a more interesting perspective. For example, a better thermally performing envelope, either by way of lower thermal transmittance or reduced air leakage (or a combination of both), could make more of the floor area comfortable for occupants in perimeter zones like classrooms, offices, or labs, thereby maximizing classroom sizes. Combined with a re-designed interior design/layout and a re-commissioned mechanical system, IEQ could improve substantially.

In contrast, the analysis of the SED building (Table 1.12) illustrates that relative savings over the base case in TEDI (37%), EUI (26%), and annual utility cost (27%) start to become sizeable when considering the effect of upgrading the roof, walls, and windows (without addressing air leakage) (Figure 1.14). It follows that because SED has a much higher 'narrow' VFAR of 0.84, it has much more conductive losses and therefore, will benefit from envelope upgrades preferably; in contrast, a lower VFAR means that there are fewer envelope losses and that internal loads such as lighting and occupants tend to dominate. Notably, energy cost savings are proportionally higher in an electrically heated building like SED (~$15,000 per year), likely due to a combination of higher cost of electricity relative to natural gas and poor base-case window performance, irrespective of the effect of the carbon tax.

Further, the last scenario in Table 1.12 demonstrates that if envelope upgrades can be coupled with mechanical heat recovery and a reduced air leakage rate there is a potential to realize almost 50% savings in EUI, more than 50% GHG reductions, and nearly a 70% reduction in TEDI. The EUI reduction was not as pronounced in CLE or MAC (last few rows in Tables 1.10 and 1.11) but was nonetheless significant. However, CLE had the biggest potential for low TEDI because of high ventilation heat recovery potential. It is worth noting that since the heat recovery system does not mix return air and fresh outdoor air, indoor air quality ~~is~~ would likely improve with this system.

The cost implications of these potential upgrades would need to be investigated since applying these measures to existing buildings from this vintage and type of construction are not straightforward. For instance, adverse humidity generation indoors or too little ventilation rates in older buildings cause moisture problems. Hence, some older buildings rely on air leakage not only as a means of fresh air supply but also to allow the building to keep the envelope dry thereby mitigating condensation/mould risk. Adding exterior insulation could reduce air leakage prohibitively in this regard and trigger the need to introduce mechanical ventilation systems. If air leakage is the only source of fresh air supply, it must not be restricted.

From the analysis, it can be deduced that buildings with similar envelope characteristics and archetypes as those modeled are likely to have similar TEDI, EUI, and GHG savings economics. Furthermore, it is recommended to prioritize the buildings heated with district hot water from the campus natural gas plant, since envelope retrofits are likely to have a dramatically higher GHG savings than electrically-heated buildings. However, more attractive energy opportunities seem to be related to optimizing the mechanical (ventilation) systems of these buildings.

To illustrate from a different perspective, by analyzing three very distinctly different buildings in terms of shape, occupant profiles, construction type, and heating/DHW fuels, the study informed the university that buildings that share characteristics of one or more of those modeled would likely yield similar conclusions. For example, even if the wood framed Sedgewick building (SED) was heated with gas, the value of energy savings would smaller, GHG savings would be higher, but the overall conclusion regarding the poor value of envelope ECMs holds. Likewise, if the Clearihue (CLE) building was electrically heated, the value of energy savings due to envelope ECMs would be more attractive; however, per Figures 1.12-1.14, the value of cost savings is on the order of ~$10k, which may be as high as ~17k in the best case scenario with electric heating

assuming a 75% efficiency of heating water distribution on campus from the natural gas plant versus 100% in the electric resistance heating case, and the differences in fuel costs per Table 1.9. Given the suggested envelope retrofits would cost on the order of several millions of dollars according to the BECA, the overall message to the University remains the same in every scenario given the above examples:

- Envelope retrofits for an electrically heated buildings are more economically worthwhile than equivalent gas-heated buildings (cost-driven priority),
- Envelope retrofits for gas heated buildings have expectedly more substantial GHG reductions than equivalent electrically-heated buildings (carbon-driven priority),
- Neither scenario is economically justifiable for the university to take on as a project for the sole purpose of cost savings. Rates for electricity, gas, and carbon need to increase substantially to make the business case worthwhile. Retrofits should be prioritized based on other criteria, with energy/cost/GHG findings serving as complementary criteria.

Table 1.10 Summary of Energy Modelling Results for Various ECMs for CLE Building

Scenario	Roof U-value ($W/m^2 K$)	Wall U-value ($W/m^2 K$)	Window U-value ($W/m^2 K$)	Air leakage in Mechanically ventilated zones ($L/s/m^2$)	HRE (%)	TEDI ($kWh/m^2/yr$)	EUI ($kWh/m^2/yr$)	GHG ($kgCO_2e/m^2/yr$)
Base case	0.57	2.54	3.2	0.25	0	162	384	43
Upgraded roof	0.19	2.54	3.2	0.25	0	159	380	42
Upgraded wall	0.57	1.49	3.2	0.25	0	159	379	42
Upgraded windows	0.57	2.54	1.8	0.25	0	156	376	41
Upgraded roof, wall & windows	0.19	1.49	1.8	0.25	0	150	368	40
Upgraded roof, wall & windows +70% HR & 50% less air leakage*	0.19	1.49	1.8	0.125	70	18	193	8

HRE: Heat Recovery Efficiency
** Mechanically ventilated zones only*

Table 1.11 Summary of Energy Modelling Results for Various ECMs for MAC Building

Scenario	Roof U-value (W/m^2K)	Wall U-value (W/m^2K)	Window U-value (W/m^2K)	Skylight U-value (W/m^2 K)	Air leakage in Mechanically ventilated zones ($L/s/m^2$)	HRE (%)	TEDI ($kWh/m^2/yr$)	EUI ($kWh/m^2/yr$)	GHG ($kgCO_2e/m^2/yr$)
Base case	0.57	2.02	6.3 & 3.2	4.5	0.5	0	105	191	26
Upgraded skylights	0.57	2.02	6.3 & 3.2	3.2	0.5	0	104	191	26
Upgraded windows	0.57	2.02	1.8	4.5	0.5	0	100	185	25
Upgraded wall	0.57	1.14	6.3 & 3.2	4.5	0.5	0	100	184	25
Upgraded roof	0.19	2.02	6.3 & 3.2	4.5	0.5	0	99	184	25
Upgraded roof, wall, windows & skylights	0.19	1.14	1.8	3.2	0.50	0	89	169	22
Upgraded roof, wall, skylight & windows +70% HR & 50% less air leakage*	0.19	1.14	1.8	3.2	0.25	70	40	102	10

HRE: Heat Recovery Efficiency
** Mechanically ventilated zones only*

Table 1.12 Summary of Energy Modelling Results for Various ECMs for SED Building

Scenario	Roof U-value (W/m^2K)	Wall U-value (W/m^2K)	Window U-value (W/m^2K)	Air leakage in Mechanically ventilated zones ($L/s/m^2$)	HRE (%)	TEDI ($kWh/m^2/yr$)	EUI ($kWh/m^2/yr$)	GHG ($kgCO_2e/m^2/yr$)
Base case	0.52	1.21	2.8	2	0	116	165	2
Upgraded windows	0.52	1.21	1.8	2	0	112	161	2
Upgraded wall	0.52	0.57	2.8	2	0	106	156	2
Upgraded roof	0.19	1.21	2.8	2	0	89	138	1
Upgraded roof, wall & windows	0.19	0.57	1.8	2	0	73	121	1
Upgraded roof, wall & windows +70% HR & 50% less air leakage*	0.19	0.57	1.8	1	70	36	85	1

HRE: Heat Recovery Efficiency
** Mechanically ventilated zones only*

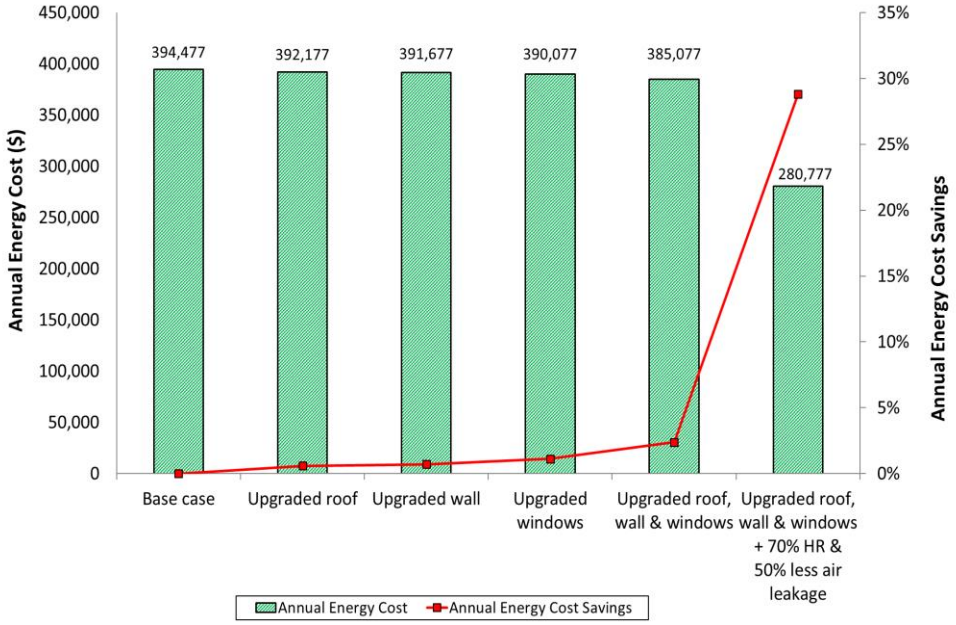

Figure 1.12 Energy cost savings of CLE for different scenarios

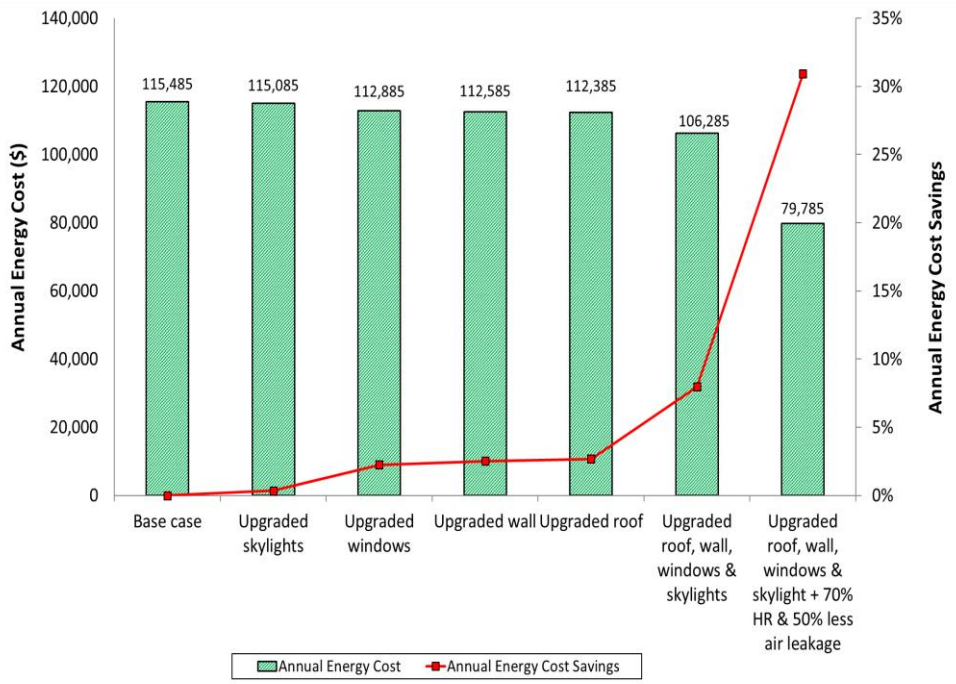

Figure 1.13 Energy cost savings of MAC for different scenarios

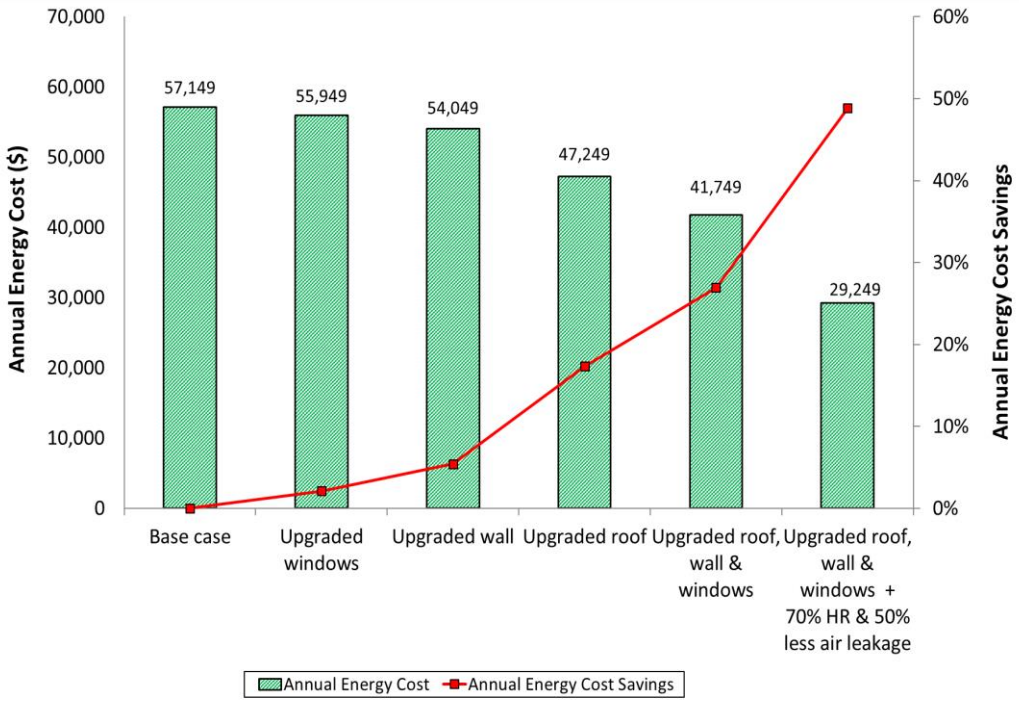

Figure 1.14 Energy cost savings of SED for different scenarios

Building energy metrics (TEDI and EUI) of the studied buildings were compared with proposed targets in the BC Energy Step Code Development for Public Sector Buildings [48] and the ASHRAE 100 [49] standard, shown in Table 1.13. It should be noted that ASHRAE 100 provides only EUIs target for several building typologies and does not consider TEDI metric for existing buildings. MAC and SED currently meet the ASHRAE 100 target for EUI, while CLE is well beyond it. This can be attributed to the fact that CLE has either much higher ventilation loads or a higher air leakage rate than the other buildings, and the significant electricity consumption used for the computers in the data centre, as well as the additional energy required for cooling it.

None of the buildings meet EUI and TEDI targets proposed for the BC Energy Step Code. Interestingly, although CLE can meet the TEDI target of BC Energy Step Code by implementing envelope upgrades coupled with mechanical heat recovery and a reduced air leakage rate, it cannot meet the EUI target, likely due to loads associated with data centre. MAC and SED were only able to meet the targets in the Energy Step Code in the best-case scenario of retrofit strategies.

In general, TEDI targets for all buildings identified in “BC Energy Step Code Development for Public Sector Buildings” can likely be achieved in these retrofits, but would require triple glazed fenestration and a better opaque wall system than our parametric analysis considered. Furthermore,

achieving EUI targets will largely be dependent on TEDI reductions – lighting, plug load, fan, and pump savings cannot be stand-alone measures. Air leakage needs to be addressed for deep TEDI reductions, but as outlined earlier, it can be confounded by ventilation code implications.

Table 1.13 Contrasting EUI and TEDI of Buildings in the Study with the BC Energy Step Code and ASHRAE 100

Building	EUI ($kWh/m^2/yr$)	TEDI ($kWh/m^2/yr$)	Proposed Targeted EUI BC step-code ($kWh/m^2/yr$)	Proposed Targeted TEDI BC step-code ($kWh/m^2/yr$)	Targeted EUI in ASHRAE 100 ($kWh/m^2/yr$)
CLE	384	162	165	20	247
MAC	191	105	165	20	247
SED	165	116	130	30	193

Although retrofit strategies have a major impact on the energy reduction of buildings, energy cost savings is also often important. As mentioned above, energy cost savings were not considerable because of a low carbon tax price and Victoria's mild climate. To analyze the impact of carbon tax on annual energy cost savings, four other different carbon tax scenarios of 40 \$/T-CO_2e, 50 \$/T-CO_2e, 100 \$/T-CO_2e and 140 \$/T-CO_2e were analyzed. It should be noted that the 140 \$/T-CO_2e is based on the highest rate of carbon tax in the world (Sweden). The results in Figure 1.15 showed that the effect of an increased carbon tax had a relatively negligible effect on energy cost savings in electrically-heated SED. Conversely, as shown in Figures 1.16 and 1.17, gas-heated buildings showed a more appreciable effect, up to 63% and 59% higher in the case of a 140 \$/tonne carbon tax in CLE and MAC, respectively. Since the increase of carbon tax price influences the annual energy cost of gas-heated buildings substantially more than electrical heated buildings, the findings of this analysis inform the university that energy retrofitting measures should be implemented and prioritized for gas-heated buildings. Alternatively, gas heating systems could be replaced by electric-based systems to reduce annual energy costs in gas-heated buildings on campus.

It is to be noted that in British Columbia, the emission factor for electricity is very low (3.0 kg/GJ) as a result of 97% of the power generated by way of clean or renewable sources, a large majority of that accounted for by hydroelectricity. In contrast, the emission factor for natural gas is ~50 kg/GJ, a factor of 15x higher. Given these, increases to carbon taxes disproportionately affect natural gas rates relative to electricity rates by an order of magnitude or more. As a result of these

points, increases in either gas utility rates, gas emission factors, or carbon taxes effectively increases the cost of gas consumption while negligibly affecting electricity costs. Therefore, in gas-heated buildings, building envelope retrofits yield better economic outcomes when any combinations of these gas variables are increased.

However, by increasing the cost of electricity in gas-heated buildings, the baseload (non-heating) energy costs will increase but does not affect the available cost savings from heating reductions. In contrast, in electrically-heated buildings, the overall cost of heating energy (and total energy) will increase and therefore presents a stronger business case for building envelope retrofits.

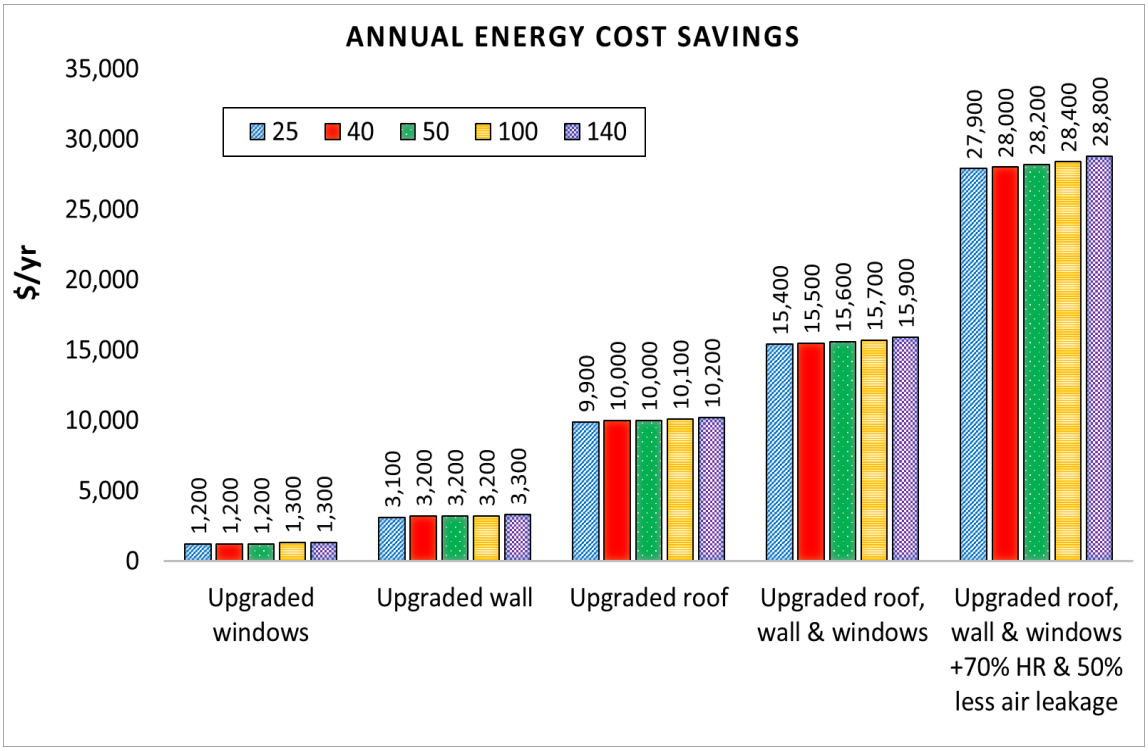

Figure 1.15 Annual energy cost saving based on different scenarios of carbon tax ($/T-CO2e) for SED Building

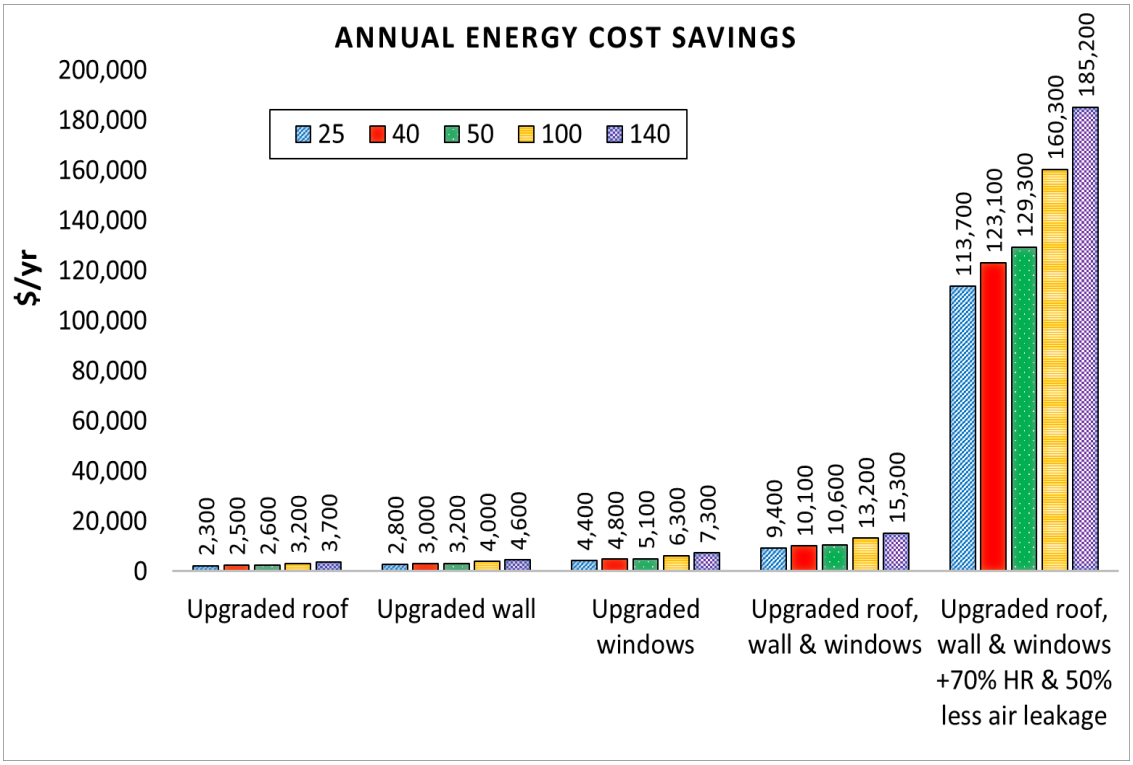

Figure 1.16 Annual energy cost saving based on different scenarios of carbon tax ($/T-CO2e) for CLE Building

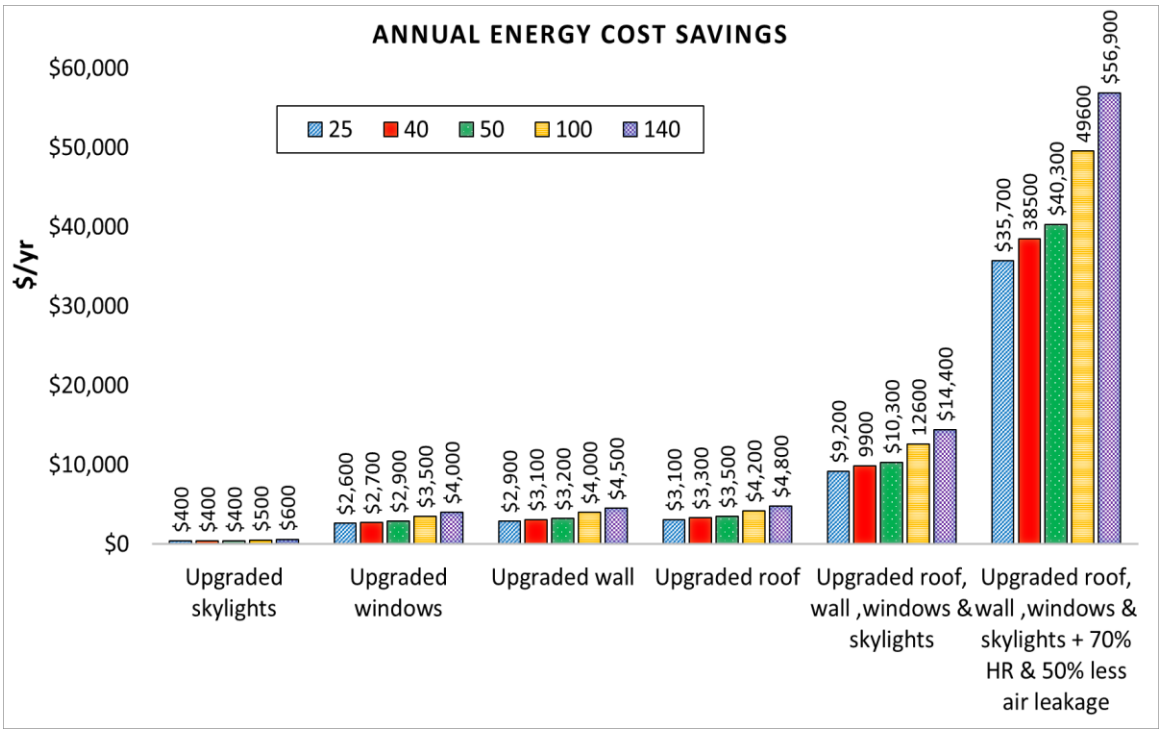

Figure 1.17 Annual energy cost saving based on different scenarios of carbon tax ($/T-CO2e) for MAC Building

1.5 Conclusions

The building prioritization method for energy retrofit presented in this chapter provided clear guidance to the University, as part of their ongoing capital plan, with respect to retrofits of existing building vertical envelopes. The implemented methodology and studied parameters unveiled a new horizon in evaluating the thermal performance of existing building envelopes in Canada, where a building code for existing buildings has not yet been established. This case study analyzed 49 buildings using a mixed methodology where building specific data was collected, and UA and other building metrics/characteristics were tabulated to provide added depth to the analysis. This was followed by a more detailed analysis using the energy simulation tool EnergyPlus on a few high priority buildings, and to a certain extent, conclusions from the detailed analysis could be applied to other similar campus buildings in Canada, and in particular British Columbia (where UVic is located), in which climate, construction practices, building codes, utility costs, carbon emission factors, and carbon taxes are similar to that of this study. The results from the building envelope condition assessment (BECA) provided yet another practical and complementary lens to recommendations from the energy efficiency perspective. The value of this study is in the development of a performance-based approach to optimize energy performance and cost effectiveness, in contrast to the simple traditional approach of prioritizing buildings based on their vintage or reference tables in building codes. The main findings of this study are outlined below:

- There was no correlation between physical condition and thermal performance of building envelopes in the building portfolio studied.
- Prioritization of buildings for envelope retrofits might be considered based on UA values if priority is given to the buildings with higher energy consumption.
- Normalized UA values with floor area or vertical envelope area is a better indicator of relative envelope performance than using absolute UA.
- Architectural characteristics such as VFAR and WWR have significant impact on the thermal performance of buildings. Buildings with higher VFAR have higher heat losses, and higher WWR not only increases thermal bridges, but also adds more of a higher U-value window area and subtracts a lower U-value wall area (“double penalty”).
- The results showed that wood framed buildings have lower U-values compared to the steel-stud and concrete framed buildings. This is justifiable from three perspectives:

    - wood is a better insulator than steel or concrete; therefore, wood framed buildings have less thermal bridging losses.
    - wood framed buildings on campus were generally older with a much lower WWR than larger non-wood buildings.
    - wood framed buildings on campus are mainly limited to a single storey, and do not include the penalty of intermediate floor thermal bridges.

- Thermal bridging impacts are substantial in all buildings studied; building construction types or vintages do not seem to have significantly different U-values once all thermal bridging is accounted for.
- Since conclusions from ranking buildings based on one metric may not be consistent with ranking based on a different metric, multiple ranked lists should be considered in combination for building envelope retrofit decision-making. Policymakers or portfolio managers may decide to assign a higher priority to certain ranked lists versus others.
- Low campus utility rates, a low carbon tax, and a mild heating climate appear to be a barrier for most envelope upgrades (not considering air leakage effects).
- High VFAR and non-student occupied buildings have the deepest EUI reductions from envelope transmittance upgrades based on simulations.
- Deep reductions in TEDI, EUI, GHG, and utility costs are more likely to be achieved by a combination of reducing air leakage and implementing mechanical heat recovery of ventilation air.
- Buildings with similar envelope characteristics and archetypes as those modeled are likely to have similar TEDI, EUI, and GHG savings economics, highlighting the value of this hybridized analysis.
- Proposed energy benchmarks for college buildings in the "BC Energy Step Code Development for Public Sector Buildings" would be challenging to meet with a suite of envelope upgrades analyzed in this study. While the EUI benchmark is achievable, meeting the TEDI benchmark would require measures over and beyond those analyzed.
- Increasing carbon tax had a relatively negligible effect on energy cost savings in electrically-heated buildings. However, gas heated buildings showed a more appreciable

effect, up to 63% and 59% higher in the case of a 140 $/tonne carbon tax in CLE and MAC, respectively.

To summarize, obtained results provided a practical perspective in the evaluation and ranking of a portfolio of buildings for envelope retrofits. The strength of the methodology was in its balance of effort and ultimate decision-making utility, where reasonable thermal bridging approximations for existing buildings can yield data accurate enough to inform a ranking exercise on a large breadth of subject buildings. Given that a large percentage of building stock (such as campus buildings) were constructed before the advent of building energy codes, and often have higher energy use compared to new construction, findings of this study could be used to inform effectiveness of energy policy at the provincial level for other buildings with similar characteristics. Furthermore, since targets for Thermal Energy Demand Intensity (TEDI) are limited only to new construction (i.e. residential, office, retail) in the current B.C. building code, the energy models developed in this study can pave the way towards informing TEDI targets for existing college/university buildings. Considering the economic findings of the envelope retrofits studied, a government-mandated requirement (code) to improve existing building envelope performance would likely require additional incentive for building owners, such as higher utility costs, higher carbon taxes, or establishing government-funded incentive programs. It can be expected that as literature becomes more populated with such studies, more data will become available to establish existing building energy codes in the Canadian context.

1.6 References

[1] International Energy Agency (IEA), Buildings A source of enormous untapped efficiency potential, Availabe at: https://www.iea.org/topics/buildings (Accessed on 15 March 2021).

[2] L. Mazzarella, Energy retrofit of historic and existing buildings. The legislative and regulatory point of view, Energy Build. 95 (2015) 23-31.

[3] S. Wang, C. Yan, F. Xiao, Quantitative energy performance assessment methods for existing buildings, Energy Build. 55 (2012) 873-888.

[4] S. Chidiac, E. Catania, E. Morofsky, S. Foo, Effectiveness of single and multiple energy retrofit measures on the energy consumption of office buildings, Energy. 36 (8) (2011) 5037-5052.

[5] J.G. Koomey, N.C. Martin, M. Brown, L.K. Price, M.D. Levine, Costs of reducing carbon emissions: US building sector scenarios, Energy Policy, 26 (5) (1998) 433-440.

[6] Z. Ma, P. Cooper, D. Daly, L. Ledo, Existing building retrofits: Methodology and state-of-the-art, Energy Build. 55 (2012) 889-902.

[7] T.A. Reddy, Literature review on calibration of building energy simulation programs: uses, problems, procedures, uncertainty, and tools, ASHRAE transactions, 112 (2006) 226.

[8] E. Fabrizio, V. Monetti, Methodologies and advancements in the calibration of building energy models, Energies, 8 (4) (2015) 2548-2574.

[9] K. H. Cho, S.S. Kim, Energy performance assessment according to data acquisition levels of existing buildings, Energies. 12(6) (2019) 1149.

[10] A. Alghamdi, H. Haider, K. Hewage, R. Sadiq, Inter-University Sustainability Benchmarking for Canadian Higher Education Institutions: Water, Energy, and Carbon Flows for Technical-Level Decision-Making, Sustainability, 11 (9) (2019) 2599.

[11] A. Zhang, R. Bokel, A. Van den Dobbelsteen, Y. Sun, Q. Huang, Q. Zhang, The effect of geometry parameters on energy and thermal performance of school buildings in cold climates of china, Sustainability, 9 (10) (2017) 1708.

[12] Natural Resources Canada (NRC), Consumption of Energy Survey for Universities, Colleges and Hospitals, 2003, Available at: https://oee.nrcan.gc.ca/corporate/statistics/neud/dpa/data_e/consumption03/universities.cfm?attr=0 (Accessed on 15 March 2021)

[13] A. Mastrucci., O. Baume, F. Stazi, U. Leopold, Estimating energy savings for the residential building stock of an entire city: A GIS-based statistical downscaling approach applied to Rotterdam, Energy Build. 75 (2014) 358-367.

[14] M. Mangold, M. Österbring, H. Wallbaum, L. Thuvander, P. Femenias, Socio-economic impact of renovation and energy retrofitting of the Gothenburg building stock, Energy Build. 123 (2016) 41-49.

[15] C. Delmastro, G. Mutani, S.P. Corgnati, A supporting method for selecting cost-optimal energy retrofit policies for residential buildings at the urban scale, Energy Policy. 99 (2016) 42-56

[16] G. Peri, G. Rizzo, G. Scaccianoce, V. Vaccaro, On the ranking criteria for energy retrofitting building stocks: Which building goes first? The role of the building size in the establishment of priority lists, Energy Build. 150 (2017) 90-99.

[17] Building Research Establishment. RdSAP Conventions for RdSAP 9.92; Building Research Establishment:Wardford, UK, 2015.

[18] S. Kelly, D. Crawford-Brown, M.G. Pollitt, Building performance evaluation and certification in the UK: Is SAP fit for purpose?, Renewable Sustainable Energy Rev. 16 (9) (2012) 6861-6878.

[19] É. Mata, A.S. Kalagasidis, F. Johnsson, Building-stock aggregation through archetype buildings: France, Germany, Spain and the UK, Build. Environ. 81 (2014) 270-282.

[20] S. Buessler, D. Badariotti, C. Weber, Evaluating the complex governance arrangements surrounding energy retrofitting programs: The case of collective ownership buildings in France, Energy Res. social Sci. 32 (2017) 131-148.

[21] Morrsion Hershfield, Building Envelope Thermal Bridging Guide—Analysis, Applications and Insights, 2014.

[22] D.F.M. Cabrera, H. Zareipour, Data association mining for identifying lighting energy waste patterns in educational institutes, Energy Build. 62 (2013) 210-216.

[23] M.d. Paris, Direction des Espaces Verts et de l'Environnement- Agence d'Ecologie Urbaine-Division Climat-Energie, Rénovation énergétique desécoles parisiennes (2014) 1–2.

[24] A. Thewes, S. Maas, F. Scholzen, D. Waldmann, A. Zürbes, Field study on the energy consumption of school buildings in Luxembourg, Energy Build. 68 (2014) 460–470.

[25] V. Butala, P. Novak, Energy consumption and potential energy savings in old school buildings, Energy Build. 29 (1999) 241–246.

[26] E.G. Dascalaki, V.G. Sermpetzoglou, Energy performance and indoor environmental quality in Hellenic schools, Energy Build. 43 (2011) 718–727.

[27] L. Dias Pereira, D. Raimondo, S.P. Corgnati, M. Gameiro da Silva, Energy consumption in schools – a review paper, Renew. Sustain. Energy Rev. 40 (2014) 911–922.

[28] M.C. Katafygiotou, D.K. Serghides, Analysis of structural elements and energyconsumption of school building stock in Cyprus: energy simulations andupgrade scenarios of a typical school. Energy Build. 72 (2014) 8–16.

[29] Y. Allab, M. Pellegrino, X. Guo, E. Nefzaoui, A. Kindinis, Energy and comfort assessment in educational building: Case study in a French university campus, Energy Build. 143 (2017) 202-219.

[30] M.H. Issa, M. Attalla, J.H. Rankin, J. Christian, Energy consumption in conventional, energy-retrofitted and green LEED Toronto schools. Construct. Manage. Econ. 29 (4) (2011) 383-395.

[31] V. Straka, M. Aleksic, Post-Occupancy Evaluation. Three schools from greater Toronto, in: PLEA 2009-26th Conference on Passive and Low Energy Architecture, Quebec City, Canada, pp. 22-24.

[32] M.M, Ouf, M.H Issa, Energy consumption analysis of school buildings in Manitoba, Canada, Int. J. Sustainable Built Environ. 6(2) (2017) 359-371.

[33] Government of Canada sets ambitious GHG reduction targets for federal operations, available at: https://www.canada.ca/en/treasury-board secretariat/news/2017/12/government_of_canadasetsambitiousghgreductiontargetsforfederalop.html (Accessed on 18 March 2021)

[34] DoE US. Energyplus engineering reference, The reference to energyplus calculations, (2010).

[35] ASHRAE, ASHRAE Handbook Fundamentals, American Society of Heating, Ventilating and Air-Conditioning Engineers, Inc., Atlanta, GA, 2017.

[36] National Research Council (NRC). National Energy Code of Canada for Buildings; National Research Council Canada: Ottawa, ON, Canada, 2015.

[37] ASHRAE, ASHRAE Standard 62.1-2010: Ventilation for Acceptable Indoor Air Quality, American Society of Heating, Refrigerating and Air-Conditioning Engineers, Inc, Atlanta, Georgia, 2010.

[38] Morrison Hershfield, Thermal performance of building envelope details for mid-and high-rise buildings, ASHRAE Research Project1365-RP Final Report, 2011.

[39] ASHRAE, ANSI/ASHRAE/IESNA Standard 90.1-2010: Energy Standard for Buildings Except Low-Rise Residential Buildings. American Society of Heating, Refrigerating and Air-Conditioning Engineers, Inc, Atlanta, Georgia, 2010.

[40] Tables for Calculating Effective Thermal Resistance of Opaque Assemblies, Available at: https://www.nrcan.gc.ca/energy/efficiency/housing/new-homes/energy-starr-new-homes-standard/tables-calculating-effective-thermal-resistance-opaque-assemblies/14176 (Accessed on 15 March 2021)

[41] EN ISO 14683, Thermal bridges in building construction – Linear thermal transmittance – Simplified methods and default values, 2007.

[42] Energy Step Code — Building Beyond the Standard, Metrics Research Full Report Update, BC Housing, British Columbia, Canada (2018).

[43] G. Hua, F. Baba, Effect of dynamic modeling of thermal bridges on the energy performance of residential buildings with high thermal mass for cold climates, Sustain Cities Soc 34 (2017): 250-263.

[44] F. Baba, Dynamic Effect of Thermal Bridges on the Energy Demand of Residential Buildings. Master Thesis at Concordia University (2015).

[45] ASHRAE, ASHRAE Guideline14: Measurement of Energy, Demand, and Water Savings, American Society of Heating Refrigerating and Air-Conditioning Engineers, Inc, Atlanta, Georgia, 2014.

[46] G. Ruiz, C.F. Bandera, Validation of calibrated energy models: Common errors, Energies. 10 (10) (2017) 1587.

[47] T. Hong, M.A. Piette, Y. Chen, S.H. Lee, S.C. Taylor-Lange, R. Zhang, K. Sun, P. Price, Commercial building energy saver: an energy retrofit analysis toolkit, Appl. Energy. 159 (2015): 298-309.

[48] Morrison Hershfield, BC Energy Step Code Development for Public Sector Buildings, Province of British Columbia, Canada (2019).

[49] ASHRAE, ANSI/ASHRAE/IEA Standard 100-2018: Energy Efficiency in Existing Buildings, American Society of Heating, Refrigerating and Air-Conditioning Engineers, Inc, Atlanta, Georgia, 2018.

Appendix 1.A1: List of studied Buildings

	BLDG	NAME	Frame	Built	Initial Description
1	BWC	Bob Wright Centre - Ocean, Earth and Atmospheric Sciences	steel	2009	offices, labs, lecture hall
2	BEC	Business and Economics Building & David Strong Building	steel	1997	Office/Faculty of Social Sciences
3	SEC	Campus Security Building	wood	1996	security offices, with power generator
4	CSR	Campus Services	steel	1996	bookstore, multifaith, offices, general store, cappucino bar
5	STA	Centennial Stadium	steel	1974	stadium facility
6	CARSA	Centre for Athletics, Recreation and Special Abilities	steel	2015	fitness/sports/world class faciilty
7	CHA	Chapel Building	wood	1984	chapel building for special events and multifaith services
8	CCC	Child Care Centre	wood	1993	child care with child activity rooms
9	CLE	Clearihue Building	steel stud/Concrete	1972	humanities and technology solution centre (offices)
10	CST	Continuing Studies Building	steel	2003	continuing studies building (office/lecture?)
11	COR	Cornett Building	steel	1966	classroom, lab, faculty office for social science
12	CUN	Cunningham Building	steel stud/Concrete	1971	animal care, aquarium, biohazard, electron microsfope, etc
13	DTB	David Turpin Building	steel	2008	labs and offices
14	ELL	Elliott Building	steel stud/Concrete	1963	3 storeys labs, 4 storeys office and research, lecture theatere, including observatory
15	ELW	Engineering Lab Wing	steel stud/Concrete	1995	laboratories, computers/mechanical eng - "technologically advanced"

16	EOW	Engineering Office Wing	concrete	1990	labs and offices for engineering/robotics, energy, subsea, electromagnetics
17	ECS	Engineering/Computer Science	concrete	2006	offices, lecture halls, labs
18	EDC	Enterprise Data Centre	steel	2009	data centre; 3000 servers
19	FIA	Fine Arts Building	steel	1990	offices, classrooms, lecture hall, darkroom, lobby
20	FPH	First Peoples House	wood	2010	cermonial hall, elders rooms, classrooms, offices
21	FRA	Fraser Building	steel	1980	classrooms, seminar rooms, moot court
22	GSC	Halpern Centre for Graduate Students	wood	1990	multi prupose study rooms, restaurant
23	HHB	Hickman Building	steel stud/Concrete	1999	lecture halls, smaller clasrooms, seminar rooms
24	HSD	Human and Social Development	steel	1992	office, computer labs, classroom
25	HTA	Hut A	wood	1940	old WW2 army hut converted to office/lab
26	HTB	Hut B	wood	1940	old WW2 army hut converted to office/lab
27	HTE	Hut E	wood	1992	old WW2 army hut converted to office/lab
28	HTQ	Hut Q	wood	1940	old WW2 army hut converted to office/lab
29	HTR	Hut R	wood	1940	old WW2 army hut converted to office/lab
30	HLP	Lou-Poy Child Care Centre	wood	2001	infant /toddler daycare
31	MAC	MacLaurin Building	steel	1978	auditorium, recital hall, practice rooms, offices, recording studio
32	MCK	McKinnon Building	steel	1975	sports facility weight room dance, tennis courts, etc (now empty or repurpsosed)?
33	LIB	McPherson Library	steel stud/Concrete	1974	library
34	MSB	Medical Sciences Building	wood	2003	offices, lecture hall, lab
35	MWB	Michael Williams Building	steel	2008	office
36	PCH	Petch Building	steel stud/Concrete	1984	lab, office, lecture hall
37	HEA	Petersen Health Centre (PEA)	wood	1969	office/clinic
38	PNX	Phoenix Theatre	steel	1981	3 theatre spaces, and studio. Shop, rehearsal space, dressing rooms
39	SAA	Saunders Annex	wood	1974	facilities management - storage, shop, offices
40	SAU	Saunders Building	wood	1965	offices
41	SED	Sedgewick Building	wood	1975	research centre and offices (mostly office)
42	SUB	Student Union Building	steel stud/Concrete	1962	office, cafeteria, coffee shop, bookstore, travel agency, hair salon, lounge, movie theatre
43	TEF	Technology Enterprise Facility	steel stud/Concrete	2003	offices, technology labs
44	UVC	University Centre	steel	1978	offices, food facility, auditorium
45	UCL	University Club	wood	1982	office, multipurpose dining/seminar
46	UH1	University House 1	wood	1969	offices in a single family home
47	UH2	University House 2	wood	2014	offices in a single family home
48	CSF	Velox Building	wood	1989	banquet hall, change rooms, storage, kitchen, dining

49	VIA	Visual Arts Building	steel stud/Concrete	1992	classroom, office, studios

Appendix 1.A2: Building Prioritization based on Façade UA Estimate; color bar percentile scale from red (100th) to green (0th).

Bldg	Frame	Façade UA Estimate (W/K)	Façade UA per Façade Area (W/m^2K)	Façade Area (m^2)	Façade UA per Floor Area (W/m^2K)	Floor Area Estimate from MH Takeoff (m^2)	WWR	VFAR	Year Built
CLE	steel stud/concrete	24,600	2.54	9670	1.40	17,537	0.30	0.55	1972
MAC	steel	16,500	2.02	8162	1.10	15,020	0.18	0.54	1978
LIB	steel stud/concrete	14,000	2.26	6181	0.62	22,473	0.39	0.28	1974
DTB	steel	11,900	2.46	4831	1.26	9,477	0.55	0.51	2008
COR	steel	11,100	1.85	5990	1.13	9,811	0.18	0.61	1966
CARSA	steel	10,600	1.15	9199	0.62	17,043	0.21	0.54	2015
ELL	steel stud/concrete	9,300	1.81	5143	0.67	13,803	0.14	0.37	1963
FRA	steel	9,200	2.15	4280	0.97	9,441	0.34	0.45	1980
BWC	steel	9,100	1.23	7374	0.71	12,849	0.20	0.57	2009
PCH	steel stud/concrete	9,000	2.55	3529	1.24	7,270	0.47	0.49	1984
BEC	steel	8,700	1.81	4803	0.95	9,169	0.26	0.52	1997
UVC	steel	8,500	2.53	3356	0.54	15,677	0.46	0.21	1978
ELW	steel stud/concrete	8,300	1.90	4357	0.77	10,832	0.25	0.40	1995
ECS	concrete	8,000	1.32	6052	0.91	8,801	0.20	0.69	2006
HSD	steel	6,800	1.74	3901	0.89	7,611	0.20	0.51	1992
CUN	steel stud/concrete	6,700	1.80	3715	1.05	6,361	0.21	0.58	1971
SUB	steel stud/concrete	6,700	1.65	4051	0.98	6,825	0.18	0.59	1962
MCK	steel	6,600	1.63	4042	0.74	8,892	0.11	0.45	1975
MWB	steel	5,000	2.36	2116	1.25	4,000	0.48	0.53	2008
CST	steel	4,800	1.57	3048	0.66	7,274	0.21	0.42	2003
CSR	steel	4,200	2.26	1860	0.94	4,474	0.38	0.42	1996
EOW	concrete	3,900	1.85	2112	1.07	3,639	0.39	0.58	1990
MSB	steel	3,700	1.62	2279	0.97	3,817	0.23	0.60	2003
FIA	steel	3,600	2.38	1512	1.51	2,378	0.42	0.64	1990
VIA	steel stud/concrete	3,400	1.26	2705	0.88	3,856	0.16	0.70	1992
TEF	steel stud/concrete	2,900	2.22	1308	1.03	2,817	0.41	0.46	2003
SED	wood	2,800	1.21	2312	1.03	2,725	0.16	0.85	1975
SAA	wood	2,300	2.72	845	1.95	1,178	0.21	0.72	1974
PNX	steel	2,200	0.73	3016	0.40	5,552	0.05	0.54	1981
FPH	wood	2,100	2.30	911	1.68	1,251	0.52	0.73	2010
SAU	wood	2,100	1.15	1819	0.91	2,312	0.13	0.79	1965
HHB	steel stud/concrete	1,400	1.57	890	1.06	1,321	0.17	0.67	1999
HTR	wood	1,300	1.95	667	1.96	664	0.11	1.00	1940
STA	steel	1,200	1.96	612	1.24	966	0.03	0.63	1974
EDC	steel	1,200	1.51	794	0.98	1,219	0.06	0.65	2009
CSF	wood	1,100	2.16	510	1.00	1,098	0.18	0.46	1989
UCL	wood	1,100	2.10	523	0.80	1,371	0.44	0.38	1982
UH1	wood	800	1.31	609	0.98	819	0.19	0.74	1969
GSC	wood	700	1.38	508	1.10	634	0.23	0.80	1990
CCC	wood	700	1.14	612	0.77	909	0.19	0.67	1993
HTE	wood	700	1.01	693	0.98	716	0.10	0.97	1992
CHA	wood	600	1.50	400	1.37	437	0.27	0.92	1984
HEA	wood	500	1.46	342	0.75	663	0.23	0.52	1969
SEC	wood	500	1.22	411	1.09	459	0.13	0.90	1996
HTB	wood	400	1.29	311	1.49	269	0.10	1.16	1940
HLP	wood	400	1.28	313	0.96	415	0.16	0.75	2001
HTQ	wood	400	0.93	431	1.04	383	0.00	1.12	1940
UH2	wood	300	1.07	281	0.82	367	0.20	0.77	2014
HTA	wood	200	1.80	111	1.76	113	0.18	0.98	1940

Appendix 1.A3: Building Prioritization based on Façade UA per Façade Area (Average U-Value); color bar percentile scale from red (100th) to green (0th)

Bldg	Frame	Façade UA Estimate (W/K)	Façade UA per Façade Area (W/m^2K)	Façade Area (m^2)	Façade UA per Floor Area (W/m^2K)	Floor Area Estimate from MH Takeoff (m^2)	WWR	VFAR	Year Built
SAA	wood	2,300	2.72	845	1.95	1,178	0.21	0.72	1974
PCH	steel stud/concrete	9,000	2.55	3529	1.24	7,270	0.47	0.49	1984
CLE	steel stud/concrete	24,600	2.54	9670	1.40	17,537	0.30	0.55	1972
UVC	steel	8,500	2.53	3356	0.54	15,677	0.46	0.21	1978
DTB	steel	11,900	2.46	4831	1.26	9,477	0.55	0.51	2008
FIA	steel	3,600	2.38	1512	1.51	2,378	0.42	0.64	1990
MWB	steel	5,000	2.36	2116	1.25	4,000	0.48	0.53	2008
FPH	wood	2,100	2.30	911	1.68	1,251	0.52	0.73	2010
LIB	steel stud/concrete	14,000	2.26	6181	0.62	22,473	0.39	0.28	1974
CSR	steel	4,200	2.26	1860	0.94	4,474	0.38	0.42	1996
TEF	steel stud/concrete	2,900	2.22	1308	1.03	2,817	0.41	0.46	2003
CSF	wood	1,100	2.16	510	1.00	1,098	0.18	0.46	1989
FRA	steel	9,200	2.15	4280	0.97	9,441	0.34	0.45	1980
UCL	wood	1,100	2.10	523	0.80	1,371	0.44	0.38	1982
MAC	steel	16,500	2.02	8162	1.10	15,020	0.18	0.54	1978
STA	steel	1,200	1.96	612	1.24	966	0.03	0.63	1974
HTR	wood	1,300	1.95	667	1.96	664	0.11	1.00	1940
ELW	steel stud/concrete	8,300	1.90	4357	0.77	10,832	0.25	0.40	1995
COR	steel	11,100	1.85	5990	1.13	9,811	0.18	0.61	1966
EOW	concrete	3,900	1.85	2112	1.07	3,639	0.39	0.58	1990
BEC	steel	8,700	1.81	4803	0.95	9,169	0.26	0.52	1997
ELL	steel stud/concrete	9,300	1.81	5143	0.67	13,803	0.14	0.37	1963
CUN	steel stud/concrete	6,700	1.80	3715	1.05	6,361	0.21	0.58	1971
HTA	wood	200	1.80	111	1.76	113	0.18	0.98	1940
HSD	steel	6,800	1.74	3901	0.89	7,611	0.20	0.51	1992
SUB	steel stud/concrete	6,700	1.65	4051	0.98	6,825	0.18	0.59	1962
MCK	steel	6,600	1.63	4042	0.74	8,892	0.11	0.45	1975
MSB	steel	3,700	1.62	2279	0.97	3,817	0.23	0.60	2003
CST	steel	4,800	1.57	3048	0.66	7,274	0.21	0.42	2003
HHB	steel stud/concrete	1,400	1.57	890	1.06	1,321	0.17	0.67	1999
EDC	steel	1,200	1.51	794	0.98	1,219	0.06	0.65	2009
CHA	wood	600	1.50	400	1.37	437	0.27	0.92	1984
HEA	wood	500	1.46	342	0.75	663	0.23	0.52	1969
GSC	wood	700	1.38	508	1.10	634	0.23	0.80	1990
ECS	concrete	8,000	1.32	6052	0.91	8,801	0.20	0.69	2006
UH1	wood	800	1.31	609	0.98	819	0.19	0.74	1969
HTB	wood	400	1.29	311	1.49	269	0.10	1.16	1940
HLP	wood	400	1.28	313	0.96	415	0.16	0.75	2001
VIA	steel stud/concrete	3,400	1.26	2705	0.88	3,856	0.16	0.70	1992
BWC	steel	9,100	1.23	7374	0.71	12,849	0.20	0.57	2009
SEC	wood	500	1.22	411	1.09	459	0.13	0.90	1996
SED	wood	2,800	1.21	2312	1.03	2,725	0.16	0.85	1975
SAU	wood	2,100	1.15	1819	0.91	2,312	0.13	0.79	1965
CARSA	steel	10,600	1.15	9199	0.62	17,043	0.21	0.54	2015
CCC	wood	700	1.14	612	0.77	909	0.19	0.67	1993
UH2	wood	300	1.07	281	0.82	367	0.20	0.77	2014
HTE	wood	700	1.01	693	0.98	716	0.10	0.97	1992
HTQ	wood	400	0.93	431	1.04	383	0.00	1.12	1940
PNX	steel	2,200	0.73	3016	0.40	5,552	0.05	0.54	1981

Chapter 2: Determining overall heat transfer coefficient (U-Value) of wood-framed wall assemblies in Canada using external infrared thermography

The content in this chapter was published in the following publication:

M. Mahmoodzadeh, V. Gretka, K. Hay, C. Steele, P. Mukhopadhyaya, Determining overall heat transfer coefficient (U-Value) of wood-framed wall assemblies in Canada using external infrared thermography, ***Journal of Building and Environment***. 199 (2021): 107897. https://doi.org/10.1016/j.buildenv.2021.107897

2.1 Abstract

Quantitative thermography is considered as a reliable method to measure the thermal transmittance U-values of opaque building envelopes. Previously developed external infrared thermography (IRT) methodologies mainly focused on comparison of measured U-values with nominal U-values of wall assemblies in European construction. This study attempted to develop an external IRT method to determine clear wall U-values, where the impacts of repeating members (studs) were considered. The proposed method was compared with two established practices in Canada, namely the parallel path method and 3D thermal simulations. The IRT measurements were conducted on a conditioned at-scale insulated wood-framed wall structure. Besides the importance of environmental conditions on the thermal images, two thermal imaging artefacts were assessed and discussed in the chapter, including nonlinear characteristics of infrared (IR) camera focal array, a.k.a. non-uniformity corrections (NUC) and vignetting. The results demonstrated that the location of the region of interest (ROI) plays a key role in U-value measurement due to the vignetting effect and colder thermal bridges at corners. It was also found that NUC should be considered during the survey. Furthermore, U-value measurement with IRT in the best-case scenario (depending on the location of ROI) deviated from nominal U-values by 6.25% to 25.00%. The clear wall U-value results with IRT were validated with three-dimensional (3D) finite element analysis software, Siemens NX, which differed by -11.53% to 10.00% (in the best case scenario). Additionally, the clear wall U-values obtained with parallel path method were comparable with simulation values for walls without highly conductive materials such as metal.

Keywords: Wood-framed wall, External infrared thermography (IRT), U-value, Clear wall, Parallel path, Region of interest (ROI), Vignetting

2.2 Introduction

Global energy consumption in the built environment has increased considerably over the last few decades. The factors leading to the increase in energy consumption include population growth, occupants spending more time indoors, increased indoor thermal comfort and air quality expectations, and a changing climate. In Canada, 69% of primary energy in 2016 was allocated to the secondary energy, where residential and commercial buildings accounted for 19% of that fraction. As a result of Canada's relatively cold winters, 80% and 63% of energy usage in residential and commercial buildings were used for space and water heating, respectively [1].

Select Canadian jurisdictions have started to introduce codes and standards to reduce energy consumption and greenhouse gas emissions while increasing resiliency and passive survivability. For example, the Toronto Green Standard, the City of Vancouver Building Bylaw, and the British Columbia Building Code (BCBC) have introduced the Thermal Energy Demand Intensity (TEDI) performance metric in an attempt to optimize building envelope performance and heat recovery on ventilation air in new construction [2].

Recently, there is a growing interest among designers, builders, and governments to encourage the use of wood as a building material. In general, wood is more cost-effective and sustainable than other commonly used materials in building construction such as steel and concrete [3]. Furthermore, wood has a lower thermal conductivity than steel or concrete, which in general results in more energy efficient buildings due to the smaller heat losses [3]. In 2009, the British Columbia Building Code (BCBC) was amended to allow construction of six-story wood-framed residential buildings, previously limited to only four, to achieve the goals of the provincial government's Climate Action Plan [4].

Thermal transmittance of the building envelope is a critical consideration in reducing space heating loads as authorities strive for lower energy consumption in the built environment. Furthermore, thermal properties of building envelope materials have a direct effect on the use of construction materials and indoor air quality. Stone et al. [5] conducted a sensitivity analysis to determine the most influential parameters in energy rating assessments of existing dwellings (i.e. gas central-heated houses) in England, showing that the U-value of the building envelope along with heating system efficiency and building geometry accounted for 75% of the energy rating variance.

Therefore, U-values of building envelopes play a crucial role in overall energy consumption and should be accurately quantified and optimized in energy audits and models.

Early approaches of estimating U-values in building energy simulations were based on nominal values provided by building material databases from standards such (theoretical method) [6]. Nominal U-value is calculated based on reciprocal of the sum of each layer's thermal resistance in the wall assembly; assuming one dimensional heat flow while ignoring lateral heat flux from thermal bridges. This methodology is limited in its application to wall assemblies with framing where thermal insulation is bridged by non-continuous members such as studs. To address this limitation, parallel path calculations are commonly used to calculate U-values of the wall assemblies with repeating non-continuous components such as studs. Typically, this is done by area-weighting the heat flow through the materials, where heat transfer perpendicular to the surfaces of building elements is assumed one-dimensional and parallel. However, this is rarely true, and highly conductive building components such as metals create lateral heat flows to other components in three dimensions that are not accounted for in basic parallel flow assumptions [7].

Modern computer simulation tools have enabled a better estimation of thermal bridging effects, in turn facilitating more accurate effective U-value estimates. For instance, lookup tables provided in ASHRAE 90.1 Appendix A incorporate the effects of studs and top/bottom plates for estimating U-value of wall assemblies [8]. Likewise, in British Columbia, the Building Envelope Thermal Bridging Guide (BETB) is a catalogue of the thermal performance of common envelope assemblies and interface details directly relevant to construction in BC and Canada. It is to be noted that the U-values in BETB Guide, known as "clear wall" U-values, do not consider thermal bridging effects of top and bottom plates, and only consider the repeating members (studs). Examples of components included in clear wall assemblies are brick ties, continuous girts or intermittent cladding attachment systems that support cladding and/or studs [7]. Notably, neither method includes for important linear transitions such as those where the opaque wall assembly intersects with fenestration, slab, or parapet. Hence, by definition, the clear wall U-value does not include transition details, and only considers the studs and attachment components.

Nonetheless, simulation methods are idealized, and do not reflect the actual performance of existing building envelopes due to the variations in quality of construction or temporal degradation of components. [9]. It is worth noting that even in new construction, using tabulated U-values for

whole building energy simulations results in inaccuracies since as-built U-values are often different than theoretical design values, due to impact of environmental conditions such as moisture and error associated with manufacturing and construction. For instance, a study of 77 new buildings in Sweden showed that energy demand was on average 20% higher than the design value [10]. Therefore, in-situ U-value measurement tools such as heat flux meters (HFMs) and infrared thermography (IRT) have drawn more attention as potential candidates for accurate estimation.

In-situ U-values are evaluated by standardized methods described in ISO 9869 [11] and ASTM C1155 [12]. HFMs and thermocouples are used to measure interior and exterior surface temperatures temporally, from which the U-value can be derived through progressive averaging. However, point source HFMs and thermocouples measure local conditions and cannot reasonably show imperfections and non-homogenous areas in the building envelope. Furthermore, HFMs are invasive and the duration of the test is lengthy (72+ hours), which is cumbersome and prohibitive from an industrial perspective [9].

Hoping to create a less invasive and more accurate means of measuring the in-situ U-value of an opaque wall assembly, researchers have developed methodologies which utilize infrared cameras as a means of data collection [9]. Given thermograms are a spatial 2D distribution of temperatures that incorporate effects of thermal bridges, natural convection inside the building, and non-homogeneity in accuracy of pixels in IR camera, the average of surface temperatures within an arbitrary region of interest (ROI) are used to measure overall thermal transmittance of wall assemblies. It is therefore a better representation of actual wall performance compared to the point source HFM measurements.

Since many existing buildings in Canada were built prior to the advent of energy policies, quantifying building envelope thermal performance is an important step in identifying retrofit opportunities in existing building stock. Hence, this study is focused on utilizing external infrared thermography to quantify U-values of wood-frame wall assemblies and compare them with common established practice methods. The overarching goal of this research is to determine the viability of an external thermographic survey technique for use in energy audits.

2.3 Literature review

In recent years, applying advanced and practical methods of in-situ building energy performance evaluation have become increasingly important with the emerging focus on energy efficiency of existing buildings. Heat flux meters (HFMs) and thermocouples are commonly used for on-site measurement of thermal characteristics of building envelope assemblies [9]. However, HFM and thermocouple characteristics can skew results by 6 to 26% [13]. For example, size and location of the heat flux meter plate could be responsible for 30% and 26% of variations in heat flux and overall heat transfer coefficient, respectively [14-15]. Other sources of error include poor contact between plate and the wall (2 to 5%), lateral heat flux (1-5%) [16], cardinal direction of the wall (up to 37.3%) [17], and average or dynamic data processing methods (up to 20%) [18]. Also, some studies demonstrated that the deviations between theoretical and measured U-value with HFM for the wall with air cavities ranged from 30 to 47% [19-22].

In contrast, IRT is a potentially rapid, non-destructive tool regarded as a possible alternative for evaluating the thermal performance of the building envelope. Data can be collected in as little as 30 minutes for homogenous heavy, multi-leaf walls [23]. Importantly, IRT data incorporates the effect of convective and radiative heat transfer, unlike HFM that considers only conduction. Shortcomings of IRT include cost [13, 23-24], requirement for qualified technician for data acquisition and analysis [13, 24], coordination of access to the building for internal IRT [25], high sensitivity to climatic conditions [23], and presence of pollution and smokes with high emissivity influencing the accuracy of results [13, 26]. It is to be noted that low temperature gradients lead to a small heat flux through the building envelope, which may result in misreading of information from thermograms [9].

While IRT has been mainly used as a qualitative investigation tool for building envelope assessment [26-28], a variety of investigations have been recently conducted on the quantification of building envelope heat losses using both internal and external IRT. The first study to quantitatively determine U-value of a building envelope using internal IRT was performed by Madding [29] in 2008, making use of the ratio of the sum of convective and radiative heat transfer and the temperature gradient between inside and outside air. The results showed that higher uncertainties of surface temperature and reflected temperature resulted in higher uncertainties in U-value measurements. It also suggested that surface temperature and reflected temperature should be measured with the same instrument to avoid systematic errors, such as with the IR camera.

Since steady-state conditions are not likely to be achieved during the test, using a high quality IR camera was recommended to avoid compounding sources of error. Depending on the U-value of the envelope, uncertainties in measured U-value were in the range of 5-10% if the proposed procedures were followed.

Fokaides et al. [30] followed the proposed method by Madding and used internal IRT surveys to determine the U-value of a building envelope. In their study, the heat balance on the interior surface of the envelope was considered, including a linearization of Stefan-Boltzmann law in the heat balance equation. The results showed that absolute deviations between notional and measured U-values with IRT were in the range of 10-20%. A sensitivity analysis was conducted to determine which parameters have the most significant impact on the accuracy of measurements and concluded that reflected temperature and emissivity of the wall surface were the most critical parameters. For instance, a deviation of 1ºC in reflected temperature resulted in 10% error of surface temperature measurements, and consequently 100% deviations in U-value. The authors stated that since IRT should ideally be performed at steady state, tests should be scheduled in early mornings or overnight when surfaces are not exposed to solar radiation and when outdoor air temperature variations are minimal.

Tejdor et al. [31] carried out IRT tests from inside a building to determine the U-value of single and multi-leaf walls. Findings indicated that the deviations of U-values with IRT from theoretical values were 1-2% and 3-4% for single-leaf and multi-leaf walls, respectively. Notably, test durations were 2-3 hours, and the interior convection heat transfer coefficient h in the IRT model was calculated using the dimensionless approach instead of using the values reported in ISO 6946:2012 [6]. Another investigation by Tejdor et al. [32] attempted to evaluate the influence operating conditions and thermophysical properties of the envelope on the accuracy of in-situ measurements of U-values using internal quantitative IRT. U-values appeared to be significantly related to the outdoor air temperature when the temperature gradient between indoors and outdoors was less than 16ºC. For temperature gradients between 16-21ºC, U-value was largely affected by wall surface temperature. The study concluded that a temperature gradient of 7-16ºC is the optimum range for U-value measurements, with a gradient of 3-4ºC resulting in overestimation of U-value and a gradient of 16-21ºC resulting in underestimation of U-value. Finally, quantitative IRT was found to be more accurate for multi-leaf walls with high thermal mass exhibiting maximum U-value deviations of only 0.20%.

Collectively, these studies have demonstrated promise in obtaining acceptable *in-situ* U-value measurements with internal IRT. In recent years, external IRT has also been of interest to researchers despite its limitations compared to internal IRT. The primary limitations of external IRT are described in the following sentences. First, the exterior surfaces in external IRT is influenced by climatic conditions considerably more than the internal environment, which is well-controlled [30]. Second, adjacent objects in the environment emit and reflect radiation onto the target which is often beyond control [30]. Finally, the exterior convective heat transfer coefficient h_c is not constant during tests and must be calculated based on instantaneous weather conditions to obtain acceptable results [33].

Previous researchers have established boundary conditions to compensate for the impacts of environmental parameters in external quantitative IRT as follows. The minimum temperature difference between inside and outside should be at least 10ºC to have sufficient thermal heat flux through the envelope [30-31, 34], and at least 15ºC for proper determination of U-value, slightly different than the suggested range of 7-16ºC for internal IRT [34]. Outdoor air temperature variations 12 hours before the test should be less than 6ºC to approximate steady state conditions [34]. Further recommendations include a local wind speed lower than 0.5 m/s near the building surface during the measurement and a free stream wind speed less than 5 m/s for a period of 24 hours before testing [26, 34]. Measurements are best performed during early mornings (at least two-hours before sunrise) or late evenings to avoid influence of solar radiation [34]. It has been suggested to start thermography at least two to three hours after sunset for low thermal mass assemblies such as glass and metal curtain walls, insulated steel stud walls, and stud walls with non-masonry cladding. In contrast, testing high thermal mass assemblies requires on the order of 8 hours after sunset to allow for heat dissipation [35]. In both cases, skies should be overcast for 12 hours prior to the test to mitigate the effects of solar and sky radiation [30,33,34,36,37]. Measurements should not be taken on rainy or snowy days, and surfaces should be dry for 24-48 hours prior to the test since moisture causes evaporative cooling and increased thermal conductivity of materials [31,34]. In general, literature suggests best results are obtained if quasi-steady state conditions are achieved 3-4 hours prior to IRT [30].

Albatici et al. [34] conducted a comprehensive study on the influence of thermal mass and cardinal direction of wall exposure on in-situ U-value measurements using external IRT. The authors used

the truncated Jurge equation in the IRT model to calculate convection heat transfer coefficient *h*. The results showed that standard deviation of U-values for north-facing light walls was substantial (37-50%) compared to heavy walls (10.8-17.8%). For south-facing walls, the standard deviation ranges were greater, with a deviation of 10.8%-58.3% for light walls, and 24.2%-31.4% for heavy walls. The standard deviation of U-values was similar to north-facing walls. The study also compared IRT and HFM results, concluding that deviations can vary significantly due to the influence of cardinal direction of wall exposure (9.0-40%).

Dall'O' et al. [33] conducted several in-situ measurements to determine wall U-values in 14 dwellings of varying constructions using external IRT. To calculate the U-value, a simplified IRT method was used incorporating the Jurge equation that considers the effect of radiation and convection. The U-values were measured and evaluated for two wind speeds of 0 and 1 m/s. The results showed that deviations of IRT with theoretical values ranged from 1.7%-154%, depending on wind speed and building construction. The paper concluded that IRT provided reliable results for high thermal mass assemblies without insulation (1.7% - 60%) but was unreliable for lower thermal mass assemblies that were exterior-insulated (more than 50%). Similar to previous studies, it suggested to avoid IRT on rainy and sunny days, to consider the average wind speed during the survey for convective heat transfer coefficient calculations, and to use the IR camera to measure both surface and outdoor temperature.

Nardi et al. [37] used four different IRT methods and a guarded hot box to compare the U-value of typical Italian building walls from the 1970s. The U-values were analyzed against different indoor-outdoor temperature gradients, reflected temperatures, and outdoor-reflected temperature differences. Results were consistent with findings from Madding [29] and Fokaides et al. [30] due to the similarity of their governing equations. The stability of the results based on these methods were tested by changing the indoor-outdoor temperature gradients, reflected temperature, and reflected-outdoor temperature differences. Similar to findings by Albatici et al. [34] and Dall'O' et al. [33], the study concluded that testing during overcast skies and larger indoor-outdoor temperature gradients is optimal.

Lu and Memari [38] developed an innovative approach that considered thermal radiation exchange from the wall with the sky, ground, and air. Various clear sky temperature models were compared to find the most acceptable model for sky temperature estimations. Ground temperature was

measured on-site, and indoor and outdoor temperatures were obtained using IRT. The results demonstrated that U-value measurement with IRT was in good agreement (±26%) with the results obtained with a HFM.

Although most studies have focused on applying quantitative thermography to determine nominal U-values, only a few have attempted to quantify the contribution of thermal bridges on U-value measurements. In these studies, the main parameters for quantifying the effect of thermal bridges were heat flux (Q), linear transmittance value (Ψ), and incident factor of the thermal bridge [39-42]. For instance, Asdrubali et al. [39] conducted indoor IRT in a laboratory-based study to quantify the increased thermal transmittance due to thermal bridges. For this purpose, an incident factor was defined, which was multiplied by the nominal U-value obtained with the HFM. Bianchi et al. [42] applied the Asdrubali approach to a full-scale building and determined the increase in building envelope heat loss due to thermal bridges was about 9%. Furthermore, the results were validated by measuring the building's energy consumption, where the difference with the proposed approach was less than 1%. O'Grady et al. [40] developed a methodology to quantify the Ψ-value and heat flow through thermal bridges, using indoor IRT in a hot box device. The results showed that IRT was in good agreement with the hot box, showing maximum deviations of only 12%. Another study by O'Grady et al. [41] used outdoor IRT in a controlled hot box environment to determine the effect of wind velocity on the Ψ-value, demonstrating that it increased by 32% with increased wind velocity. It also found that IRT is a reliable tool for determination of Ψ-value where in the case of wind speeds between 0.5-4 m/s, deviations from hot box measurements ranged from +5% to -9%. The IRT methodology in these studies was based on an analysis of a line of pixels with and without a known thermal bridge [31-34]. It is to be noted that in these studies, the one-dimensional effect of thermal bridges (line of interest) was quantified, while the 2D effect of thermal bridges was neglected.

A recent study by Tejedor et al. [9] used thermography to produce 2D U-value maps of opaque facades that included thermal bridges in a climate chamber. Three heavy walls were tested where the combined effect of all building elements was evaluated by internal IRT. The 2D U-value map was found to be useful in identifying the most significant thermal bridges and measuring U-value at any point in the wall surface; deviations in U-value measurements ranged from only 0.08-8.55% between IRT and HFM in non-homogeneous wall areas.

Validation of IRT measurements have included simulation methods such as computational fluid dynamics (CFD) [39-41], finite element analysis (FEA) [43, 44] and continuous time stochastic modelling [44]. These methodologies require stratigraphy, thickness, order of each layer in the assembly, and thermal properties of each layer, including, but not limited to material conductivity, density, thermal mass, vapour pressure resistance and emissivity as input data. A key limitation of these computer methods is the accuracy of input data, where it has been suggested that inaccurate estimation of thermal properties of heavyweight construction could result in up to 77% error [45]. Additionally, simulations often overlook the impact of meteorological conditions and condensation risk [46-49].

The body of academic literature is showing some promise in using IRT as a quantitative tool for evaluating building envelope thermal performance. However, research to date is preliminary and many other conditions need to be tested. The majority of the studies were performed in European climates and wall assemblies were consistent with construction practices of the region [30-37]. Hence, part of the motivation for this experimental study is due to an absence of studies in a Canadian setting with low thermal mass assemblies. Furthermore, external IRT previously focused on determining U-value of wall assemblies and comparing them with nominal values [30-34,36-38] while only a few recent studies have attempted to incorporate the effect of thermal bridges using a hot box device [23, 39-42]. However, in-situ U-value measurements of a wall assembly with external IRT that take into consideration the effects of repeating thermal bridges (studs) were not investigated in literature. Furthermore, previous studies have not evaluated the effects of location and size of region of interests (ROIs) on U-value measurements, by considering thermal imaging artefacts such as nonlinear characteristics of an infrared (IR) camera focal array or vignetting.

Consequently, this chapter attempts to analyze thermal performance of typical Canadian insulated wood-framed assemblies with external IRT while providing some insights into its techniques. Two areas were considered for U-value measurements, as shown in Figure 2.1: (1) the clear wall U-value (including studs and attachment components), and (2) the nominal U-value (excluding studs and attachment components). Measured clear wall U-values obtained with IRT were validated using the three-dimensional (3D) finite element analysis software, Siemens NX [50], and compared with the parallel path method. Furthermore, sources of error in obtaining U-values with

external IRT were also identified and analyzed. The findings complement existing literature leading to a more comprehensive understanding of IRT for building science.

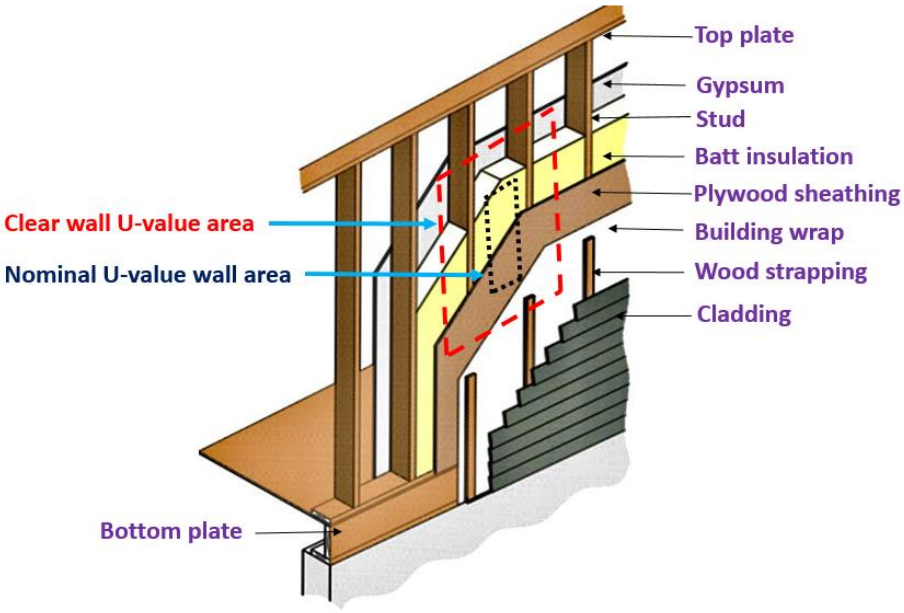

Figure 2.1 schematic of nominal and clear wall areas

2.4 Methodology

2.4.1 Test object

The experiment was carried out on a wood-framed test structure adjacent to an existing conditioned campus building at the University of Victoria, Victoria, BC, Canada. The structure has a square floor plate (9.30 m^2 floor area) and a ceiling height of approximately 3.05 m, built with four different wall assemblies per Figure 2.2. The plan view and cross section of the structure are shown in Figure 2.3 and Figure 2.4, respectively. The structure was constructed on pier blocks instead of a typical foundation slab, and the floor and roof assemblies were highly insulated (RSI-8.8) to minimize heat losses through these elements, facilitating better thermal performance comparisons between wall assemblies (details shown in Figure 2.4). Indoor temperature was controlled via a portable oil-filled electric radiant heater connected to a thermostat set to 20°C.

The three wall assemblies (W1, W2 and W3) studied are used in typical low-rise Canadian construction. The wall assemblies incorporate an air gap (19 mm) between the exterior sheathing and cladding, commonly referred to as “rainscreen cavity”. The components and material properties of the wall assemblies are described below and shown in Figure 2.5 and Table 2.1.

(1) **W1**: Interior insulated wood framed assembly, composed of 38 $mm \times 140\ mm$ wood framing, 406 mm on center, insulated with RSI-3.87 fiberglass batt in the stud cavity, with wood strapping supporting vinyl cladding (Figure 2.5a)

(2) **W2**: Split insulated wood framed assembly, composed of 38 $mm \times 140\ mm$ wood framing, 406 mm on center, insulated with RSI-3.87 fiberglass batt in the stud cavity, RSI-1.76 exterior rigid insulation, and wood strapping supporting vinyl cladding (Figure 2.5b)

(3) **W3**: Split insulated wood framed assembly, composed of 38 $mm \times 140\ mm$ wood framing, 406 mm on center, insulated with RSI-3.87 fiberglass batt in the stud cavity, RSI-1.76 exterior rigid insulation, and continuous horizontal metal z-girts supporting vinyl cladding on vertical metal furring (Figure 2.5c).

W1, W2 and W3 are facing North, West and South, respectively, and each incorporate a double-glazed window ((0.4 m × 0.4 m) & U=1.59 W/m^2 K). It should be noted that W3 is facing the adjacent lab building while W1 and W2 are facing outdoor parking areas. W4, included an entrance door (2 m × 1 m), was not the focus of the investigation. To assess the effect of the rainscreen cavity on surface temperature, and consequently U-value, only the bottom portion of the walls were clad in W1 and W2 (per Figure 2.5(a-b)). However, due to the high reflectivity of the steel furring, it was decided to fully clad W3.

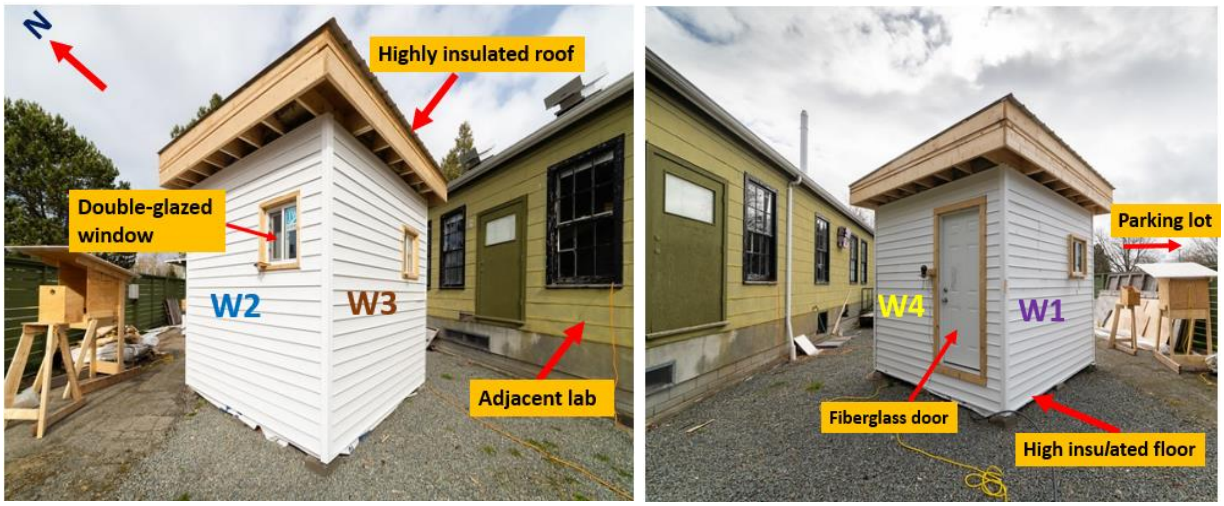

Figure 2.2 The experimental structure (fully clad)

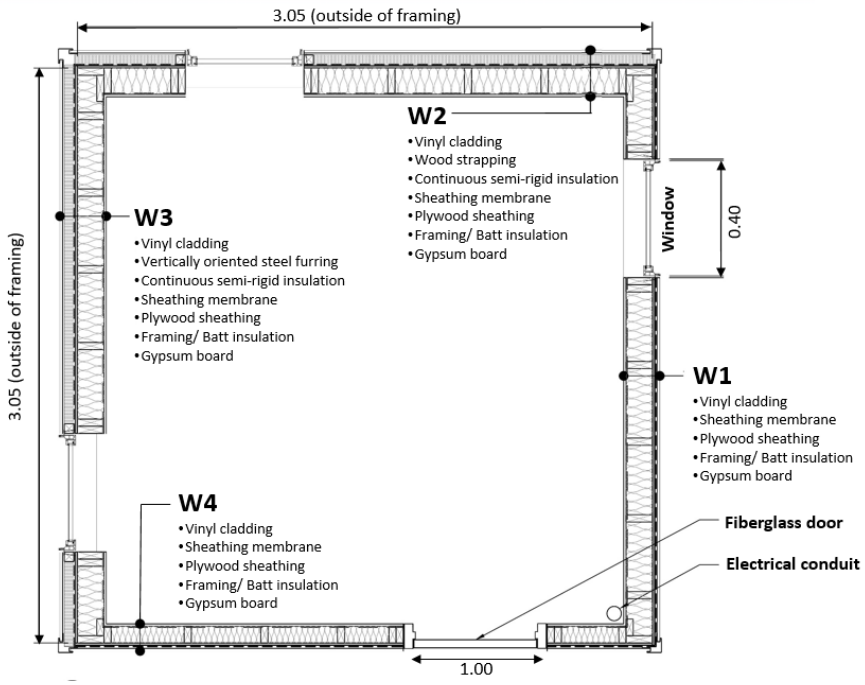

Figure 2.3 Plan of the experimental structure (dimensions in metres)

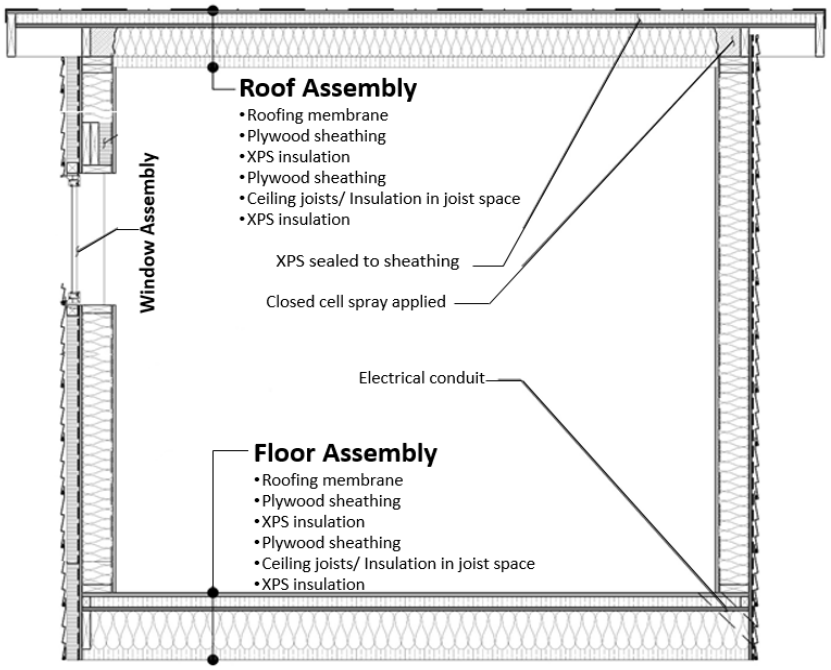

Figure 2.4 Cross-section of the experimental structure

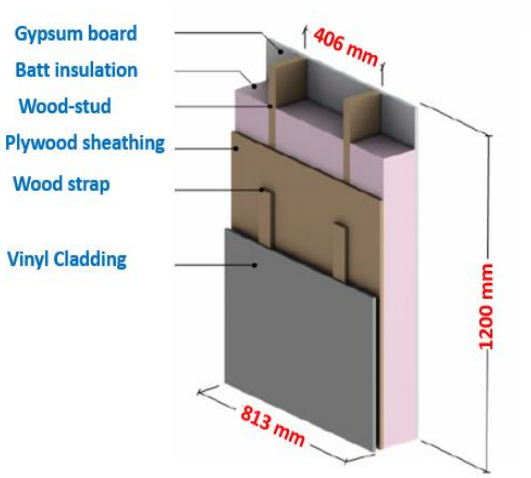
Gypsum board
Batt insulation
Wood-stud
Plywood sheathing
Wood strap
Vinyl Cladding
406 mm
1200 mm
813 mm

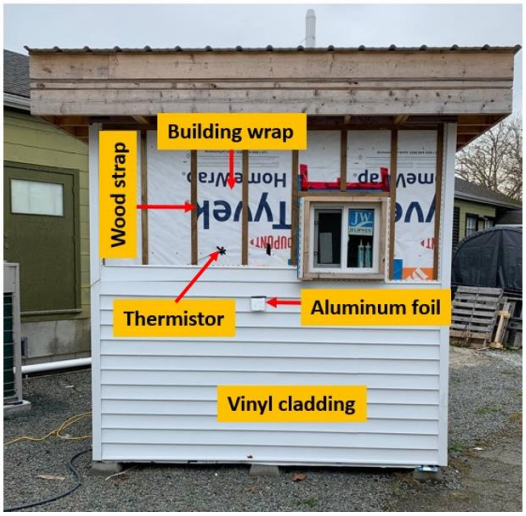
Building wrap
Wood strap
Thermistor
Aluminum foil
Vinyl cladding

(a)

(a)

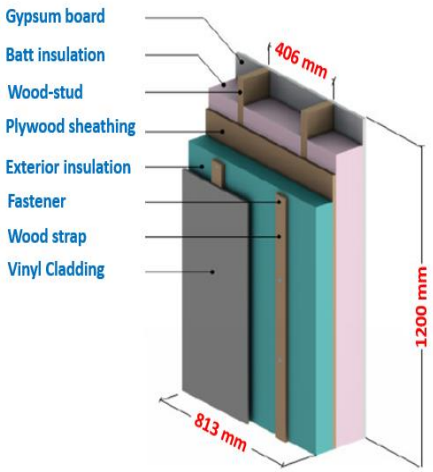
Gypsum board
Batt insulation
Wood-stud
Plywood sheathing
Exterior insulation
Fastener
Wood strap
Vinyl Cladding
406 mm
1200 mm
813 mm

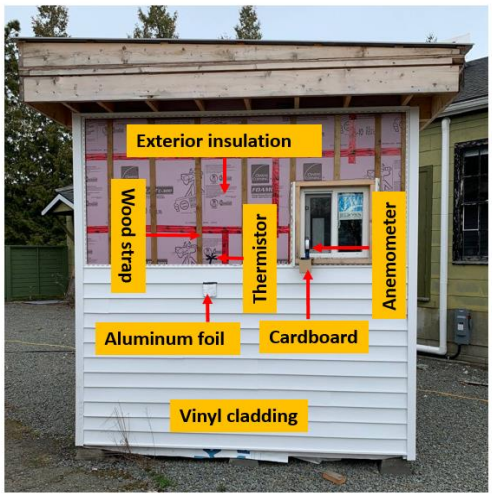
Exterior insulation
Wood strap
Thermistor
Anemometer
Aluminum foil
Cardboard
Vinyl cladding

(b)

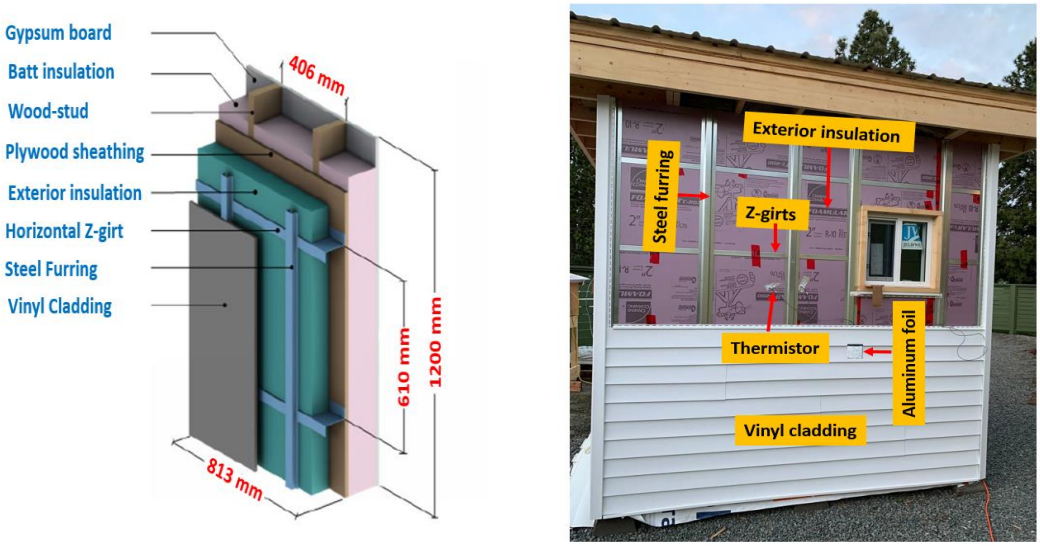

(c)

Figure 2.5 Schematic and front view of studied walls (a) W1; (b) W2, and; (c) W3

Table 2.1 Thermophysical properties of investigated walls

Wall type	Component	Thickness (mm)	Conductivity (W/m K)	Nominal Resistance (m^2 K/W)	Density (kg/m^3)	Specific Heat (J/kg K)
W1	Interior film	-	-	0.12	-	-
	Gypsum Board	13	0.16	0.08	800	1090
	Fiberglass Batt Insulation	140	0.036	3.89	14	710
	2 × 6 wood stud	140	0.10	-	500	1880
	Exterior plywood sheathing	13	0.10	0.13	500	1880
	1 × 3 wood strapping	19	0.10	-	500	1880
	Vinyl Cladding with 19mm vented airspace incorporated into exterior heat transfer coefficient					
	Exterior film	-	-	0.12	-	-
	Nominal RSI-value (m^2 K/W)	**4.34**				
W2	Interior film	-	-	0.12	-	-
	Gypsum Board	13	0.16	0.08	800	1090
	Fiberglass Batt Insulation	140	0.036	3.89	14	710
	2 × 6 wood stud	140	0.10	-	500	1880
	Exterior plywood sheathing	13	0.10	0.13	500	1880
	Exterior insulation	50	0.028	1.79	28	1220
	Wood strapping	38	0.10	-	500	1880
	#14 steel fastener	11	50	-	7830	500
	Vinyl Cladding with 19mm vented airspace incorporated into exterior heat transfer coefficient					
	Exterior film	-	-	0.12	-	-
	Nominal RSI-value (m^2 K/W)	**6.13**				
W3	Interior film	-	-	0.12	-	-
	Gypsum Board	13	0.16	0.08	800	1090
	Fiberglass Batt Insulation	140	0.036	3.89	14	710
	2 × 6 wood stud	140	0.10	-	500	1880
	Exterior plywood sheathing	13	0.10	0.13	500	1880
	Exterior insulation	50	0.028	1.79	28	1220
	Horizontal Z-Girt with 1 1/2” Flange	18 Gauge	62	-	7830	500
	Steel Furring Hat Track	18 Gauge	62	-	7830	500
	Vinyl Cladding with 19mm vented airspace incorporated into exterior heat transfer coefficient					
	Exterior film	-	-	0.12	-	-
	Nominal RSI-value (m^2 K/W)	**6.13**				

2.4.2 Equipment

Measurement equipment included a FLIR A65 IR camera, temperature sensors with a data logger, and an anemometer to measure wind speed. Indoor and outdoor air temperatures were measured by thermistors with an accuracy of ±0.01 ºC. To confirm indoor air temperature uniformity on each wall, thermistors were located at three heights (0.5, 1.5, and 2.5 m) in three columns forming a grid of 9 measurement locations (Figure 2.6). The anemometer was placed 1.5 m above grade and 0.1 m away from the wall's exterior surface, to measure the local wind speed in the vicinity of surface, and was accurate to ±0.1 m/s. Tables 2.2 and 2.3 outline technical specifications of the IR camera and equipment that was used to perform IRT. All equipment was calibrated according to manufacturers' specifications before testing.

Figure 2.6 Location of thermocouples and heater

Table 2.2 Technical specifications of equipment

Equipment	Measurement range	Resolution	Accuracy
Thermistor	-55 ºC to 125 ºC	0.001 ºC	±0.01 ºC
Anemometer	0.3- 40 m/s	0.01 m/s	±0.1 m/s

Table 2.3 Specification of IR camera (FLIR A65)

Measuring range	−25 ºC to 135 ºC
Accuracy	±5 ºC (±9°F) or 5% of reading
Thermal sensitivity	0.05 ºC at 30 ºC
Wavelength range	7.5–13µm
IR resolution	640 × 512 pixels
Field of view	45°× 37°
Instantaneous field of view (IFOV)	1.31 mrad
Detector	Uncooled VOx microblometer

2.4.3 Test Procedure and data acquisition

The IR camera was situated on a tripod 1.5 m above grade and positioned 5 m from each wall, such that the whole wall was in the field of view of the camera (Figure 2.7). As recommended by Colantonio et. al [35], a minimum spot size spatial resolution of 18 mm is required for exterior inspection of low-rise residential buildings to adequately detect gross thermal patterns such as missing insulation, thermal bridges, and significant air leakage. In this study, a spot size spatial resolution of 6.5 mm was obtained based on the instantaneous field of view of the IR camera at 5 m. Since stability of weather conditions was necessary to approximate steady state, this experiment focused on instantaneous IRT. Therefore, the similarity in the boundary conditions of each of the walls facilitates the comparison of their U-value measurements.

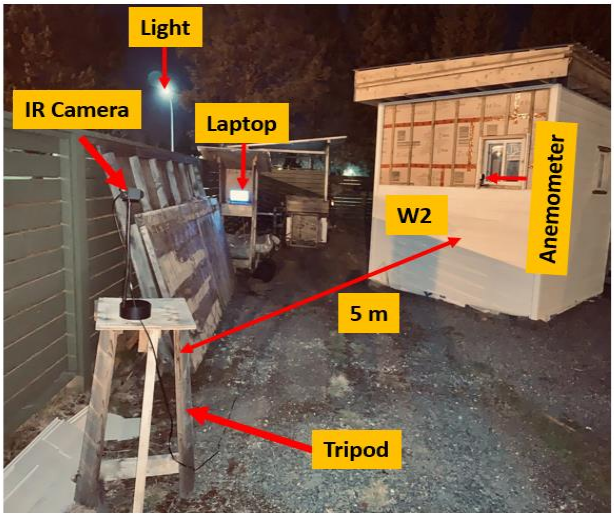

Figure 2.7 Experimental set-up

Environmental factors such as solar radiation, wind speed, rain, sky conditions, and temperature gradient were accounted for in the IRT survey procedures. The structure was not exposed to rain or snow 48 hours prior to the test and the sky was cloudy 12 hours prior to the test. Indoor and outdoor air temperatures were 20.13 ºC and 5.02 ºC (measured with thermistor) during the test, respectively. Indoor air temperature was approximately constant 24 hours before the test (2 ºC deadband), while outdoor temperature variations held constant during the test and were less than 0.5 ºC for a period of 3 hours leading up to the test. The average free stream wind speed during the day of test was less than 4 m/s and the average during the test was 0.41 m/s. The test was performed in the late evening on an overcast night (almost 6 hours after sunset) to minimize the effect of solar and night-sky radiation. IR thermograms were recorded at 1s intervals.

To calibrate IR results, reflected ambient temperature and emissivity of wall exterior surfaces was determined. Reflected ambient temperature was determined based on the method suggested by ASTM E1862 [51]. A crumpled and stretched aluminum foil was used as the reflector. The foil was attached to a piece of cardboard and placed in front of the wall. The reflected temperature is equal to the average temperature of foil by setting the emissivity (ε) to 1.0. Since the orientations of walls and their surrounding environment were different, reflected temperature was measured for each wall separately. To estimate emissivity, black electrical tape with a known emissivity ($\varepsilon = 0.95$) was attached to the object surface at least two hours before measurements to reach thermal equilibrium with the object. The emissivity of target was then determined by adjusting the emissivity of images until the target temperature was equivalent to the temperature of the tape [52]. Using this methodology, the emissivity of the cladding, XPS insulation, and building wrap were found to be 0.95, 0.92 and 0.90, respectively. Finally, surface temperatures of targets were calculated by correcting for reflected temperature and surface emissivity values.

Due to the high uncertainty of the IR camera, the researchers decided to examine the calibration of the IR camera by measuring the temperature of objects with known temperatures in the lab and outdoor environment to complement the manufacturer's calibration. To this end, the temperatures of boiling water (100 ºC) and a bucket of melted ice (0 ºC) were measured with the IR camera in the lab. The temperatures measured with the IR camera were 102 ºC for boiling water and -1 ºC for melted ice, and were therefore within the range of camera accuracy (± 5 ºC). However, since the accuracy of the IR camera reported by the manufacturer is based on lab conditions, it should also be evaluated in outdoor

environmental conditions to ensure its accuracy. Therefore, since the IR camera had considerably larger uncertainties (±5 ºC) than the thermistors (±0.01 ºC), outdoor air and surface temperature of walls were measured by thermistors and considered as reference values to ensure the camera calibration. It was found that the measurements with the IR camera were on average 1.63 ºC higher than the thermistor in the same location, again confirming it was within the range of camera accuracy (±5 ºC) and confirming acceptability for in-situ measurements. It is to be noted that this deviation was expected due to differences in accuracy between the IR camera and the thermistors, considering differences in their methods of measurement (non-contact & 2D temperature measurement vs. contact & point measurement), and influences of environmental conditions.

Therefore, to minimize systematic measurement errors, it was decided to acquire as many temperature data as possible with the same instrument [34]. For instance, the outdoor air temperature was measured with the IR camera instead of thermistors to eliminate possible equipment measurement error. A piece of cardboard (ε=0.95) was placed outside the building 1-2 hours before the test to ensure it reached thermal equilibrium with the surrounding environment. The average cardboard surface temperature in the IR image was then considered as the outdoor air temperature (6.50 ºC), compared to that of the thermistor (5.02 ºC). It is worth noting that variations in outdoor air temperature and humidity before the test, influence the ability of the cardboard to achieve equilibrium with the environment. In this study, steady state was approximated since the variation of outdoor air temperature was less than 0.5 ºC for a period of three hours before the test, and held constant during the test similar to the humidity. Therefore, it was reasonable to use instantaneous IRT to measure the temperature of the cardboard as an approximation of outdoor air temperature. It should be noted that humidity was measured hourly at the local weather station (University of Victoria), and is made publicly available by the Government of Canada [53]

2.4.4 Thermal radiation and convection heat exchange with surface

Heat transfer at the exterior surfaces of the building envelope is largely from radiation and convection. Radiation is energy that the exterior surface of building envelope emits to or absorbs from its surroundings. Convection is the exchange of heat between the envelope surface and adjacent air and depends on a number of factors such as surface and air temperature, wind velocity and direction, and surface geometry and coarseness. Convection occurs by two different phenomena: free convection and forced convection. The equation of convection heat transfer can be expressed as:

$$q_{conv} = h_c(T_s - T_{out}) \tag{2.1}$$

where q_{conv} is specific heat flux by convection (W/m^2), h_c is the convective heat transfer coefficient (W/m^2 K), T_s represents the exterior surface temperature of wall (K), and T_{out} denotes the exterior air temperature near the target (K).

There are a variety of methods to calculate the convective heat transfer coefficient h_c. According to Dall'O' the tabulated value for external convective heat transfer coefficient in ISO 6946 [6] is overestimated and not representative of real conditions. Jurges' equation has also been used to calculate the h in some investigations; however, it incorporates radiative effects which limits its accuracy [33,34,43]. Several studies have instead used the simplified Jurges' equation without a valid experimental or theoritical basis [34,54,55]. This simplification also results in inaccurate h_c at high wind speeds. For these reasons, this study calculated h_c for both internal and external surfaces based on the dimensionless method, which is a function of flow regimes, target geometry characteristics, and air properties, calculated as shown in Equation 2.2.

$$h_c = \frac{Nu\ k}{L} \tag{2.2}$$

where h_c is the convective heat transfer coefficient (W/m^2 K), Nu is the Nusselt number [dimensionless], L is the height of the wall (m) measured from the exterior, and k is the thermal conductivity of the fluid. For air at 5-10 ºC, k is 0.024 W/m K.

Nu depends on dimensionless Reynolds (Re) and Prandtl (Pr) numbers in forced convection. To determine flow regime, the ratio of inertial to viscous forces is defined by Re:

$$Re = \frac{vL}{\vartheta} \tag{2.3}$$

where v is the wind speed (m/s), L is the height of wall (m) and ϑ is air viscosity.

The relationship between Nu, Re, and Pr numbers depend on the flow regime. For laminar flow over a wall surface, Nu is determined by using the following equation:

$$Nu = 0.664\ Re^{1/2} Pr^{1/3} \qquad Pr > 0.6 \tag{2.4}$$

For air at 5-10 ºC, Pr=0.71 was used.

Likewise, Nu for natural convection on the interior surface was calculated as follows:

$$Nu = \left\{ 0.825 + \frac{0.387.\ Ra^{1/6}}{\left[1+\left(\frac{0.492}{Pr}\right)^{9/16}\right]^{8/27}} \right\}^2 \quad (2.5)$$

where *Ra* is the dimensionless Rayleigh number. For air at 20-25 ºC, *Pr*=0.73 was used. *Ra* is obtained by product of dimensionless Grashof (*Gr*) and *Pr* numbers.

$$Gr = \frac{g.\beta.(T_{in}-T_{si}).L^3}{\vartheta^2} \quad (2.6)$$

$$Ra = Gr.Pr = \frac{g.\beta.(T_{in}-T_{si}).L^3}{\vartheta^2}.Pr \quad (2.7)$$

where g refers to gravity (9.8 m/s^2), T_{si} is the interior surface temperature (K), and T_{in} is indoor air temperature (K). The volumetric temperature expansion coefficient β (1/K) is found by evaluating all fluids at their film temperatures T_m; therefore β = 1/T$_m$, where T_m= (T_{in}+ T_{si})/2. Air viscosity ϑ is 1.5 × 10^{-5} m^2/s for air at 20-25 ºC.

The interaction between the indoor and outdoor environments and a surface was defined by the equivalent surface resistance coefficient R_s that includes radiative and convective components. Evaluation of these coefficients is necessary to define internal and external boundary conditions. These boundary conditions were also implemented in simulations outlined in section 3.8 and used for theoretical calculations of U-value, rather than reference values in ISO 6946 [6] or ASHRAE 90.1 [7] which are not based on real conditions.

The radiative coefficient h_r can be found from Equation 2.8:

$$h_r = \varepsilon\sigma(T_s + T_e)(T_s^2 + T_e^2) \quad (2.8)$$

where ε is surface emissivity, σ is the Stefan-Boltzmann constant and T_s and T_e are the surface and air temperatures, respectively. Hence, the total surface resistance coefficient in this study were calculated using following equations:

$$R_{si} = \frac{1}{h_{ci}+h_{ri}}; \qquad h_{ri} = \varepsilon\sigma(T_{si} + T_{in})(T_{si}^2 + T_{in}^2) \qquad h_{ci} = \frac{Nu_i K}{L} \quad (2.9)$$

$$R_{so} = \frac{1}{h_{co}+h_{ro}}; \qquad h_{ro} = \varepsilon\sigma(T_{so} + T_{out})(T_{so}^2 + T_{out}^2) \qquad h_{co} = \frac{Nu_e K}{L} \quad (2.10)$$

2.4.5 Determination of instantaneous measured U-value with external IRT

Besides the transient effects of environmental conditions, surrounding buildings and objects in the field of view of the target also have a strong impact on building surface temperatures. Usually, any object (e.g., a building) is surrounded by others of varying temperatures (buildings, air, ground, sky, etc.; see Figure 2.8). In this case, the radiation heat exchange between them should be considered during thermography by determining the view factor between them. View factor is a geometrical parameter and depends on the orientation of surfaces. According to energy conservation, the summation of radiation leaving a surface and incident on other surfaces is equal to 1, shown in Equation 2.11.

$$\sum F_{sky} + F_{ground} + F_{air} + F_{objects} = 1 \tag{2.11}$$

where F_{sky} is the view factor of sky, F_{ground} is the view factor of ground, F_{air} is the view factor of ambient air and F_{object} is the view factor of surrounding objects.

Determination of the target's view factor with all surrounding objects is difficult in real conditions, often requiring simulations to maximize accuracy. In this study, it was assumed that sky (cloudy) temperatures, ground surface temperatures [34, 56], and all surrounding objects (trees, buildings, etc.) are in thermal equilibrium with ambient air. Therefore, radiation heat exchange of surfaces was assumed to be only with ambient air (view factor of 1). Instantaneous measured U-value [W/(m^2 K)] was then calculated using Equation 2.12:

$$U_{overall} = \frac{q}{T_{in} - T_{out}} = \frac{q_r + q_c}{T_{in} - T_{out}} \tag{2.12}$$

where q (W/m^2) is the heat flux passing through the element, dissipated from exterior surface, and subsequently transferred to the IR camera sensors through radiation q_r (W/m^2) and convection q_c (W/m^2); T_{in} is the indoor air temperature (ºC) and T_{out} is the outdoor air temperature in the vicinity of the target (ºC). Hence, overall U-value was defined as follows:

$$U_{overall} = \frac{\varepsilon\sigma\left(T_s{}^4 - T_{out}{}^4\right) + h_c(T_s - T_{out})}{T_{in} - T_{out}} \tag{2.13}$$

where ε is emissivity of wall, σ Stefan-Boltzmann constant (5.67×10^{-8}), h_c is convective heat transfer coefficient (W/m^2 K), T_{in} and T_{out} are indoor and outdoor air temperature (ºC).

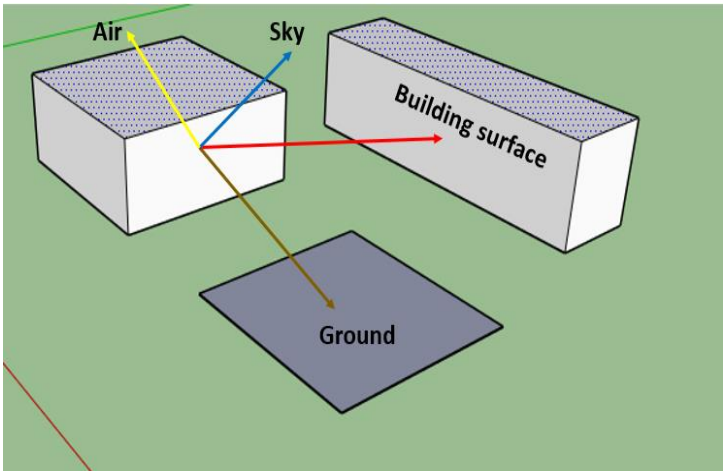

Figure 2.8 Schematic representaiton of radiation heat transfer on an exterior surface

2.4.6 Selection of region of interest (ROI)

IR cameras typically use microbolometer focal plane arrays (FPAS) as a detector, whose temperature changes by absorbing incident radiation from the object and its surroundings. However, each sensor in the FPA has a slightly different offset and gain inherent to the manufacturing process. This causes non-homogenous pixel intensity, resulting in inaccurate temperature measurements and consequently low-quality data. The influence of thermal image non-uniformities can be evaluated and quantified based on temperature values in a selected region of interest (ROI). In thermographic surveys, selection of an appropriate ROI in terms of size, shape, and location is a critical consideration. Size, shape and location of ROIs largely influence how measurements are interpreted due to severity of thermal bridges (cold/hot spots) and non-uniformity of pixel intensity. This study evaluates the impacts of size and location on U-value measurements by considering two thermal image artefacts, which are explained below.

There are two important parameters should be considered in selection of ROIs: (1) Non-uniformity (NU) noise and (2) the vignetting effect. NU of pixels is due to instability of camera temperature and ambient conditions during the thermographic survey. Since variations in camera temperature are inherent to its normal operation, manufacturers and users need to compensate for the read-out data prior to obtaining a measurement [57]. To address this issue in an IR camera and producing a higher quality and more accurate thermal image, Non-Uniformity Correction (NUC) is required to adjust gain and offset of each pixel. For instance, the temperature of Box 1 in Figure 2.9a and 2.9b before and after NUC were 9.13 ºC and 7.24 ºC, respectively, consequently resulting in substantially different U-values. NUC functionality in IR cameras should therefore be applied

before acquiring an IR image; in this study, all thermal images were taken after manually applying NUC for each wall. Most IR cameras automatically perform NUC when deemed necessary, and more often when the camera is first powered up and approaching temperature stability. Therefore, it is recommended to avoid thermography for ~30 minutes to allow the camera to warm up.

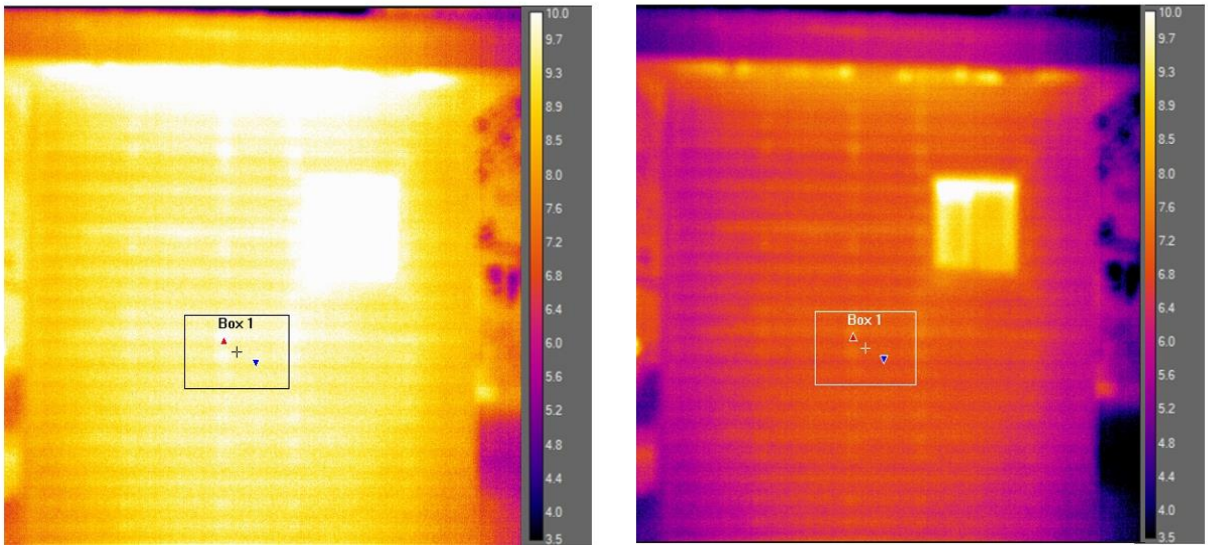

(a) (b)

Figure 2.9 Effect of Non-Uniformity (NU) on surface temperature; (a) before NUC; (b) after NUC

The vignetting effect is a non-linearity artefact in images, presenting as a central image region with higher signal intensity in contrast to edge/corners regions of lower signal intensity known as the *halo effect*, as shown in Figure 2.10a [58]. This geometric phenomenon is due to radiation illumination reaching detector's surface gradually decreasing as off-axis distance increases. Consequently, the imaging system receives unequal effective energy of incident light-rays from different angles, significantly degrading quality at the corners of an image. For example, Figure 2.10a shows the temperature in regions 1, 2 and 3 are 5.81 ºC, 7.23 ºC and 5.72 ºC, respectively, which would result in substantially different U-value measurements. Thermographers should also be aware that detecting vignetting is subject to the temperature span of the thermogram. For instance, the effect of vignetting cannot be detected in Figure 2.10b due to the wide temperature span. Therefore, in this study, special care was taken in selecting a temperature span to identify possible regions of vignetting artefact and its influence on the results(Figure 2.10a).

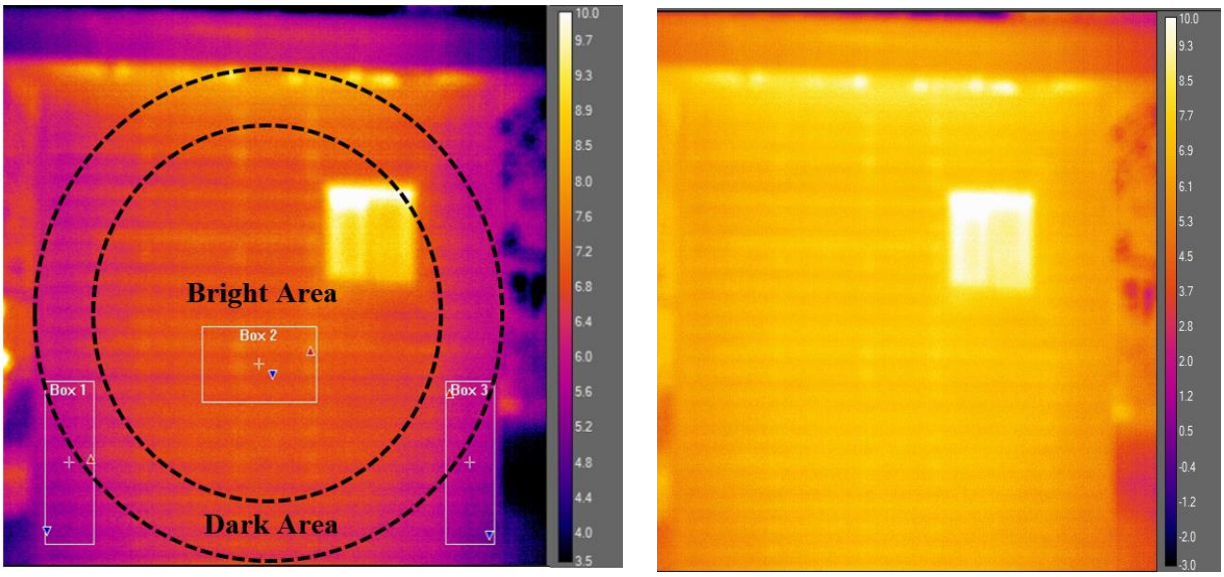

(a) (b)

Figure 2.10 Effect of vignetting effect on surface temperature distribution of wall; (a) Narrow span; (b) Wide span

2.4.7 Clear wall U-value calculation based on parallel path method

Heat flow through the envelope is analogous to current flow in an electrical circuit, where each layer of the assembly provides thermal resistance in series. When there is an element bridging the insulation, heat flows preferentially through that element since it provides less resistance. It has been established as common practice in the building industry to calculate the overall thermal transmittance for wood framed assemblies by using the parallel path method when lateral heat transfer is minimal. Two main parallel paths are considered in wood framed walls: (1) high heat flux path through higher conductivity materials such as the wood framing elements, and (2) lower heat flux path through lower thermal conductivity materials such as cavity insulation, as shown in Figure 2.11. There are two parallel path methods, including weighted area and isothermal plane methods [59]. In the weighted area method used in this study, the total thermal resistance is obtained using Equation 2.14:

$$\frac{1}{R_{tot}} = \frac{f_A}{R_{tot,A}} + \frac{f_B}{R_{tot,B}} \tag{2.14}$$

where f_A and f_B are the fractional areas of sections A and B, respectively, and $R_{tot,A}$ and $R_{tot,B}$ are the total thermal resistances of each section or path (m^2 K / W) as illustrated in Figure 2.11. The total thermal resistance is obtained by summation of the thermal resistances in each path [59].

This approach does not apply to W3 due to the effect of metal Z-girts and steel furring which result in multi-dimensional heat flux.

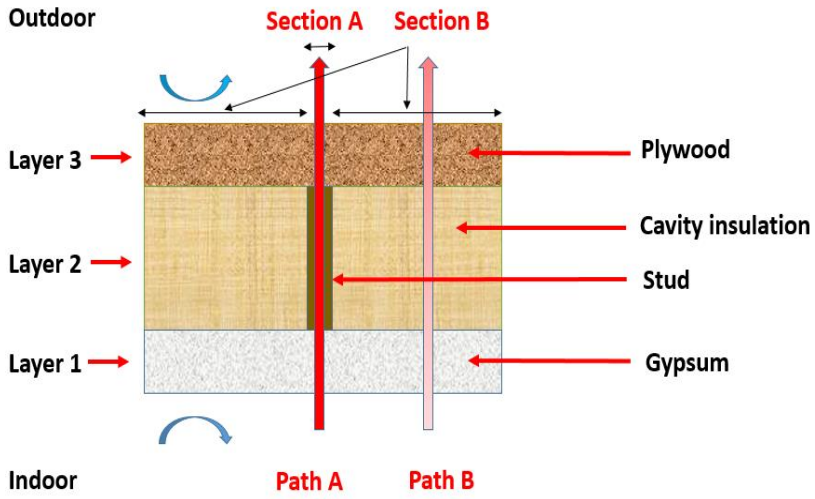

Figure 2.11 Parallel path method schematic illustration for calculating clear wall U-value

2.4.8 Simulation model for determining clear wall U-value

The results of experimental analysis were validated using a 3D thermal modeling using the Nx software package from Siemens, which is a general purpose computer aided design (CAD) and finite element analysis (FEA) package. The thermal solver and modelling procedures utilized for this study were extensively calibrated and validated to within +/- 5% of hotbox testing for ASHRAE Research Project Report RP-1365 [60] and for the BETB Guide [7]. The thermal analysis was based on steady-state conditions where thermal properties of materials, contact resistances between materials and air film coefficients are considered constant. Interior and exterior air films were calculated based on equations 9 and 10 and taken from Table 10, p. 26.21 of 2017 ASHRAE Handbook of Fundamentals depending on surface orientation. The exterior air films were based on an exterior wind speed of 6.71 m/s on the cladding surface (the rainscreen cavity is not directly exposed to wind). It is worth noting that in ASHRAE 1365-RP, for rainscreen cavity systems, most lightweight claddings have an insignificant impact on the thermal performance other than shielding the insulation from direct wind exposure. The cladding and secondary structure outboard of the cladding attachment system were not explicitly modelled but were incorporated into the exterior film coefficient. Hence, the total exterior air film coefficient consists of three terms: (1) film resistances of the rainscreen cavity between wall surface and

cladding, (2) thermal resistance of cladding, and (3) film resistance on the cladding. From the calibration in 1365-RP, contact resistances between materials were modelled and varied between 0.002 m^2 K/W and 0.004 m^2 K/W depending on the materials and interfaces. Insulation and other components were considered tight to adjacent interfaces. Finally, the clear field transmittances included in this analysis include uniform thermal bridges such as studs and girts. The main outcomes of the simulations are temperature profiles and total rate of heat transfer from indoors to outdoors. The overall U-value is then calculated by dividing total heat flux by the area of the component.

2.5 Results and Discussion

2.5.1 Infrared thermography measurements results

Table 2.4 compares nominal U-values (obtained without considering thermal bridging effects of studs and attachment components) with clear wall U-values calculated using the parallel path method (including the thermal bridging effect of studs) for W1 and W2. The calculated parallel path clear wall U-values were expectedly larger compared to the nominal U-values due to the impact of the framing; however, the difference was small due to small lateral heat flux of wood studs. As mentioned earlier, the parallel path method does not apply to W3 due to the presence of highly conductive metal components resulting in multi-dimensional heat flux. Hence, the clear wall U-value of W3 was measured using IRT and validated with 3D simulation tools, which incorporates the effect of lateral heat flux.

Table 2.4 Nominal (Nom) design value, and calculated (CALC) clear wall U-Values of wall assemblies

Wall assemblies	**U_{Nom} (W/ m^2 K)**	**U_{CALC} (W/m^2 K)**
W1	0.23	0.24
W2	0.16	0.17

The IRT U-value method was compared with the parallel path method to assess the reliability of the proposed IRT technique, and to identify if there are limitations in its applicability. Figures 2.12 to 2.14 illustrate the surface temperature distribution on the W1, W2, and W3, respectively. The "Fusion Palette" colour rendering scheme was chosen to symbolize surface temperature where

bright yellow corresponds to warmer areas, while dark blue represents colder areas. To evaluate the effect of ROI size and location on U-value measurements, multiple ROIs for each wall were selected. ROIs used for clear wall U-value measurements were corresponded to the size of simulated models in the BETB Guide (1220×813mm) [7, 61]. This size was based on standard construction techniques, large enough to evaluate the interaction of repeating thermal bridges (studs). For comparison with nominal design values the ROIs were selected smaller and far from the framing to avoid the effect of lateral heat flux on the surface temperature reading and U-value measurement.

Non-uniformity of wall surface temperature is evident in Figures 2.12 to 2.14 due to thermal bridges from wood framing, the window frame, and the parapet. These irregularities caused variation in pixel intensity, which is higher around the area of thermal bridges and lower around the corners because of different boundary conditions, contributions from the vignetting effect, and non-uniformity of thermal images. Results in Tables 2.5 to 2.9 confirmed the sensitivity of ROI location.

Table 2.5 depicts deviations of U-value measurements of W1 from nominal value that range from -60.87 % to 8.70 %. However, differences between clear wall U-value measurements with IRT and calculated values using the parallel path method varied from -16.16% to 66.66% (Table 2.6). Measured clear wall U-values were larger than nominal design U-values, confirming the thermal bridging effect of framing. Likewise, for W2, Tables 2.7 and 2.8 present deviations of -75.00% to 31.25% for nominal design U-values and -17.64% to 23.52% for clear wall U-values, respectively. Expectedly, since W2 was more insulated than W1, it had a lower surface temperature compared to W1, which resulted in lower U-values. Notably, U-value measurements of three ROIs were negative (surface temperatures were smaller than outdoor air temperature), likely due to profound effects of vignetting and corner thermal bridges, as discussed earlier. Finally, Table 2.9 showed that U-value measurements of W3 with IRT deviated between 25.00 % 62.50% from the nominal value. Higher deviations in the nominal U-value of W3 compared to that of W1 and W2 is likely due to multi-dimensional heat flux (metal components).

The results in Table 2.5 to 2.8 indicated that installation of cladding (Boxes 4-6 & Boxes 9-11) on the walls was not a barrier for thermal assessment of wall assemblies with IRT. For instance, the U-value measurement from Boxes 5 and 10 in W1 and W2 showed good agreement with the

parallel path method. However, thermal images of W3 without cladding were confounded because of highly reflective metal, which act like a mirror to the IR camera (see Figure 2.15). In other words, instead of measuring the temperature of the metal itself, the IR camera detected the reflected temperature from surrounding environment (cold (-3ºC) and hot (12ºC) spots are shown in Figure 2.15). Hence, W3 was evaluated fully clad to avoid temperature non-uniformities associated with reflective materials.

It is worth pointing out that in walls with rainscreen cladding, the temperature of cladding may not represent the actual temperature of the surface behind the cladding, due to air movement in the rainscreen cavity. However, because of the relatively small size of the rainscreen cavity (19 mm) and low wind speed at the time of the test, it can be deduced that the convection heat losses were relatively low (limited airflow movement in the rainscreen cavity), implying radiation heat exchange between the cladding and the surface behind the cladding is dominant. Therefore, the discrepancy in temperature between the cladding and the surface behind the cladding likely did not have a significant effect on the results.

The findings also suggest the location of ROI plays a key role in the accuracy of U-value measurements. Also, it was found that ROIs far from the low signal intensity area had more accurate U-values.

(a) (b)

Figure 2.12 Regions of interest (ROIs) for W; (a) thermal image; (b) visible image

Table 2.5 Comparison between measured IRT and nominal (Nom) U-values of different regions of interest (ROIs) for W1

ROI	Surface temperature (ºC)	U_{IRT} (W/m^2 K)	U_{Nom} (W/m^2 K)	Difference %
Box 1	6.71	0.09	0.23	-60.87
Box 2	6.87	0.16		-30.43
Box 3	7.07	0.25		8.70
Box 4	6.41	NA[2]		NA
Box 5	6.92	0.19		-17.39
Box 6	6.87	0.17		-26.09

Table 2.6 Comparison between measured IRT and calculated (CALC) clear wall U-value of different regions of interest (ROIs) for W1

ROI	Surface temperature (ºC)	U_{IRT} (W/m^2 K)	U_{CALC} (W/m^2 K)	Difference %
Box 7	7.20	0.30	0.24	25.00
Box 8	7.43	0.40		66.66
Box 9	6.43	NA[1]		NA
Box 10	7.01	0.23		-4.16
Box 11	6.94	0.20		-16.66

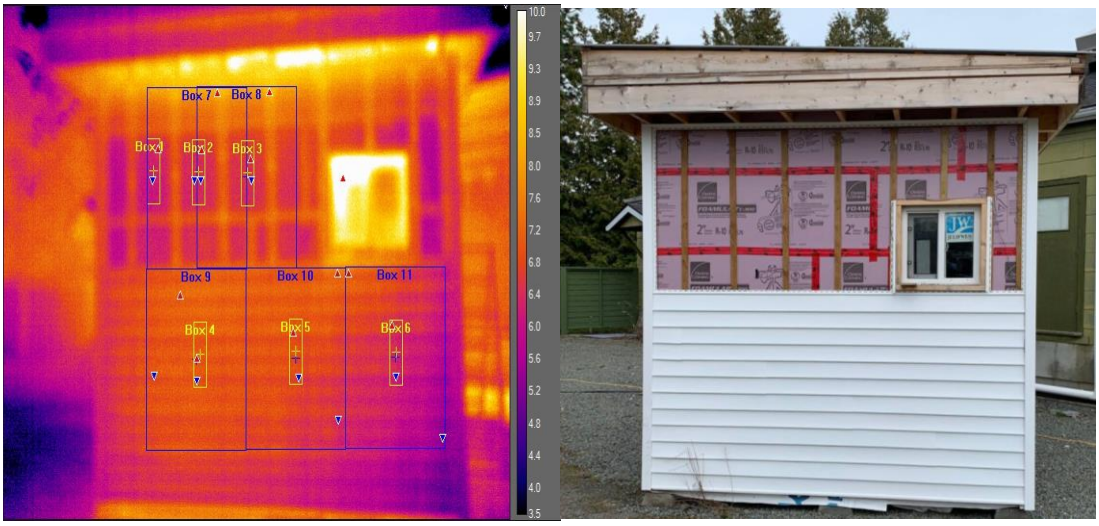

(a) (b)

Figure 2.13 Regions of interest (ROI) for W2; (a) thermal image; (b) visible image

[2] Not Applicable due to negative U-value

Table 2.7 Comparison between measured IRT and nominal (Nom) U-values of different regions of interest (ROIs) for W2

ROI	Surface temperature (°C)	U_{IRT} (W/m² K)	U_{Nom} (W/m² K)	Difference (%)
Box 1	6.26	NA[1]	0.16	NA
Box 2	6.60	0.04		-75.00
Box 3	6.65	0.07		-56.25
Box 4	6.97	0.21		31.25
Box 5	6.84	0.15		-6.25
Box 6	6.29	NA[1]		NA

Table 2.8 Comparison between measured IRT and calculated (CALC) clear wall U-value of different regions of interest (ROIs) for W2

ROI	Surface temperature (°C)	U_{IRT} (W/m² K)	U_{CALC} (W/m² K)	Difference (%)
Box 7	6.95	0.19	0.17	11.76
Box 8	6.97	0.21		23.52
Box 9	6.86	0.16		-5.88
Box 10	6.82	0.14		-17.64
Box 11	6.27	NA[1]		NA

(a) (b)

Figure 2.14 Regions of interest (ROI) for W3; (a) thermal image; (b) visible image

Table 2.9 Comparison between measured IRT and nominal (Nom) U-values of different regions of interest (ROIs) for W3

ROI	Surface temperature (°C)	U_{IRT} (W/m^2 K)	U_{Nom} (W/m^2 K)	Difference (%)
Box 1	6.95	0.20	0.16	25.00
Box 2	7.08	0.26		62.50
Box 3	6.98	0.22		37.50

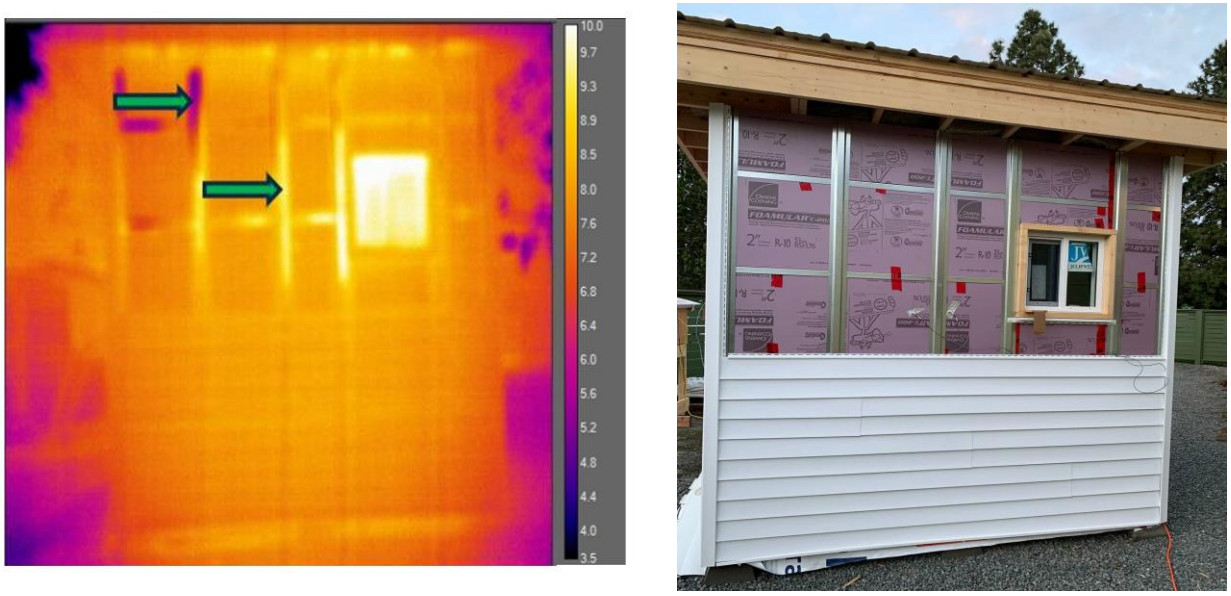

(a) (b)

Figure 2.15 The effect of high reflective component on IRT measurement in W3; (a) thermal image; (b) visible image

The accuracy of using one large ROI to measure clear wall U-value with IRT was tested using the IRT weighted area method. Five ROIs were selected for each clear wall U-value measurement including two of only framing and three of only cavity insulation (1D), as shown in Figures 2.16 and 2.17. The U-value of each area was measured, as shown in Table 2.10 to 2.13. Results of the weighted area method are similar to results of the one large ROI approach in Tables 2.6 and 2.8; for example, the U-value of Box 10 in Table 2.6 is comparable to the U-value in Table 2.12. This shows that considering one large ROI is a reasonable estimate to determine the clear wall U-value of wall assemblies, and further validates using the calculated parallel path method to estimate U-values in wood framed assemblies (due to minimal lateral heat flux).

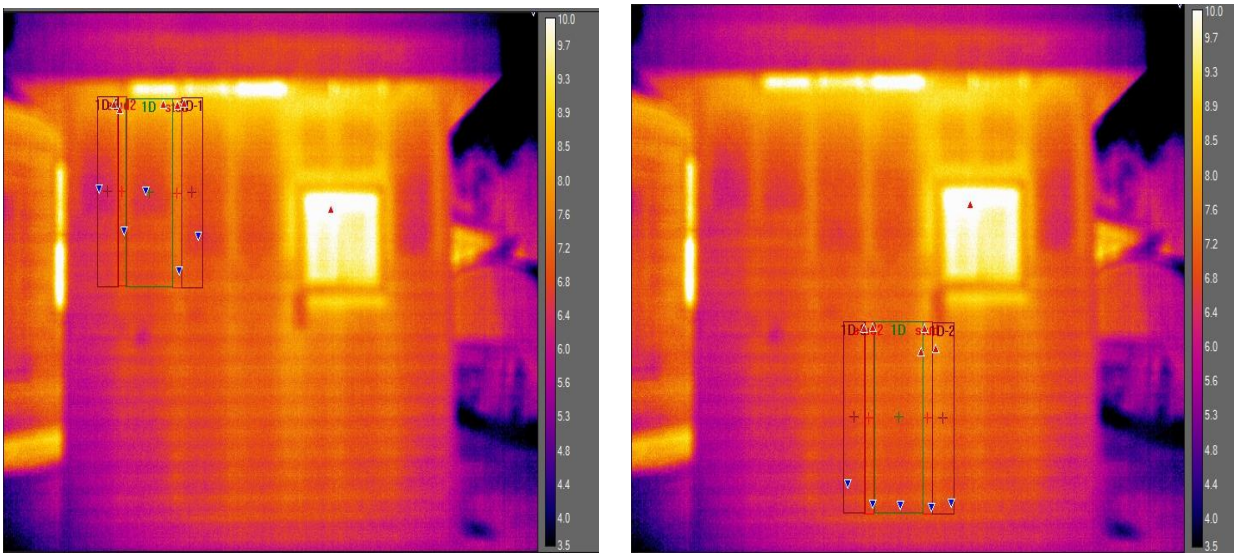

(a) (b)

Figure 2.16 Weighted area method for W1; (a) Box 7 (ROI); (b) Box 10

Table 2.10 Comparison between weighted area (WA) measured IRT and calculated (CALC) clear wall U-value Box 7 (ROI)- W1

ROI (Box7)	**Surface temperature (ºC)**	**Area (cm^2)**	**U_{IRT} (W/m^2 K)**	**U_{WA-IRT} (W/m^2 K)**	**U_{CALC} (W/m^2 K)**	**Differences (%)**
Stud 1	7.71	796.19	0.53	0.30	0.24	20.83
Stud 2	7.20	796.19	0.31			
1D	7.20	4354.59	0.31			
1D-1	7.31	1921.54	0.36			
1D-2	6.82	1921.54	0.14			

Table 2.11 Comparison between weighted area (WA) measured IRT and calculated (CALC) clear wall U-value Box 10 (ROI)- W1

ROI (Box10)	**Surface temperature (ºC)**	**Area (cm^2)**	**U_{IRT} (W/m^2 K)**	**U_{WA-IRT} (W/m^2 K)**	**U_{CALC} (W/m^2 K)**	**Differences (%)**
Stud 1	7.31	796.19	0.36	0.24	0.24	0
Stud 2	7.01	796.19	0.23			
1D	7.01	4354.59	0.23			
1D-1	7.21	1921.54	0.32			
1D-2	6.83	1921.54	0.15			

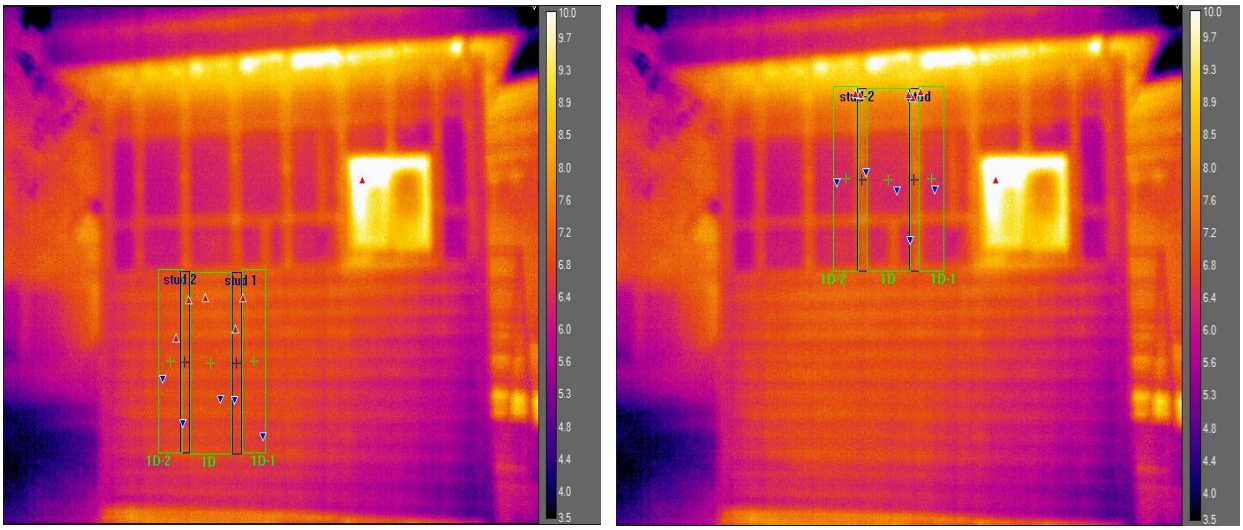

(a) (b)

Figure 2.17 Weighted area method for W2; (a) Box 9 (ROI); (b) Box 8

Table 2.12 Comparison between weighted area (WA) measured IRT and calculated (CALC) clear wall value Box 9 (ROI)-W2

ROI (Box 9)	Surface temperature (°C)	Area (cm^2)	U_{IRT} (W/m^2 K)	U_{WA-IRT} (W/m^2 K)	U_{CALC} (W/m^2 K)	Difference (%)
Stud 1	6.80	796.19	0.13	0.16	0.17	-5.88
Stud 2	6.91	796.19	0.18			
1D	6.92	3821.60	0.19			
1D-1	6.81	2173.70	0.14			
1D-2	6.80	2173.70	0.13			

Table 2.13 Comparison between weighted area (WA) measured IRT and calculated (CALC) clear wall U-value Box 8 (ROI)-W2

ROI (Box 8)	Surface temperature (°C)	Area (cm^2)	U_{IRT} (W/m^2 K)	U_{WA-IRT} (W/m^2 K)	U_{CALC} (W/m^2 K)	Difference %
Stud 1	7.32	796.19	0.36	0.17	0.17	0
Stud 2	7.30	796.19	0.34			
1D	6.81	3821.60	0.14			
1D-1	6.81	2173.70	0.14			
1D-2	6.83	2173.70	0.14			

2.5.2 Simulation Results

Table 2.14 shows the comparison between two industry accepted methods to determine U-value of wood framed wall assemblies. The difference between U-values obtained by simulations and the parallel path method for W1 and W2 was less than 8%, while the difference was 15% in W3 due to highly conductive materials in its wall assembly. Therefore, the parallel path method appears to be an adequate validation technique for W1 and W2, while wall assemblies like W3 with highly conductive elements (multi-dimensional heat flux) are better validated with computer simulations. It follows that IRT U-value measurements can be validated using the parallel path method and 3D simulation tools for W1 and W2; however, it is more appropriate to use 3D simulation tools for W3.

Table 2.14 Comparison between 3D simulation (SIM) and calculated (CALC) clear wall U-values

Wall assemblies	**U_{CALC} (W/m^2 K)**	**U_{SIM} (W/m^2 K)**	**Differences %**
W1	0.24	0.26	-7.69
W2	0.17	0.18	-5.55
W3	0.17	0.20	-15.00

Figure 2.18 (a-c) maps temperature distribution through the components of each wall assembly for illustrative purposes. The thermal models were evaluated using a parametric temperature index. The temperature index is the ratio of the surface temperature relative to the interior and exterior temperatures. The temperature index has a value between 0 and 1, where 0 is the exterior temperature and 1 is the interior temperature. If T_i is known, Equation 2.15 can be rearranged for $T_{surface}$. This arrangement allows the modeled surface temperatures to be applicable to any climate.

$$T_i = \frac{T_{surface} - T_{out}}{T_{in} - T_{out}} \tag{2.15}$$

Note, these indices shown in the temperature profiles for this analysis are for general information only and are not intended to predict in-service surface temperatures subject to transient conditions, variable heating systems, and/ or interior obstructions that restrict heating of the assembly.

Three-dimensional temperature profiles in Figure 2.18 inform the impacts of thermal bridges and attachment systems on the thermal performance of wall assemblies. For instance, when Figure 2.18 is observed from a side profile, it is seen that the surface temperature around the areas of thermal bridges (studs) in W1 and W2 is approximately uniform (small lateral heat flux). However, non-uniformity of temperature around the sheathing and cavity in W3 is more evident than W1

and W2, due to the high conductivity of metal girts. Furthermore, although W2 and W3 have similar nominal U-values, their clear wall U-values (studs + cavity + attachment components) are different since thermal bridging effects of components in their assemblies are dissimilar. These non-uniformities are not evident on the exterior surface due to the presence of exterior insulation. Furthermore, the thermal bridging effect of studs on interior surface temperature is more evident in W1 compared to W2 and W3 due to its higher U-value (appear colder by virtue of higher heat flux from the interior to the exterior).

U-values from the three best ROIs on each wall were compared with 3D simulations and showed promising results (Tables 2.15-2.17). Deviations ranged from -23.07% to 15.38% in the case of W1, -11.11% to 16.66 % in the case of W2, and 10.00 to 40.00% in the case of W3. In contrast, previous quantitative IRT studies on well-insulated walls showed deviations between theoretical and measured U-values in the range of 37% to 154% [33, 34].

W1

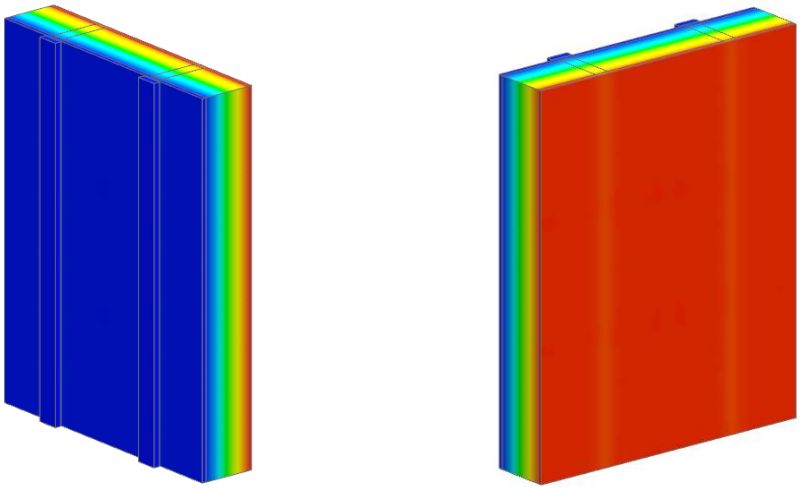

Exterior Interior

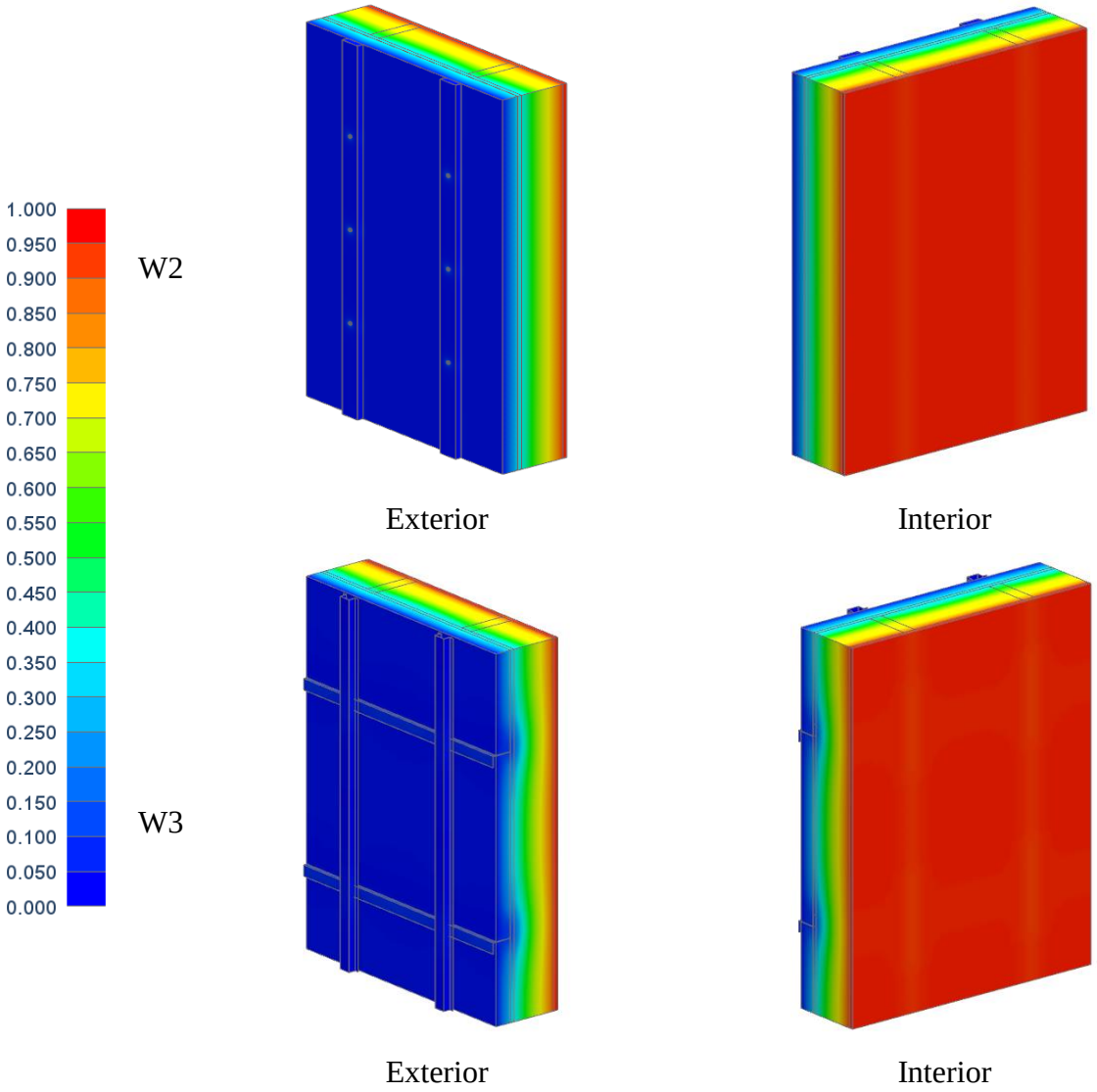

Figure 2.18 3D simulations of W1, W2 and W3

Table 2.15 Comparison between measured IRT and 3D simulation (SIM) clear wall U-value for W1

Region of Interest (ROI)	**U_{IRT} (W/m^{2}K)**	**U_{SIM} (W/m^2 K)**	**Differences %**
Box 7	0.30	0.26	15.38
Box 10	0.23		-11.53
Box 11	0.20		-23.07

Table 2.16 Comparison between measured IRT and 3D simulation (SIM) clear wall U-value for W2

Region of Interest (ROI)	U_{IRT} (W/m^2 K)	U_{SIM} (W/m^2 K)	Differences %
Box 8	0.21	0.18	16.66
Box 9	0.16		-11.11
Box 7	0.19		5.55

Table 2.17 Comparison between measured IRT and 3D simulation (SIM) clear wall U-value for W3

Region of Interest (ROI)	U_{IRT} (W/m^2 K)	U_{SIM} (W/m^2 K)	Differences %
Box 6	0.22	0.20	10.00
Box 5	0.25		25.00
Box 4	0.28		40.00

2.5.3 Sources of error

Several potential sources of error were present in this experiment. Although the wind speed during the test was in the range recommended by previous studies, the impact of occasional wind gusts a few hours before the test caused forced convective cooling on the surface. It was assumed that all the surrounding objects, the sky, and the ground have similar temperatures to the ambient air. However, sky and ground temperatures should be measured separately for accurate measurement of U-value, which was not possible during the survey. Radiative sources such as lighting and adjacent buildings in the field of view of wall assemblies also represent a source of IRT measurement error. In this study, the projection of street and parking area lighting on W1 and W2 influenced reflected temperature measurements, and subsequently surface temperature measurements. W3 was in the field of view of the adjacent conditioned lab building where the exchange of radiation between surfaces was present. Finally, indoor air temperature was measured with thermistors in this experiment, which may have introduced equipment measurement error as previously discussed.

2.6 Conclusions

While previously developed external infrared thermography (IRT) methodologies mainly focused on U-value measurement of wall assemblies in European constructions without considering the effect of thermal bridges, this study attempted to develop an external IRT method comparable with established practice for clear wall U-value measurement of wood-framed wall assemblies commonly used in Canada.

The main findings of this study are highlighted as follows:

- Size and location of the region of interest (ROI) plays a key role in U-value measurements due to the effects of (1) thermal bridges (studs & corners), and (2) thermal image artefacts such as vignetting where images appears colder around the corners than in the centre of the camera field-of-view.
- Non-uniformity correction (NUC) should be considered by the thermographer to reduce measurement error and produce higher quality thermal images.
- It was found that cladding is not a barrier for thermal assessments of rainscreen wall assemblies with IRT.
- U-value measurement with IRT in the best-case scenario (depending on the ROI) deviated from nominal U-values by 13.63%, 6.25% and 25.00% for W1, W2, and W3, respectively.
- In the best-case scenario, deviations of clear wall U-value measurements between IRT and the parallel path method were -4.16% and -5.88% for W1 and W2, respectively.
- In the best-case scenario, clear wall U-values obtained with IRT differed from 3D simulations by -11.53 to 10.00%.
- The parallel path method is a good approximation for clear wall U-values of wood-framed wall assemblies without highly conductive elements (W1 & W2), as validated by 3D simulations.
- The clear wall U-value of W3 was only validated with 3D simulations since the parallel path cannot be applied to the assemblies with highly conductive metal elements.
- U-value measurements of W3 with IRT deviated more from 3D simulations than those for W1 and W2, implying 3D simulations are a better indicator of thermal performance than IRT for wall assemblies that include highly conductive attachment components.

It is recommended to use an infrared (IR) camera with a higher focal length to avoid the effect of vignetting (less “stretch” in the thermal image). For highly insulated assemblies like W2 and W3,

increasing the heat flux through the wall by increasing the indoor-outdoor temperature gradients could enhance accuracy. In this study, sky and ground temperature was assumed to have a similar temperature to ambient air; however, they should be measured separately to improve the accuracy of measurements.

A number of Canadian jurisdictions have initiated policies to mitigate their carbon footprint by addressing energy efficiency of buildings in a variety of ways. Many existing buildings were built prior to today's more stringent building codes and may require in-situ assessment of the opaque clear wall U-value for energy modelling for retrofit purposes. The methodology presented in this study could be considered as a quick and non-invasive method to estimate the U-value of wood framed assemblies for this purpose. This study is a first step towards developing a quick and reliable method for the inspection and quantification of building envelope thermal performance for energy audits or retrofits, and potentially a basis for governments to develop policies for existing building energy performance.

2.7 References

[1] Energy and Greenhouse Gas Emissions (GHGs), Natural Resources Canada, Ottawa, Canada, June 2020, available at: https://www.nrcan.gc.ca/science-data/data-analysis/energy-data-analysis/energy-facts/energy-and-greenhouse-gas-emissions-ghgs/20063 (Accessed on 23 March 2021).

[2] Guide to Low Thermal Energy Demand for Large Buildings, BC Housing, February 2018

[3] J. Kwan, An investigation of the new opportunities of wood in mid-rise construction in British Columbia. University of British Columbia, Forestry Undergraduate Essay/Theses, 2013 Winter Session, WOOD 493

[4] Mid-rise Best practice guide, proven construction techniques for five and six storey wood-frame buildings, BC Housing, 2014.

[5] A. Stone, D. Shipworth, P. Biddulph, T. Oreszczyn, Key factors determining the energy rating of existing English houses, Building Research & Information. 42 (2014) (6) 725-738.

[6] International Standard ISO 6946, Building components and building elements. Thermal resistance and thermal transmittance - Calculation method, 2007.

[7] Morrison Hershfield, Building Envelope Thermal Bridging Guide—Analysis, Applications and Insights, 2014.

[8] ASHRAE, ANSI/ASHRAE/IESNA Standard 90.1-2010: Energy Standard for Buildings Except Low-Rise Residential Buildings. American Society of Heating, Refrigerating and Air-Conditioning Engineers, Inc, Atlanta, GA, 2010.

[9] B. Tejedor, E. Barreira, R.M.S.F. Almeida, M. Casals, 2020, Thermographic 2D U-value map for quantifying thermal bridges in building façades, *Energy Build*. 224 (2020):110176.

[10] I. Danielski, M. Fröling, Diagnosis of buildings' thermal performance-a quantitative method using thermography under non-steady state heat flow, Energy Procedia. 83 (2015) 320-329.

[11] International Standard ISO 9869-1, Thermal insulation - Building elements, In-situ measurement of thermal resistance and thermal transmittance. Part 1: Heat flow meter method, 2014.

12. American Society for Testing and Materials, ASTM C1155-95 Standard Practice for Determining Thermal Resistance of Building Envelope Components from the In-Situ Data, West Conshohocken, PA, 2013.

[13] N. Soares, C. Martins, M. Gonçalves, P. Santos, L.S. da Silva, J.J. Costa, Laboratory and in-situ non-destructive methods to evaluate the thermal transmittance and behavior of walls, windows, and construction elements with innovative materials: A review, Energy Build. 182 (2019) 88-110.

[14] M. Cucumo, V. Ferraro, D. Kaliakatsos, M. Mele, On the distortion of thermal flux and of surface temperature induced by heat flux sensors positioned on the inner surface of buildings, Energy Build. 158 (2018) 677-683.

[15] X. Meng, B. Yan, Y. Gao, J. Wang, W. Zhang, E. Long, Factors affecting the in situ measurement accuracy of the wall heat transfer coefficient using the heat flow meter method, Energy Build. 86 (2015) 754-765.

[16] G. Ficco, F. Iannetta, E. Ianniello, F. R. D.A. Alfano, M. Dell'Isola, U-value in situ measurement for energy diagnosis of existing buildings, Energy Build. 104 (2015) 108-121.

[17] A. Ahmad, M. Maslehuddin, L.M. Al-Hadhrami, In situ measurement of thermal transmittance and thermal resistance of hollow reinforced precast concrete walls, Energy Build. 84 (2014) 132-141.

[18] P.G. Cesaratto, M. De Carli, A measuring campaign of thermal conductance in situ and possible impacts on net energy demand in buildings, Energy Build. 59 (2013) 29-36.

[19] S. Doran, Field of investigations of the thermal performance of constructions elements as built. Report No.78132, 2000.

[20] P. Baker, U-values and Traditional Buildings: in Situ Measurements and Their Comparisons to Calculated Values, Historic Scotland, Edinburgh, 2011.

[21] E. Lucchi, Thermal transmittance of historical stone masonries: A comparison among standard, calculated and measured data, Energy Build. 151 (2017) 393 – 405.

[22] E. Lucchi, F. Roberti, T. Alexandra, Definition of an experimental procedure with the hot box method for the thermal performance evaluation of inhomogeneous walls, Energy Build. 179 (2018) 99-111.

[23] B. Tejedor, M. Casals, M. Macarulla, A. Giretti, U-value time series analyses: Evaluating the feasibility of in-situ short-lasting IRT tests for heavy multi-leaf walls, Build Environ. 159 (2019) 1-19

[24] X.P. Maldagu, Introduction to NDT by active infrared thermography, Materials Evaluation 60 (2002) 1060-1073.

[25] D. Bienvenido-Huertas, J. Moyano, D. Marín, R. Fresco-Contreras, Review of in situ methods for assessing the thermal transmittance of walls, Renewable Sustainable Energy Rev. 102 (2019) 356-371.

[26] C.A. Balaras, A.A. Argirou, Infrared thermography for building diagnostics, Energy Build. 34 (2002) 171 – 183.

[27] F. Asdrubali, G. Baldinelli, F. Bianchi, A quantitative methodology to evaluate thermal bridges in buildings, Appl. Energy. 97 (2012) 365-373.

[28] M. Mahmoodzadeh, V. Gretka, S. Wong, T. Froese, P. Mukhopadhyaya, Evaluating Patterns of Building Envelope Air Leakage with Infrared Thermography, Energies. (2020) 13 (14), 3545.

[29] R. Madding, Finding R-values of stud frame constructed houses with IR thermography, in Proceedings of InfraMation, Reno, USA, 2008.

[30] P.A. Fokaides, S.A. Kalogirou, Application of infrared thermography for the determination of the overall heat transfer coefficient (U-Value) in building envelopes, Appl. Energy. 88 (2011) (12) 4358-4365.

[31] B. Tejedor, M. Casals, M. Gangolells, X. Roca, Quantitative internal infrared thermography for determining in-situ thermal behaviour of façades, Energy Build. 151 (2017) 187-197.

[32] B. Tejedor, M. Casals, M. Gangolells, Assessing the influence of operating conditions and thermophysical properties on the accuracy of in-situ measured U-values using quantitative internal infrared thermography, Energy Build. 171 (2018) 64-75.

[33] G. Dall'O, L. Sarto, A. Panza, Infrared screening of residential buildings for energy audit purposes: results of a field test, Energies. (2013) 6 (8) 3859-3878.

[34] R. Albatici, A.M. Tonelli, M. Chiogna, A comprehensive experimental approach for the validation of quantitative infrared thermography in the evaluation of building thermal transmittance, Appl. Energy. 141 (2015) 218-228.

[35]A. Colantonio, G. McIntosh, The differences between large buildings and residential infrared thermographic inspections is like night and day, 11th Canadian Conference on Building Science and Technology, Banff, 2007

[36] I. Nardi, S. Sfarra, D. Ambrosini, In Quantitative thermography for the estimation of the U-value: state of the art and a case study, 32nd IUT (Italian Union of Thermo-fluid-dynamics) Heat Transfer Conference, Journal of Physics, Conference Series. 547 (2014) 012016

[37] I. Nardi, D. Paoletti, D. Ambrosini, T. De Rubeis, S. Sfarra, U-value assessment by infrared thermography: A comparison of different calculation methods in a Guarded Hot Box, Energy Build. 122 (2016) 211-221.

[38] X. Lu, A. Memari, Application of infrared thermography for in-situ determination of building envelope thermal properties, J. Build. Eng. 26 (2019) 100885.

[39] F. Asdrubali, G. Baldinelli, F. Bianchi, A quantitative methodology to evaluate thermal bridges in buildings, Appl. Energy. 97 (2012) 365-373.

[40] M. O'Grady, A.A. Lechowska, A.M. Harte, Infrared thermography technique as an in-situ method of assessing heat loss through thermal bridging, Energy Build. 135 (2017) 20-32.

[41] M. O'Grady, A.A. Lechowska, A.M. Harte, Quantification of heat losses through building envelope thermal bridges influenced by wind velocity using the outdoor infrared thermography technique, Appl. Energy. 208 (2017) 1038-1052.

[42] F. Bianchi, A. Pisello, G. Baldinelli, F. Asdrubali, Infrared thermography assessment of thermal bridges in building envelope: experimental validation in a test room setup, Sustainability. (2014) 6:7 107–20.

[43] I. Nardi, D. Paoletti, D. Ambrosini, T. De Rubeis, S. Sfarra, Validation of quantitative IR thermography for estimating the U-value by a hot box apparatus, Journal of Physics. Conference 655 (2015) 012006.

[44] K. Martin, C. Escudero, A. Erkoreka, I. Flores, J. Sala, Equivalent wall method for dynamic characterisation of thermal bridges, *Energy Build. 55 (2012) 704-714.*

[45] C. Rye, C. Scott, The SPAB research report 1: U-value report, *Society for the Protection of Ancient Buildings: London, UK*, 2012.

[46] B. Lehmann, K.G. Wakili, T. Frank, B.V. Collado, C. Tanner, Effects of individual climatic parameters on the infrared thermography of buildings, *Appli. Energy.*110 (2013) 29-43.

[47] A. Wróbel, T. Kisilewicz, Detection of thermal bridges-aims, possibilities and conditions, in: Proceedings of International Conference on Quantitative Infrared Thermography Qirt, Cracow, Poland, 2008.

[48] I. Nardi, E. Lucchi, T. de Rubeis, D. Ambrosini, Quantification of heat energy losses through the building envelope: A state-of-the-art analysis with critical and comprehensive review on infrared thermography, *Build. Environ.* 146 (2018) 190-205.

[49] E. Lucchi, Thermal transmittance of historical stone masonries: A comparison among standard, calculated and measured data, *Energy Build.*151 (2017) 393-405.

[50] Siemens NX software, available at: https://www.plm.automation.siemens.com/global/en/products/nx/ (Accessed on 23 March 2021)

[51] American Society for Testing and Materials, ASTM E1862-14, *Standard Practice for Measuring and Compensating for Reflected Temperature Using Infrared Imaging Radiometers*; ASTM: West Conshohocken, PA, USA, 2014.

[52] American Society for Testing and Materials, ASTM E1933-14, *Standard Practice for Measuring and Compensating for Emissivity Using Infrared Imaging Radiometers;* ASTM: West Conshohocken, PA, USA, 2014.

[53] Government of Canada, Historical Climate Data, available at: https://climate.weather.gc.ca/index_e.html (Accessed on 23 March 2021)

[54] I. Simões, N. Simões, A. Tadeu, J. Riachos, Laboratory assessment of thermal transmittance of homogeneous building elements using infrared thermography, QIRT 2014—Civil Engineering & Buildings (2014).

[55] R. Albatici, A.M. Tonelli, Infrared thermovision technique for the assessment of thermal transmittance value of opaque building elements on site, Energy Build. 42 (2010) (11), 2177-2183.

[56] Engineering Reference — EnergyPlus 8.0, US Department of Energy, USA, 2013, https://bigladdersoftware.com/epx/docs/8-0/engineering-reference/page-020.html

[57] R. Calik, E. Tunali, B. Ercan and S. Oz, A Study on Calibration Methods for Infrared Focal Plane Array Cameras, In: Proceedings of the 13th International Joint Conference on Computer Vision Imaging and Computer Graphics Theory and Applications (VISIGRAPP 2018), vol. 4, pp. 219-226.

[58] Li, Haiyan, and Min Zhu. "Simulation of vignetting effect in thermal imaging system." In *MIPPR 2009: Multispectral Image Acquisition and Processing*, vol. 7494, p. 749427. International Society for Optics and Photonics, 2009.

[59] P. Santos, G. Lemes, D. Mateus, Analytical Methods to Estimate the Thermal Transmittance of LSF Walls: Calculation Procedures Review and Accuracy Comparison, Energies. (2020) 13 (4), 840.

[60] Morrison Hershfield, Thermal performance of building envelope details for mid-and high-rise buildings, ASHRAE Research Project1365-RP Final Report, 2011.

[61] P. Roppel, M. Lawton, N. Norris, Thermal Performance of Building Envelope Details for Mid-and High-Rise Buildings, ASHRAE Trans. 118 (2012) 569-584.

Chapter 3: Infrared Thermography for Quantitative Thermal Performance Assessment of Wood-Framed Building Envelopes in Canada

The content in this chapter was published in the following publication:

M. Mahmoodzadeh, V. Gretka, I. Lee, P. Mukhopadhyaya, Utilizing External Infrared Thermography to Assess Thermal Performance of Wood-Framed Building Envelopes in Canada, ***Journal of Energy and Buildings***. (2021) 111807. https://doi.org/10.1016/j.enbuild.2021.111807

3.1 Abstract

Since many buildings in Canada were built prior to the advent of national and provincial energy codes and standards, quantifying building envelope thermal performance is an important step in identifying retrofit opportunities in existing buildings. This study aimed to use external quantitative infrared thermography (IRT) to estimate effective U-value of opaque building envelopes (considering the effect of thermal bridging sources) of a conditioned at-scale structure comprised of four wood-framed wall assemblies commonly used in Canada. Furthermore, the effect of vignetting artefacts on effective U-value measurements was assessed, followed by a practical approach to correcting for it to improve accuracy of U-value estimation and calibration of energy models. Additionally, a comprehensive uncertainty analysis was performed to evaluate the impact of input variables on the accuracy and uncertainty of results. Finally, apart from qualitative and quantitative thermal assessment of the building envelope, a relative quantitative infrared index (IRI) methodology was proposed as a means to facilitate rapid evaluation and subsequent ranking of building envelope thermal performance. The results indicated that vignetting effect has an adverse impact on the accuracy of results, in particular for well-insulated walls where deviations of -42.31% to -83.33% were observed. However, when the proposed practical approach was implemented, substantial improvements in accuracy of walls' U-value were obtained, ranging from -2.33% to -12.50% after correction versus -13.95% to -58.33% without correction. Moreover, the results indicated that the energy model was substantially more accurate when the effect of thermal bridges were accounted for, and the adverse effect of vignetting was addressed in the estimation of U-value. In this case, ASHRAE Guideline 14 criteria were satisfied: Normalized Mean Bias Error (NMBE) < 5%, and Coefficient of Variation of the Root Mean Square Error (CVRMSE) < 15%. The findings of the uncertainty budget demonstrated that the influence of parameters on U-value depends on the type of wall assembly. Ultimately, wall thermal performance rankings based on IRI were consistent with their U-value rankings, implying that IRI can be a reliable metric for relative quantitative comparison of building envelope thermal performance, regardless of boundary conditions.

Keywords: External infrared thermography, Effective U-value, Vignetting effect, Energy modelling, Uncertainty budget, Infrared index

3.2 Introduction

Globally, space heating and cooling accounts for over one-third of overall energy consumptions in buildings. With a revived concern for building energy consumption, aggressive energy conservation policies have been adopted at national and regional levels. For instance, the province of British Columbia, and later Canada, committed to reduced net greenhouse emissions by 80% of 2007 and 2005 levels, respectively, by 2050 [1-2], as have been adopted by other G7 nations at the recent Paris Climate Summit [3]. In the wake of these policies, building certifications through energy audits are becoming a common means of grading energy performance, and in part the overall building sustainability. Since existing buildings in Canada are predicted to account for almost half of total building stock by 2050, Canadian policymakers are gradually focus on improving the energy use intensity (EUI) of these buildings [4].

One of the most critical considerations in a building energy assessment is the thermal performance of the building envelope. It is evident that with more heat transfer through the building envelope, a a greater amount of energy needs to be consumed to maintain a similar indoor air temperature [5]. IEA's technology roadmap for energy-efficient buildings indicated that improving the thermal performance of the building envelope can lead to an energy use reduction of 57% and 42% in commercial and residential buildings, respectively [6]. To this end, researchers worldwide have conducted various studies to evaluate the impact of the building envelope on building energy performance. For instance, Osma et al. [7] considered different retrofit design strategies to achieve a net-zero energy performance of a university building in Tripoli, Lebanon. It was found that by retrofitting the building envelope through upgrading the walls and floor with additional insulation, the EUI of a building can be reduced by 28%, which was more effective than upgrading HVAC and lighting systems. Lin et al. [8] showed that optimizing the thermal performance of building envelope of office buildings in Taiwan can save almost 41% of energy costs. Elsewhere, Balaras et al. [9] indicated that the energy consumption of well-insulated apartment buildings in Greece was 20-40% less than non-insulated buildings. It can be deduced that identifying the actual thermal performance of building envelopes is essential to understand any potential opportunities for improvement.

Currently, a detailed energy assessment of a building is performed with simulation tools. Achieving accurate results requires reasonably accurate inputs such as climate data, building

envelope thermal properties, internal load profiles (lighting, equipment, levels of activity, ...), air leakage rates, type of mechanical systems, and occupant behaviour. Uncertainties in input values can adversely affect the selection of appropriate retrofit strategies [10]. One of the most uncertain inputs in energy models is the building envelope's thermal characteristics, which are mainly applied in models based on design values obtained from reference tables. However, the actual U-value of the building envelope differs from its design due to the ageing of insulation materials, variation of materials moisture content, quality of installation, structural defects (cracks; voids), and fluctuation of external conditions such as temperature, humidity, solar radiation and precipitation [10-11]. For instance, the Italian Standard UNI 10351 reported differences of 5% to 50% between the field and lab measurements of material thermal conductivity [12]. Similarly, Evangelisti et al. [13] through a study using a heat flow meter in a lab environment, concluded that deviations between theoretical and measured U-values of wall assemblies can be as high as 153%. Therefore, in-situ quantification of building envelope thermal performance is required to reduce the uncertainties in energy modelling results, and inform implementation of the most appropriate energy conservation measures (ECMs) [12].

In the last few decades, non-destructive testing techniques such as heat flux meters (HFMs) and infrared thermography (IRT) have become prominent tools for on-site assessments of building envelope thermal performance [14]. However, HFMs are only a point source measurement that ignores the impact of thermal bridges or material irregularities, ultimately limiting its effectiveness as a data collection technique for spreadsheet-based energy audits or dynamic whole-building energy modelling. Furthermore, measurements require a minimum test duration of 72 hours (at least 96 hours for materials with high specific heat capacities), which is often not practical for practitioners; in this context, IRT has drawn attention as a viable alternative [14].

IRT is a non-destructive tool that determines the temperature of objects based on the radiation emitted from the object's surface. Traditionally, IRT has been used mainly for military purposes [15-16], medical applications such as visualizing the early stages of breast cancer [17], identifying the hot spots during the inspection of high-voltage power lines [15, 17], and inspections of HVAC and electric systems in buildings [18]. By the early 2000s, the application of IRT was expanded as a means to identify thermal irregularities for energy audit purposes in buildings [19]. Following this, International standards such as ISO 6781:1983 [20], UNE EN 13187:1998 [21], ASTM E1311 [22], ASTM E1862 [23], and guidelines (i.e., RESNET [24]) have established required boundary

conditions and procedures for the use of qualitative IRT in the energy audits of buildings, to ensure reliable and comparable results. Nevertheless, many authors have recently attempted to develop an accurate approach for estimating the in-situ U-value of building envelope using quantitative IRT [25-32].

Decreasing costs and improved portability of infrared cameras with the ability to connect to smartphones have collectively provided opportunities for energy advisors, homeowners, and property managers to observe temperature anomalies in thermal images. The widespread accessibility of this technology implies it could eventually be a ubiquitous inspection tool that helps inform building envelope retrofit strategies for the purposes of energy efficiency [33].

Although the majority of studies were conducted in European countries [26-31], this research aims to provide some insights into how quantitative IRT can evaluate thermal performance of wood-framed wall assemblies in Canada in the context of local construction practices and building codes.

This chapter consists of three main sections: 1) background, which provides an overview of recent applied methodologies in the evaluation of building envelopes using IRT; 2) methodology, which describes how the wall assemblies of a simple one-zone structure were assessed, outlines data collection procedures, followed by the development of a dynamic whole-building energy model of the structure to examine the feasibility of using external IRT in calibrating energy simulation models; 3) results, which summarizes findings from the IRT measurement and the calibration of the simulated model, and; 4) conclusion, that highlights the major contribution of this research and potential next steps in refining the techniques herein for utilization by practitioners.

3.3 Background

Over the last 25 years, IRT has been widely utilized in the inspection of building envelope physical deterioration [10]. Most building envelope defects are ultimately a result of moisture accumulation, which can occur either by poor envelope detailing allowing precipitation ingress from the exterior, or by via condensation at locations with thermal bridging from air leakage [34]. However, thermal patterns associated with either scenario are different, which are important to identify. For instance, moisture or pooling water within the building envelope presents as a non-homogenous thermal pattern on the surfaces, often reducing the measured temperature due to evaporative cooling. Areas with thermal bridging have a higher pixel intensity compared to undisturbed areas when analyzed with external IRT, in general. Likewise, hot spots in building envelope due to the degradation/missing of thermal insulation or air leakage effects are detectable

by IRT. These anomalies in thermal behavior of building components are mainly determined with qualitative IRT, while quantification of thermal irregularities and assessment of insulation thermal performance require quantitative methods [34]. Generally, in both quantitative and qualitative approaches, anomalies on the surface are evaluated visually or numerically based on their temperature patterns in thermal images (explained further in the following subsections).

3.3.1 Qualitative IRT

Qualitative IRT is widely adopted in building inspections to obtain a variety of information. For example, it is used to identify sources of air leakage, locations of thermal bridging, trapped moisture and water, thermal insulation discontinuity, performance of HVAC and electrical systems after installation such as detection of air and water leakage from pipes and ducts, insulation of distribution ducts and pipes, failure in bearing, lubrication and/or electrical motors (hot spots due to the mechanical stress), thermal comfort assessment by visualizing variations in skin temperature on different parts of a human face, and measurement of indoor and surface temperatures [19]. Irregularities can be quickly interpreted based on colour patterns and intensity differences in thermal images. In other words, qualitative IRT determines the anomalies, but it does not necessarily inform about the severity of defects [34].

A range of studies have been conducted to assess the performance of building envelope assemblies using qualitative thermography. For instance, a study on a historical building was undertaken to analyze earthquake damage using qualitative IRT [35]. Images showed locations of thermal anomalies after the earthquake, leading the authors to conclude that qualitative IRT was a useful technique to advise safety precautions for historical building renovations. Goodhew et al. [36] conducted a study to assess the heat losses of ten houses in the UK using qualitative IRT. Psychological reactions of household members after the thermographic survey were recorded, in particular their tendencies to adopt energy-saving behaviours. The results revealed that the outcomes of qualitative surveys were satisfying for each individual and motivated them to apply energy conservation measures (ECMs). A thermographic survey was conducted by Ocana et al. [37] on two different buildings (modern vs. historical) in Spanish rural areas to evaluate the usefulness of IRT in thermal assessment of rural buildings. The surveys were performed at two times, one in the late evening and the other in the early morning. IRT results indicated that for modern building whose walls were non-load bearing and relatively thin, the best results were

obtained during the daybreak inspection. However, for the inspection of traditional building which had thicker walls with high thermal inertia, IRT provided better results during the evening inspection. Mahmoodzadeh et al. [38] combined IRT with a blower door test to determine the minimum required pressure difference for detecting sources of air leakage around a window frame. It was found that a minimum pressure difference of 25 Pa is required to visualize the air leakage pattern with IRT at the window-to-wall interface as well as differentiate air leakage from a known thermal bridge (window frame). In addition, an IRT survey of 135 residential units in the Boston, MA metropolitan area indicated that heat losses through the windows, windows crack, chimney, and soffits were the dominant sources of heat loss, observed in almost 70% of buildings analyzed. Furthermore, to assess the contribution of heat transfer modes in energy losses, it was found that on a heated residential building, air leakage through cracks (windows & doors) and ducts account for nearly 40% of total energy losses, and conduction heat transfer through the walls and windows account for the other 40% of energy lost. This provided a simplified framework to identify which sources should be focused to reduce the energy losses in buildings [39]. Given these findings, it can be inferred that qualitative IRT can be a reliable method for the identification of building envelope defects and thermal bridges. When used in an energy audit setting, it can help homeowners and property managers implement targeted, cost-effective envelope retrofits [34].

3.3.2 Relative quantitative IRT

Building envelope retrofits are typically performed when its physical condition at the end of its service life, aesthetic (vintage), or the building energy use intensity (EUI) dictates it is required [40]. In the case of a portfolio or campus of buildings under the purview of a single property manager, prioritizing envelope retrofits is not a straightforward exercise. Compiling building-level envelope data is time-consuming, while global approximations that are applied to the whole portfolio may lack enough accuracy to inform conclusions about relative energy performance [40]. For instance, Mahmoodzadeh et al. [40] showed that the rank of buildings based on a single criterion such as age and physical condition yielded different results, with no correlation to overall heat loss (UA) through the building envelope. While qualitative IRT demonstrated a robust method for determining the thermal anomalies and visualizing their thermal patterns, a metric for identification and prioritization of thermal anomalies in the building envelope is required. To this end, researchers have used the concept of Temperature Index (TI), which is defined as the ratio of the temperature difference between the interior surface and outdoor air to the temperature

difference between the indoor and outdoor air (assuming one-dimensional heat transfer and steady state conditions). TI has been used to determine and prioritize the thermal irregularities in building envelope such as thermal bridges, condensation, mould growth, and air leakage. For instance, the International Energy Agency (IEA) has proposed to use TI as a metric to assess relative impacts of thermal bridges [41]. Similarly, the Building Envelope Thermal Bridging Guide (BETB) has applied the concept of TI to determine potential areas of condensation risk due to the effect of thermal bridging in building components [42]. Ilomets et al. [43] used TI for a critical analysis of thermal bridging sources and probability of failure in six dwelling units before renovation. To this end, IRT was used to measure the temperature of internal surfaces at different points and TIs were measured accordingly. The results indicated that the risk of surface condensation due to thermal bridging was 51% in concrete buildings and almost 50% for wood and brick buildings. However, the probability of mould growth in the concrete building was determined to be 54% compared to 46% and 45% in wood and brick buildings, respectively. Additionally, many countries have established various TI design values to assess condensation in the building envelope. For example, TI should be at least 0.75 for dwellings in the United Kingdom to avoid moisture damage and surface condensation [44]. Similarly, Dutch building regulations set the minimum TI of 0.65 for new residential buildings [45]. Finland recommended a TI of 0.97 for floors, 0.87 for walls, and 0.65 at the junction of the external walls. Several other studies have used TI to determine sources of air leakage [46]; for instance, Kalamees [47] studied houses in Estonia and found that ceiling/floor-wall, window-wall, and interior/exterior wall-roof interfaces were the main sources of air leakage. Similarly, Mahmoodzadeh et al. [38] used TI as a metric to identify sources of air infiltration around an interior window frame by depressurizing the surrounding room.

In the aforementioned investigations, TI was obtained using internal IRT based on the surface temperature of spots around the areas of thermal anomalies to infer potential conclusions about the building envelope thermal performance. However, in practice, internal IRT may disturb building programming (occupant activities) and is a cumbersome procedure. Furthermore, temperature measurement based on spots informs only the relative comparison of a particular thermal anomaly at different areas and does not indicate the overall thermal performance of a building envelope assembly compared to others. Hence, a rapid metric (i.e., index) which considers the overall impact of all sources of heat losses such as an opaque wall, windows, doors, thermal bridge, air leakage, and defects (entire surface of an envelope) based on external IRT is required for relative

quantitative comparison of the entire building envelope. It should be noted that the development of a ranking metric could serve as a good indicator for policymakers, homeowners, home inspectors, and property managers to compare thermal performance of building envelope assemblies of various buildings on a regional or portfolio scale for prioritization of energy retrofit strategies.

3.3.3 Quantitative IRT

In the hopes of creating less invasive and more accurate quantitative measurements, researchers have developed methodologies that utilize infrared cameras as a means of data collection to quantify thermal anomalies, measure in-situ U-value, determine dynamic characterization of building elements, estimate linear thermal transmittance (psi-value), evaluate insulation effectiveness, and identify moisture ingress [19]. These methodologies study the subject under in-situ conditions (passive thermography), in contrast to active thermography which utilizes an external thermal stimulus [48]. Passive thermography has the advantage in that it can be employed to inspect the entirety of the building envelope quickly and has also shown promise as a potential candidate for automation [49].

IRT surveys are performed both from the interior and exterior; typically indoor IRT results are more acceptable than external IRT due to reduced climatic fluctuations and unknown thermal reflections from the surroundings, and relatively mitigated air movement implying a only minor variations in convective heat transfer coefficient [11,19,33]. Theoretical and measured U-values have been shown to deviate between 10-60% for external thermography compared to a range of only 2-12% for internal thermography [33]. Danielski and Fröling [50] also demonstrated an improved indoor infrared thermography method for determining U-values that produced results with only a 4% difference from standardized HFM measurements, suggesting that the two methods could be equally effective in 1-D measurements, and that the thermography approach is more appropriate given its ability to record measurements of the entire wall segments (2-D) yielding more representative results. However, Dall'O' et al. [28] and Albatici et al. [29] stated that the deviation between measured data and theoretical values in external IRT could exceed 50%, depending on wind speed and assembly construction. Although the stability of indoor conditions in indoor IRT can help practitioners obtain more precise results, current methodologies in literature suggest it is possible to estimate the U-value of a building element, and in turn estimate heat loss

through it utilizing an external thermographic survey and accompanying internal temperature measurement of the walls' surface or internal air temperature. This leads to the potential of creating a strictly external thermographic survey methodology auditing the entire building envelope in a short period of time. Consequently, development of this kind of external IRT technique facilitates future utilization of unmanned aerial vehicles (UAVs) equipped with infrared cameras for conducting large-scale quantitative surveys in a fraction of the time without the need for current intrusive methods.

Currently, infrared camera technology touts temperature sensitivity as low as 30 mK, which is often misinterpreted as the accuracy of the surface temperature estimate produced by the system as a colourized image. Thermographic sensors have built-in computers that interpret the signal received as a temperature using a simple radiometric model based on the subject's emissivity, the surrounding ambient temperature reflected off the Gray Body subject, and the subject's emitted radiation [51-54]. These parameters have been shown to greatly influence the temperature estimate, and if not properly measured and compensated for, can result in an error in estimated U-value on the order of 100% due to a surface temperature measurement error of only 1°-3°K [26,31]. Additionally, environmental parameters such as solar irradiation, sky condition, wind, and moisture could have a substantial effect on the accuracy of thermographic readings. Recently conducted studies have led to the establishment of a handful of best practices for thermographic surveys to improve the accuracy of results by reducing noise [19, 55-56]. Recommended solutions to obtain more reliable data are 1) performing the tests in stable weather [28-29, 57]; (2) avoiding IRT surveys during rainy and sunny days [14, 29]; (3) calculating the convective heat transfer coefficient based on average wind speed [28, 58]; (4) considering compensation parameters such as emissivity and reflected temperature [26-29]; (5) using the IR camera to measure surface, indoor and outdoor temperature to minimize the systematic error [29, 59] ; (6) conducting a sensitivity analysis to analyze the impact of radiation and boundary conditions on the results [26, 28-29]; and (7) ensuring temperature differences of at least 10-15°K between the interior and exterior to allow sufficient heat flux through the element [26-29]. Moreover, it was suggested to select the region of interest (ROI) in the centre of thermal images due to profound vignetting artefacts, where temperature around the image perimeter appears colder than the actual surface temperature [59]. Furthermore, long-lasting surveys and averaged data were more reliable than short-term surveys due to a normalization of weather variations. In general, a short-term survey may not represent the

actual performance of a building if the boundary conditions are not steady [19]. Due to these weather stability challenges, a number of research studies have measured U-value in controlled environments such as climate chambers or Guarded Hot Boxes [5, 11, 60].

A few investigations have devoted attention to the development of IRT methodologies to quantify the contribution of thermal bridges on measured U-values. In these studies, the variations in U-value due to thermal bridging were mainly determined based on the calculation of heat flux, linear thermal transmittance (psi-values) and incidence factor of thermal bridging [5, 60-62]. The incidence factor is defined as the ratio between heat flux due to the influence of thermal bridging and the theoretical one-dimensional heat flux without thermal bridging [11, 61]. The IRT methodology in these studies was based on an analysis of a line of pixels with and without a known thermal bridge. In other words, the contribution of thermal bridging to the deviation of U-value was based surface temperature of each pixel on a line selected by researchers [11, 62]. Therefore, the 2D and 3D effect of thermal bridging were not necessarily accounted for. Building on these limitations, a few recent studies have attempted to quantify the 2D effect of thermal bridging in U-value measurements using IRT. For instance, Tejedor et al. [11] used internal IRT in a climate chamber to create a 2D U-value map for an entire façade of three common construction solutions in Southern European countries. The walls had different levels of thermal anomalies such as air void and gaps, defects with different depths, and large horizontal internal thermal bridges. The findings of this research facilitated a better and more accurate diagnosis of thermal bridging by measuring U-value at any point in the wall surface, as well as determining the average 2D U-value of facades by considering the effect of thermal anomalies. Mahmoodzadeh et al. [59] conducted an external IRT on three wood framed wall assemblies commonly found in buildings constructed in Canada to determine the U-value by considering the effect of repeated thermal bridging such as studs and attachment components. The U-values were determined by averaging the surface temperature of ROIs in thermal images, where the size of ROIs in the analysis closely corresponded to the size of simulated models (1220×813mm). The results indicate measured U-values were comparable with the results of the 3D simulation, which differed by -11.53% to 10.00%. It was also concluded that due to the low level of lateral heat flux of wood framing (thermal bridging), external IRT could be a reliable method for quantification of U-values with thermal bridging in these wall assemblies. Although the 2D effect of thermal bridging was identified in previous studies, in-situ measurements utilizing external IRT for the purposes of

estimating overall U-value including all thermal bridging details (*effective* U-Value) such as intersections of wall-roof, window-wall, wall-floor, and corners is missing in literature. It should be noted that correct interoperation of thermograms requires an understanding of temperature distribution, test conditions and thermal image artefacts (ie. non-uniformity and vignetting) [59]. Therefore, employing external IRT in-situ to determine overall effective U-value requires further investigation.

The importance of estimating U-value in-situ from an energy perspective was also investigated by researchers. For instance, a study of 77 new buildings in Sweden showed that energy data was on average 20% higher than simulations suggested. It was found that this deviation can be explained by simulations that used design U-values rather than in-situ measurements (actual values) [50]. A study by Francis et al. [63] to evaluate the energy performance of dwellings with solid walls in the UK indicated that using assumed U-values instead of actual U-value can result in underestimation of annual space heating demand by 16%. A few recent studies have tried to incorporate the results of IRT into a building energy model to study the sensitivity of in-situ measurements on the accuracy of models. For instance, Bayomi et al. [10] conducted a survey with an infrared camera mounted on a UAV to determine the U-value of the building envelope for input to a building energy model. It was found that the goodness of fit, a statistical index defined by ASHRAE Research Procedure 1051 for evaluating the accuracy of simulation results, was improved from 21.8% to 0.9% for the calibrated energy model when the U-value determined by IRT was used. Benhmidou et al. [64] used the in-situ IRT U-value to simulate energy consumption of an existing building in Tangier (North of Morocco) and compared it with a reference model that used nominal U-values. The results showed that the reference model underestimated the energy consumption of the building, citing that heating and cooling loads were 44.47% and 48.21% lower than the model that used the in-situ U-value, respectively. It follows from literature that using IRT for energy model inputs can result in better estimation of building energy performance, and consequently more accurate conclusions about the economics of potential envelope retrofits. However, these studies neglected to account for the effect of all thermal bridging (*effective* U-value), which may result in substantial deviations in the accuracy of building energy models.

3.3.4 Problem statement and research objectives

The extensive literature review indicated that (1) qualitative IRT have been widely used to determine the source of thermal anomalies in building envelope, (2) the relative comparison of thermal irregularities severity in thermographic images were performed based on surface temperature of spots using temperature index, (3) quantitative IRT methodologies have been mainly performed to estimate U-value of a wall assembly without thermal bridging effects and how they compared with nominal design values, and (4) a few recent studies have attempted to quantify the contribution of thermal bridges in U-value measurement of wall assemblies in European construction practice using a climate chamber. However, it was found that in-situ estimation of effective U-value of a whole opaque wall using external IRT that comprehensively accounts for the effects of all thermal bridges (studs, wall-roof interface (parapet), window frame and corners) were not investigated yet. Also, previous studies have neither evaluated the effects of thermal imaging artefacts such as vignetting on the determination of U-value and its influence on the accuracy of building energy models, nor has a practical approach been developed to address or correct for this issue. Finally, quasi-quantitative comparisons of an entire building's vertical envelope thermal performance using external IRT has not been investigated.

To address the current gap in the literature, this study aims to assess the use of external IRT for determining the overall effective U-value of four insulated wood-framed wall assemblies typically found in Canada while introducing some practical techniques to improve the accuracy of measurements. U-values obtained with the IRT methodology are validated using the 3D finite element analysis software, Siemens NX [65]. Furthermore, the impact of estimated U-values on the accuracy of building energy models is examined. Finally, an infrared index (IRI) based on external IRT is introduced, as a metric that can help to rapidly evaluate and rank building envelope thermal performance. The findings of this research will help practitioners, energy auditors, and thermographers arrive at more sound conclusions. Figure 1 below summarizes how IRT can be used in the context of the built environment.

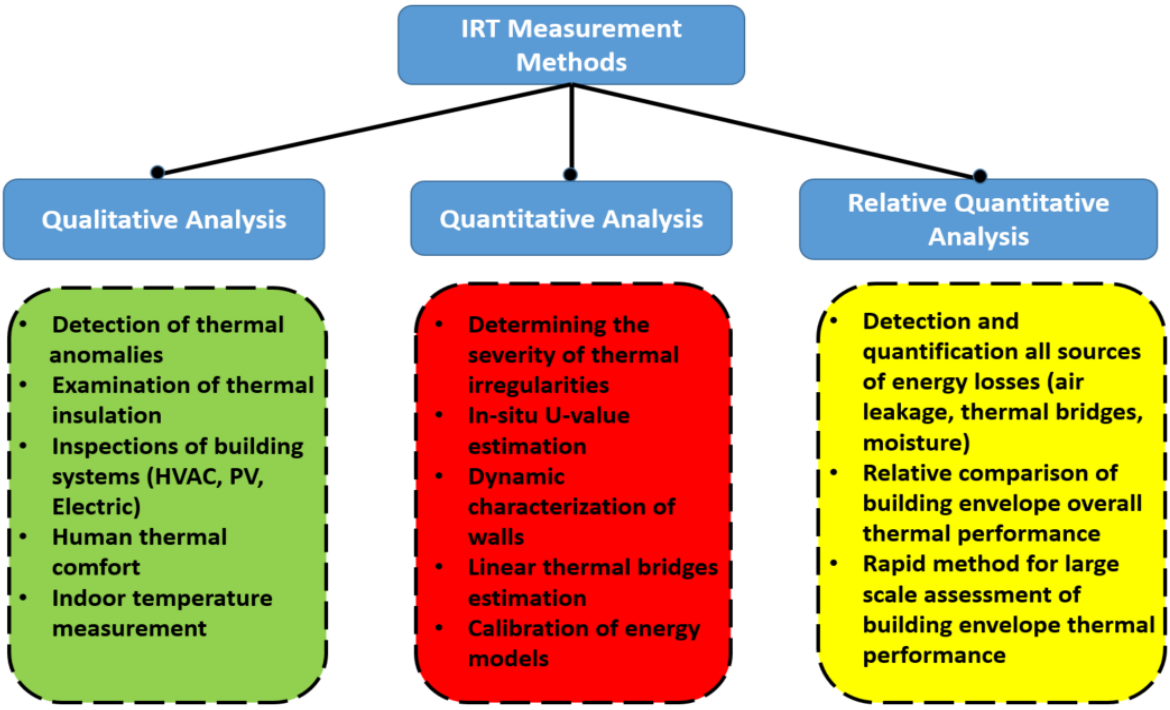

Figure 3.1 Application of IRT in Buildings

3.4 Research method

3.4.1 Case study

The overall thermal transmittance coefficients measurement was carried out on a wood-framed test structure adjacent to an existing conditioned campus building at the University of Victoria, Victoria, BC, Canada. The structure was constructed on pier blocks instead of a typical foundation slab and has an area of 9.30 m^2 and a ceiling height of approximately 3.05 m. It consists of four different rain-screen wall assemblies (W1, W2, W3, and W4), shown in Figure 3.2, which are representative of low-rise Canadian west-coast construction. The plan view and cross-section of the structure are shown in Figure 3.3 and Figure 3.4, respectively. Highly insulated floor and roof assemblies (RSI-8.8) facilitate a better comparison of the different wall assemblies' thermal performance. An air gap of 19 mm exists behind the cladding due to mimic building code requirements for exterior walls in climate zones with high rain load, effectively improving drying potential of moisture that penetrates beyond the cladding. The components and material properties of the wall assemblies are described in Table 3.1.

W1, W2, W3, and W4 are facing East, North, South and West, respectively. Other than W1 which has an entrance door (2 m^2 & U= 2.5 W/m^2 K), other walls each incorporate a double-glazed window with fiberglass frame (0.16 m^2 & U=1.59 W/m^2 K). It should be noted that W1 & W3 are facing the adjacent building while W2 and W4 are facing outdoor parking areas.

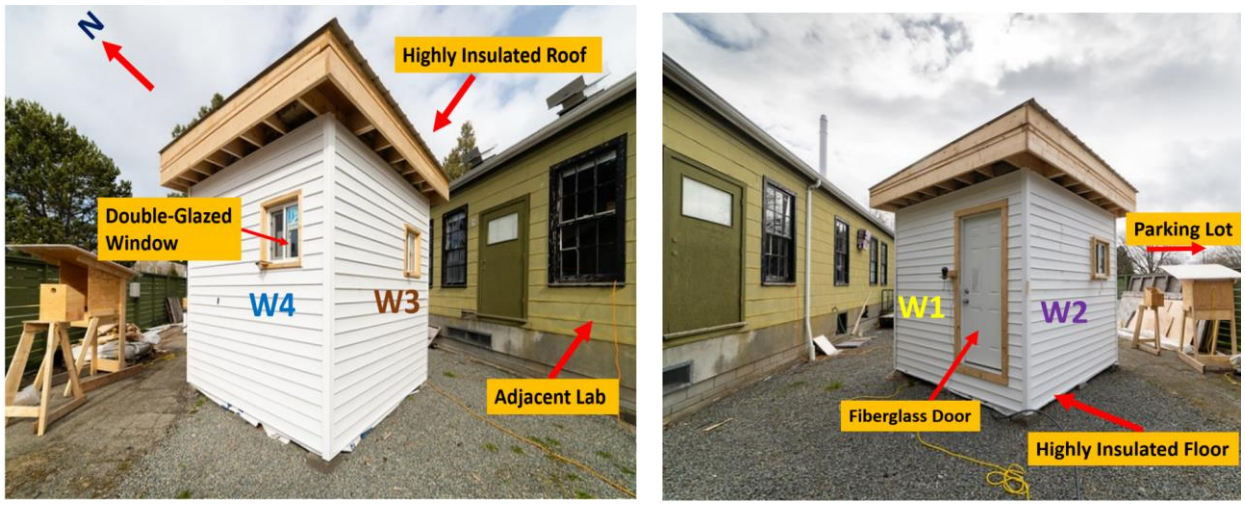

Figure 3.2 The experimental structure

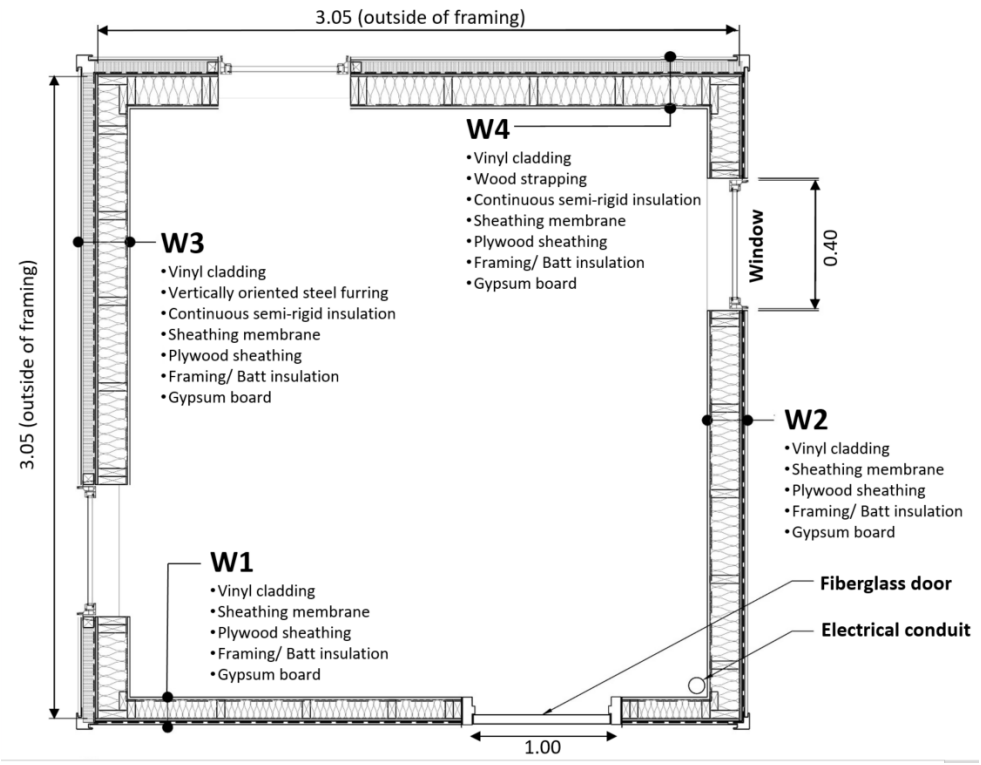

Figure 3.3 Plan of the experimental structure (dimensions in metres)

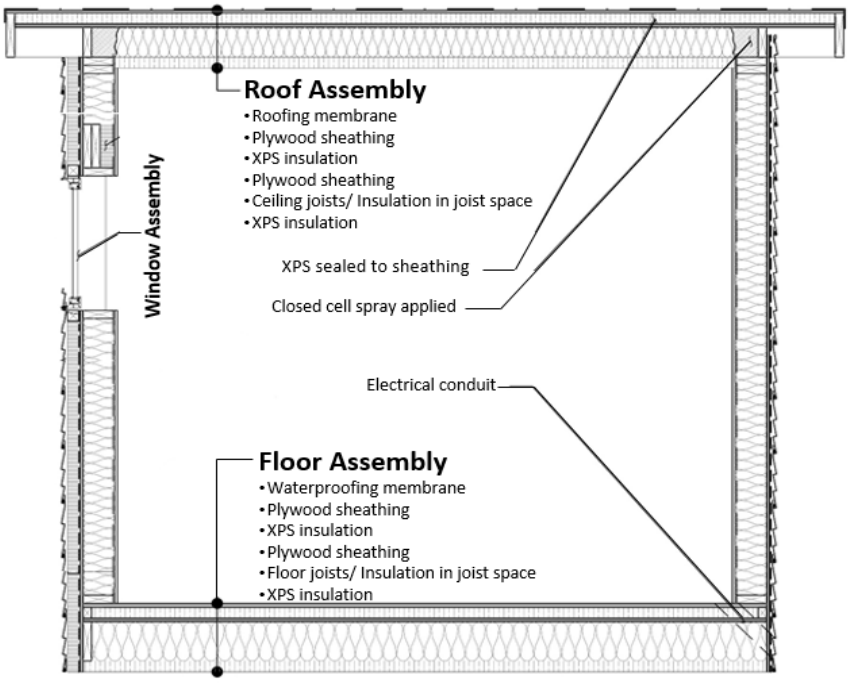

Figure 3.4 Cross-section of the experimental structure

Table 3.1 Thermophysical properties of wall assemblies

Wall type	#	Component	Thickness (mm)	Conductivity (W/m K)	RSI-value (m^2 K/W)	3D Sketch
W1		Interior film	-	-	0.12	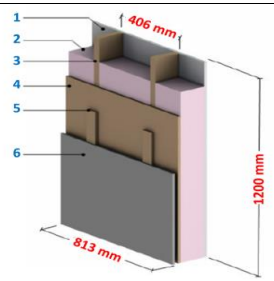
	1	Gypsum Board	13	0.16	0.08	
	2	Fiberglass Batt Insulation	89	0.036	2.47	
	3	2 × 4 wood stud	89	0.10	-	
	4	Exterior plywood sheathing	13	0.10	0.13	
	5	1 × 3 wood strapping	19	0.10	-	
	6	Vinyl Cladding with 19mm vented airspace incorporated into exterior heat transfer coefficient				
		Exterior film	-	-	0.12	
		Nominal RSI-value (m^2 K/W)	**2.92**			
W2		Interior film	-	-	0.12	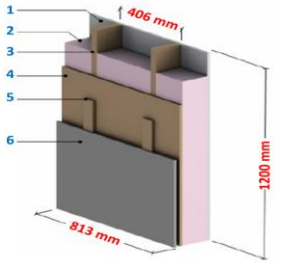
	1	Gypsum Board	13	0.16	0.08	
	2	Fiberglass Batt Insulation	140	0.036	3.89	
	3	2 × 6 wood stud	140	0.10	-	
	4	Exterior plywood sheathing	13	0.10	0.13	
	5	1 × 3 wood strapping	19	0.10	-	
	6	Vinyl Cladding with 19mm vented airspace incorporated into exterior heat transfer coefficient				
		Exterior film	-	-	0.12	
		Nominal RSI-value (m^2 K/W)	**4.34**			
W3		Interior film	-	-	0.12	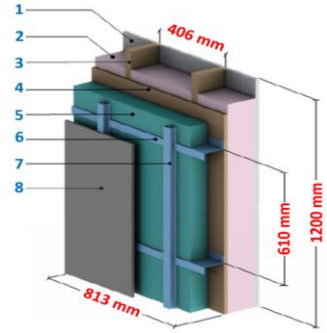
	1	Gypsum Board	13	0.16	0.08	
	2	Fiberglass Batt Insulation	140	0.036	3.89	
	3	2 × 6 wood stud	140	0.10	-	
	4	Exterior plywood sheathing	13	0.10	0.13	
	5	Exterior insulation	50	0.028	1.79	
	6	Horizontal Z-Girt with 1 1/2” Flange	18 Gauge	62	-	
	7	Steel Furring Hat Track	18 Gauge	62	-	
	8	Vinyl Cladding with 19mm vented airspace incorporated into exterior heat transfer coefficient				
		Exterior film	-	-	0.12	
		Nominal RSI-value (m^2 K/W)	**6.13**			
W4		Interior film	-	-	0.12	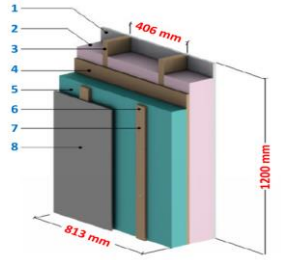
	1	Gypsum Board	13	0.16	0.08	
	2	Fiberglass Batt Insulation	140	0.036	3.89	
	3	2 × 6 wood stud	140	0.10	-	
	4	Exterior plywood sheathing	13	0.10	0.13	
	5	Exterior insulation	50	0.028	1.79	
	6	Wood strapping	38	0.10	-	
	7	#14 steel fastener	11	50	-	
	8	Vinyl Cladding with 19mm vented airspace incorporated into exterior heat transfer coefficient				
		Exterior film	-	-	0.12	
		Nominal RSI-value (m^2 K/W)	**6.13**			

3.4.2 Measurement setup and data acquisition procedure

The equipment for this study included an IR camera, an oil-filled electric radiant heater, a metered power usage data logger, temperature sensors integrated with a data logger, and an anemometer to measure wind speed. All equipment was calibrated before the tests according to manufacturers' specifications. The infrared thermal camera model was a FLIR A65, with a 640 × 512 pixel focal plane array detector, 1.31 mrad geometric resolution, and a reported accuracy of 5ºC. Its spectral range was 7.5–13 µm, had a reported Noise Equivalent Temperature Difference (NETD) < 0.05 K at 30 ºC, and had been calibrated against a blackbody by the manufacturer. Since the reported uncertainty of the IR camera by the manufacturer is based on lab conditions while this study is based on external IRT, the calibration of IR camera was further examined in outdoor environmental conditions by comparing the IRT measurement with a highly accurate temperature sensor. Accuracy of measurements with the IR camera were higher than those of the temperature sensor on average and were within the range of the camera's accuracy of 5°C, confirming camera calibration. The calibration process is explained elsewhere by Mahmoodzadeh et al. [59].

The structure is heated with the portable oil-filled electric radiant heater, and the total power usage associated with the heater was metered at 1-minute intervals. The surrounding environmental conditions were continuously monitored and recorded during and prior to the tests by data loggers, temperature sensors and anemometers. Since wind direction and intensity are not identical at different wall orientations, the wind speed for each wall was measured independently. An anemometer was positioned 1.5 m above grade and 0.1 m away from the wall exterior surface, and measured local wind speed in the vicinity of the exterior surface accurate to ±0.1 m/s. Temperature sensors accurate to ±0.01ºC and were positioned at different locations, both indoors and outdoors, to evaluate the variation of temperatures in the vicinity of the walls. To appreciate variations in indoor air temperature spatially, sensors were located at three different heights from the floor (0.5, 1.5, and 2.5 m) in three columns, forming a grid of 9 measurement locations per wall as shown in Figure 3.5.

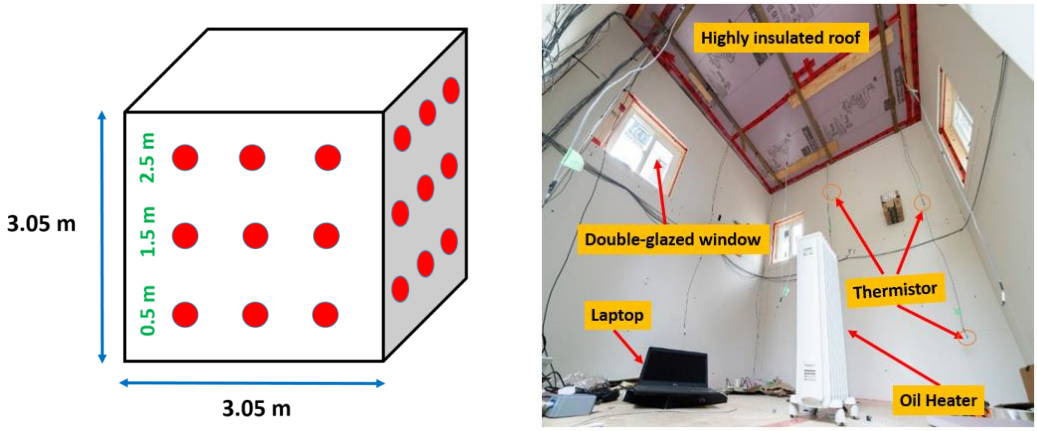

(a) (b)

Figure 3.5 (a) Schematic depiction of thermocouple locations (b) image of the interior

Two criteria were considered in positioning the IR camera; (1) having the walls fully in the field of view, and (2) obtaining a minimum spot size ratio of 18 mm for detection of gross thermal patterns around insulation, thermal bridging components, and air leakage [59, 66]. To this end, the IR camera was placed on a tripod perpendicular at a distance of 5m from the wall, achieving a spot size ratio of 6.5 mm (Figure 3.6). Surveys were performed based on instantaneous IRT and weather conditions were quite stable thus steady-state conditions were reasonably approximated (cloudy sky, no precipitation, low wind speed <1 m/s, and temperatures were constant). This allowed for U-value and infrared index of the walls to be comparatively analyzed, since boundary conditions were similar in all cases.

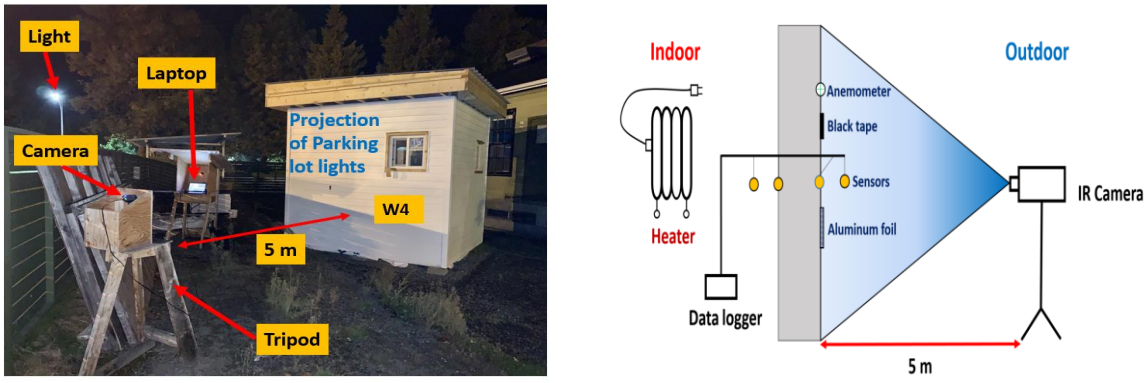

(a) (b)

Figure 3.6 Experimental set-up; (a) In-situ, (b) Schematic

To validate the methodology, tests were performed on different days with varying exterior and interior conditions outlined in Table 3.2. Environmental factors such as solar radiation, wind speed, rain, sky conditions, and temperature gradient were monitored before and during the IRT surveys. The structure was not exposed to rain or snow 48 hours prior to the tests and the sky was cloudy before (~ 12 hours) and during the tests. Indoor air temperature was approximately constant before and during the tests (within ~2 ºC tolerance of the thermostat deadband), and variations in outdoor temperature about 3-4 hours prior the test were less than 0.5ºC and held constant during the tests. It should be noted that since the indoor temperature at different heights varied due to natural convection (stack effect), overall average indoor air temperature at the time of survey was considered and reported in Table 3.2. Relative humidity was measured hourly at the local weather station (University of Victoria) which is made publicly available by the Government of Canada [67]. The average free stream wind speed during the day and the during test were also recorded. The tests were performed in the late evening on an overcast night (almost 6 hours after sunset) to minimize the effect of solar and night-sky radiation, and to minimize thermal mass effects. IR thermograms were recorded at 1-second intervals.

Table 3.2 Environmental conditions of tests

Boundary conditions	**Day 1**	**Day 2**	**Day 3**	**Day 4**	**Day 5**
Outdoor Temperature (°C)	5.50	6.22	7.00	4.61	3.13
Outdoor air relative humidity (%)	85	82	80	83	80
Wind speed (m/s)	0.31	0.23	0.10	0.12	0.71
Sky condition	Cloudy	Cloudy	Cloudy	Cloudy	Cloudy
Average Indoor Air Temperature (°C)	22.56	22.52	22.50	25.53	23.56

3.4.3 Surface temperature measurement

To obtain an accurate surface temperature measurement with an IR camera, accurate values of ambient air temperature, relative humidity, atmospheric transmittance (τ), reflected apparent temperature, and emissivity should be determined during the post-processing of thermal images [68]. The atmospheric transmittance depends on infrared wavelength, the distance of the IR camera

to the target, relative humidity and ambient air temperature. Infrared radiation that propagates through the air is absorbed by various particles such as O_3, CO_2, and H_2O. However, infrared energy absorption by the atmosphere varies by wavelength. For instance, wavelengths of 5-7μm are almost entirely absorbed by the atmosphere. However, mid-wave (2-5μm) and long-wave (8-14μm) radiation is not well absorbed by the atmosphere, allowing more infrared energy to reach the sensor of the camera. Since the range of measured temperatures in this study was low (long-wavelength band), the absorption of long-wavelength radiation by IR camera is high considering the specifications of camera [68]. Furthermore, to incorporate the effect of atmosphere's temperature and relative humidity, and the effect of the distance between the target and camera on atmospheric transmittance (τ), the following formula was used by FLIR in the internal camera algorithm [69]:

$$\tau(d,w) = K_{atm}.\exp\left[-\sqrt{d}\left(\alpha_1 + \beta_1\sqrt{w}\right)\right] + (1 - K_{atm}).\exp[-\sqrt{d}\left(\alpha_2 + \beta_2\sqrt{w}\right) \quad (3.1)$$

$$w(w\%, T_{atm}) = w\%.\exp(h_1 + h_2.T_{atm} + h_3.T^2{}_{atm} + h_4.T^3{}_{atm}) \quad (3.2)$$

where, ω is the coefficient indicating the content of water vapor in the atmosphere, w% is relative humidity, d is distance, K_{atm} is the scaling factor for the atmosphere damping (K_{atm} = 1.9), α_1 and α_2 are attenuation factors for atmosphere without water vapour, β_1 and β_2 are attenuation factors for water vapour, and h_1=1.5587, h_2=6.939×10^{-2}, h_3=-2.7816×10^{-4}, and h_4= -6.8455×10^{-7}. With the environmental conditions during the tests and a relatively short distance between the IR camera and the targets, the atmospheric transmission (τ) was almost equal to 1 in each test. It is to be noted the coefficients in the above equations were obtained based on experimental studies, which may not be similar to the conditions of this study. However, since the distance between camera and target was relatively short, deviations in these coefficients have a negligible impact on the atmospheric transmittance.

The reflected apparent temperature and emissivity (ranges from 0 to 1) were determined with the IR camera. It is to be noted that the emissivity of a material surface changes at different wavelengths, depending on the temperature of object, conditions of surface, and the inclination between IR camera and surface. Reflected apparent temperature is regarded as the apparent temperature of surrounding objects which was determined based on the method suggested by ASTM E1862 [70]. Since the orientation of each wall and its surrounding environment is different, the reflected apparent temperature was measured for each wall separately. To estimate the

emissivity, a sample of 3M Scotch Super 88 Vinyl black electrical tape with a known emissivity value equal to 0.95 ± 0.02 was used following ASTM E1933 procedures [71]. It is to be noted that the emissivity of material is nearly independent of the ambient and material temperatures expected during building inspections. Furthermore, according to the Ref [72], the emissivity of materials remains constant in the range of 0°C to 48°C. To ensure accuracy, several measurements were performed, and the emissivity was estimated using the average of values.

Window glass is opaque in the long-wave IR range (4-14μm) and the insulated glass unit (IGU) has relatively lower thermal mass than the opaque building materials [73]. Consequently, the time for windows to achieve quasi stead-state conditions is significantly shorter than the opaque components. However, glass emissivity is lower than most opaque building materials, which ranges from 076 to 0.87 depending on the type of window materials and accuracy of sensors and the camera [73]. Also, since glass has specular reflections, emissivity measurement by IRT surveys are more influenced by surrounding radiation than opaque elements [73]. Furthermore, the reflection of the IR camera and thermographer as well as the incident angle can influence the accuracy of measurements. In this study, the W2 window was selected to determine the emissivity of glass since it was less exposed to the surrounding environment than other windows, namely adjacent buildings and parking lights. Ref [73-74] suggested that both reflectance and emissivity of glass remain almost constant for an incident angle under 45°. Therefore, to measure the emissivity of glass, the IR camera was positioned at the distance of 2 m from the outer surface of glass and thermal images were taken at different angles, including in front of the glass as well to either side of the glass within 45°, shown in Figure 3.7. For each direction, the emissivity and reflected temperature was measured according to ASTM E1862 and ASTM E1933, respectively. The mean of measured values (0.85) was obtained as emissivity of the window.

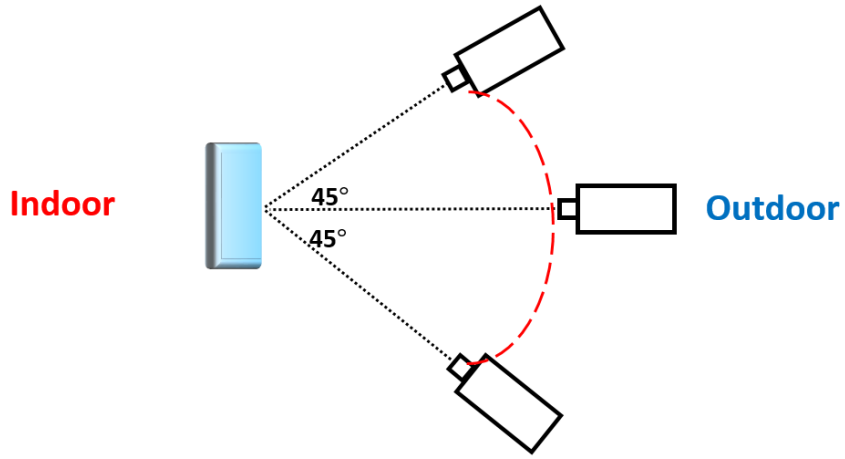

Figure 3.7 Schematic of window emissivity measurement at different incident angles

Finally, to eliminate the impact of systematic error on U-value estimation, it is suggested to acquire as much data as possible with the same instrument [29, 75]. Hence, apart from emissivity, reflected temperature and surface temperature, outdoor air temperature was also measured with the IR camera. In other words, the large uncertainty (±5°C) of the IR camera compared to the thermistors (±0.01°C), as well as differences in their methods of measurement (non-contact & 2D temperature measurement vs. contact & point measurement), would result in different outdoor air temperature measurements and subsequent error in estimation of U-value [59]. To this end, a piece of cardboard (10cm × 10cm) with an emissivity of 0.95 was positioned near the wall exterior surface 2-3 hours before the tests to ensure it reached thermal equilibrium with the environment. Since outdoor environmental conditions vary over time, the measurement was performed when the variations were minor prior to the tests (~3-4 hours) and were relatively consistent at the time of survey. Consequently, outdoor air temperature was estimated by measuring the surface temperature of cardboard using instantaneous IRT [59].

Besides the impacts of the above-mentioned parameters on surface temperature measurements with IR cameras, uncertainties associated with the IR camera detector (composed of an uncooled microbolometer) were also considered in the analysis. The gain and offset of pixels in the detector are not identical due to camera temperature instability and ambient condition variability during the thermographic survey, as well as errors associated with manufacturing [59]. In general terms, the microbolometers also receive radiation from the camera's interior, which can be considerably higher than radiation from the objects, ultimately resulting in severe non-uniformity artefacts (a

low-quality image). To improve the accuracy and reduce non-uniformity, the camera takes an image with the shutter closed and measures the IR radiation from its own optics [76]. The temperature of the shutter acts as a reference value for correcting images and is assumed to have a similar temperature with other IR camera components such as lens and optics [76]. This process is called Non-Uniformity Correction (NUC) andensures a harmonized response signal across the sensors. NUC functionality can be performed automatically by the camera itself or manually by a thermographer. It is worth noting that these non-uniformities are present more often when the camera is first powered up and attempting to achieve temperature stability. Therefore, it is recommended to avoid thermography for the initial ~30 minutes to allow the camera to warm up in a stable environment to obtain the best temperature measurement accuracy [77]. To reduce uncertainties in this study, all surveys were started after a 30-minute camera warm-up period and NUC was performed manually before recording thermal images.

3.4.4 Overall effective U-value measurement with IRT

The overall thermal transmittance of wall assemblies was estimated by assuming that the heat flux is passing through the elements, and transferred to the IR camera sensors through radiation q_r (W/m^2) and convection q_c. Accurate calculation of radiation heat flux necessitates considering the view factor of all surrounding objects and their temperatures in the field of view of the wall assembly being studied as shown in Equation 3.3 [78].

$$q_r = \varepsilon\sigma[F_{sky}\left({T_{s,avg}}^4 - {T_{sky}}^4\right) + F_{ground}\left({T_{s,avg}}^4 - {T_{ground}}^4\right) + F_{air}\left({T_{s,avg}}^4 - {T_{air}}^4\right) + F_{object-1}\left({T_{s,avg}}^4 - {T_{object-1}}^4\right) + F_{object-2}\left({T_{s,avg}}^4 - {T_{object-2}}^4\right) + \cdots \quad (3.3)$$

where F_{sky} is the view factor of the sky, F_{ground} is the view factor of the ground, F_{air} is the view factor of the ambient air, F_{object} is the view factor of surrounding objects, T_{sky} is the temperature of the sky (defined as the temperature that the sky exchanges heat via radiation as a black body), T_{ground} is the temperature of the ground, T_{air} is the temperature of ambient air, and T_{object} is the surface temperature of surrounding objects. The sum of all view factors is equal to 1.

$$\sum F_{sky} + F_{ground} + F_{air} + F_{objects} = 1 \quad (3.4)$$

Since experiments in this study were performed on overcast skies and ambient air temperature was stable several hours prior to the tests, it was approximated that temperatures of the sky [29], the ground [79] and surrounding objects are in thermal equilibrium with ambient air. Therefore,

radiation heat exchange of surfaces was assumed to be with the ambient air and view factor is equal to 1 [59].

In this study, the instantaneous U-value (W/(m^2 K)) was calculated using Equation 3.5:

$$U_{overall} = \frac{q_r + q_c}{T_{in} - T_{out}} = \frac{\varepsilon\sigma\left({T_{s,avg}}^4 - {T_{out}}^4\right) + h_c(T_s - T_{out})}{T_{in} - T_{out}} \quad (3.5)$$

where $T_{s,avg}$ is the average of surface temperature of the opaque wall including thermal bridging (parapet, corners, and window frame), T_{in} is the indoor air temperature (ºC), T_{out} is the outdoor air temperature in the vicinity of the target (ºC), ε is emissivity of wall, σ Stefan-Boltzmann constant (5.67×10^{-8}), and h_c is the convective heat transfer coefficient (W/m^2 K).

The surface temperature of the opaque wall was measured using combinations of different-sized ROIs to exclude window and doors from analysis. Thermal images in Figure 3.8 depicted the areas of thermal bridging and sources of air leakage in the wall assemblies. The average of surface temperature of ROIs was then determined based on an area-weighted approach:

$$T_{s,avg} = \frac{T_1 * A_1 + T_2 * A_2 + T_3 * A_3 + \cdots + T_i * A_i}{A_T} \quad (3.6)$$

where $T_{s,avg}$ is the average surface temperature of opaque areas, A_i is the area of ROI, T_i is the average of surface temperature corresponding to area A_i, and A_T is the collective area of all ROIs.

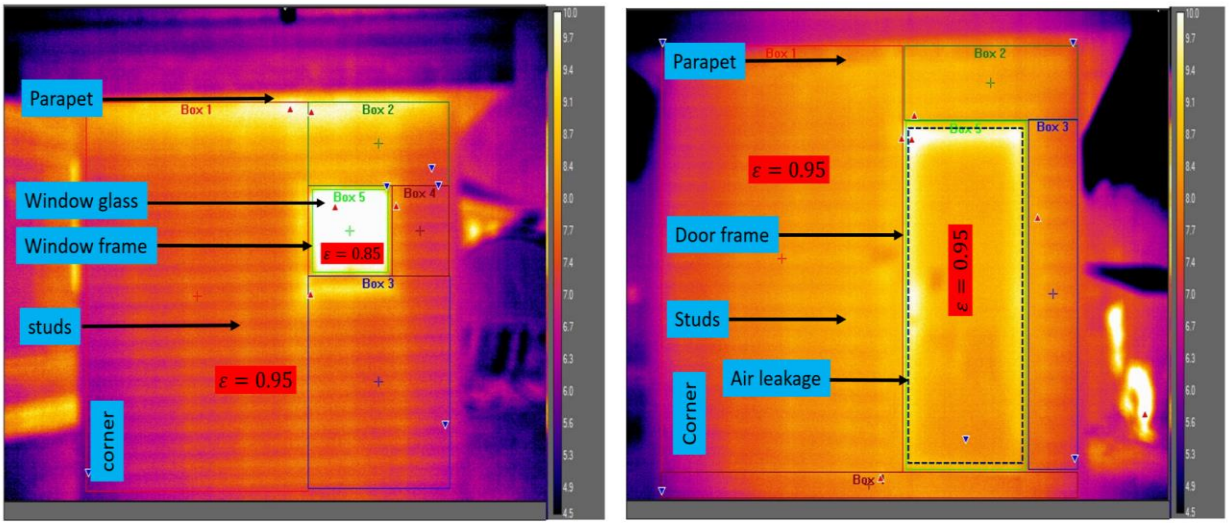

(a) (b)

Figure 3.8 Thermal images of (a) W2, (b) W1. Example ROIs are denoted "Boxes"

The convective heat transfer coefficient h_c was calculated based on the dimensionless method, which is a function of flow regimes, target geometry characteristics and air properties, calculated as shown in Equation 3.7.

$$h_c = \frac{Nu\ k}{L} \tag{3.7}$$

where *Nu* is the Nusselt number [dimensionless], *L* is the height of the wall (m) measured from the exterior, and *k* is the thermal conductivity of the fluid (air). For air at 5-10 ºC, *k* is 0.024 W/m K.

For laminar flow over a wall surface, *Nu* is determined by using the following equation:

$$Nu = 0.664\ Re^{1/2} Pr^{1/3} \qquad Pr > 0.6 \tag{3.8}$$

where (*Re*) and (*Pr*) are dimensionless Reynolds and Prandtl numbers. For air at 5-10 ºC, *Pr*=0.71 was used [59].

3.4.5 Infrared Index (IRI)

The Infrared Index (IRI) was obtained based on the approximation of a steady-state condition where the rate of heat flux from the interior to the exterior is equal to the heat flux from the exterior surface to the outdoor air (assuming one-dimensional heat transfer). IRI is expressed as:

$$IRI = \frac{T_{s,avg} - T_{out}}{T_{in} - T_{out}} \tag{3.9}$$

where T_{in} and T_{out} are indoor and outdoor air temperatures, and $T_{s,avg}$ is average surface temperature of whole vertical building envelope measured by external IRT. As shown in Equation 3.6, measured $T_{s,avg}$ is comprised of thermal effects from the opaque wall including thermal bridging, fenestration (windows & doors), air leakage, and any other imperfections in the wall assembly.

A flowchart describing the procedure to calculate U-value and IRI is illustrated in Figure 3.9.

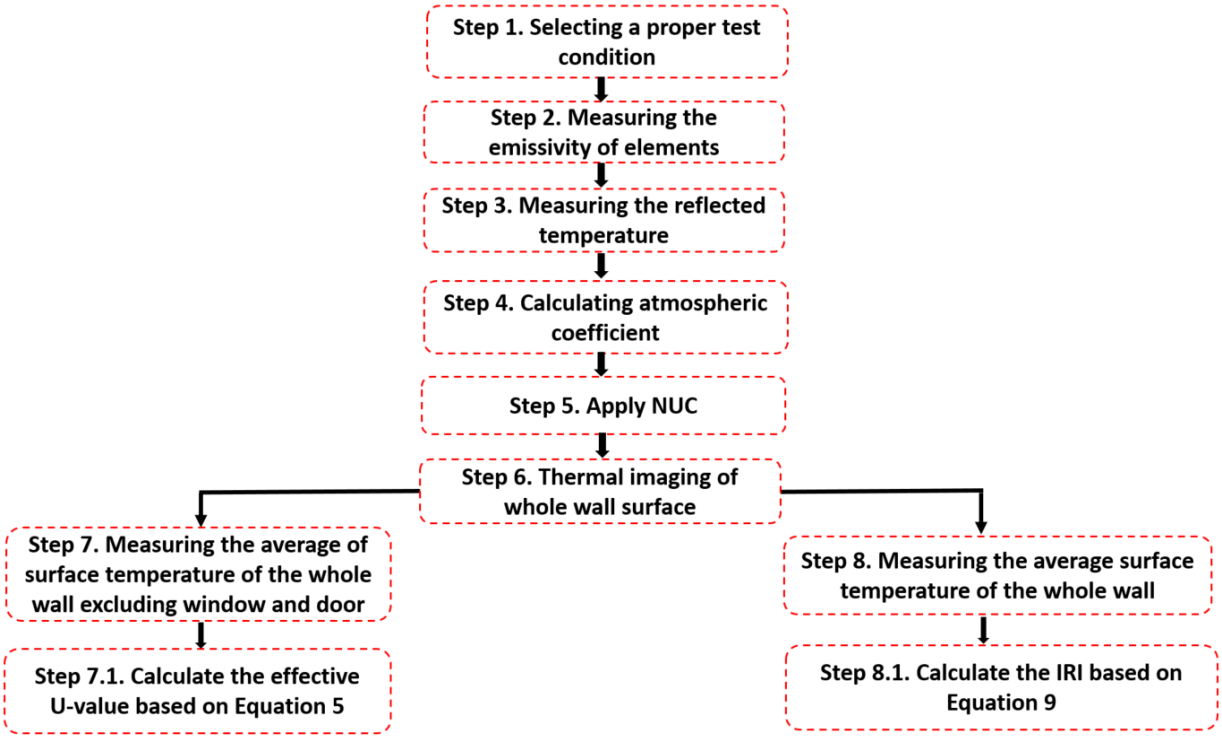

Figure 3.9 External IRT measurement procedure to determine U-value and IRI

3.4.6 Measurement uncertainty analysis on U-values and IRI

The U-value depends on several parameters, which was shown in Equation 3.5. The law of propagation of uncertainties was applied to determine the combined standard uncertainty of U-value based on all the measured parameters [64]. The uncertainty (ΔU) was then obtained using the following expression:

$$\Delta U^2 = \sum_{i=1}^{n} \left(\frac{\partial U}{\partial X_i}\right)^2 \Delta X_i{}^2 \tag{3.10}$$

$$\Delta U^2 = \left(\frac{\partial U}{\partial T_{in}}\right)^2 . (\Delta T_{in})^2 + \left(\frac{\partial U}{\partial T_{out}}\right)^2 . (\Delta T_{out})^2 + \left(\frac{\partial U}{\partial T_s}\right)^2 . (\Delta T_s)^2 + \left(\frac{\partial U}{\partial \varepsilon}\right)^2 . (\Delta \varepsilon)^2 + \left(\frac{\partial U}{\partial h}\right)^2 . (\Delta h)^2 \tag{3.11}$$

where ΔT_{in} is the uncertainty associated with indoor air temperature measuring equipment, ΔT_s, ΔT_{out} and $\Delta \varepsilon$ are the uncertainties associated with infrared camera, and Δh is the uncertainty in wind speed measured by the anemometer. The standard uncertainty of each variable (ΔX_i) was measured based on Type B uncertainty since no statistical treatment or repeated measurements analysis was performed. In other words, the data was not collected from a series of measurements, instead taken from manufactures' specifications. Furthermore, to convert manufacturer reported

figures to standard uncertainty, a rectangular probability distribution of possible values was considered for all parameters, implying that all outcomes have an identical chance to occur.

The uncertainties of all variables were considered based on the half-width of the uncertainty limit as shown in Table 3.3. The standard uncertainty of emissivity obtained was 0.02, similar to the black tape uncertainty that was used during measurements. The sensitivity coefficients ($\frac{\partial U}{\partial X_i}$) of U-value are presented in Table 3.4, where by multiplying the sensitivity of each variable by its standard uncertainty ($\frac{\partial U}{\partial X_i}.\Delta X_i$), the uncertainty contribution of each variable on the output (U-value) can be obtained.

Table 3.3 Uncertainties of equipment used for U-value measurements

Parameters	**Sensors**	**Uncertainty half-width limit** $\pm$
Wall surface temperature	IR camera	5 ºC
Outdoor air temperature	IR camera	5 ºC
Indoor air temperature	Temperature sensor	0.01 ºC
Wind velocity	Anemometer	0.1 m/s

Table 3.4 Sensitivity coefficients for the implementation of the law of error propagation in U-value estimation by using outdoor infrared thermography

Variable X_i	**Sensitivity coefficient $\frac{\partial U}{\partial X_i}$**
T_s	$\frac{h + 4.\varepsilon.\sigma.{T_s}^3}{T_{in} - T_{out}}$
T_{in}	$-\frac{\varepsilon.\sigma.\left({T_s}^4 - {T_{out}}^4\right) + h_c.(T_s - T_{out})}{(T_{in} - T_{out})^2}$

$\mathbf{T_{out}}$	$\frac{-\left(4.\varepsilon.\sigma.{T_{out}}^3+h\right).(T_{in}-T_{out})+[h_c.(T_s-T_{out})+\varepsilon\sigma\left({T_s}^4-{T_{out}}^4\right)]}{(T_{in}-T_{out})^2}$
$\boldsymbol{\varepsilon}$	$\frac{\sigma\left({T_s}^4-{T_{out}}^4\right)}{T_{in}-T_{out}}$
$\boldsymbol{h_c}$	$\frac{T_s-T_{out}}{T_{in}-T_{out}}$

Similar to U-value, sensitivity coefficients for IRI are shown in Table 3.5.

Table 3.5 Sensitivity coefficients for IRI estimation with external IRT

Variable X_i	Sensitivity coefficient $\frac{\partial IRI}{\partial X_i}$
$\mathbf{T_s}$	$\frac{1}{T_{in}-T_{out}}$
$\mathbf{T_{in}}$	$-\frac{T_s-T_{out}}{(T_{in}-T_{out})^2}$
$\mathbf{T_{out}}$	$\frac{T_s-T_{in}}{(T_{in}-T_{out})^2}$

3.4.7 Calculation of effective thermal transmittance (U-value)

The effective thermal transmittance (U-value) of walls were determined using Equation 3.12. To summarize this approach, the overall thermal transmittance comprised of three components:

(1) **Clear field transmittance** (U_o) is the heat flow from the wall assembly including the effects of uniformly distributed thermal bridging components, such as structural framing (studs), and structural cladding attachments.

(2) **Linear transmittance** (Ψ).is the additional heat flow caused by linear thermal bridging details including slab edges, corners, parapets, and transitions between assemblies.

(3) **Point transmittance** (χ) is the heat flow caused by thermal bridging details that occur only at a single or infrequent locations including building components such as structural beam penetrations and intersections between linear details.

$$U_{effective} = \frac{\sum(\Psi \cdot L)+\sum(\chi)}{A_{total}} + U_o \tag{3.12}$$

Where U_{Total} is total effective assembly thermal transmittance (W/m^{2}K), U_o is the clear field thermal transmittance (W/m^{2}K) which calculated from from 3D simulation values [42, 80], A_{total} is the total opaque wall area (m^2), Ψ is heat flow from linear a thermal bridge (W/m K) obtained from 3D simulation details in the BETB [42], L is the length of a linear thermal bridging detail as shown in Table 3.6 and Figure 3.10, and χ is a point source thermal transmittance (W/K). It should be noted that since the structure was constructed on pier blocks instead of a typical foundation slab, thermal bridging to the ground is negligible. Likewise, due to a lack of structural penetrations point source thermal bridges are effectively absent. Hence, the remaining thermal bridging recorded in the measurements are a result of the wall-roof interface (parapet), corners, window/door-wall interfaces, studs, and cladding structural attachment systems (girts). The overall thermal transmittance of wall assemblies in this study is shown in Table 3.7.

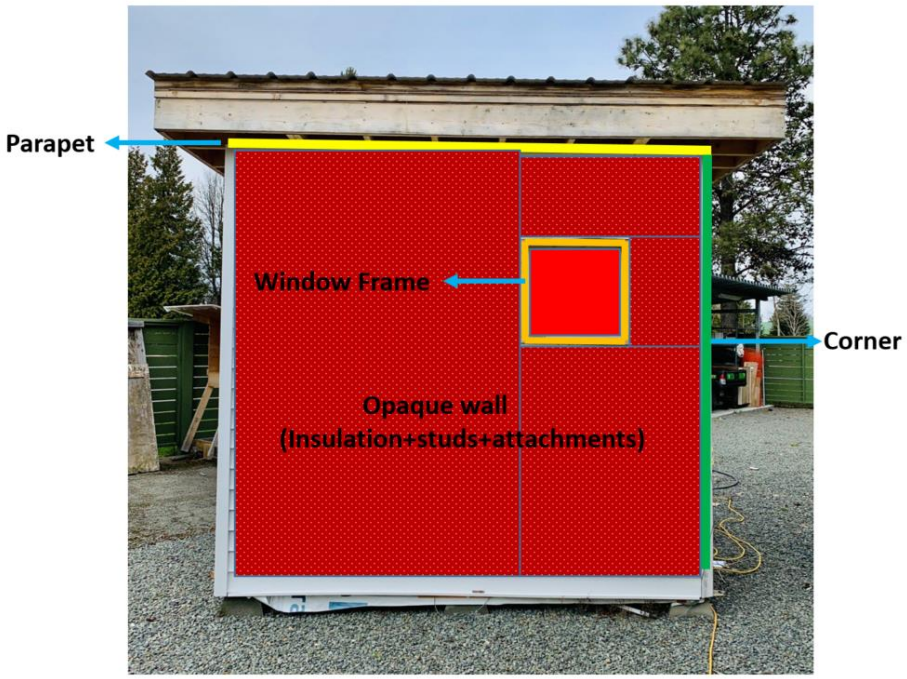

Figure 3.10 Example of structure thermal bridges length takeoffs

Table 3.6 Summary of linear thermal bridges

Thermal Bridge Type	Ψ-value (W/m K)	Length (m)	Heat Flow (W/K)
wall-roof interface (interior insulated walls)	0.05	3.05	0.09
wall-roof interface (exterior insulated walls)	0.08	3.05	0.15
window/door-wall interface (interior insulated walls)	0.001	1.6	0.38
window-wall interface (exterior insulated walls)	0.035	1.6	0.14
Corner	0.04	6.10	0.24

Table 3.7 U-values of walls

Wall Assembly	Nominal U-value ($W/m^2 K$)	Clear field U_0-value ($W/m^2 K$)	Effective U-value ($W/m^2 K$)
W1	0.34	0.37	0.43
W2	0.23	0.26	0.31
W3	0.16	0.20	0.26
W4	0.16	0.18	0.24

3.4.8 Dynamic energy model

An energy model was developed using EnergyPlus, which included inputs for U-value (walls, roof, window, door, floor), internal loads (a laptop), air leakage rate, and electric resistance heating. Building geometry was developed in SketchUp, integrated with an OpenStudio plug-in that translates information to EnergyPlus syntax. The building rendering is shown in Figure 3.11.

To assess sensitivity of IRT measurements on the energy model, three model scenarios were considered with different building envelope inputs:

- 1D U-values (without considering the impact of thermal bridging and attachment components) inferred from IRT measurements
- 2D effective U-values inferred by IRT
- 2D effective U-values inferred by IRT with vignetting artefact correction

Simulation outputs were compared against metered energy consumption. The energy modelling framework is illustrated in Figure 3.12.

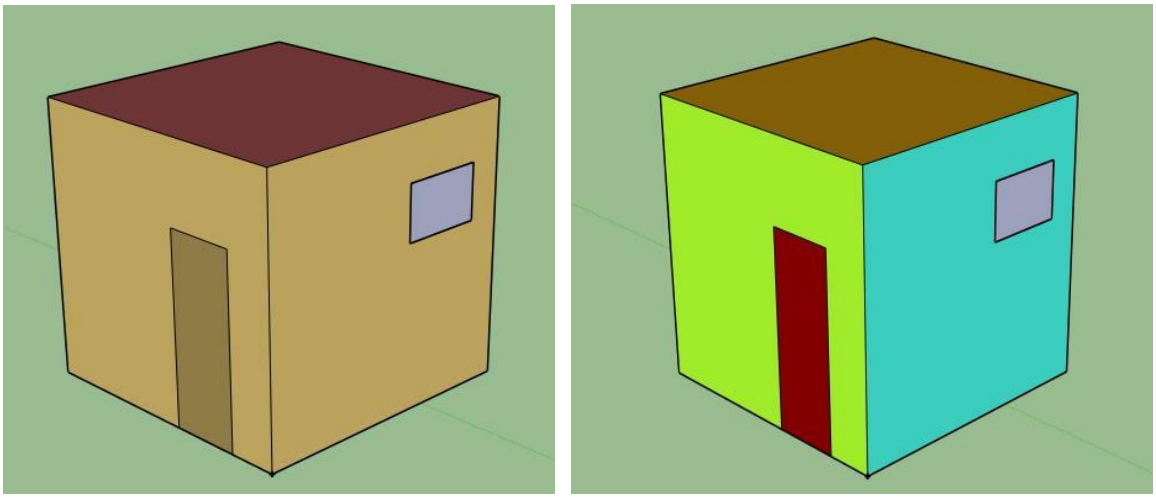

(a) (b)

Figure 3.11 SketchUp/OpenStudio renderings of the modeled structure based on: (a) thermal zone; (b) construction type

Accuracy of energy models were examined based on two statistical uncertainty indices (1) Normalized Mean Bias Error (NMBE), and (2) the Coefficient of Variation of the Root Mean Square Error (CVRMSE). These indices are defined by ASHRAE Guideline 14-2014 [81] for the calibration of energy models. Equation 3.13 shows the calculation of NMBE where m_i is the measured value, s_i is the simulated data, n is the number of measured data points, and p is the number of adjustable model parameters, which for calibration is suggested to be 0.

$$\text{NMBE} = \frac{1}{\bar{m}} \cdot \frac{\sum_{i=1}^{n}(m_i - s_i)}{n-p} \times 100\ (\%) \tag{3.13}$$

CV (RMSE) is obtained based on Equation 3.14, where the value of p is suggested to be 1.

$$\text{CV (RMSE)} = \frac{1}{\bar{m}} \sqrt{\frac{\sum_{i=1}^{n}(m_i - s_i)^2}{n-p}} \times 100\ (\%) \tag{3.14}$$

The model is then considered calibrated if NMBE and CVRMSE are less than $\pm$5% and 15%, respectively [40].

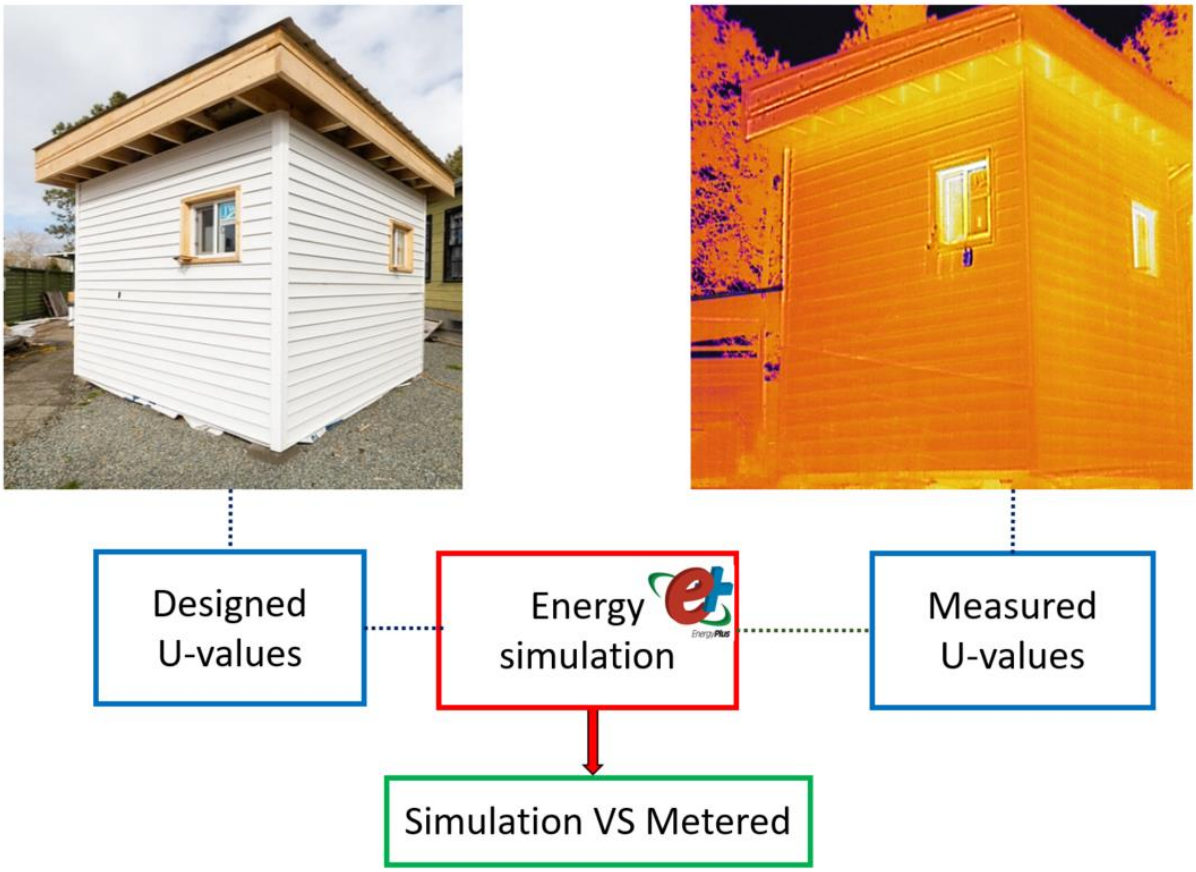

Figure 3.12 Development of a building energy model based different approaches

3.5 Results and Discussion

3.5.1 Determination of U-value

The effective U-value for the entire wall system was estimated for Day 1 to Day 3. Figures 3.13 and 3.14 show the surface temperature distribution in W1 and W2, illustrating non-uniformity distribution around thermal bridging such as wood framing, the window frame, the parapet, and likely due to air leakage at the wall-to-door interface in W1. ROIs were selected to cover the opaque wall (excluding fenestration). W3 and W4 are not presented for brevity, since thermal patterns are similar to that of W2. The “Fusion Palette” colour rendering scheme was chosen to represent surface temperature where bright yellow corresponds to warmer pixels and dark blue represents colder pixels. For instance, pixel intensity around the parapet and window frame were higher most likely as a result of thermal bridging. In contrast, pixel intensity at the corners of the structure appear colder than in the centre which is an artefact of a profound vignetting effect, but could also be confounded by thermal bridging to some extent. It is worth mentioning that although

the wall-to-roof interface does not have a large psi-value, temperature gradients inside the structure due to stack effect (temperature around the ceiling is higher) led to a higher conductive heat loss (higher pixel intensity in thermal images) around that area. Thermocouple measurements confirm temperature gradients of ~1 ºC between the lowest and highest reading heights. It is unknown to what extent air leakage could also contribute to this finding.

The results in Table 3.8 show U-values were not identical on different days, even though tests were performed under relatively steady-state conditions. This implies that in practice, steady-state conditions are never achieved, unlike calculated values which are obtained under steady-state conditions. In other words, calculated U-values obtained using 3D simulation tools ignore the impact of surrounding objects' radiation (both emission and reflection) and fluctuations of the outdoor condition such as temperature, relative humidity and wind before and during the tests. Hence, U-value of a wall changes based on its location, orientation of buildings, the construction type (i.e., wood vs. concrete), number of surrounding buildings, and the variation of environmental conditions (wind, temperature, humidity). For instance, W1 & W3 were in the field of view of the adjacent conditioned lab building where the exchange of radiation between surfaces was present at the time of tests even though the lab building was wood-framed building (low thermal mass) and tests were performed in late night (ensuring a relatively steady-state condition). Higher reflected temperature in W1 & W3 (~ 1.5 ºC) compared to the W2 & W4 confirmed this fact. It should be remarked that U-values by IRT were obtained based on 2D thermal images and their deviations with 3D simulation values are undeniable and should be considered in practice.

Additionally, interior insulated walls (W1 & W2) had relatively lower deviations compared to those with split-insulated assemblies (W3 & W4), confirming the findings of Albatici et al. [29] and Dall'O' et al. [28] that IRT is less accurate for well-insulated walls: a lower thermal heat flux implies a small difference between the exterior wall surface (exterior insulation) and the surrounding outdoor air, allowing environmental and climatic variability to impact exterior surface temperatures to a more significant extent. This trend was repeated on all days; however, results on Day 3 were slightly better for W3 and W4, which can be attributed to a lower wind speed. It is worth pointing out that U-value estimations were based on cladding surface temperatures which may not represent the actual surface temperature of exterior surface due to the 19 mm gap between cladding and wall exterior surface. However, as mentioned in Ref [59], assuming the cladding has

a relatively similar temperature to the exterior surface is justifiable due to low wind speed at the time of the tests, resulting in limited air flow and little convection heat exchange in the cavity (radiation heat exchange between surfaces was dominant).

To understand if the lower pixel intensity around corners was a result of vignetting or thermal bridging, other images were taken from different incident angles. Figure 3.15 illustrates histograms of ROIs selected to form a baseline comparison, confirming that temperatures in Box 1 (near the corner) were lower than Box 2 (centre of wall) by ~1 ºC and had a wider distribution (greater standard deviation). However, thermal images taken from a different angle with the same corner in the centre (Figure 3.16) showed temperature data similar to that of Box 2 in Figure 3.15. It can be deduced that the vignetting effect is dominant around the corners of a thermogram and should be accounted for to improve accuracy. Hence, it was decided to divide the wall into six segments (Figure 3.17). The thermal image for each segment was taken separately to ensure that the segment was in the centre of thermal images, limiting the effect of vignetting. Finally, segments were stitched together to form a new thermal image with corrected values as shown in Figure 3.18. U-values for all walls were re-calculated yielding substantial improvements in accuracy, ranging from -2.33% to -12.50% (Table 3.9) versus -13.95% to -58.33% using the single-thermogram methodology (Table 3.8). It should be noted that vignetting effect intensified surface temperature reduction in W3 & W4 (surface temperature was closer to outdoor air compared to W1 & W2), particularly around the corners where temperatures were below the outdoor air temperature (negative U-value), unlike W1 & W2. Therefore, improvement in accuracy of U-values in W3 & W4 was considerably larger than those in W1 & W2, suggesting that vignetting effect could have a more adverse impact in well-insulated wall assemblies.

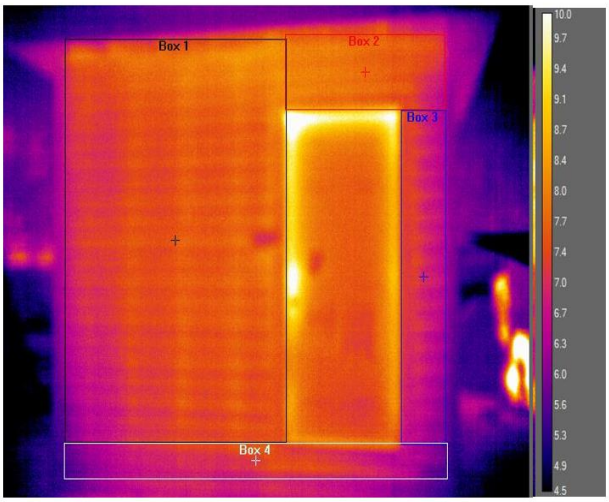

(a) (b)

Figure 3.13 Selection of region of interests (ROIs) to estimate U-value of W2: (a) thermal image; and (b) photograph

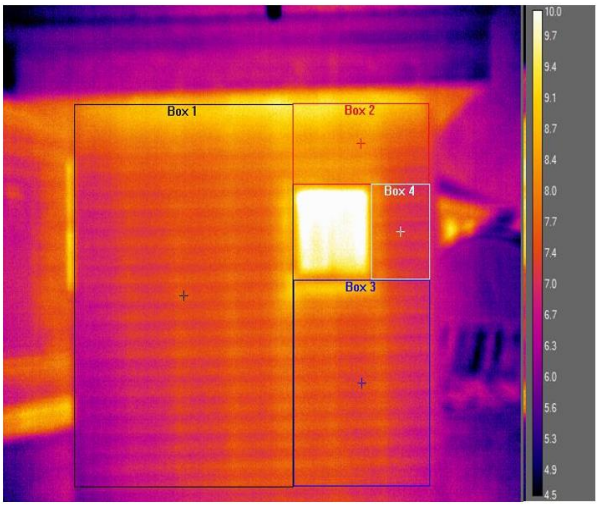

(a) (b)

Figure 3.14 Selection of region of interests (ROIs) to estimate U-value of W1: (a) thermal image; and (b) photograph

Table 3.8 Comparison of IRT-estimated and simulated U-values on different days

Wall assemblies	IRT-estimated U-value (W/m^2 K)	3D simulated U-value (W/m^2 K)	Deviations (%)
Day1			
W1	0.37	0.43	-13.95
W2	0.22	0.31	-29.03
W3	0.09	0.26	-65.38
W4	0.04	0.24	-83.33
Day 2			
W1	0.35	0.43	-18.60
W2	0.26	0.31	-16.13
W3	0.11	0.26	-57.69
W4	0.06	0.24	-75.00
Day 3			
W1	0.37	0.43	-13.95
W2	0.25	0.31	-19.35
W3	0.15	0.26	-42.31
W4	0.10	0.24	-58.33

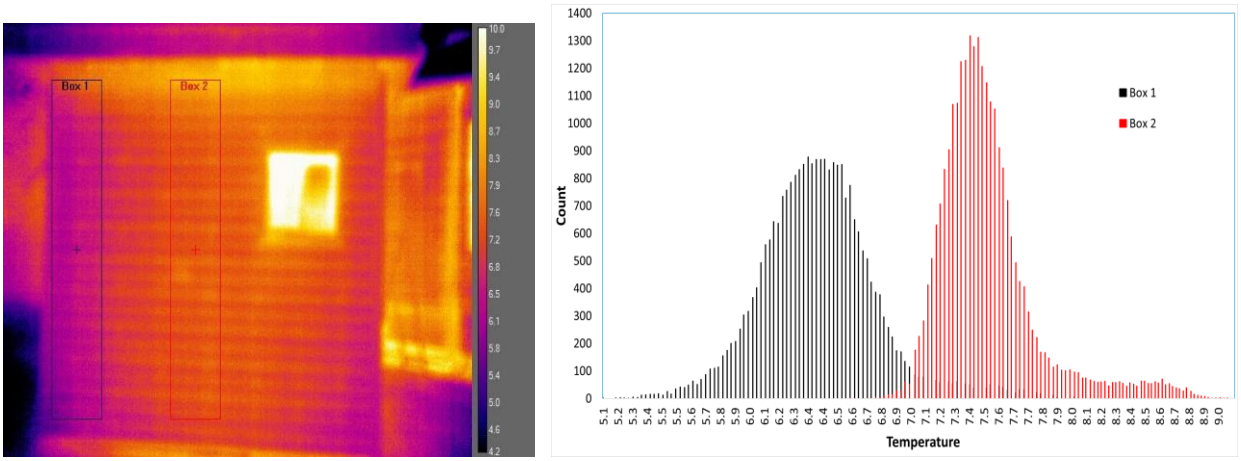

(a) (b)

Figure 3.15 Evaluation of corners based on (a) two selected ROIs (Boxes 1 & 2) thermal images; and (b) temperature distribution histograms

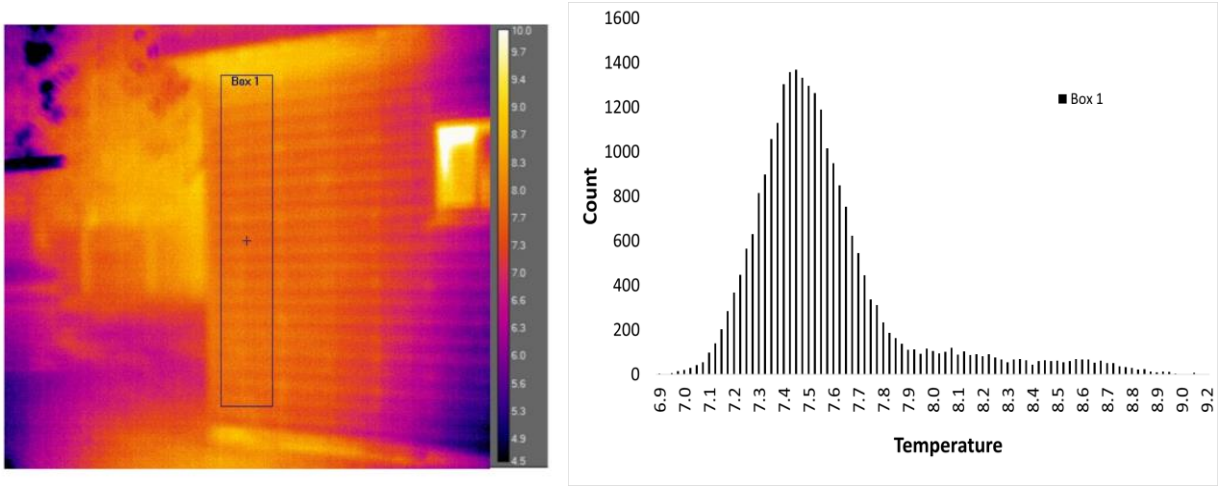

(a) (b)

Figure 3.16 Evaluation of temperature distribution of Box 1 from a different angle: (a) Box 1 located in the centre of the image; and (b) temperature distribution histograms

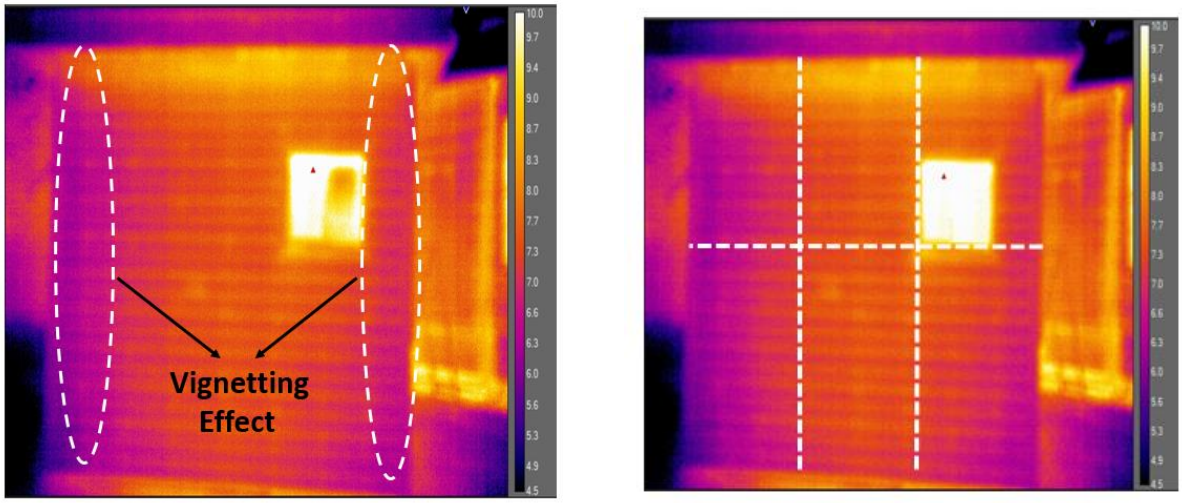

(a) (b)

Figure 3.17 (a) identification of vignetting effect; (b) Dividing the thermal image into six segments

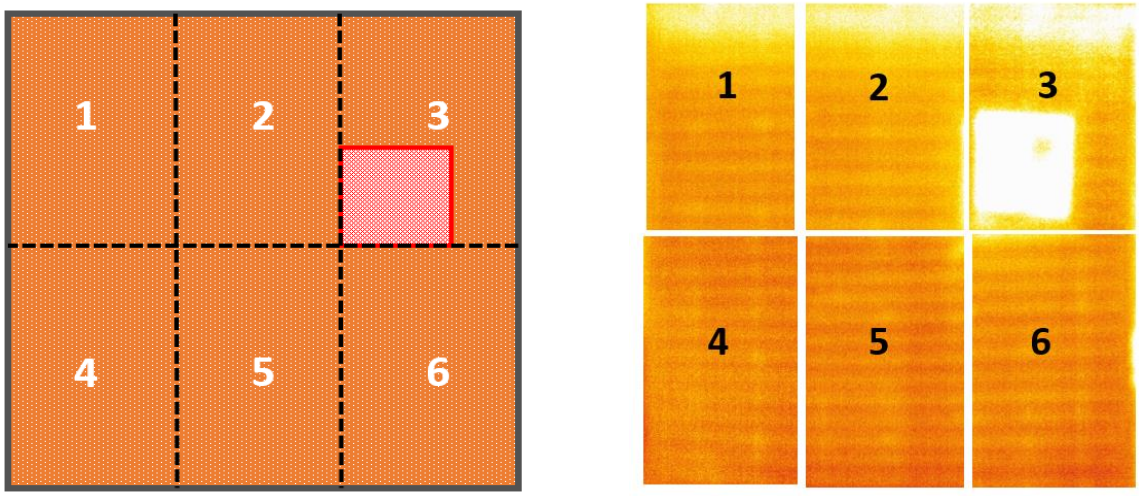

(a) (b)

Figure 3.18 (a) Schematic segments of thermal images; (b) Combined thermal images from different angle

Table 3.9 Comparison of IRT-estimated and simulated U-values on Day 3 after accounting for the vignetting effect

Wall assemblies	IRT-estimated U-value (W/m^2 K)	3D simulated U-value (W/m^2 K)	Deviation (%)
W1	0.42	0.43	-2.33
W2	0.29	0.31	-6.45
W3	0.23	0.26	-11.53
W4	0.21	0.24	-12.50

3.5.2 Infrared index (relative quantitative comparison)

Results in Section 4.1 showed that due to the instability of outdoor conditions, U-values estimated with IRT may differ on different days, even if the tests are each performed in approximately steady-state conditions. To validate IRI as a ranking metric for building envelope thermal performance, index values were calculated on five different days with varying external conditions; IRI rankings were then compared with their overall U-values. Notably, the calculation of overall building envelope U-values also included the door and windows. Ranking based on simulated U-values demonstrated that W4 had the best thermal performance, followed by W3, W2 and W1. Simulated values only consider heat loss through the clear field areas and the effect of thermal bridging, while the impact of air leakage or any other defects was ignored in this ranking (Figure 3.19). Since W2, W3 and W4 have windows (similar sources of thermal bridging), only W2 is presented in Figure 3.19 for brevity. In IRI calculations, surface temperature of the entire wall (including windows and door) were considered. Figure 3.20 depicts IRI for each wall measured on different days and shows a similar ranking in spite of variations in external conditions. Furthermore, IRI ranking was identical to U-value ranking (Figure 3.21). In other words, higher IRIs correlate to higher U-values. This implies that IRI can be appropriate for ranking and/or relative comparison of building envelope thermal performance. It should be noted that IRI considers the aggregated impact of building envelope effective thermal performance (opaque area) as well as air leakage, defects, and fenestration (Figure 3.19). Hence, more thermal anomalies in the building envelope can lead to a higher IRI and a poorer overall thermal performance. This informs that higher levels of insulation do not necessarily ensure better building energy performance if air leakage, construction defects, and thermal bridging effects are substantial. In

this sense, IRI can be more representative of the overall thermal performance of building envelope assemblies than IRT-estimated or 3D-simulated U-values. Perhaps most importantly, it provides the opportunity for quick surveys for a large number of buildings.

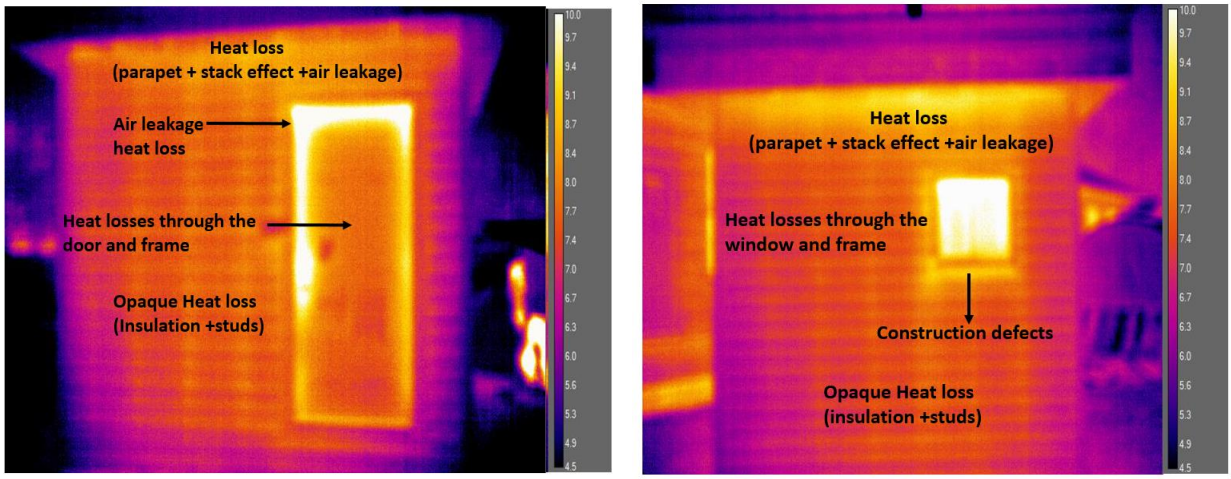

(a) (b)

Figure 3.19 Sources of heat losses through the building envelope: (a) W1; (b) W2

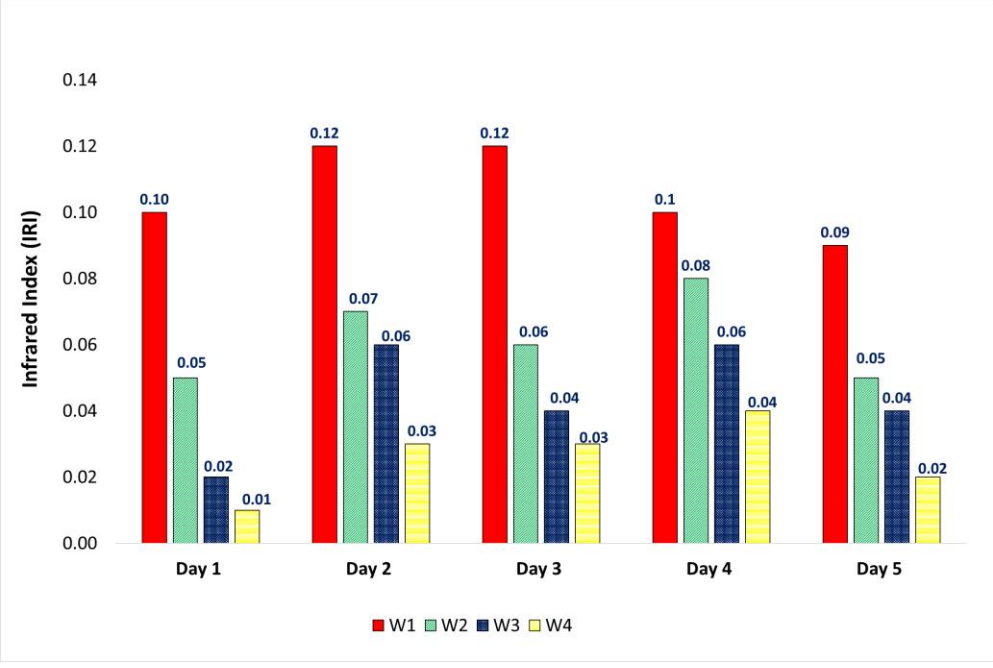

Figure 3.20 IRI of walls on different days

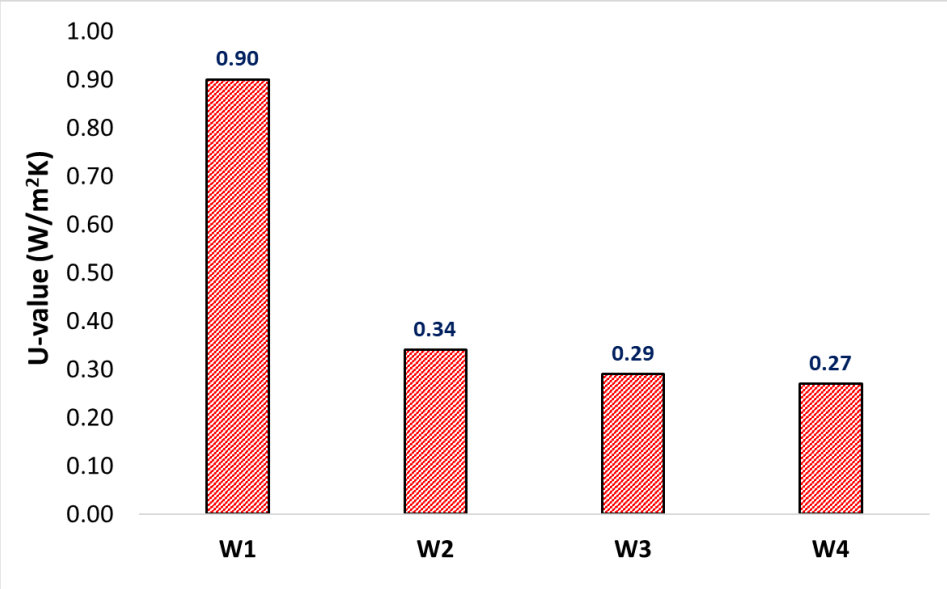

Figure 3.21 Wall rankings based on calculated U-values

3.5.3 Uncertainty analysis

Uncertainties in U-value measurements with external IRT for each wall are shown in Tables 3.10 to 3.13, as a function of each input. Input values were taken from the test measurement on Day 3 after correcting the vignetting effect in thermal images. The reported values for surface temperature in Tables 3.10 to 3.13 were based on average surface temperature (Equation 3.6). Since the variations of coefficients between the walls were too small, it was decided to report the U-values and uncertainties with three decimals in Table 3.10 to 3.13. The total standard uncertainty of measured U-values was 2-7 times larger than the calculated U-values suggesting significant uncertainty in U-value estimation with external IRT. This can be attributed to the high uncertainty of the IR camera (±5ºC) used for surface and outdoor air temperature measurements. Hence, although obtaining as many data as possible with the same instrument improved accuracy of results, it had an adverse effect on uncertainty.

The sensitivity of the U-value to parameters for each wall is reported in the second column of Tables 3.10-3.13. Differences in wall thermal performance resulted in deviations in the sensitivity coefficient accordingly. It is seen that the sensitivity coefficient for surface temperature in W1 was larger than in other walls, but had the smallest sensitivity to outdoor air temperature. This confirms the significant impact of outdoor air temperature on U-values of well-insulated walls (W3 & W4) which is similar to the findings of Albatici et al. [29]. In general, it can be deduced that outdoor

air temperature has a significant impact on external IRT of well-insulated wall assemblies. Interestingly, emissivity had the highest sensitivity coefficient in W1, while it was the third-highest coefficient for other walls. This was consistent with the findings of Fokaides et al. [26] and Madding [25] that indicated emissivity has a significant impact on surface temperature measurements, and consequently U-value. However, since variations in wind speed influence the convective heat transfer coefficient, it is seen that uncertainty in the calculation of convective heat transfer coefficient resulted in higher uncertainty in W1, due to a larger difference between surface temperature and outdoor air temperature (larger variation in the convection heat transfer term in the U-value equation). Finally, all walls were least sensitive to indoor air temperature (smallest in the case of W4). This trend was consistent for IRI of each wall, which was most sensitive to surface temperature and outdoor air temperature and least sensitive to indoor air temperature (Table 3.14). This is important from a practical perspective since it supports the feasibility of non-invasive thermography, effectively not requiring access to the building interior or building automation system (BAS) data to obtain reasonable results [82].

High sensitivity of wall assemblies to variables does not ensure high uncertainty contribution since uncertainty contribution considers both sensitivity coefficient and standard uncertainty of variables. For instance, all walls were sensitive to emissivity (highest in the case of W1). However, emissivity, along with indoor air temperature and convective heat transfer coefficient, contributes considerably less than 1% to the total uncertainty of the walls analyzed. However, surface temperature and outdoor air temperature had the highest contribution to total U-value uncertainty since both were measured with the IR camera, which has large standard uncertainty compared to sensors. The index column shows these variables collectively account for almost 98% of the total standard U-value uncertainty budget. Finally, indoor air temperature had the least uncertainty contribution due to small uncertainty temperature sensor (very accurate) and sensitivity coefficient.

Table 3.10 Uncertainty budget in U-value estimation with IRT for W1

	Uncertainty Budget - W1				
	Value	Sensitivity Coefficient	Standard Uncertainty	Uncertainty Contribution	Index (%)
Emissivity	0.95	0.389	0.02	0.008	0.003
Stephan-Boltzmann	5.67×10^{-8}	-	-	-	-
Wall temperature (K)	281.35	0.355	2.886	1.025	54.71
Outdoor air temperature (K)	280.15	-0.323	2.886	-0.932	45.29
Indoor air temperature (K)	295.65	-0.027	0.006	-0.000	0.00
Convection heat transfer coefficient (W/m^2 K)	0.701	0.077	0.057	0.004	0.001
U-value (W/m^2 K)	**0.419**			**1.385**	

Table 3.11 Uncertainty budget of U-value measurement with IRT for W2

	Uncertainty Budget- W2				
	Value	Sensitivity Coefficient	Standard Uncertainty	Uncertainty Contribution	Index (%)
Emissivity	0.95	0.268	0.02	0.005	0.001
Stephan-Boltzmann	5.67×10^{-8}	-	-	-	-
Wall temperature (K)	280.930	0.354	2.886	1.022	53.35
Outdoor air temperature (K)	280.150	-0.331	2.886	-0.955	46.65
Indoor air temperature (K)	295.650	-0.019	0.006	-0.000	0.00

Convection heat transfer coefficient (W/m^2 K)	0.701	0.054	0.057	0.003	0.0005
U-value (W/m^2 K)	**0.289**			**1.398**	

Table 3.12 Uncertainty budget of U-value measurement with IRT for W3

	Uncertainty Budget- W3				
	Value	Sensitivity Coefficient	Standard Uncertainty	Uncertainty Contribution	Index (%)
Emissivity	0.95	0.219	0.02	0.004	0.001
Stephan-Boltzmann	5.67×10^{-8}	-	-	-	-
Wall temperature (K)	280.820	0.353	2.886	1.020	52.61
Outdoor air temperature (K)	280.150	-0.335	2.886	-0.978	47.38
Indoor air temperature (K)	295.650	-0.015	0.006	-0.000	0.00
Convection heat transfer coefficient (W/m^2 K)	0.701	0.043	0.057	0.002	0.0002
U-value (W/m^2 K)	**0.233**			**1.404**	

Table 3.13 Uncertainty budget of U-value measurement with IRT for W4

	Uncertainty Budget- W4				
	Value	Sensitivity Coefficient	Standard Uncertainty	Uncertainty contribution	Index (%)
Emissivity	0.95	0.193	0.02	0.003	0.001
Stephan-Boltzmann	5.67×10^{-8}	-	-	-	-
Wall temperature (K)	280.750	0.352	2.886	1.017	52.17
Outdoor air temperature (K)	280.150	-0.337	2.886	-0.977	47.82

Indoor air temperature (K)	295.650	-0.013	0.006	-0.000	0.00
Convection heat transfer coefficient (W/m^2 K)	0.701	0.038	0.057	0.002	0.0001
U-value (W/m^2 K)	**0.209**			**1.406**	

Table 3.14 IRI sensitivity coefficients

	Sensitivity Coefficient ($\frac{\partial IRI}{\partial X_i}$)			
	W1	W2	W3	W4
Wall temperature (K)	0.065	0.065	0.065	0.065
Outdoor air temperature (K)	-0.058	-0.061	-0.063	-0.064
Indoor air temperature (K)	-0.006	-0.003	-0.002	-0.001

3.5.4 Energy simulation analysis

Building energy models were developed in EnergyPlus to study impacts of the IRT methodologies in more practical terms. Figure 3.22 compares the energy use of the structure for three scenarios including simulations based on (1) 1D U-values inferred from IRT measurements, (2) 2D effective U-values inferred by IRT, and (3) 2D effective U-values inferred by IRT with vignetting artefact correction. Energy models were compared with monthly metered energy data to examine accuracy of simulations. Simulations used weather data corresponding to the time period of metered consumption data.

To quantify the effect of 1D U-value determination by IRT (Table 3.15) on energy model accuracy, a region of interest (ROI) was considered in the centre of thermal images as suggested by Ref [59] to avoid the vignetting effect (Figure 3.23). The ROI was selected between framing (studs) to minimize any thermal bridging or lateral heat flux contributions to surface temperature, and

consequently U-value. Table 3.16 summarizes deviations of -8.70 to 23.53% between estimated 1D U-value by IRT and nominal 1D U-values (obtained without considering thermal bridging effects of studs and attachment components). Figure 3.22 illustrates that simulations based on estimated U-values underestimate energy consumption (positive CVRMSE & NMBE values); or in other words, overestimated the thermal performance of the wall. The error became more substantial when the models were based on 1D U-values or effective U-values with vignetting, evident also in Figure 3.22. However, model error is significantly reduced after correcting for vignetting (increased the accuracy of U-value calculations): NMBE < 5% and CVRMSE < 15% were satisfied per ASHRAE Guideline 14 criteria. Interestingly, models based 1D U-value and effective U-values with vignetting were almost similar. In 1D U-value calculations, the effect of any thermal bridging was neglected, which resulted in lower temperatures and ultimately a lower U-value. It appears that the combined effect of including for thermal bridging effects and vignetting artefacts had an approximately net-zero effect on effective U-value, and therefore also on energy consumption. This may be strictly a coincidence with the current experimental set-up. Nonetheless, these findings suggest utilizing IRT to estimate U-value for use as inputs in an energy model should first (1) consider the effect of thermal bridging, and (2) address the adverse effect of vignetting.

In Section 4.1, it was shown that U-values calculated on different days can vary and impact energy model results. Hence, calibrating the energy model based on U-value calculated on a single day may not be representative. As with any model calibration, it is suggested that the climate data is from the nearest or otherwise most representative climate station and temporally corresponding to metered data. Energy model input U-values estimated using IRT should be obtained from the same time period.

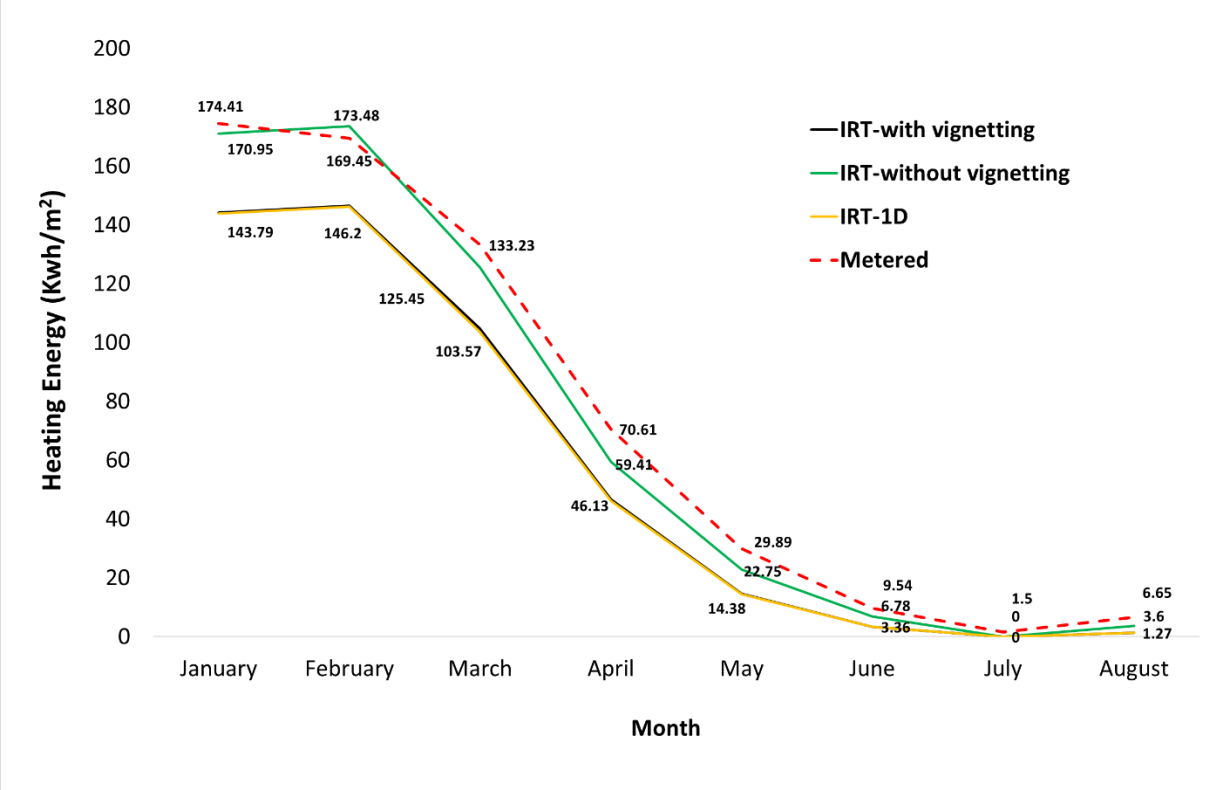

Figure 3.22 Comparative assessment of energy models and metered energy data

Table 3.15 Magnitude of error in simulated energy models and actual data

Calibration criteria	**Deviations of Models**			
	1D- IRT	IRT-with vignetting	IRT-with vingetting correction	ASHRAE Guideline 14
NMBE (%)	22.04%	21.60%	3.59%	±5%
CVRMSE (%)	39.30%	38.52%	8.93%	15%

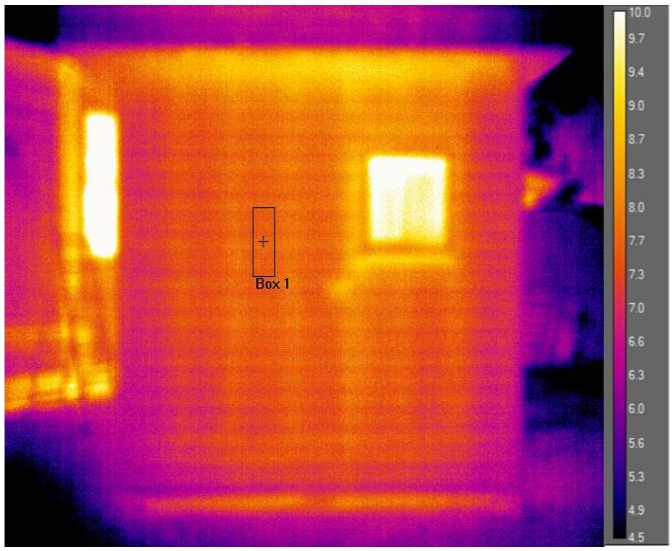

Figure 3.231D U-value ROI

Table 3.16 Comparison of calculated U-values with IRT and nominal (1D) U-values on Day 3

Wall assemblies	**Measured 1D U-value (W/m^2 K)**	**Nominal 1D U-value (W/m^2 K)**	**Deviations (%)**
W1	0.36	0.34	5.88
W2	0.21	0.23	-8.70
W3	0.18	0.16	12.50
W4	0.15	0.16	-6.25

3.6 Conclusions

This chapter attempted to demonstrate the application of external IRT for quantitative analysis of building envelope thermal performance. The thermal characteristics of four different insulated wood-framed wall assemblies were estimated and compared with designed values obtained by 3D simulation tools. Also, the impact of vignetting artefact on the accuracy of results was examined, and a practical approach was developed to limit deviation of results with design values. Furthermore, impact of the accuracy of U-value estimated with IRT on the deviation of energy simulation outputs with metered data was examined. A comprehensive uncertainty analysis was conducted to determine the most influential parameters and their contribution to the uncertainty of

results. Finally, an infrared index (IRI) was introduced as a metric for rapid evaluation and comparison of building envelope thermal performance.

The main findings of this study are highlighted as follows:

- Due to variation of outdoor environmental parameters, U-value estimates were not identical on different days.
- Vignetting has a substantial effect on the accuracy of results, particularly for well-insulated walls due to small differences between external surface and outdoor air temperatures.
- The proposed approach for addressing the vignetting effect resulted in substantial improvements in accuracy, ranging from -2.13% to -12.50% versus -13.95% to -58.33%.
- Although in-situ 2D U-value estimation of whole opaque wall assemblies using external IRT in this study has not been conducted previously, the findings of this investigation are in line with previous conducted quantitative IRT studies in a climate chamber from Tejedor et al. [11, 62], which informed that the average 2D U-value estimation of facades by considering the effect of thermal anomalies facilitated a better and more accurate diagnosis of building envelope thermal performance.
- Wall thermal performance rankings based on infrared index (IRI) were consistent with their U-value rankings, implying that IRI can be a reliable metric for relative quantitative comparison of building envelope thermal performance, regardless of boundary conditions.
- Unlike effective U-value calculations that only considers heat loss through the clear field assemblies and the impact of thermal bridging in the building envelope, IRI considers all sources of heat losses including air leakage, thermal bridging and construction defects in building envelope. For the relatively new and carefully constructed at-scale structure used in this study, these other thermal anomalies are expected to be minor; however, for older buildings or poorly detailed building envelope assemblies, IRI may be a more holistic representation of relative thermal performance, although further research is needed to confirm the extent and to quantify the effects scientifically.
- The findings of the uncertainty budget demonstrated:
    - the influence of parameters on U-value depends on the type of wall assembly. For instance, emissivity was the most sensitive parameter in W1 (interior-insulated)

while it was the third-highest coefficient for the other walls that included interior and exterior insulation.

  - surface temperature and outdoor temperature measurements with the IR camera had the largest contribution to the uncertainty of results. However, emissivity and indoor air temperature had very little impact on the uncertainty of results.
  - the relatively low level of uncertainty of indoor air temperature to both U-value and IRI promotes performing external measurements with IRT without entering the building (non-invasive)

- When utilizing IRT-inferred U-values as inputs in an energy model, two criteria should be considered: (1) considering the effect of thermal bridging in the building envelope, and (2) addressing the adverse effect of vignetting. The results also were consistent with the study from Bayomi et al. [10] and Benhmidou et al. [64] where accurate estimation of U-value with IRT could enhance the accuracy of energy model calibration and selection of more appropriate retrofits for existing buildings.

Given the optimization of quantitative stationary IRT in this study, the next stage of scientific and technological advancement may involve utilizing unmanned aerial vehicles (UAVs) equipped with infrared cameras as real-time data-driven tool for conducting large-scale quantitative surveys in a fraction of the time. Also, the obtained thermal imaging data of building envelope and sensors' data (temperature, relative humidity, and wind speed) inside/outside the building can be integrated with building information model (BIM) towards development of real-time energy audits and accurate energy simulation of buildings.

Future work should expand the viability of proposed methods for other components such as the roof or fenestration, as well as other building construction types (e.g., steel framed, concrete and mass timber buildings). Also, the reliability of the proposed methodology should be examined for various buildings types, such as office buildings in urban areas which are surrounded by different buildings (both construction and architectural aspects) and environmental objects. Finally, since the strength of the IRI approach is in its speed of analysis, the feasibility of this approach should be examined for assessing multiple buildings, for example at the neighbourhood or portfolio-levels, to ultimately rank buildings on a thermal performance basis serving as a complementary decision-making criterion for potential retrofits.

3.7 References

[1] BC's Greenhouse Gas Reduction Targets Act, Government of British Columbia, 2007, available at: http://www.bclaws.ca/EPLibraries/bclaws_new/document/ID/freeside/00_07042_01 (Accessed on 23 September 2021).

[2] Canada's Mid-century Long-term Low-greenhouse Gas Development Strategy, Government of Canada, 2016, available at: http://unfccc.int/files/focus/long term_strategies/application/pdf/canadas_mid-century_long-term_strategy.pdf (Accessed on 23 September 2021).

[3] 2050 Low-carbon Economy – Climate Strategies and Targets, European Commission, 2016, available at: https://ec.europa.eu/clima/policies/strategies/2050_en (Accessed on 23 September 2021).

[4]https://www.iea.org/reports/heating-and-cooling-strategies-in-the-clean-energy-transition (Accessed on 23 September 2021).

[5] M. O'Grady, A.A. Lechowska, A.M. Harte, Quantification of heat losses through building envelope thermal bridges influenced by wind velocity using the outdoor infrared thermography technique, Appl. Energy. 208 (2017) 1038-1052.

[6] International Energy Agency (IEA), Technology Roadmap ''Energy Efficient Building Envelopes, 2014. doi:10.1787/9789264118492-en.

[7] O. Osama et al, Zero energy university buildings energy performance evaluation of faculty of architectural engineering, Arch. Plan. J. 23 (2015) 13–21

[8] Lin, Yu-Hao, Kang-Ting Tsai, Min-Der Lin, and Ming-Der Yang. "Design optimization of office building envelope configurations for energy conservation, Appl. Energy. 171 (2016) 336-346.

[9] C. Balaras, K. Droutsa, A..A, Argiriou, and D. N. Asimakopoulos, Potential for energy conservation in apartment buildings, Energy Build. 31 2 (2000) 143-154.

[10] N. Bayomi, Sh. Nagpal, T. Rakha, and J. E. Fernandez, Building envelope modeling calibration using aerial thermography, Energy Build. 233 (2021) 110648.
[11] B. Tejedor, E. Barreira, R.M.S.F. Almeida, M. Casals, 2020, Thermographic 2D U-value map for quantifying thermal bridges in building façades, Energy Build. 224 (2020) 110176.

[12] M. Teni, H. Krstić, P. Kosiński, Review and comparison of current experimental approaches for in-situ measurements of building walls thermal transmittance, Energy Build. 203 (2019) 109417.

[13] L. Evangelisti, C. Guattari, P. Gori, R. Vollaro, In situ thermal transmittance measurements for investigating differences between wall models and actual building performance, Sustainability 7 (8) (2015) 10388.

[14] B. Tejedor, M. Casals, M. Gangolells, X. Roca, Quantitative internal infrared thermography for determining in-situ thermal behaviour of façades, Energy Build. 151 (2017) 187-197.

[15] C. Meola, Infrared thermography: recent advances and future trends. Beijing: Bentham Science Publishers, 2012.

[16] RA. Smith RA, FE. Jones , RP. Chasmar, The detection and measurement of infrared radiation. Oxford: Clarendon, 1958.

[17] F. Luzi, M. Malcolm, L. Nanni Costa,V. Redaelli, Thermography: current status and advances in livestock animals and in veterinary medicine. Fondazione Iniziative Zooprofilattiche e Zootecniche, 2013.

[18] CA. Balaras, AA. Argiriou, Infrared thermography for building diagnostics, Energy Build (2002) 34 171–83.

[19] E. Lucchi, Applications of the infrared thermography in the energy audit of buildings: A review, Renew. Sust. Energ. Rev. 82 (2018) 3077-3090.

[20] International Organization for Standardization. Performance of Buildings. Detection of Heat, Air and Moisture Irregularities in Buildings by Infrared Methods—Part 3: Qualifications of Equipment Operators, Data Analysts and Report Writers; ISO 6781-3:2015; ISO: Geneva, Switzerland, 2015.

[21] International Organization for Standardization. Thermal Performance of Buildings. Qualitative Detection of Thermal Irregularities in Building Envelopes. Infrared Method; UNE EN 13187:1998; ISO: Geneva, Switzerland, 1998.

[22] American Society for Testing Materials. Standard Test Method for Minimum Detectable Temperature Di_erence for Thermal Imaging Systems; ASTM E1311; American Society for Testing Materials: West Conshohocken, PA, USA, 2004.

[23] American Society for Testing Materials. Standard Test Method for Measuring and Compensating for Reflected Ambient Temperature Using Infrared Imaging Radiometers; ASTM E1862; American Society for Testing Materials: West Conshohocken, PA, USA, 1997.

[24] RESNET—Residential Energy Services Network. RESNET Interim Guideline for Thermographic Inspections of Buildings. 2012. Available online: http://www.resnet.us/standards/RESNET_IR_interim_guidelines.pdf (Accessed on 4 October 2020).

[25] R. Madding, Finding R-values of stud frame constructed houses with IR thermography, in Proceedings of InfraMation, Reno, USA, 2008.

[26] P.A. Fokaides, S.A. Kalogirou, Application of infrared thermography for the determination of the overall heat transfer coefficient (U-Value) in building envelopes, Appl. Energy. 88 (2011) (12) 4358-4365.

[27] B. Tejedor, M. Casals, M. Gangolells, Assessing the influence of operating conditions and thermophysical properties on the accuracy of in-situ measured U-values using quantitative internal infrared thermography, Energy Build. 171 (2018) 64-75.

[28] G. Dall'O, L. Sarto, A. Panza, Infrared screening of residential buildings for energy audit purposes: results of a field test, Energies. (2013) 6 (8) 3859-3878.

[29] R. Albatici, A.M. Tonelli, M. Chiogna, A comprehensive experimental approach for the validation of quantitative infrared thermography in the evaluation of building thermal transmittance, Appl. Energy. 141 (2015) 218-228.

[30] I. Nardi, S. Sfarra, D. Ambrosini, In Quantitative thermography for the estimation of the U-value: state of the art and a case study, 32nd IUT (Italian Union of Thermo-fluid-dynamics) Heat Transfer Conference, Journal of Physics, Conference Series. 547 (2014) 012016

[31] I. Nardi, D. Paoletti, D. Ambrosini, T. De Rubeis, S. Sfarra, U-value assessment by infrared thermography: A comparison of different calculation methods in a Guarded Hot Box, Energy Build. 122 (2016) 211-221.

[32] X. Lu, A. Memari, Application of infrared thermography for in-situ determination of building envelope thermal properties, J. Build. Eng. 26 (2019) 100885.

[33] B. Tejedor, K. Gaspar, M. Casals, M. Gangolells, Analysis of the Applicability of Non-Destructive Techniques to Determine In Situ Thermal Transmittance in Passive House Façades, Appl. Sci., 10 23 (2020) 8337.

[34] Kirimtat, Ayca, and Ondrej Krejcar. "A review of infrared thermography for the investigation of building envelopes: Advances and prospects, Energy Build. 176 (2018): 390-406.

[35] D. Paoletti, D. Ambrosini, S. Sfarra, F. Bisegna, Preventive thermographic diag- nosis of historical buildings for consolidation, J. Cult. Heritage 14 (2013) 116–121.

[36] J. Goodhew , S. Goodhew , T. Auburn , P. De Wilde , A preliminary investigation of the potential for thermographic images to influence householders ' under- standing of home energy consumption, in: Proc. 25th Annu. ARCOM Conf., (2009) 971–979.

[37] Ocaña, Silvia Martın, Ignacio Cañas Guerrero, and Ignacio González Requena. "Thermographic survey of two rural buildings in Spain, Energy Build. 36 6 (2004) 515-523.

[38] M. Mahmoodzadeh, V. Gretka, S. Wong, T. Froese, P. Mukhopadhyaya, Evaluating Patterns of Building Envelope Air Leakage with Infrared Thermography, Energies. (2020) 13 (14), 3545.

[39] EC Shao, Detecting sources of heat loss in residential buildings from infrared imaging." PhD diss., Massachusetts Institute of Technology, 2011.

[40] M. Mahmoodzadeh, V. Gretka, A. Blue, D. Adams, B. Dallimore, Ph. Mukhopadhyaya, Evaluating thermal performance of vertical building envelopes: Case studies in a Canadian university campus, J. Build. Eng. 40 (2021) 102712.

[41]T. Kalamees, Critical values for the temperature factor to assess thermal bridges, *Proc.* Estonian Acad. Sci. Eng. 12 3-1 (2006) 218-229.

[42] Morrison Hershfield, Building Envelope Thermal Bridging Guide—Analysis, Applications and Insights, 2014.

[43] S. Ilomets, T. Kalamees, Evaluation of the criticality of thermal bridges, *Journal of Building Pathology and Rehabilitation* 1 1 (2016): 1-13.

[44] BRE IP 17/01. Assessing the Effects of Thermal Bridging at Junctions and Around Openings. BRE, Building Research Establishment Ltd, Garston, 2001.

[45] NEN 2778:1991. Vochtwering in gebouwen, Bepalingsmethoden. Nederlands Normalisatieinstituut, Delft, 1991.

[46] Asumisterveysohje. Sosiaali- ja terveysministeriön oppaita 2003:1, Sosiaali- ja terveysministeriö, Helsinki, 2003.

[47] T. Kalamees, Air tightness and air leakages of new lightweight single-family detached houses in Estonia, Build Environ. 42 6 (2007) 2369-2377.

[48] M. Fox, D. Coley, S. Goodhew, P.D. Wilde, Thermography methodologies for detecting energy related building defects, Renew Sustain Energy Rev. 40 (2014) 296-310.

[49] D. González-Aguilera, S. Lagueela, P. Rodríguez-Gonzálvez, D. Hernández-López, Image-based thermographic modeling for assessing energy efficiency of buildings façades, Energy Build 65 (2013) 29-36.

[50] I. Danielski, M. Fröling, Diagnosis of buildings' thermal performance-a quantitative method using thermography under non-steady state heat flow, Energy Procedia. 83 (2015) 320-329.

[51] C. Meola, GM. Carlomagno, Recent advances in the use of infrared thermography, Measurement science and technology. 15 9 (2004) 27.

[52] FLIR, Radiometry Application Note, May 2014

[53] E. Bauer, VP. de Freitas, N. Mustelier, E. Barreira, S. Stingl de Freitas, Infrared thermography–evaluation of the results reproducibility, *Structural survey.* (2015).

[54] E. Bauer, E. Pavon, E. Barreira, E. Kraus De Castro, Analysis of building facade defects using infrared thermography: Laboratory studies, J. Build. Eng. 6 (2016) 93-104.

[55] B. Lehmann, KG. Wakili, T. Frank, BV. Collado, C. Tanner, Effects of individual climatic parameters on the infrared thermography of buildings, Appl. Energy. 110 (2013) 29-43.

[56] E. Barreira, V.P. de Freitas, Evaluation of building materials using infrared thermography, Constr Build Mater. 21 1 (2007) 218-224.

[57] A. Hoyano, K. Asano, T Kanamaru, Analysis of the sensible heat flux from the exterior surface of buildings using time sequential thermography, Atmos Environ. (1999) 33 3941–51

[58] R. Albatici, AM Tonelli, Infrared thermovision technique for the assessment of thermal transmittance value of opaque building elements on site, Energy Build. (2010) 42 2177–83

[59] M. Mahmoodzadeh, V. Gretka, K. Hay, C. Steele, Ph Mukhopadhyaya, Determining overall heat transfer coefficient (U-Value) of wood-framed wall assemblies in Canada using external infrared thermography, Build Environ. 199 (2021): 107897.

[60] M. O'Grady, A.A. Lechowska, A.M. Harte, Infrared thermography technique as an in-situ method of assessing heat loss through thermal bridging, Energy Build. 135 (2017) 20-32.

[61] F. Asdrubali, G. Baldinelli, F. Bianchi, A quantitative methodology to evaluate thermal bridges in buildings, Appl. Energy. 97 (2012) 365-373.

[62] B. Tejedor, E Barreira, RMSF Almeida, M. Casals, Automated data-processing technique: 2D Map for identifying the distribution of the U-value in building elements by quantitative internal thermography, *Autom. Constr.* 122 (2021): 103478.

[63]F.G.N. Li, A.Z.P. Smith, P. Biddulph, I.G. Hamilton, R. Lowe, A. Mavrogianni, E. Oikonomou, R. Raslan, S. Stamp, A. Stone, A.J. Summerfield, D. Veitch, V. Gori, T. Oreszczyn, Solid-wall U-values: heat flux measurements compared with standard assumptions, ***Build. Res. Inf***. 43 2 (2015) 238-252.

[64] H. Benhmidou, Z. Romani, M. El Mankibi, A. Draoui, Thermal performance prediction of an existing building with framing system using the IRT method, Adv. Build. Energy Res. (2020) 1-25.

[65] Siemens NX software, available at: https://www.plm.automation.siemens.com/global/en/products/nx/ (Accessed on 23 September 2021).

[66] A. Colantonio, G. McIntosh, The differences between large buildings and residential infrared thermographic inspections is like night and day, 11th Canadian Conference on Building Science and Technology, Banff, 2007

[67] Government of Canada, Historical Climate Data, available at: https://climate.weather.gc.ca/index_e.html (Accessed on 23 September 2021).

[68] R. Usamentiaga, P. Venegas, J. Guerediaga, L. Vega, J. Molleda, F. G. Bulnes, Infrared thermography for temperature measurement and non-destructive testing." *Sensors* 14 7 (2014): 12305-12348.

[69] QH. Tran, D. Han, C. Kang, A. Haldar, J. Huh, Effects of ambient temperature and relative humidity on subsurface defect detection in concrete structures by active thermal imaging, *Sensors* 17 8 (2017): 1718.

[70] American Society for Testing and Materials, ASTM E1862-14, *Standard Practice for Measuring and Compensating for Reflected Temperature Using Infrared Imaging Radiometers*; ASTM: West Conshohocken, PA, USA, 2014.

[71] American Society for Testing and Materials, ASTM E1933-14, *Standard Practice for Measuring and Compensating for Emissivity Using Infrared Imaging Radiometers;* ASTM: West Conshohocken, PA, USA, 2014.

[72] P. Avdelidis, A. Moropoulou, Emissivity considerations in building thermography, Energy Build. 35 (2002) 663–667.

[73] K. Maroy, K. Carbonez, M. Steeman, N. Van Den Bossche, Assessing the thermal performance of insulating glass units with infrared thermography: Potential and limitations, Energy Build. 138 (2017): 175-192.

[74] S. Larsen, M. Flores, Determining the infrared reflectance of specular surfaces by using thermographic analysis, Renew. Energy. 64 (2014) 306-313.

[75] G. Papadakos, V. Marinakis, C Konstas, H Doukas, A Papadopoulos, Managing the uncertainty of the U-value measurement using an auxiliary set along with a thermal camera, Energy Build 242 (2021) 110984.

[76] J. Kelly, N. Kljun, PO. Olsson, L. Mihai, B. Liljeblad, P. Weslien, L. Klemedtsson, L. Eklundh, Challenges and best practices for deriving temperature data from an uncalibrated UAV thermal infrared camera, Remote Sens. 11 5 (2019) 567.

[77] https://www.flir.com/discover/professional-tools/what-is-a-non-uniformity-correction-nuc/

[78] X. Luo, T Hong, and YH Tang, Modeling thermal interactions between buildings in an urban context, *Energies* 13 9 (2020) 2382.

[79] Engineering Reference — EnergyPlus 8.0, US Department of Energy, USA, 2013, https://bigladdersoftware.com/epx/docs/8-0/engineering-reference/page-020.html (Accessed on 23 September 2021).

[80] Morrison Hershfield, Thermal performance of building envelope details for mid-and high-rise buildings, ASHRAE Research Project1365-RP Final Report, 2011.

[81] ASHRAE, ASHRAE Guideline14: Measurement of Energy, Demand, and Water Savings, American Society of Heating Refrigerating and Air-Conditioning Engineers, Inc, Atlanta, Georgia, 2014.

[82] D. Patel, J Estevam Schmiedt, M. Röger, B Hoffschmidt, Approach for external measurements of the heat transfer coefficient (U-value) of building envelope components using UAV based infrared thermography, In Proceedings of the 14th Quantitative InfraRed Thermography Conference (QIRT), Berlin, Germany, 25–29 June 2018; QIRTCouncil: Berlin, Germany, (2018) 379–386.

Chapter 4: Evaluating Patterns of Building Envelope Air Leakage with Infrared Thermography

The content in this chapter was published in the following publication:

M. Mahmoodzadeh, V. Gretka, S. Wong, T. Froese, P. Mukhopadhyaya, Evaluating Patterns of Building Envelope Air Leakage with Infrared Thermography, ***Energies***. (2020) 13 (14), 3545. https://www.mdpi.com/1996-1073/13/14/3545

4.1 Abstract

The next-generation performance-based building energy codes are focusing on minimizing building envelope air leakage. The quantification of air leakage in buildings is typically performed with a blower door test. However, this test does not provide information about the locations of air leakage. The aim of this study is to demonstrate a method involving qualitative and quantitative components that can be used to characterize locations of air leakage with infrared thermography. Since air leakage can have a significant impact on building energy consumption in cold climates, like in Canada, this approach can quickly inform where air barrier discontinuities occurred during construction or where to selectively target air sealing efforts in existing buildings. The observations from this study are presented, based on a thermographic image analysis during a depressurized blower door test at various pressures, in an attempt to quantify the relative rates of air leakage. The results from the investigation showed that infrared thermography (IRT) was able to discern locations and infer relative ratios of air leakage. The qualitative analysis showed that areas of air leakage are more evident under higher pressure difference. The quantitative approach showed that a minimum of 25 Pa pressure difference was required to detect the air leakage in the vicinity of the window frame, as the surface temperature decreased rapidly (almost 60% of the indoor surface/outdoor air temperature difference) at this pressure. A temperature index was defined to prioritize the areas of air leakage for retrofitting purposes. Furthermore, a thermal image subtraction method was used to determine the characteristics of the cracks based on thermal patterns. Finally, the practical implication of this study, for building developers, home inspectors, property mangers, and homeowners, is the early detection of air leakage for both existing and newly constructed buildings which could result in energy and cost savings.

Keywords: infrared thermography; air leakage area; quantitative analysis; qualitative analysis; pressure differences

4.2 Introduction

Energy consumption in the built environment has increased considerably over the past decade as a result of population growth, occupants spending more time indoors, indoor air quality, and climate change. According to the International Energy Agency (IEA), buildings and building construction sectors together consume 36% of the total global energy consumption and are responsible for almost 40% of direct and indirect greenhouse gas (GHG) emissions [1]. To achieve a low-energy building, a number of early design decisions need to be considered.

Building re-commissioning and occupant behavioral measures are low-cost and fast-payback pursuits, often considered first. However, re-commissioning should occur on a regular basis, to ensure continuing energy savings, every 3–5 years, or more frequently with occupancy or usage changes [2]. Likewise, fostering sustainable occupant behaviour can be a challenging endeavour and needs to be reinforced continuously due to occupant forgetfulness and turnover [3].

Therefore, physical building components typically need to be addressed such as lighting, domestic hot water, heating, ventilation, and air conditioning (HVAC) systems and the building envelope [4]. Among these methods, air leakage (unintentional air movement through the building envelope) is one of the most influential factors on energy efficiency and thermal comfort [5]. According to previous studies, air leakage is responsible for 10–50% of building energy demand on an annual basis, largely dependent on age, archetype, and climate [6]. For instance, in cold climates, almost 25% of the heating load is due to infiltration [7] while a study based in Spain by Meiss and Feijo-Munoz found that air leakage represents 10–27% of energy demand in the winter [8]. In the US, air leakage is responsible for 13% and 4% of heating and cooling loads in office buildings, respectively [9].

Building energy codes and standards are beginning to include air leakage provisions for new construction. For instance, British Columbia's Energy Step Code requires an energy model to demonstrate compliance with energy use intensity (EUI) and thermal energy demand intensity (TEDI) targets, both of which are dependent on the as-tested air leakage rate at occupancy phase [5]. The Passive House Standard requires a maximum air leakage rate of 0.6 ACH (air change per hour) at an induced pressure difference of 50 Pa [10]. While the National Energy Code for Buildings (NECB) 2011 defined airtightness targets for fenestration and the 2015 edition further

introduced targets for the exterior envelope of 0.25 L/s/m^2 at ambient pressure [11], neither have historically required an air leakage test to demonstrate compliance.

Air leakage is usually measured by the means of the fan pressurization method ("Blower Door Test") described in standards such as ASTM E779, EN 9972:2015 and USACE 2012 [12–14]. The fan pressurization method is based on measuring the total volume of airflow at a pressure difference that is established between the interior and exterior of a building. The ASTM E779 procedure is performed between 10 and 60 Pa at increments up to 10 Pa. The airflow Q rate (m^3/h) is calculated based on pressure differences ΔP (Pa), using the power law as shown in Equation (4.1). The test is performed under positive and negative pressure to reduce the bias due to wind pressure and/or the stack effect. The result will be the average of the both tests:

$$Q = C\,(\Delta P)^n \tag{4.1}$$

where 'C' is the flow coefficient (m^3/(h Pa^n)) and 'n' is the flow exponent that depends on the flow regime (dimensionless) [12]. It should be noted that in an energy modeling program such as EnergyPlus, the rate of infiltration input is defined based on the L/s/m^2 of an exterior envelope area, which is as per the NECB 2015. Furthermore, as the induced pressure with the blower door test is high and not considered as a typical operating condition, this rate is calculated at an ambient pressure (~5 Pa) for energy modeling input which was considered as normal operating conditions.

Although this test is useful for assessing the airtightness of the whole building, it does not give information regarding its location(s) and relative magnitude [10]. In recent years, infrared thermography (IRT) has been investigated as a potential forensic tool for evaluating the thermal performance of building envelopes. This method uses the principles of heat transfer to capture thermal images (thermograms) of surface temperatures. IRT has been used for various research purposes such as comparing and validating simulations of building envelope thermal performance [15]. IRT can also provide immediate spatial information about heat losses due to compromised or poorly installed insulation, moisture accumulation, thermal bridging, and sources of air leakage [16–18]. Areas of potential air leakage can be identified with IRT, as air leakage induces temperature differences at and around the point of air leakage. The magnitude of temperature differences can depend on the size of the leakage point, pressure differences between the inside and outside, and the indoor–outdoor temperature difference. These areas can be identifiable with

IRT from the inside when the building is depressurized, or from the outside when the building is pressurized [10].

The application of IRT to qualitatively detect air leakage through the building envelope has been the focus of many researchers. For instance, Van De Vijver et.al [19] used IRT with a blower door test to detect sources of air leakage in a building, and studied the impact of pressure differences and temperature differences on the IRT survey. The simulation results showed that higher pressure differences have a negligible benefit for detecting surface temperature differences with IRT after 30 min. However, temperature differences have a more pronounced effect. In another air leakage investigation, Kalamees [9] performed blower door and IRT tests simultaneously on houses in Estonia and showed that the main sources for air leakage were ceiling/floor–wall interfaces, window–wall interfaces and the interface of interior walls with exterior walls and roofs. In a different study, Colantonio and Desroches [18] studied how pressurization- and depressurization-induced air leakage created unique thermal patterns on walls in different types of masonry-clad buildings. Fabrizio Ascione et al. [20] performed an energy audit with thermography on a historical building in Italy, and showed that improving airtightness was one of the most effective energy upgrades while preserving its historical appearance.

A few recent studies have attempted a quantitative application of IRT in this field with some success. The most recent studies in Mediterranean climates showed that a test window has considerably more air leakage than the roller shutter handle, and that the cold area around the leakage locations grows gradually with increasing pressure; however, temperature differences did not have significant influence on the qualitative approach [7,10], contrary to findings by Van De Vijver et al. [19]. Interestingly, the study found that pressure differences up to 25 Pa were responsible for 60% of the changes in surface temperature and had a much smaller effect thereafter. Liu et al. [21] simulated air leakage through cracks using a combination of heat transfer and fluid dynamics principles, validated with simulations using IRT on a pressurized test chamber and in an office building (in-situ). Their results demonstrated that crack size could be predicted within a relative error of 20%, while predicting the air infiltration rate had a relative error of only 3% in situ.

Pressurization by means of a fan offers a much more uniform pressure distribution than can be achieved by natural pressure differences (climate-dependent stack effect, wind, and building

mechanical systems), and is therefore recommended for IRT. Hart [22] concluded that pressure differences between the interior and exterior should be at least 10 Pa, and the temperature differences should be constant for the most accurate results (minimum $\Delta T = 5$ °C). Wahlgren and Sikander [23] similarly concluded a minimum ΔT of 5 °C, ideally 10 °C. However, the guidelines do not agree on the recommended temperature and pressure differences for a reliable evaluation of air leakage using IRT [24] as outlined in Table 4.1.

Table 4.1 Recommended temperature and pressure differences for detection of air leakage with infrared thermography (IRT).

Standard	**Recommended Minimum ΔT for Detection of Air Leakage**	**Recommended Pressure Difference (ΔP)**
RESNET [25]	1.7 °C	10 Pa
ASTM E1186-03 [26]	5 °C	10–50 Pa
NMS 022713 [27]	20 °C	5–10 Pa
	10 °C	10–25 Pa
ASTM C 1060-11a [28]; ISO 6781[29]; EN 13187 [30]	None (10 °C minimum for IRT)	5 Pa (IRT from low-pressure side)

Aforementioned published literatures indicate that the majority of the researchers focused on the qualitative approach with IRT to determine sources of air leakage, and only a few recent studies in a cooling-dominated Mediterranean climate attempted a quantitative analysis. An absence of quantitative investigations with IRT in colder climates like Canada, where air leakage plays a significant role in thermal energy demand intensity forms part of the motivation for this experimental study. Furthermore, prioritizing areas of air leakage for sealing purposes have not been studied yet, whereas this study has attempted to address this issue by developing different quantitative approaches. Finally, the proposed study aims to uncover a new horizon in the thermal assessment of building envelopes where quantitatively distinguishing areas of air leakage from thermal bridges is often challenging.

4.3 Objective

The objective of this study is to assess the potential of infrared thermography (IRT) as a tool for both qualitative localization and the relative quantitative comparison of air leakage. Thermal patterns created by air leakage are evaluated at different pressure differences, in an attempt to correlate surface temperatures with relative magnitudes of crack sizes and positions.

4.4 Methodology

4.4.1 Test object

The experimental study was performed in a room of a laboratory building constructed in 1948 and is located in Victoria, BC, Canada. The room has a floor area of 95 m^2 and a ceiling height of approximately 2.5 m, including two exterior walls, one interior wall and one interior corridor wall with two doors. During the measurement period, the room was heated by the HVAC system, controlled at 20 °C by a thermostat. Fenestration was single glazed in original wood frames, with aluminum frame retrofit inserts (hybrid frames). The largest window facing southeast was selected to assess the air leakage, containing both fixed and operable components as shown in Figure 4.1a. Thermal images captured the interface between the glazing and aluminum frame, aluminum frame and wood frame, and the wood frame and drywall as shown in Figure 4.1b. The camera was positioned at a distance of 1 m from the window as shown in Figure 4.1c. It should be noted that to avoid any reflection from the photographer, the angle of tilt is 5 degrees from the photographer to the targeted objects.

(a) (b) (c)

Figure 4.1 Test area viewed from (a) the exterior; (b) the interior, showing the window frames; and (c) the camera position.

4.4.2 Equipment

Measurement equipment included an infrared (IR) camera, temperature sensors (thermocouples), a wind speed measurement tool (anemometer), and a blower door test apparatus. Before the measurements were carried out, all the equipment was calibrated according to the manufacturers' specifications. During the IR camera calibration, the reflected temperature was measured and the emissivity values of the materials were defined before the tests. Specifications of the equipment and the IR camera are described in Table 4.2 and Table 4.3. Inside and outdoor air temperatures were recorded by means of a 4-channel data logger, with an accuracy of ±1%. The blower door used was capable of achieving a maximum flow of 12,631 m^3/h at a 50 Pa pressure difference and minimum flow of 12.5 m^3/h at 10 Pa pressure difference. The gauge pressure accuracy is ±0.25 Pa or ±5%, which ever is greater.

Table 4.2 Technical specification of the equipment.

Sensor	Measurement range	Uncertainties	Resolution
Thermocouple Type k	−200 °C to 1250 °C	±2.2 °C or ± 0.75%	0.01 °C
Data logger	−200 ° C to 1372 °C	±1%	0.1 °C < 1000, 1 °C > 1000
Hot wire anemometer	20 mm/sec to 40 m/sec	±3%	0.01 m/s

Table 4.3 Specification of the IR camera (FLIR A65).

Measuring range	−25 °C to 135 °C
Accuracy	±5 °C (±9 °F) or 5% of reading
Observation display range	0.05 °C at 30 °C
Wavelength range	7.5–13 µm
IR resolution	640 × 512
Field of view	45˚× 37˚
Instantaneous field of view (IFOV)	1.31 mrad
Detector	Uncooled VOx microblometer

4.4.3 Test Procedure

Fan-pressurized tests were performed to quantify the air leakage characteristics of the room. Furthermore, to detect the areas of air leakage with IRT, thermal images were taken simultaneously while the room was depressurized with the fan. To validate the methodology, the tests were performed on different days with varying exterior conditions outlined in Table 4.4. For all the days studied, indoor temperatures were higher than outdoor temperatures because the tests were performed during the heating months. The initial temperature difference was around 10 ºC on each day. The first three tests were performed in the evening after sunset or in the early morning to avoid the impact of solar radiation on surface temperature. Moreover, since the building surfaces radiate energy to the sky, the tests were performed on both overcast (Days 1 to 3) and clear sky (Days 4 and 5) days to evaluate the variability of thee results. To reduce the effect of transmitted exterior radiation onto the measurement surface, cardboard was placed over the window as shown in Figure 1c.

Table 4.4 Climatic conditions at the beginning of each test.

		Day 1	**Day 2**	**Day 3**	**Day 4**	**Day 5**
Outdoor	Temperature (°C)	9	8	7	12	6
	Humidity (%)	85	90	93	75	80
	Wind speed (m/s)	1.6	1.2	2	2.5	1
	Sky condition	Cloudy	Cloudy	Cloudy	Sunny day and clear sky	Sunny day and clear night sky
	Time of test	before sunrise; 5:00 a.m.	after sunset 8:00 p.m.	before sunrise 5:00 a.m.	after sunrise 10:00 a.m.	after sunset 8:30 p.m.
Inside	Temperature (°C)	20	19.6	19.6	19.8	20
	Humidity (%)	45	45	47	48	50

For each test, thermal images were taken at 0 Pa, followed by 15 to 65 Pa in increments of 10 Pa, for a total of six pressure differences (e.g., 15,25,35,45,55,65 Pa). It should be noted that due to the poor airtightness of the room, the blower door test was not able to generate pressure difference lower than 15 Pa. Measurements were performed and recorded continuously over a period of 5 min at each pressure level (for a total of ~30 min), with a data acquisition interval of 1 sec by the

IR camera. Therefore, each test involved a sequential video with 300 thermograms where the result of the last thermogram at each pressure difference was used for the analysis with FLIR ResearchIR software. All data loggers were configured to collect measurements from the temperature sensors with the same data acquisition interval as the IR camera (1 sec). The wind speed measurement device (anemometer) was located adjacent to the window to measure the outdoor air speed, recorded by data loggers. The pressure difference is defined by the user and controlled by the blower door apparatus software. The system includes a manometer that measures the pressure difference across the fan. The pressure sensor, associated with the blower door, was in a location was carefully selected to prevent any influence of airflow from the fan.

In order to calibrate the IR camera, the emissivity of a material and reflected ambient temperature should be determined. The reflected ambient temperature was determined by using crumpled aluminum foil stretched onto a surface in the field of view of an IR camera. The reflected temperature is the average temperature of the foil if the emissivity is set to 1 in the IR camera [31]. For emissivity, black electrical tape with known emissivity (0.95) was attached to the target at least two hours before the measurements to achieve thermal equilibrium. The emissivity of the target was then determined by adjusting the emissivity of the images until the target temperature was equivalent to the temperature of the tape [32]. Hence, the emissivity of the painted drywall, wood frame, and aluminum frame were found to be 0.95, 0.90 and 0.83, respectively. Finally, the surface temperatures of the targets were calculated by correcting for reflective temperature and the surface emissivity values.

4.5 Results and Discussion

4.5.1 Air leakage evaluation

Results showed that the measured airflow at a pressure differential of 50 Pa was 4013.0 m^3/h (16.9 air changes per hour (ACH)). Applying Equation (4.1), it results a flow exponent (n) of 0.517 and a flow coefficient of 0.147 $m^3/s/Pa^{0.517}$.For context, air leakage was considerably higher (~0.6 $L/s/m^2$ at ambient pressure “5 Pa”) than the requirement in Part 8 of the NECB 2015 [11] where a building envelope airtightness target of 0.25 $L/s/m^2$ of the exterior envelope area is suggested as a model input at ambient conditions (5 Pa). It is to be noted that some leakage may be occurring from the adjacent conditioned space. The results indicate that the room is relatively poorly air-sealed and requires further investigation to identify all sources of air leakage. A combined blower

door test with IRT was applied to evaluate the areas of air leakage both qualitatively and quantitatively, as discussed in the following sections.

4.5.2 Qualitative observation of infrared thermography

Figure 4.2 shows the thermal images taken to the window frame (WF) during the tests carried out on Day 1. This day was selected as representative because similar qualitative results were obtained on Day 2 and Day 3. However, the results on Day 3 and Day 4 showed that external conditions such as solar and night sky radiation had a major impact on thermal imagery. For instance, during the sunny day (Day 4), the effect of ΔP variations on the surface temperature were marginal as a result of direct solar radiation on the window. The test on Day 5 showed, due to night sky radiation, the window frame surface temperatures dropped to below that of the outdoor air at higher ΔP.

In Figure 4.2, the warmer appearing vertical areas are cardboard which was used to shield the IR camera from the outdoor radiation. Colder appearing areas are the window glazing and the aluminum frame, which closely resemble the temperature of outdoor air as a result of higher thermal conductivity. Without higher pressures, it is challenging to: (1) determine the presence of air leakage, and (2) identify the source/location of air leakage. However, air leakage becomes more evident with increasing pressure difference (ΔP) as previously suggested by Hart [21]. When analyzing the following thermal images at 25 Pa or less, one can potentially interpret these images as only thermal bridges of the higher conductive window frames, since the color differences around the frames still appear solid (no streaks/lines) and thus, one may not be able to definitively detect any signs of air leakage pathways under a 25 Pa pressure differential. However, at higher magnitudes of enclosure pressurization/depressurization ((ΔP greater than 25 Pa), it starts to become more visually apparent where the streaks of air leakage patterns are actually located. Based on these images, it appears that pressure differential magnitudes of about 25 Pa and above can more effectively illustrate where the air leakage pathways are located [10]. Therefore, the minimum ΔP of 5 and 10 Pa proposed by other standards [27 30] and Hart [22], respectively, were not appropriate to obtain meaningful results in this particular case.

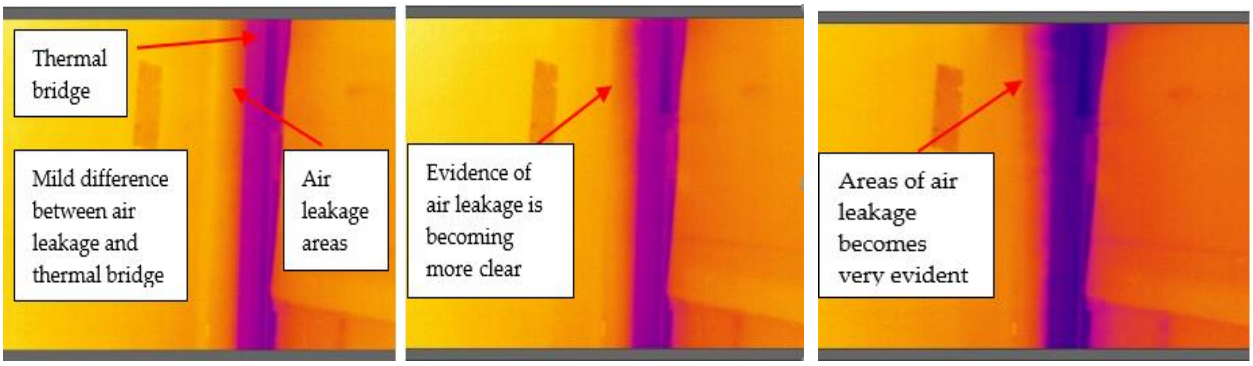

(a) 0 Pa (b) 15 Pa (c) 25 Pa

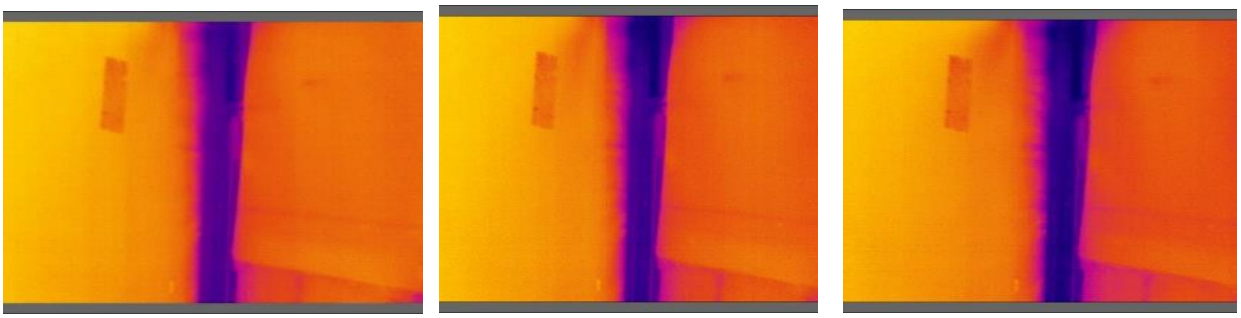

(d) 35 Pa (e) 45 Pa (f) 55 Pa

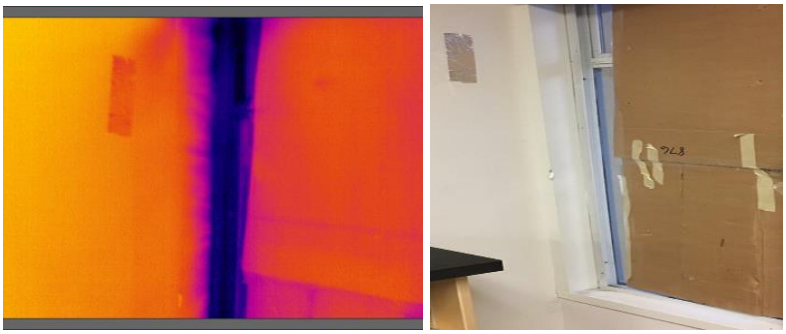

(g) 65 Pa (h) Visual image

Figure 4.2 Window frame thermal images (temperature difference in degrees Celsius) taken from the interior in a depressurized room, at varying ΔP: (a) 0 Pa; (b) 15 Pa; (c) 25 Pa; (d) 35 Pa; (e) 45 Pa; (f) 55 Pa; (g) 65 Pa; (h) Visual image.

4.5.3 Quantitative results of infrared thermography

Figure 4.3 is a visual representation of where the data was selected for further analysis. Three regions of interest with the same dimensions (Boxes 1–3) were defined for the wood frame. Two other regions of interest were defined for the aluminum foil (Box 4; reflected temperature) and the aluminum frame (Box 5). The exterior air temperature held approximately constant during each test. However, since the depressurization test constantly introduced outdoor air with lower temperature and heating supply air was masked off, the inside air temperature decreased by ~1.7 °C during the course of the 25 min test. It is to be noted that the indoor air temperature varies during the test, and in this study all the calculations are based on temperature differences.

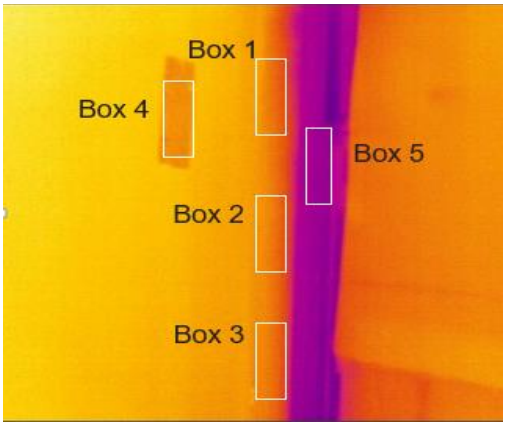

Figure 4.3 Regions of interest: Box 1–3: wood frame; Box 4: aluminum foil; Box 5: aluminum frame.

Figure 4.4 shows that by increasing ΔP, the mean temperature of boxes 1 to 3 decreased due to the higher air flow and velocity of the colder outdoor air to indoors through the corresponding adjacent cracks. Therefore, it can be concluded that a more convective heat transfer occurs as a result of increased ΔP. This effect was more significant within box 1, indicating a larger crack in the vicinity of this box compared to others. It is also seen that the decrease in temperature at $\Delta P < 25$ Pa appeared to be insignificant, likewise, as shown in the qualitative approach. However, it is notable that surface temperatures decreased significantly at ΔP of 25 Pa which were approximately 3, 2, and 1 °C for boxes 1 to 3, respectively. The effect of a higher ΔP is less important as the surface temperature in each of the boxes approaches that of the outdoor air. The surface temperature of box 1 at the end of the test approached the exterior air temperature, while Boxes 2 and 3 had differences of about 1.5–2.5 °C compared to the exterior.

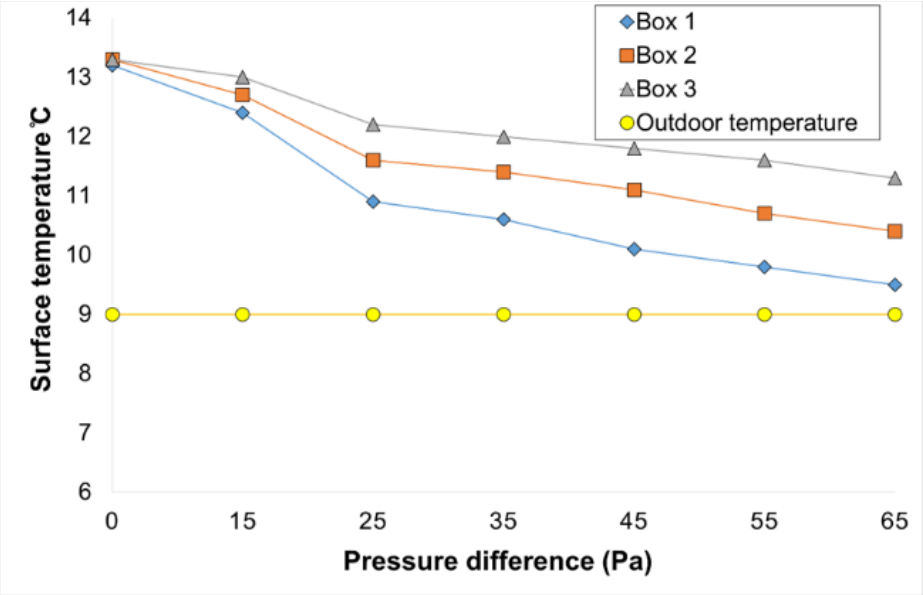

Figure 4.4 Variation of the surface temperature at the different pressures (Day 1).

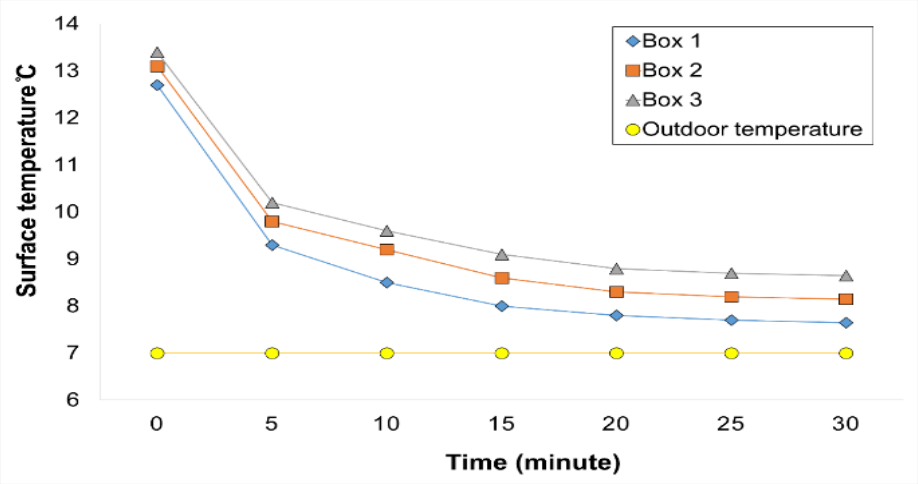

Figure 4.5 Variation of the surface temperature over time at 60 Pa (Day 3).

Furthermore, an alternative approach, a dimensionless temperature index (TI), was implemented to identify and prioritize the areas of air leakage. This index is often used for the hygrothermal performance assessment of the exterior building envelopes in any climate [33]. The index is defined as in Equation (4.2):

$$TI = \frac{T_{s,in} - T_o}{T_i - T_o} \tag{4.2}$$

where $T_{s,in}$ is the indoor surface temperature, T_o is the outdoor temperature and T_i is the indoor temperature. The temperature index (TI) has a value between 0 and 1, where 0 represents an equal

exterior air and interior surface temperatures, while 1 represents equal interior surface and interior temperature. From Equation (4.2) it can be deduced that a higher TI represents a lower air leakage rate at the vicinity of the air leakage areas.

Equation (4.2) is based on the assumption that the building envelope is in a steady-state condition. Therefore, a test on Day 3 was performed where the pressure was maintained at $\Delta P = 60$ Pa for at least 30 min and thermal images were recorded. As shown in Figure 4.5, the surface temperature of three areas (Boxes) decreased significantly in the first 15 min because of the high rate of convective heat transfer, while after around 20 min the decrease in temperature between measurements was negligible due to the reduced convective heat transfer.

In order to determine the air leakage contribution of an area, temperature indices (TIs) were calculated for the three selected regions of interest (Boxes) as shown in Table 4.5. At 30 min, the TIs for Boxes 1 to 3 were 0.06, 0.10 and 0.14, respectively. However, before the depressurization test (t = 0) these values were 0.45, 0.48 and 0.51 for boxes 1 to 3, respectively, implying that the contribution of air leakage to the surface temperature of Box 1 was more than that of Boxes 2 or 3. As mentioned above, the variation of indoor air temperature from 19.60 °C to 18.60 °C was considered in the calculations of TIs (Table 4.5). It should be noted that considering the constant indoor air temperature after 30 min would vary TIs between 6% and 16%.

It is also seen that after depressurization, TI was reduced by a factor of 7.5, 4.8, and 3.6 for Boxes 1, 2 and 3, respectively. This analysis suggests that the TI ratio can be a quantitative indicator of relative air leakage in this scenario. Hence, this approach could be helpful on a whole building scale, where areas of air leakage identified in this manner should likely be prioritized compared to other sources for air sealing.

Table 4.5 Variation of the temperature index (TI) over the time ($\Delta P = 60$ Pa).

Time (minutes)	**Surface Temperature (°C)**			**Temperature index (TI)**			**Outdoor temperature (°C)**	**Indoor temperature (°C)**
	Box 1	Box 2	Box 3	Box 1	Box 2	Box 3		
0	12.72	13.12	13.41	0.45	0.48	0.51	7	19.60
30	7.65	8.15	8.65	0.06	0.10	0.14	7	18.60

Figure 4.6 illustrates an image subtraction approach in an effort to study air leakage thermal pattern delineation at a different ΔP. The subtracted thermogram ($\Delta T_{\Delta P}$) depicts the difference between the initial thermogram (i.e., at ΔP = 0) and the thermogram at different pressure differential levels (i.e., ΔP = 15, 25, 35, 45, 55 and 65 Pa) as shown in Figure 4.6. The motivation for this approach originated from analyzing Figure 4.2 at a higher ΔP (55 Pa or 65 Pa) or lower ΔP (15 Pa or 25 Pa) where the thermal patterns appear to be similar and show poor air leakage delineation (i.e., the locations of air leakage were unclear).

Higher $\Delta T_{\Delta P}$ shows an increased directional resolution of thermal patterns (see Figure 4.6) at sources of air leakage. Another advantage of this method is that the characteristics of air leakage through cracks are potentially better identified by thermal patterns and temperature differences, such as the direction of air infiltration (crack geometry), or the relative rate of infiltration. Finally, image subtraction could be helpful in the detection of small cracks where surface temperature variation is within the temperature detection error of the infrared camera. For example, in Figure 4.2 at lower pressure differences (15–25 Pa), small cracks were not visible, while in Figure 4.6 these differences are considerably more pronounced.

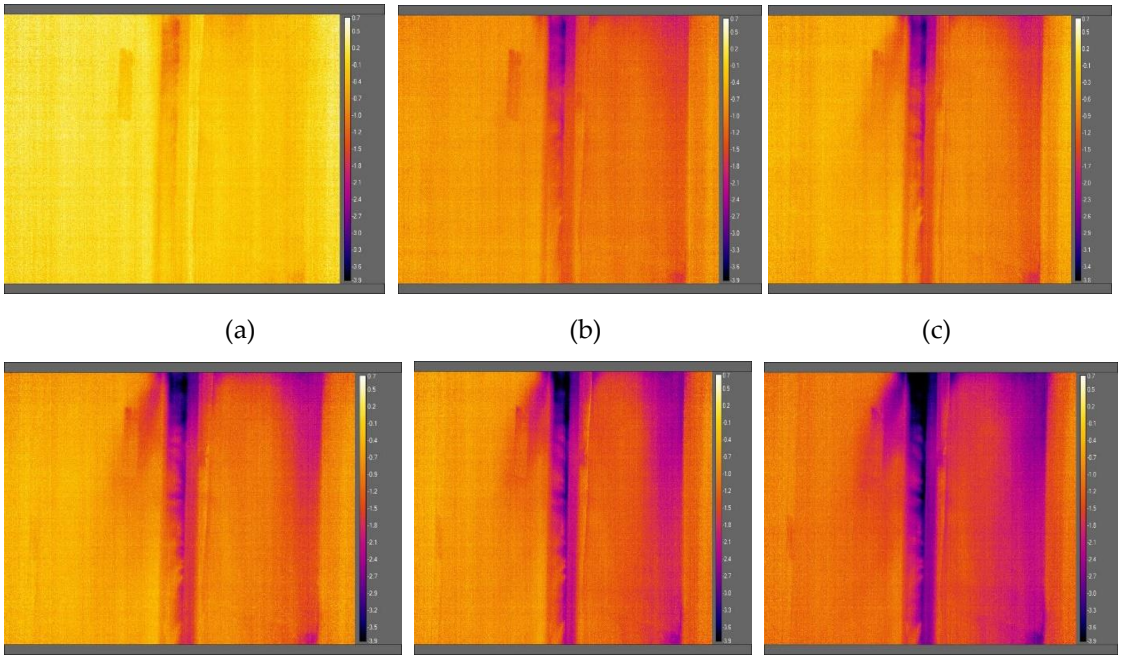

(a) (b) (c)

(d) (e) (f)

Figure 4.6 Subtracted thermograms (a) (ΔP=15)-(ΔP=0); (b) (ΔP=25)-(ΔP=0); (c) (ΔP=35)-(ΔP=0); (d) (ΔP=45)-(ΔP=0); (e) (ΔP=55)-(ΔP=0); (f) (ΔP=65)-(ΔP=0)

Based on the thermal patterns in Figure 4.6 (along the probable path of air flow), a subsequent analysis was conducted on the data by selecting three lines of interest as outlined in Figure 4.7a. Figure 4.7(b–d) shows the temperature difference variation through the lines at three different $\Delta T_{\Delta P}$. The power trend line ($y=ax^b$) fit coefficients and goodness of fit are shown in Table 4.6 for the range of $\Delta T_{\Delta P}$ studied for each line of interest.

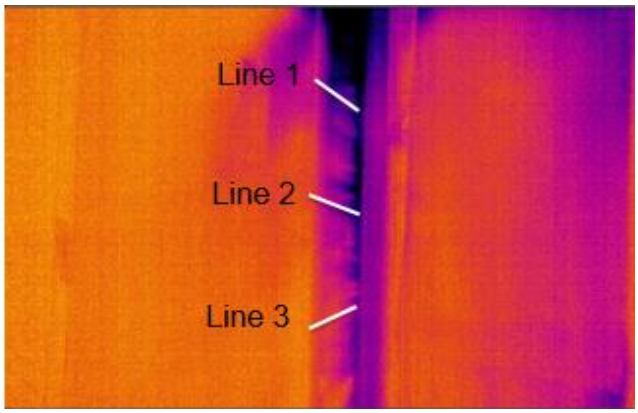

(**a**)

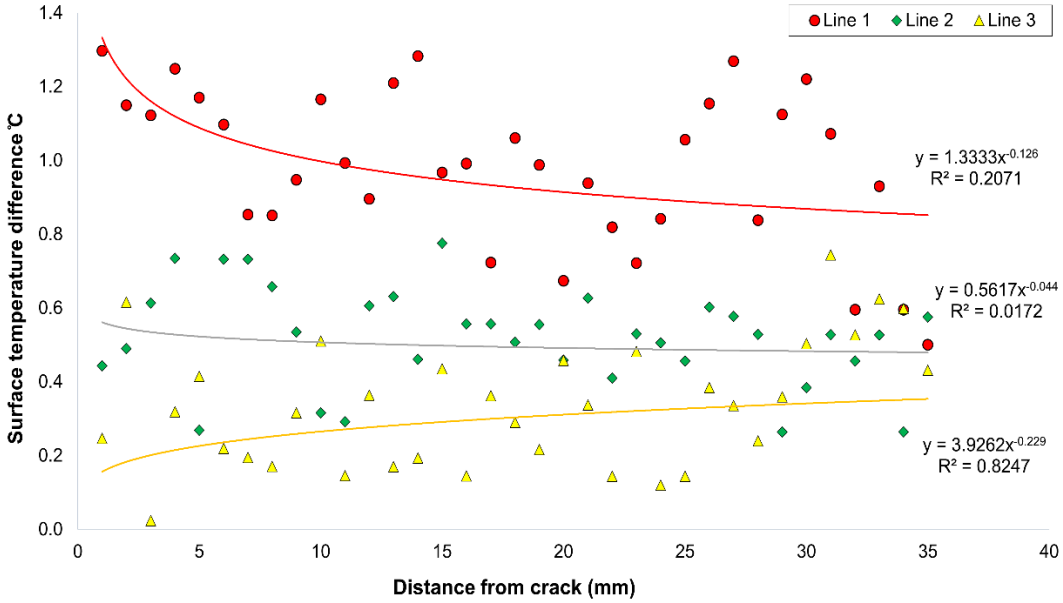

(**b**) (15–0 Pa)

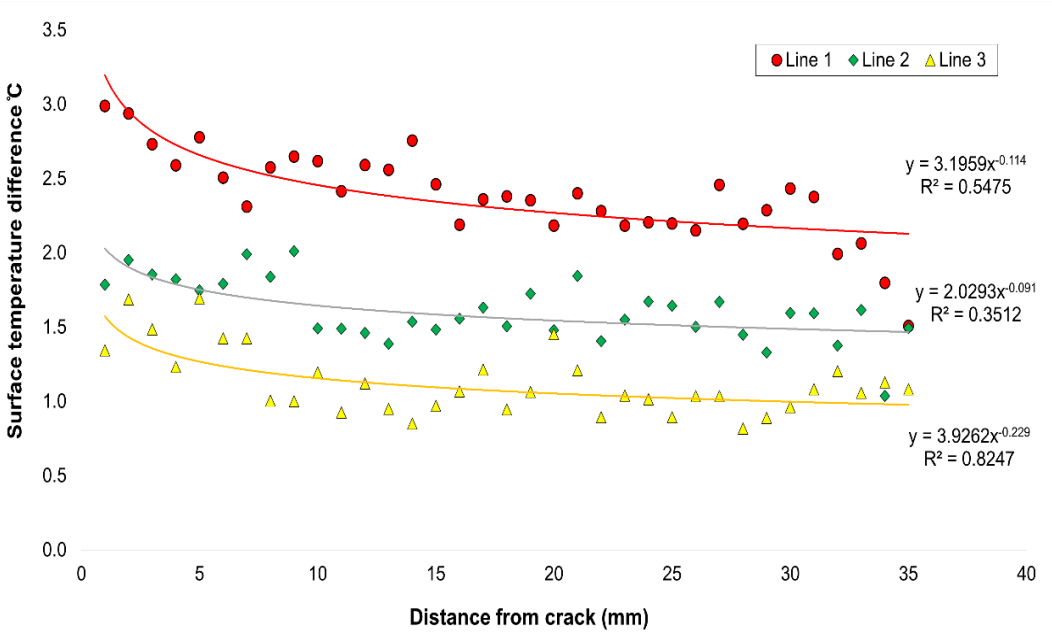

(**c**) (25–0 Pa)

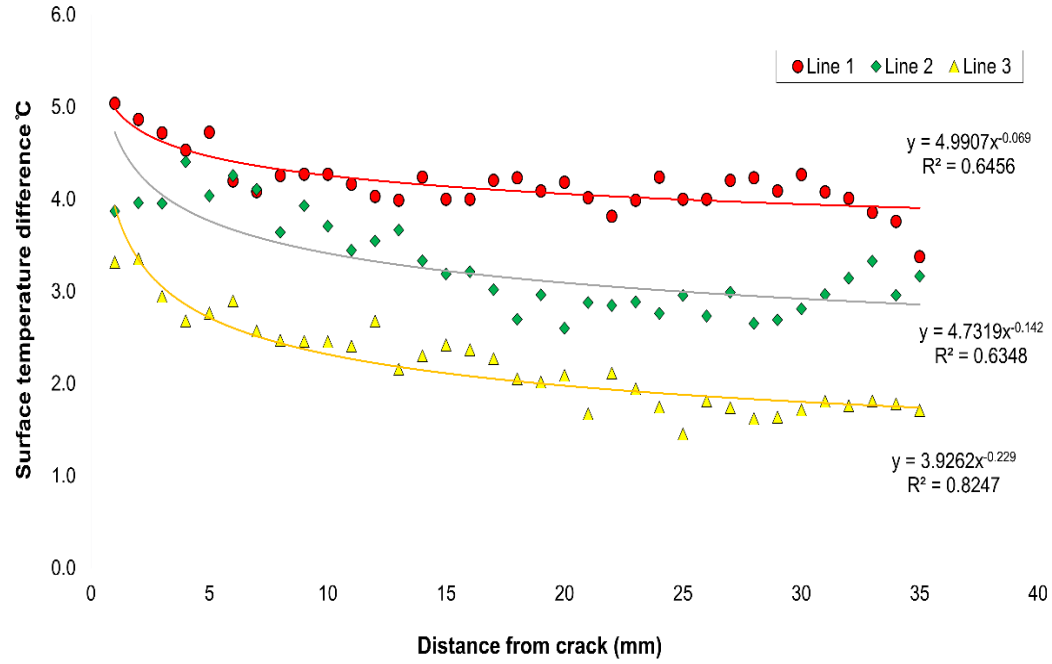

(**d**) 65–0 Pa

Figure 4.7(a) Paths of air leakage analyzed, and the surface temperature differences vs. the distance from the crack at: (b) 15–0 Pa, (c) 25–0 Pa, and (d) 65–0 Pa.

Subtracted pressure differential (Δ(ΔP))	*a**			*b***			R^2		
	Line 1	Line 2	Line 3	Line 1	Line 2	Line 3	Line 1	Line 2	Line 3
15–0 Pa	1.33	0.56	0.15	−0.13	−0.04	0.22	0.20	0.01	0.09
25–0 Pa	3.19	2.02	1.57	-0.11	-0.09	-0.13	0.54	0.35	0.38
35–0 Pa	3.69	2.58	1.82	-0.13	-0.15	-0.24	0.59	0.53	0.47
45–0 Pa	4.36	3.04	2.77	-0.09	-0.13	-0.32	0.56	0.42	0.76
55–0 Pa	4.60	3.91	3.21	-0.08	-0.11	-0.24	0.60	0.61	0.79
65–0 Pa	4.99	4.73	3.92	-0.07	-0.10	-0.23	0.64	0.63	0.82

a*: intercept coefficient
b**: decay coefficient.

Interestingly, the intercept coefficient a (i.e., the temperature difference adjacent to crack) appears to be largest for line 1 and smallest for line 3 in each scenario, indicating a larger temperature difference and consequent heat loss at the crack. The surface temperature close to the crack is influenced more at a higher pressure differential along line 1 than along lines 2 and 3, likely indicating a corresponding difference in the air leakage rate. This is justifiable based on thermal patterns in Figure 4.6. The intensity of flow streamlines around line 1 is larger compared to other lines, which suggests a higher rate of airflow around it.

When comparing the lines studied, the coefficient b does not exhibit a meaningful trend until the subtracted pressure differential (Δ(ΔP)) is 45 Pa, where it increases in magnitude (|bLine1|< |bLine2|<|bLine3|); this threshold Δ(ΔP) is possibly as a result of higher induced pressures required for accurately characterizing relative air leakage contribution on surface temperatures around different cracks. In terms of the b coefficient, it is conceivable that smaller cracks have less air infiltration and consequently induce less heat transfer, therefore surface temperature effects are smaller at higher distances from the crack. Furthermore, it is noted that the goodness of fit (R^2) increases with each increasing Δ(ΔP) for all the lines.

4.6 Conclusions

The result of the blower door test showed that the air leakage rate for the test object (laboratory room) was considerably higher in the test than suggested by the building codes. Combining the blower door test with thermography identified that certain regions at the window frame to wall interface were considerable sources of air leakage, and should be prioritized for air sealing. It was also demonstrated that the information obtained from the infrared thermography can be used for both qualitative and quantitative analyses for the comparison of air leakage characteristics.

From a qualitative perspective, the surface temperature near the aluminum and wood frame interface appeared colder than in other areas, and the increasing ΔP resulted in even lower temperatures. Areas of air leakage were slightly detectable at a lower ΔP; however, they could be easily missed due to the surrounding thermal bridging of building assemblies. Higher ΔP was more effective at delineating the air leakage from thermal bridges or other potential thermal anomalies. Notably, in this study, thermograms at 25 Pa were required for the reasonable detection of air leakage with thermography, contrary to some published standards citing 5–10 Pa.

From a quantitative perspective, IRT showed that most of the surface temperature decrease (~60% of ΔT) occurred between 0 and 25 Pa. Increasing ΔP above 25 Pa appeared to have a smaller impact on the surface temperature since the surface approached the outdoor air temperature, likely due to the effect of higher convection heat transfer. It should be noted that the contribution of a lower temperature difference vs. a higher flow rate to overall heat transfer needs further study. For further evaluation, two approaches of quantitative prioritization of air leakage were adopted: (1) the assessment of the average temperature index in three pre-defined regions of interest, and (2) an assessment of the surface temperature profile along a path of air infiltration at different ΔP using the image subtraction technique. These approaches showed promise in inferring the location of air leakage and the relative size of cracks based on streamline intensities, which were not evident in previous studies. It is desirable to keep room temperature constant to enhance the accuracy of quantitative approaches as well as delineate the sources of air leakage from thermal bridging effects in buildings. Reducing the duration of the test would presumably achieve this outcome, not allowing enough time for room temperature to decrease appreciably. Future modifications to this methodology could explore how to apply a correction technique to the results as an additional normalization exercise.

The qualitative and quantitative approaches used in this study could potentially be implemented by practitioners for the identification and prioritization of sources of air leakage in buildings. Furthermore, as a blower door test becomes a building code requirement in an increasing number of Canadian jurisdictions, performing IRT simultaneously is a potentially valuable complement to characterizing/prioritizing sources of air leakage.

To absolutely quantify the air leakage contribution of each component, additional information, such as the flow exponent “n” and flow coefficient “C”, are required independently for each

building component deficiency (cracks or gaps). The crack geometry and the air velocity can then be obtained based on the image subtraction and TI approach. This will form part of future investigations.

It should be noted that the tests were performed during the heating months, where high temperature differences between the interior and exterior were achievable. Future work will test the feasibility of the performing IRT at lower temperature differences as a sensitivity analysis exercise. A pressurized condition will also be evaluated to confirm the feasibility of obtaining meaningful results from exterior thermography. Moreover, during the next phase of this research initiative, larger areas of building will be investigated to differentiate areas of air leakage from thermal bridges, for a more complete evaluation of where and how much air leakage is occurring through a building envelope.

4.7 References

[1] International Energy Agency. Available online:

https://www.iea.org/topics/energyefficiency/buildings/ (Accessed on 28 April 2020).

[2] ASHRAE. ASHRAE Guideline 0–2019, The Commissioning Process; American Society of Heating, Refrigerating and Air-Conditioning Engineers: Atlanta, GA, USA, 2019.

[3] McKenzie-Mohr, D. Fostering Sustainable Behavior: An Introduction to Community-Based Social Marketing, 3rd ed.; New Society Publishers: Gabriola Island, BC, Canada, 2011.

[4] Cho, K.H.; Kim, S.S. Energy Performance Assessment According to Data Acquisition Levels of Existing Buildings. Energies 2019, 12, 1149.

[5] RDH Building Science Inc. Illustrated Guide: Achieving Airtight Buildings; BC Housing, BC Hydro, and the City of Vancouver: Burnaby, BC, Canada, 2017.

[6] Pinto, M.; Viegas, J.; de Freitas, V. Air permeability measurements of dwellings and building components in Portugal. Build. Environ. 2011, 46, 2480–2489.

[7] Lerma, C.; Barreira, E.; Almeida, R.M. A discussion concerning active infrared thermography in the evaluation of buildings air infiltration. Energy Build 2018, 168, 56–66.

[8] Meiss, A.; Feijó-Muñoz, J. The energy impact of infiltration: A study on buildings located in north central Spain. Energy Effic. 2015, 8, 51–64.

[9] Kalamees, T. Air tightness and air leakages of new lightweight single-family detached houses in Estonia. Build. Environ. 2007, 42, 2369–2377.

[10] Barreira, E.; Almeida, R.M.; Moreira, M. An infrared thermography passive approach to assess the effect of leakage points in buildings. Energy Build. 2017, 140, 224–235.

[11] National Research Council (NRC). National Energy Code of Canada for Buildings; National Research Council Canada: Ottawa, ON, Canada, 2015.

[12] ASTM International (American Society for Testing and Materials). E779-19. Standard Test Method for Determining Air Leakage Rate by Fan Pressurization; ASTM: West Conshohocken, PA, USA, 2019.

[13] International Organization for Standardization (ISO). EN ISO 9972: 2015-Determination of Air Permeability of Buildings-Fan Pressurization Method; ISO: Geneva, Switzerland, 2015.

[14] US Army Corps of Engineers (USACE). Air Leakage Test Protocol for Building Envelopes—Version 3; US Army Corps of Engineers: Champaign, IL, USA, 2012.

[15] Emanuela, G.; Sanjuan, C.; Blanco, E.; Heras, M.R. Experimental assessment and modelling of the performance of an open joint ventilated façade during actual operating conditions in Mediterranean climate. Energy Build. 2012, 54, 363–375.

[16] Balaras, C.A.; Argiriou, A. Infrared thermography for building diagnostics. Energy Build. 2002, 34, 171–183.

[17] Asdrubali, F.; Baldinelli, G.; Bianchi, F. A quantitative methodology to evaluate thermal bridges in buildings. Appl. Energy 2012, 97, 365–373.

[18] Gonçalves, M.D.; Gendron, P.; Colantonio, A. Commissioning of Exterior Building Envelopes of Large Buildings for Air Leakage and Resultant Moisture Accumulation Using Infrared Thermography and Other Diagnostic Tools; Thermal Solutions: Sarasota, FL, USA, 2007.

[19] Van De Vijver, S.; Steeman, M.; Carbonez, K.; Van Den Bossche, N. On the Use of Infrared Thermography to Assess Air Infiltration in Building Envelopes, International Workshop : Quality of Methods for Measuring Ventilation and Air Infiltration in Buildings, Proceedings; Air Infiltration and Ventilation Centre (AIVC): Brussels, Belgium, 2014.

[20] Ascione, F.; Bianco, N.; De Masi, R.F.; de'Rossi, F.; Vanoli, G.P. Energy retrofit of an educational building in the ancient center of Benevento. Feasibility study of energy savings and respect of the historical value. Energy Build. 2015, 95, 172–183.

[21] Liu, W.; Zhao, X.; Chen, Q. A novel method for measuring air infiltration rate in buildings. Energy Build. 2018, 168, 309–318.

[22] Hart, J. A Practical Guide to Infrared Thermography for Building Surveys; Building Research Establishment: Watford, UK, 1991.

[23] Wahlgren, P.; Sikander, E. In Methods and materials for an airtight building. In Proceedings of the 11th International Conference on Thermal Performance of the Exterior Envelopes of Whole Buildings, Buildings XI, Clearwater Beach, FL, United States, December (5-9), 2010.

[24] Dufour, M.B.; Derome, D.; Zmeureanu, R. Analysis of thermograms for the estimation of dimensions of cracks in building envelope. Infrared Phys. Technol. 2009, 52, 70–78.

[25] Residential Energy Services Network (RESNET). RESENET Interim Guidelines for Thermographic Inspections of Buildings; Residential Energy Services Network: Oceanside, CA, USA, 2012.

[26] ASTM International (American Society for Testing and Materials). E1186-17. Standard Practices for Air Leakage Site Detection in Building Envelopes and Air Barrier Systems; ASTM: West Conshohocken, PA, USA, 2017.

[27] National Master Specification (NMS). NMS 022713 Thermographic Assessment- Building Envelope; National Research Council Canada: Ottawa, ON, Canada, 2007.

[28] ASTM International (American Society for Testing and Materials). C1060-11a. Standard Practice for Thermographic Inspection of Insulation Installations in Envelope Cavities of Frame Buildings; ASTM: West Conshohocken, PA, USA, 2015.

[29] International Organization for Standardization (ISO). ISO 6781-3: 2015, Performance of Buildings—Detection of Heat, Air and Moisture Irregularities in Buildings by Infrared Methods—

Part 3: Qualifications of Equipment Operators, Data Analysts and Report Writers; ISO: Geneva, Switzerland, 2015.

[30] British Standards Institution (BSI). BS EN 13187:1999, Thermal Performance of Buildings-Qualitative Detection of Thermal Irregularities in Building Envelops-Infrared Method, Brussels; BSI: London, UK, 1999.

[31] ASTM International (American Society for Testing and Materials). E1933-14. Standard Practice for Measuring and Compensating for Emissivity Using Infrared Imaging Radiometers; ASTM: West Conshohocken, PA, USA, 2014.

[32] ASTM International (American Society for Testing and Materials). E1862-14. Standard Practice for Measuring and Compensating for Reflected Temperature Using Infrared Imaging Radiometers; ASTM: West Conshohocken, PA, USA, 2014.

[33] Mill. P.A.D. Thermographic Diagnosis of Building Envelope Deficiencies, Fathers of Confederation Center; Report Series No. 28; Public Works Canada: Ottawa, Ontario, Canada, 1979; ISBN 0-662-50335-X.

Chapter 5: Quantitative IRT with UAVs for Thermal Assessments of Building Envelopes: Challenges & Best Practices

5.1 Abstract

Early detection and repair of building envelope defects can help improve durability and energy performance. Utilizing the emergent technology of small unmanned aerial vehicles (UAVs) equipped with an infrared camera provides an opportunity to perform quick thermal assessments of building envelopes. This study outlines the advantages and limitations of aerial surveys compared to conventional stationary infrared thermography (IRT). Furthermore, a set of best practices for UAV-IRT were presented to minimize dynamic measurement uncertainty. Results showed that induced convection from drone propellers significantly influences performance of the IR camera and subsequently measurement accuracy. Deviations between dynamic and stationary measurements decreased over time as a result of IR camera microbolometer stabilization with surrounding environmental conditions. To reduce the required time for camera stabilization and improve accuracy of measurements, subsequent investigations utilized a shield around the camera to minimize the convective turbulence on the lens and thermal sensors. It was concluded that with the current IR camera technology, aerial surveys for quantitative thermal assessment of building envelope are not as accurate as with conventional infrared thermography; further investigations by manufacturers and researchers are recommended.

Keywords: UAV, Infrared Thermography, Dynamic, Stationary, Wind, Microbolometer

5.2 Introduction

Infrared (thermographic) cameras were first developed for military applications [1] and became available to the commercial market in the late 1960s as bulky and cumbersome packaged equipment that required extensive cooling [2]. Current infrared (IR) cameras have improved in size efficiency but effectively follow similar physical properties and operation as their predecessors. Within the camera, a thermal detector interprets the infrared radiation emitted from a subject based on Plank's Law and the Theory of Grey Body Radiation, producing an image in the form of a colorized or greyscale temperature map [1]. The most common thermal detector in IR cameras is a microbolometer focal plane array (FPA) which works at room temperature and does not require an expensive cooling component. This method of temperature measurement, known as infrared thermography (IRT), is non-contact, non-destructive and quick, and can provide real-time two-dimensional data. IRT has been used in different fields, in particular as a promising investigative tool for building envelope inspections over the last few decades [3].

Current building envelope inspections using handheld cameras are time-consuming and may require surveys from the interior as well as the exterior to fully understand façade condition. This method of data collection provides an overview of the building envelope but often neglects smaller details and defects, which necessitates utilization of unaided ground crew or traditional lift equipment in most cases. In other words, a comprehensive thermographic inspection of all façade elements becomes very time-consuming depending on building size, and is potentially disruptive to building occupants [4]. As technology has advanced, infrared (IR) sensors have become significantly smaller and lighter facilitating integration with unmanned aerial vehicles (UAVs) or "drones" for survey purposes, such as for building energy audits. In this context, an opportunity exists for practitioners to rapidly analyze building envelope thermal performance considering pixel intensities in thermal images. Also, with recent advancements in quantitative IRT and capabilities of building energy simulation tools, aerial survey platforms provide a unique opportunity for the development of a more cost-effective, accurate, and automated building envelope energy auditing technique, as well as opportunities to apply it for the monitoring and maintenance of built environment infrastructure [4] at the municipal level.

UAVs enable professionals and researchers to rapidly analyze and identify thermal anomalies in building envelopes while reducing operations costs compared to traditional methods and

minimizing the safety risks during the surveys [5]. This allows easy access to remote or inaccessible areas of a building and gives the operator unprecedented flexibility during the thermographic surveys as they are able to position the camera to overcome obstructions and reflections from nearby buildings and other radiative sources. For instance, inspections of upper floor façade elements in taller structures are otherwise only feasible with internal thermography since external IRT with a handheld camera at grade cannot provide accurate data due to the importance of distance and angle of view. However, UAVs capable of vertical take-off and landing have the ability to hover in midair and are far less restricted in their ability to collect meaningful data. In addition, when thermal anomalies are found, a UAV can be maneuvered to document it with improved resolution and to mitigate the impact of other reflections [6].

Today's flight procedures can be performed with full automation to record, photograph and hover at each location using an onboard Global Positioning System (GPS), a method that can further minimize the time required to conduct a survey. Automation allows for the collection of data in a repeatable and consistent manner, ensuring survey parameters such as viewing angle, speed of flight, and distance from the subject façade are kept near-constant [4]. Taher compared the accuracy of GPS with ground control points informed by Google Earth Pro and found onboard GPS to be more accurate [7]. Despite this advantage, a critical UAV flight obstacle is battery life, in particular for long flight situations (such as in the case of large buildings). Son et al. suggested pre-flight planning should be based on construction drawings or knowledge of where potential thermal anomalies exist. This method could minimize the flight time but may increase the error in determining the thermal leaks in buildings since the flight path is not based on areas of thermal anomalies [8]. It is to be noted that more than one audit is often required to evaluate the entire building accurately due to the presence of environmental obstacles such as buildings and tress which may obscure the façade details.

Other flight parameters such as distance to target, flight altitude, speed and flight pattern are also critical considerations in thermography with UAVs. Some researchers suggest various flight altitudes, ranging from 30 to 75 m above grade, in order to have an complete view, depending on the size of the building and IR camera specifications [9]. Similarly, various target distances were considered, such as 2-5m for evaluating damage in post-disaster areas [10] and <1m for identification of small cracks in concrete or masonry [11]. However, literature is not clear regarding an ideal distance for thermal inspection of building envelopes. Likewise, the flight path

plays a key role in quality of data collected, where researchers have suggested to fly the drone either vertically or horizontally in a zig-zag pattern across the regions of interest [12-16]; Eschamann and Wundsam showed that vertical strips result in lens movement which decreases data quality image clarity, while horizontal strips were found to be ideal especially when paired with a low flight speed [15].

With current methodologies in literature, it is possible to identify sources of heat loss through a building envelope in a short period of time using qualitative UAV thermographic surveys; however, there is a gap in research regarding quantitative UAV-IRT. This study investigates the potential of thermographic analysis using UAVs for quantitative thermal analysis of building envelopes. The results of dynamic measurements with drone are compared with stationary external IRT (handheld camera).

5.3 Research Method

The experiment was performed from the outside, on an insulated and conditioned wood-framed structure. The wall considered in the analysis is facing north and incorporates a double glazed window (Figure 5.1). The properties of the wall assembly are presented in Table 5.1. Surface temperature measurements were performed with a DJI Matrice 200 Series drone, paired with a FLIR Zenmuse XT2 IR camera which is specially designed to be mounted on the drone (Figure 5.2). To compare and validate the results, IRT measurements with a conventional hand-held IR camera (FLIR A65) was also considered. Camera specifications are shown in Table 5.2 and Figure 5.3.

Figure 5.1 The experimental structure, showing the wall considered for analysis

Table 5.1 Thermophysical properties of the wall assembly

Layer #	Component	Thickness (mm)	Conductivity (W/m K)	RSI-value (m^2 K/W)	3D Sketch
	Interior film	-	-	0.12	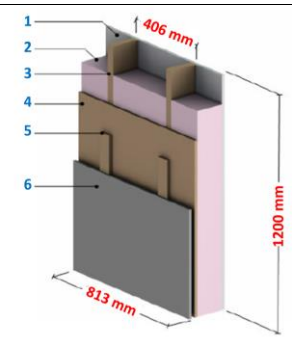
1	Gypsum Board	13	0.16	0.08	
2	Fiberglass Batt Insulation	140	0.036	3.89	
3	2 × 6 wood stud	140	0.10	-	
4	Exterior plywood sheathing	13	0.10	0.13	
5	1 × 3 wood strapping	19	0.10	-	
6	Vinyl Cladding with 19mm vented airspace incorporated into exterior heat transfer coefficient				
	Exterior film	-	-	0.12	
	Nominal RSI-value (m^2 K/W)	**4.34**			

Figure 5.2 Images of the drone with mounted Zenmuse XT2

The drone location was pre-determined with a flight altitude of 3 m above grade, and its distance from the target was ~8 m to ensure the entire wall was in the field of view of camera. FLIR ResearchIR[3] software was used to perform further analysis on thermal images, with functionality to change temperature span, colour palette, adjustments to parameters such as emissivity, reflected temperature, ambient air temperature, humidity, air transmission coefficient, and distance of camera to target. The tests were performed on a cloudy night with a stable outdoor air temperature, without wind or precipitation. A minimum temperature difference of 15 K was maintained during the surveys.

[3] https://www.flir.com/support-center/instruments/try-out-researchir-software

Table 5.2 Technical specifications of IR cameras

Model	Resolution (Pixels)	Thermal sensitivity	Field of view	Accuracy	Application
FLIR Zenmuse XT2	640 × 512	0.05 ºC	32° × 26°	±10 ºC	Drone mounted camera (powered by battery)
FLIR A65	640 × 512	0.05 ºC	45° × 37°	±5 ºC	Handheld camera (powered by AC)

Figure 5.3 IR cameras; (a) Zenmuse XT2 (drone-mounted camera); (b) FLIR A65 (handheld camera)

5.4 Results and Discussion

The results in Figure 5.4 are based on a survey on a cloudy day where the indoor and outdoor temperature were 22.12 ℃ and 7.22 ℃, respectively. Substantial deviations between surface temperature measurements with FLIR Zenmuse XT2 (airborne) and FLIR A65 (stationary) were observed during the test. Unexpectedly, the drone measurement showed temperature below 0 ℃, which was completely different from measurements obtained with stationary IRT. Also, the measured temperature gradually decreased from -8.31 ℃ to -24.42 ℃ after ~10 minutes while the drone was hovering. As illustrated in Figure 5.3, the surface temperature (Box 2) measured with the stationary camera was almost 8 ℃ while the measurement with the drone-mounted camera was about -24 ℃ (Box 1). To ensure the validity of measurements, several tests were performed on different days yielding a similar trend.

Considering these results, it was assumed that the Zenmuse XT2 IR camera was not adequately calibrated properly. However, due to the possibility of dynamic measurement uncertainty, it was decided to perform a static (grounded) measurement with the drone-mounted Zenmuse XT2 to understand potential confounding effects of flight. The drone was placed on a tripod and its propellers were turned off while thermal images were taken with its mounted camera. Results were more representative than the dynamic in-flight case (-4.52 ℃ vs -24.42 ℃) suggesting major interference from flight operation, likely from convective cooling effects induced by drone propellers on the camera. However, even in the grounded experiment the surface temperature registered below 0 ℃ (Figure 5.5), indicating that the camera may not be calibrated or external environmental conditions adversely affect its performance to a greater extent. Discussions with the manufacturer confirmed camera calibration, but also revealed that the temperature measurement accuracy of the Zenmuse XT2 can be affected by environmental factors since its accuracy (±10 ℃) was obtained in lab conditions. Indeed, the outdoor in-situ measurements in this experiment were beyond the camera's reported accuracy (±10 ℃). Finally, a subsequent experiment was performed under lab conditions where the surface temperature of a target was measured with both cameras. The result of measurement was relatively similar for both IR cameras (deviation of ~0.51 ℃). Therefore, it can be deduced that in-situ environmental conditions affect the Zenmuse XT2 more significantly than the FLIR A65.

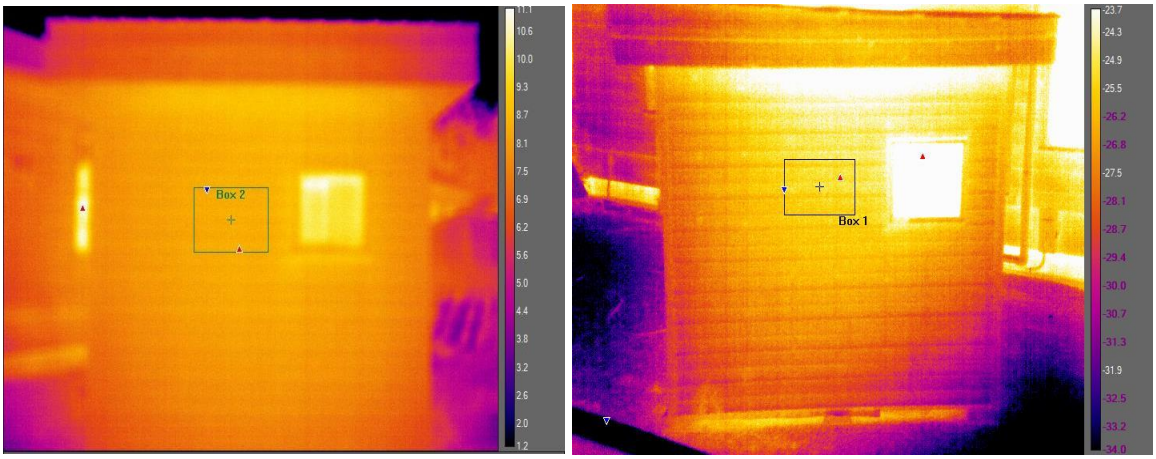

(a) (b)

Figure 5.4 Themral images obtained with (a) handheld camera (FLIR A65) with positive color scale; (b) drone-mounted camera (Zenmuse XT2) in-flight with negative color scale

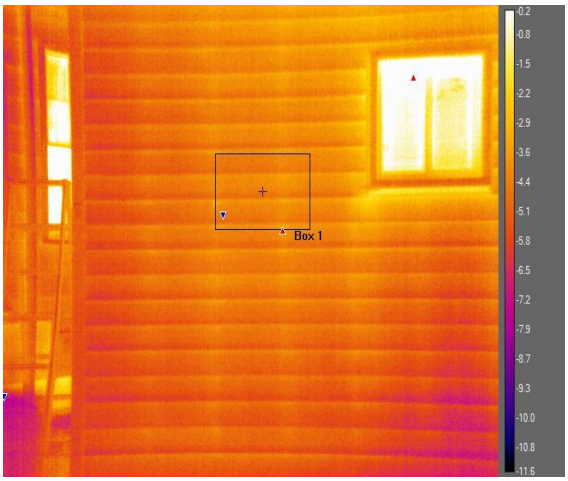

Figure 5.5 Thermal images obtained with grounded drone-mounted Zenmuse XT2 (propellers off)

However, temporal variations in temperature were not justifiable since wall surface temperature is not likely to have changed dramatically in a short period of time (~3 minutes). Therefore, three possible explanations were considered for these deviations: 1) the Zenmuse XT2 is not accurate enough for quantitative measurements and should be limited to qualitative measurements such as identifying locations of hot spots or large thermal contrasts (i.e., detecting wildfires where a deviation of 10-20 ℃ does not affect the conclusion of investigations); 2) the induced wind effect by drone's propeller influence the performance of IR camera (unstable environmental conditions around the camera) and consequently affect surface temperature measurements; or 3) depending

on the distance of camera to target, induced wind from the drone flight may increase convection heat transfer on the wall surface thereby magnifying surface temperature reduction. To this end, due to the reliability and better accuracy of static measurements with the handheld IR camera (FLIR A65), it was decided to mount this camera on the drone instead to understand dynamic accuracy in the presence of other factors (i.e., wind, ambient temperature, convection, distance).

A test (Case 1) was performed on a cloudy night where the wind speed was about 0.1 m/s, and indoor and outdoor temperatures were 24.22 ℃ and 9.24 ℃, respectively. The IR camera was warmed up for almost 30 minutes prior to the test to stabilize the IR camera microblometer with ambient temperature. Before the dynamic measurement, a static measurement was performed to for validation purposes (Figure 5.6). The dynamic measurements were conducted at two distances from the target (2m and 8m) to study the effect of forced convection on the wall surface due to drone-induced wind (Figure 5.7). Thermal images were recorded continuously for ~15 minutes, with a data acquisition interval of 1 second for each distance while the drone was hovering. The results of dynamic (green line) and static (dashed line) measurements belong to the Box 1 in Figure 5.7 are shown in Figures 5.8 and 5.9. It is seen that the temperatures decreased over time (dropped to 3.53 ℃), similar to the trend exhibited by the Zenmuse XT2, and were lower than stationary measurements. However, the accuracy of measurement was substantially better than Zenmuse XT2 since temperatures (1) were above 0 ℃, and (2) stabilized during the test (after ~14 minutes). Interestingly, the drone's distance to the target did not markedly influence the accuracy of measurements: temperature variation trends were almost identical for both distances studied, in spite of wind speed differences at the wall surface (about 1.52 m/s and 0.11 m/s at a drone distance of 2m and 8m, respectively). In other words, variations in convective heat transfer did not affect results. This finding suggests that drones may be able to get into close proximity with a building envelope to detect small defects or air leakage using IRT, without compromising results.

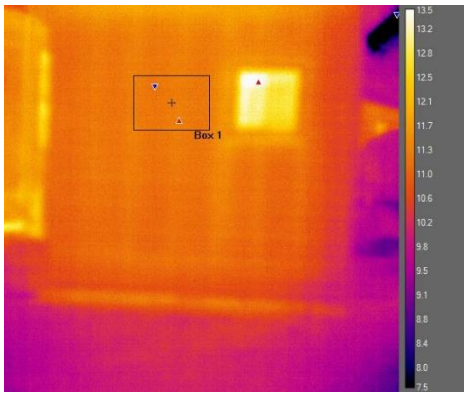

Figure 5.6 Stationary thermal image taken before dynamic measurement with drone

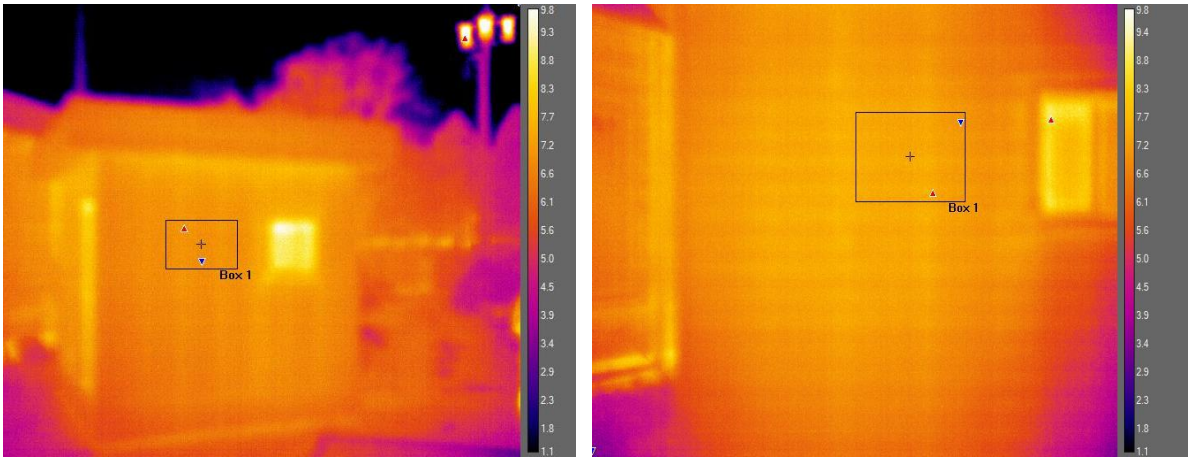

Figure 5.7 Thermal images taken with drone-mounted FLIR A65; (a) at distance of 8 m; (b) at distance of 2 m

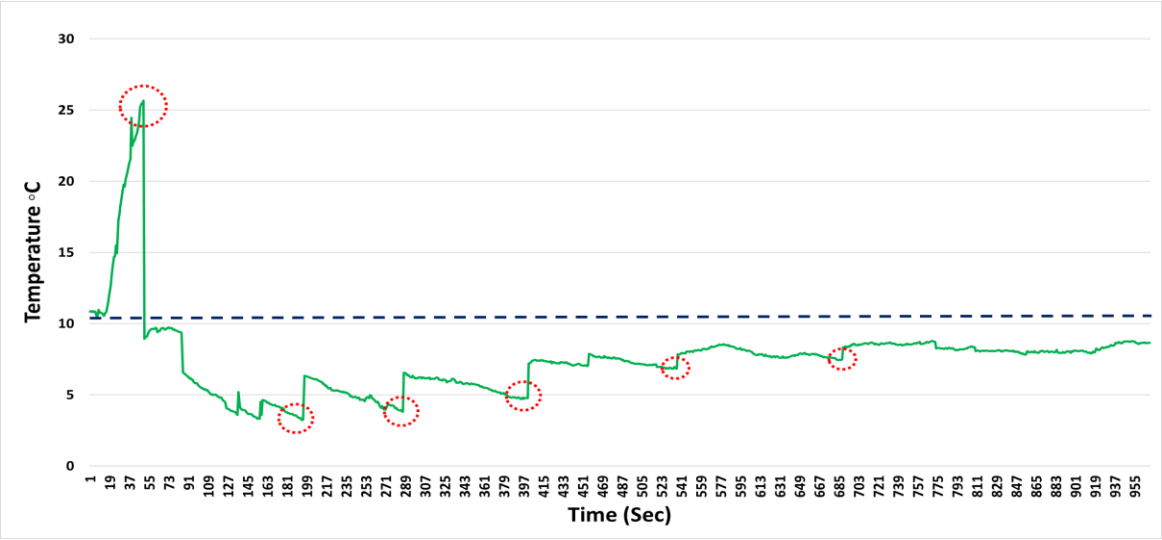

Figure 5.8 Dynamic (in-flight) thermal imaging with drone-mounted FLIR A65 at a distance of 8m from the wall surface; Static measurment (dashed line); Dynamic measurment (green line); Activation of NUC (red circles)

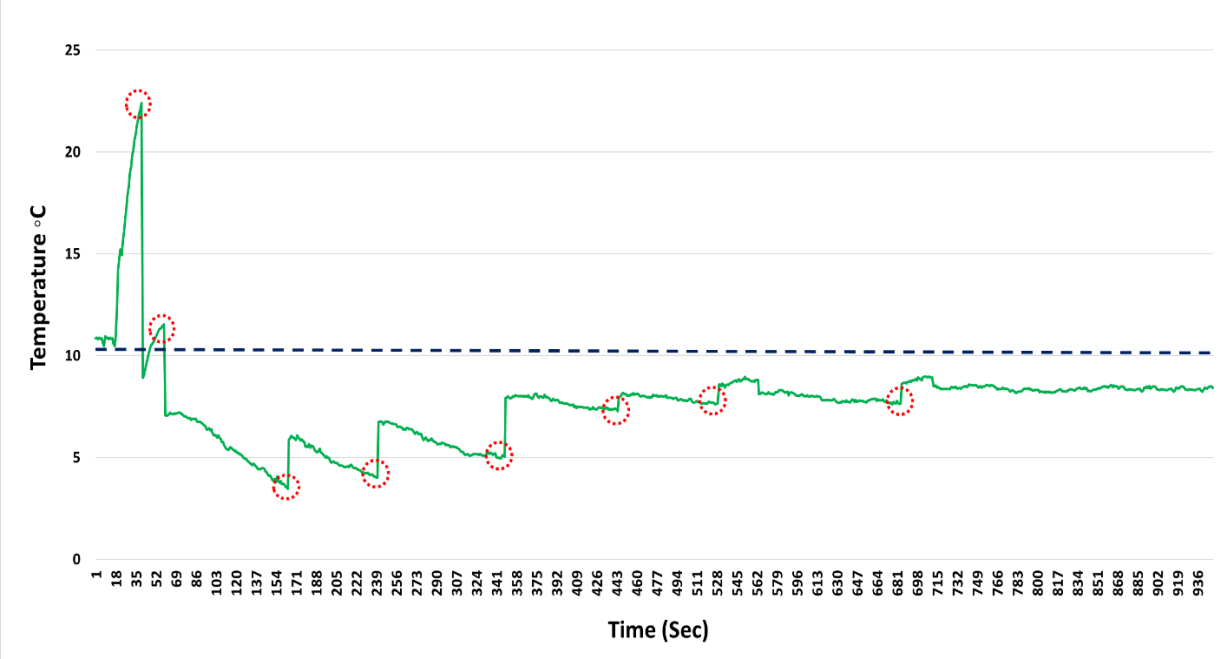

Figure 5.9 Dynamic (in-flight) thermal imaging with drone-mounted FLIR A65 at a distance of 2m from the wall surafce; Static measurment (dashed line); Dynamic measurment (green line); Activation of NUC (red circles)

Figures 5.8 and 5.9 also show a dramatic increase in temperature measurement shortly after take-off. This camera behaviour can be attributed to a sudden change in surrounding environmental conditions are created by drone-induced wind, where internal components of the camera are overcompensating before non-uniformity correction (NUC) function is activated (red circles) [17]. In other words, the camera experiences sudden changes where the rate of NUC activation (interval between NUCs) might be slower than environmental changes around the camera [17]. Since the microbolometer in an uncooled IR camera works at ambient temperature, any variation in ambient temperature would result in temperature variations of camera's interior and focal array plane (FPA), and eventually affect temperature measurement [3,17]. Budzier et al. [18] explained that some IR camera manufacturers use a predictive model which estimates the expected temperature of the camera interior based on its previous temperature variations. This may explain the over-compensation when the camera experiences larger temperature differences (ambient and camera temperatures) than those which have previously occurred [17, 18]. These findings were consistent with Kelly et al.'s [17] study where inconsistencies in camera output were explained during the take-off; the camera's temperature had a inverse correlation with temperature measurements.

After take-off and activation of the NUC function, the temperature measurement dropped to a lower magnitude than the stationary measurement highlighting the influence of drone-induced wind. To illustrate this in more detail, the variation of ambient temperature due to wind influences the stability of the focal plane array (FPA) temperature, which results in temperature drift. The temperature of the FPA is influenced by ambient air temperature since the lens of the camera is exposed to wind and the thermal conductivity from the lens to the FPA is high. Hence, due to the instability of the FPA temperature, further time is required for the FPA to reach thermal equilibrium. It should be noted that this time depends on the camera housing's heat dissipation characteristics which affects the magnitude of the temperature difference between the FPA and the ambient air temperature [3].

The spikes in temperature measurement at different intervals indicate the activation of NUC to harmonize signal response across the sensor. The non-uniformity correction (NUC) in the IR camera should be applied more frequently during aerial measurements than during stationary measurements to reduce the temperature drift. As illustrated in Figures 5.8 and 5.9, the difference between dynamic and static measurement decreases as the camera stabilizes with ambient air temperature. In both scenarios, the temperature almost converged with initial values after approximately 14 minutes. However, IRT-UAV data collection was limited by its almost 20-minute battery life which was insufficient for complete camera stabilization. It should be pointed out that it is not recommended to run the drone at its maximum battery life (20-minute) and this is why the tests were performed almost 14 minutes.

A lab-based experiment (indoor temperature of 25.46 °C) was performed to determine the required time for camera stabilization. To this end, a fan was positioned at a distance of 20 cm from a stationary IR camera while the surface temperature of the lab wall was recorded every second. A wind speed of ~4 m/s on the camera was measured with an anemometer, to mimic the flight condition (drone-induced wind). As shown in Figure 5.10, a rapid increase in temperature measurement was observed because of a sudden induced wind around the camera, a similar trend to the one observed in the flight experiment. However, after activation of first NUC the temperature dropped to 24.63 °C and after that fell to the 17.78 °C. This is consistent with earlier findings during the flight where the FPA had not yet reached thermal equilibrium at the beginning of the flight. However, after about 20 minutes the temperature approached its initial reading

converging to a nominal 0.54 °C temperature difference. This confirms the necessity of additional time for stabilization of FPA to improve measurement accuracy. However, because of constraints on flight time due to limited battery power and issues with powering the camera during flights, an extra flight time of 20 minutes or more may not be feasible despite reducing temperature drift.

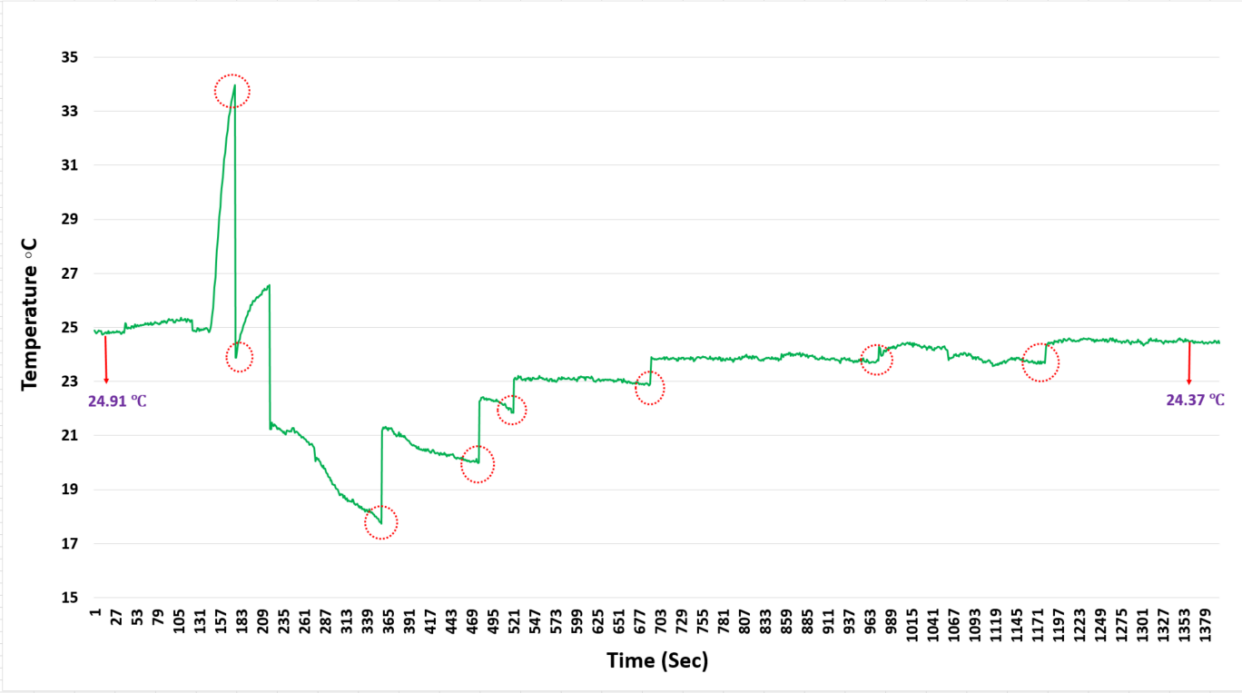

Figure 5.10 Temporal variation of surface temperature measurments in the lab; stationary IR camera exposed to fan-induced wind; Activation of NUC (red circles)

To minimize the impact of wind during the flight, a plexiglass wind shield was fabricated around the IR camera with a small opening for the lens (shown in Figure 5.11). A test flight (Case 2) for data collection was performed on a cloudy day where the indoor and outdoor temperatures were 24.42 ℃ and 9.12 ℃, respectively. It was found that temperature measurements decreased during take-off unlike the experiment that did not employ a windshield, which confirmed that the impact of wind on the performance of the camera is significant. Nonetheless, temperature deviations between stationary and dynamic conditions persisted (Figure 5.12). One possible explanation for this finding is that air turbulence around the camera influences the exposed lens, and consequently the microbolometer stability. Similar to the previous condition, the temperature measurement became more stable, and deviations became smaller. The findings of this experiment are summarized as follows:

1- The shield mitigates camera overcompensation (increase of temperature) during take-off.
2- The shield does not have a substantial effect on IR camera stabilization.
3- IR camera stabilization depends on the extent of lens exposure to surrounding environmental conditions
4- To improve results, it is suggested to shield the lens as much as possible from turbulent air around it

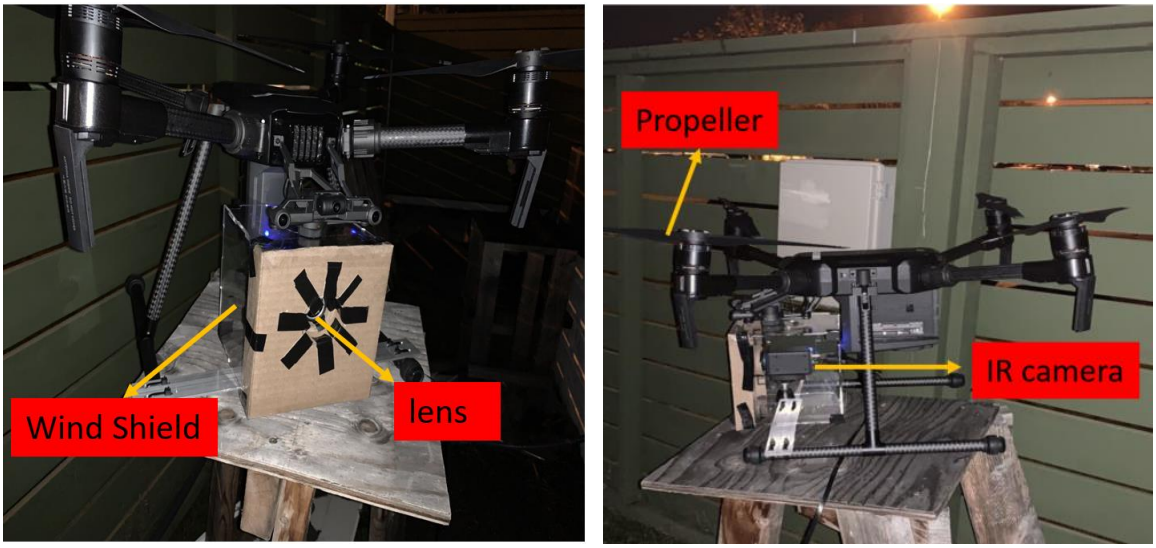

Figure 5.11 Prototype wind shield around the IR camera

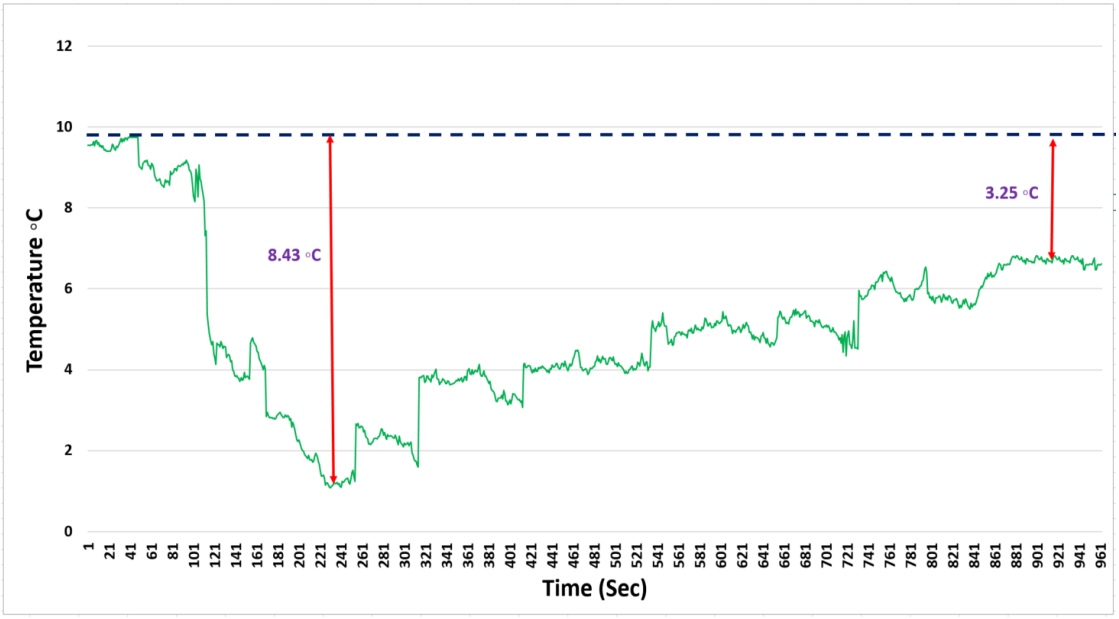

Figure 5.12 Temporal variation of surface temperature measurments with IR camera shielding; Static measurment (dashed line); Dynamic measurment (green line)

At the time of the survey, a cylinder was positioned around the lens (Case 3) to minimize the effect of turbulence on the lens of camera (Figure 5.13). From the resulting temperature measurements shown in Figure 5.14, it can be seen that:

- The temperature reduction was substantially smaller than scenarios without a cylindrical lens shield
- The temperature stabilized much faster than scenarios without a cylindrical lens shield
- The deviation between the stationary and dynamic temperature measurements was considerably lower than scenarios without a cylindrical lens shield (less than 1 ℃).

It can be concluded that since the lens was less exposed to turbulent air, its internal temperature deviation was mitigated and the camera stabilized faster.

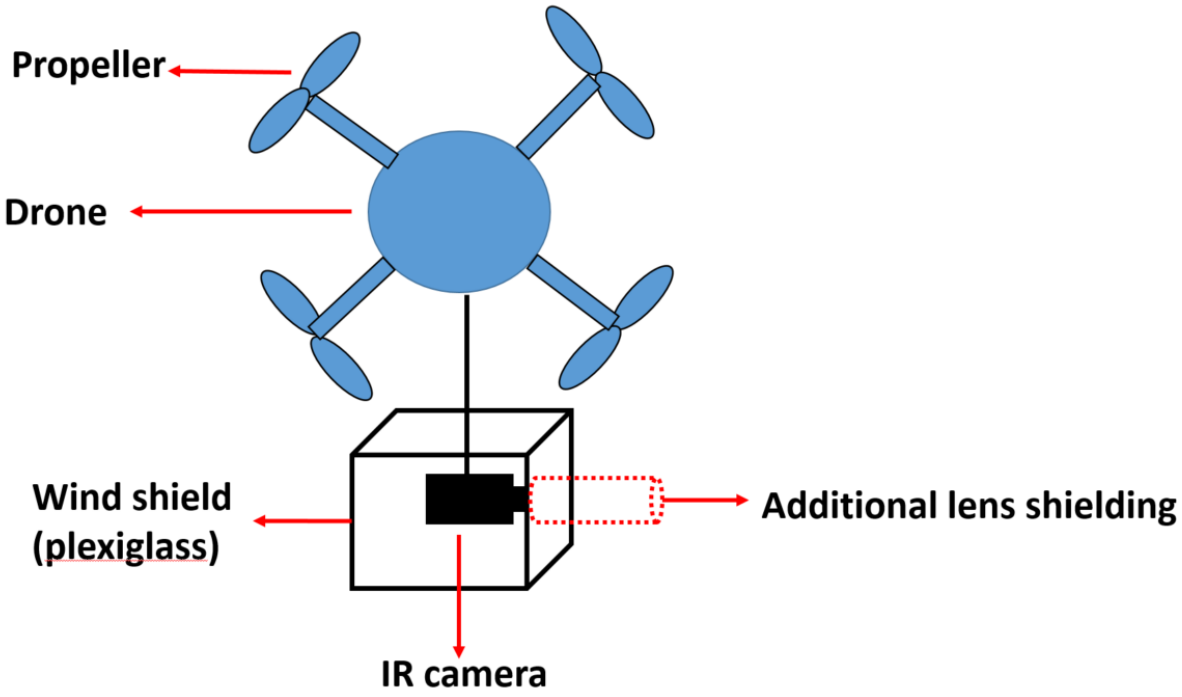

Figure 5.13 Schematic of additional lens shielding

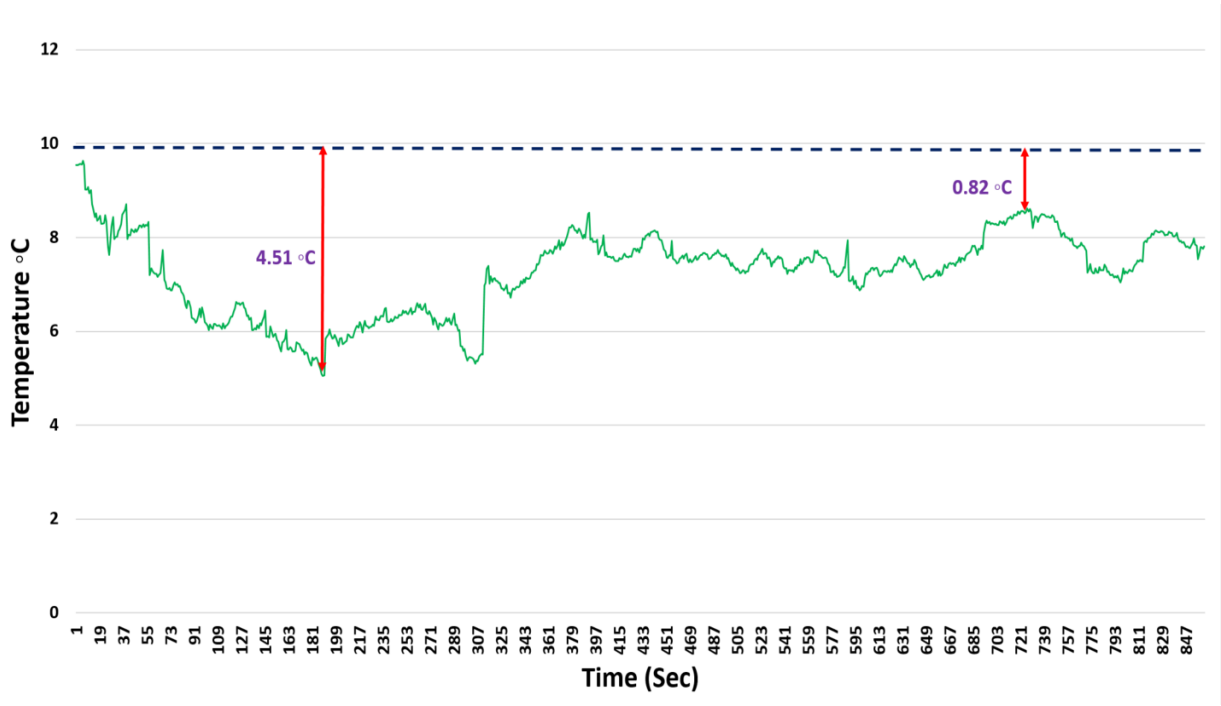

Figure 5.14 Temporal variation of surface temperature measurments with camera and additional lens shielding; Static measurment (dashed line); Dynamic measurment (green line)

5.5 Conclusions

In this study, dynamic IRT surveys were conducted on an insulated wood-framed wall assembly using an aerial UAV survey to evaluate the accuracy of dynamic measurement for quantitative thermal assessment of a building envelope. Furthermore, to validate the results of dynamic IRT measurements, stationary measurements were also conducted during the surveys. The main findings of this investigation are highlighted as follows:

- Dynamic and stationary IRT measurements can identify thermal anomalies in building envelopes qualitatively.
- The deviation of results between dynamic and stationary thermography were substantial; dynamic IRT measurements are not as accurate as stationary measurements.
- The thermal sensor is affected by drone-induced wind during the flight, resulting in sensor temperature instability affecting accuracy of results.

- The deviation of dynamic and stationary measurements became smaller over time, suggesting that as the sensors stabilize with environmental conditions during the flight, i.e., accuracy of results improves.
- Non-uniformity correction should be applied much more frequently during dynamic measurements than in stationary measurements, to reduce temperature drift.
- To minimize the effect of sudden turbulence around the camera during the flight, it is suggested to shield the camera as much as possible, particularly the lens.
- Due to the limitation of battery life in aerial surveys, a shield facilitates faster camera stabilization, consequently allowing more data collection.

This work initiated a step towards a highly automated and reliable method for inspecting and quantifying a building envelope thermal performance. Although the implications of UAV for qualitative thermal assessment of building envelope has been widely studied, more research is required to develop a robust protocol for quantitative thermal assessment of building envelope. The future work of this investigation will focus on development of a robust protocols to enhance the accuracy of dynamic surveys. Furthermore, the limitations and suggestions in this study require further study on various IR camera technologies. It should be remarked that enhancement of this limitation requires further attention and investigation from researchers and manufacturers towards improving the technology of IR camera for aerial surveys similar to that of a stationary one.

5.6 References

[1] C. Meola, G. M. Carlomagno, Recent advances in the use of infrared thermography, *Measurement Science and Technology*, vol 15, pg R27-R58, 2004

[2] M. Fox, D. Coley, S. Goodhew, and P. De Wilde, Thermography methodologies for detecting energy related building defects, *Renewable and Sustainable Energy Review*, vol 40, pg 296-310, 2014

[3] B. Aragon, K. Johansen, S. Parkes, Y. Malbeteau, S. Al-Mashharawi, T. Al-Amoudi, M.F. McCabe, A calibration procedure for field and UAV-based uncooled thermal infrared instruments. *Sensors*, *20*(11) (2020), 3316.

[4] T. Rakha, A. Gorodetsky, Review of Unmanned Aerial System (UAS) applications in the built environment: Towards automated building inspection procedures using drones. Automation in Construction, 93 (2018) 252-264.

[5] L.E. Mavromatidis, D.J. L, R. Saleri, J.C. Batsale, First experiments for the diagnosis and thermophysical sampling using impulse IR thermography from unmanned aerial vehicle (UAV), Quantitative InfraRed Thermography Conference, Bordeaux, (2014).

[6] L. Ma, M. Li, L. Tong, Y. Wang, L. Cheng, Using unmanned aerial vehicle for remote sensing application, 21st International Conference on Geoinformatics, Kaifeng, (2014).

[7] K.N. Tahar, Aerial terrain mapping using unmanned aerial vehicle approach, Int. Arch. Photogramm. Remote. Sens. Spat. Inf. Sci. XXXIX (B7) (2012) 493–498,

[8] H. Son, S. Lee, C. Kim, Automated 3D model reconstruction to support energy efficiency, Procedia Eng. 145 (2016) 571–578,/

[9] T.D. Stek, Drones over Mediterranean landscapes. The potential of small UAV's (drones) for site detection and heritage management in archaeological survey projects: a case study from le Pianelle in the Tappino Valley, Molise (Italy), J. Cult. Herit. 22 (2016) 1066–1071.

[10] S.M. Adams, M.L. Levitan, C.J. Friedland, High resolution imagery collection utilizing unmanned aerial vehicles (UAVs) for post-disaster studies, Adv. Hurricane Eng. Learning from our Past (2013) 777–793.

[11] A. Ellenberg, A. Kontsos, I. Bartoli, A. Pradhan, Masonry crack detection application of an unmanned aerial vehicle, International Conference on Computing in Civil and Building Engineering, Orlando, (2014).

[12] R. Steffen, W. Forstner, On visual real time mapping for unmanned aerial vehicles, Int. Arch. Photogramm. Remote. Sens. Spat. Inf. Sci. XXXVII (B3a) (2011) 57–62

[13] S. Laguela, L. Diaz-Vilarino, D. Roca, J. Armesto, Aerial oblique thermographic imagery for the generation of building 3D models to complement geographic information systems, 12th International Conference on Quantitative Infrared Thermography (QIRT), Bordeaux, (2015).

[14] I. Lizarazo, V. Angulo, J. Rodriguez, Automatic mapping of land surface elevation changes from UAV- based imagery, Int. J. Remote Sens. 38 (8–10) (2017) 2603–2622.

[15] C. Eschmann, T. Wundsam, Web-based georeferenced 3D inspection and monitoring of bridges with unmanned aircraft systems, J. Surv. Eng. 143 (3) (2017).

[16] S. Laguela, L. Diaz-Vilarino, D. Roca, H. Lorenzo, Aerial thermography from lowcost UAV for the generation of thermographic digital terrain models, Opto-Electron. Rev. 23 (1) (2015) 76–82.

[17] J. Kelly, N. Kljun, P.O. Olsson, L. Mihai, B. Liljeblad, P. Weslien, L. Eklundh, Challenges and best practices for deriving temperature data from an uncalibrated UAV thermal infrared camera. *Remote Sensing*, *11*(5) (2019), 567.

[18] Budzier, H.; Gerlach, G. Calibration of uncooled thermal infrared cameras. J. Sensors Sens. Syst. 4 (2015) 187–197

Chapter 6: Future work

This research presented a first step towards: (1) application of quantitative infrared thermography for thermal assessment of opaque wall assemblies in Canada; and (2) challenges of quantitative infrared thermography with the drone for buildings' energy inspection. Future research can be performed on the following topics:

i. Expanding the viability of proposed methods for other components such as the roof or fenestration.
ii. Determining the reliability of the proposed methodology for various buildings types, such as office buildings in urban areas which are surrounded by different buildings (both construction and architectural aspects) and environmental objects.
iii. Development of a robust protocol for quantitative infrared thermography with UAVs
iv. Developing a methodology for integrating 3D geometry with time (time-coded thermal imaging data) to create a 4D thermographic model that enables real-time visualization of patterns of surface temperature changes in buildings.